Fluvial Landforms and the Post-Noachian Environment on Mars

Sharon Atirah Wilson Purdy
Brooklyn, Wisconsin

B. A., Middlebury College, 2001
M. S., University of Virginia, 2006

A Dissertation presented to the Graduate Faculty
of the University of Virginia in Candidacy for the Degree of
Doctor of Philosophy

Department of Environmental Sciences

University of Virginia
November, 2017

ABSTRACT

Several paradigm shifts have occurred over the past several decades as our understanding of the hydrologic and climatic history of Mars has evolved. It is generally accepted that the early climate on Mars was capable of sustaining an active hydrological cycle, and that (possibly episodic) precipitation and runoff formed the low-to-mid latitude belt of valley networks. Age analyses from crater counts suggests a sudden decline in fluvial activity around the Noachian-Hesperian boundary, presumably associated with the loss of the early denser atmosphere. The climate in the Hesperian and Amazonian was generally considered less favorable for precipitation (most likely snow) and runoff. This paradigm, however, is being challenged by a growing suite of post-Noachian fluvial landforms that support evidence for a late, widespread episode(s) of aqueous activity. Because modification by water and ice on a paleolandscape is one of the most unambiguous markers of past climate, this dissertation investigates fresh shallow valleys (FSVs), deltas, paleolakes, alluvial fans and aqueous-rich ejecta deposits in northern Arabia Terra and northwestern Noachis Terra that formed in the Hesperian and Amazonian. The objective of this dissertation is to provide insight into the environment and associated climate regime that permitted the formation of these post-Noachian fluvial landforms, which furthers our understanding of the potential late-stage habitability of Mars.

TABLE OF CONTENTS

LIST OF FIGURES

LIST OF TABLES

modeling and associated studies of Earth, Mars, Titan and Pluto. The graduate program in the Department of Environmental Sciences was unique in that it offered terrestrial coursework with planetary-focused thesis. Their reasoning was simple: "If you want to be a good planetary geologist, you have to understand Earth processes first."

I cannot express enough gratitude for my advisor, mentor and periodic collaborator, Alan D. Howard. After serving as my adviser for my master's degree, he encouraged me to return to UVa several years later for a PhD and complete my degree while working full-time and raising three young children. Alan is a productive and motivated researcher with an amazing ability to approach scientific problems from every possible angle, leaving no stone left unturned. He is also kind, open-minded, supportive and endlessly generous with his time. I have greatly valued his academic and professional guidance throughout my time in Charlottesville and beyond, and thank him for his friendship, patience and sense of humor as I traveled down this long road.

After receiving my master's degree in 2005, John Grant hired me as a Physical Sciences Technician at CEPS. John has been a wonderful manager, colleague, and friend. Because of his empathy and kindness, he has (somewhat unbelievably) made it possible for me to work at the Smithsonian while earning my PhD. Because of John, I have grown professionally through participation on the HiRISE and Mars Science Laboratory (MSL) rover science teams and through involvement in the Mars landing site selection process. I have greatly enjoyed our conversations ranging from mapping techniques and crater statistics to professional football and stories about raising kids. In short, John's understanding as a fellow parent and encouragement has made my PhD possible.

Many thanks to Pat Wiberg, Paolo D'Odorico, and Bob Johnson, for their ability to instruct and inspire as members of my dissertation committee. Thank you to Michael Pace and the Department of Environmental Sciences Faculty for awarding me the 2017 Maury Prize, which I was humbled and honored to receive.

The work presented in this dissertation resulted from collaborations with fellow scientists who deserve recognition here. In the investigation of fresh shallow valleys in northern Arabia Terra (Chapter 2), I collaborated with Alan Howard, Jeff Moore and John Grant and gained insight from helpful conversations with Nicolas Mangold and reviews from Cathy Quantin-Nataf and Nick Warner. I completed mapping in northwestern Noachis Terra (Chapter 3) in collaboration with John Grant, with constructive conversations with Ross Irwin and Cathy Weitz, and technical support from the mapping experts at the USGS Flagstaff (Corey Fortezzo, Jim Skinner and Trent Hare). The study in Uzboi Vallis (Chapter 4) will be submitted for peer-review with co-authors John Grant, Alan Howard and Debra Buczkowski. The distal deposits from Hale (Chapter 5) was published with John Grant and was enhanced by comments from Peter J. Mouginis-Mark.

In addition to the previously mentioned colleagues, I have greatly enjoyed the intellectual conversations, collaborations and friendships with many others in this field, experiences that have contributed to this dissertation in more subtle ways by refining my thinking and stoking my curiosity. Rebecca Williams, Yo Matsubara, Alex Morgan, Emily Martin, Gareth Morgan, James Wray, Joe Michalski, Becky Ghent, Stephen Tooth, and numerous others on the HiRISE and MSL teams, thank you. Finally, thank you to Bob Craddock for my formative fieldwork experiences in the far-off lands of the Ka'ū Desert in Hawaii and the Simpson Desert in Australia.

I am blessed most importantly with an amazing group of friends and a family whose love and support means the world to me. Thank you to my parents, John and Carole, for believing in me and always being there. Thank you to my siblings, Tricia, Drew, John, Elana, and Leanne, for challenging me to be my best. Thank you to my husband, Michael, and to our three beautiful children (Elijah, 8, Jacob, 6, and Tirzah, 4), and also to our dog, Lucy, for making my life incredibly full and exciting. Completing a PhD, working full-time, moving across the county now and then, losing my father, and raising a young family would not have been possible without an ironclad support system – namely Michael – in addition to seemingly endless love and help from my mother and mother-in-law, Nami. Special thanks to my sister, Elana, for reading parts of this dissertation, and to my friends Ellen Guettler, Lisa Fleisher, and Sufia Dadabhai, for picking up the phone and making me chuckle. Completing a PhD is a privilege, and I am grateful for having the means and opportunity to complete this challenge. Throughout this rewarding experience, I was reminded of something my Dad frequently said throughout our childhood: "no pain, no gain."

Sharon Atirah Wilson Purdy

November 30, 2017

DEDICATION

****

I dedicate this work to my three little explorers:

Tirzah Mae, Jacob Charles and *Elijah Lee*

May you always be curious, inquisitive and loving human beings.

Arlington, Virginia, October, 2014

****

CHAPTER 1. Introduction

The human species is hard-wired to explore. We are inquisitive. We seek to identify patterns in our surroundings as a means to understand our physical world. The vastness and beauty of our night sky invites us to wonder about the origin of the universe, our place in it, how life began, and if life exists (or existed) beyond our home planet. One small red point of light in that night sky – Mars – has captured the imagination of many generations of humans before us. The fascination with our neighboring planet – most likely initially motivated by its brightness and unique red color – is fueled in large part by the myriad similarities between our Earth and Mars. Although Mars is roughly half the diameter of Earth, the two planets have seasons, similar length of day, present-day obliquity, and host familiar landforms including volcanoes, canyons, valleys, and polar ice caps. The present-day conditions on Mars, however, are cold, dry and liquid water is not stable. The atmosphere is thin and there is no evidence of life. Thus, the planets are at once similar and strikingly different, which adds to the mystery and fascination with our red neighbor, named somewhat menacingly after the Roman god of war.

When telescopic investigations of Mars began in the 1600s, astronomers observed variations in the brightness of the planet's surface. Based on their terrestrial experience, this pattern was interpreted as variations in types or amount of vegetation [*Miller*, 2011]. Early explorers gave surface features on Mars romantic, terrestrial-inspired names, such as Margaritifer Sinus (meaning *pearl-bearing gulf or bay*) or Chryse Planitia (Greek for *golden plains*). In the 1870s, the Italian astronomer Giovanni Schiaparelli created beautiful maps of the Martian surface that connected some of the dark regions. Schiaparelli assumed these lines were natural features, like canals, and named them "canali," the Italian word for

"channel." In English, "canali" translates to "canal," which are human-made features and interpreted to be evidence for global-scale engineering by intelligent life – an idea that was popularized during the "Romantic Age" of Martian literature that began near the turn of the 19th century [*Miller*, 2011]. The idea that Mars sustained intelligent life, often depicted as a dying or struggling civilization, was popularized by fiction works such as *War of the Worlds* by H. G. Wells and *Mars as an Abode for Life* by Percival Lowell, an American astronomer.

By the 1960s, telescopic observations of Mars, along with our grand ideas of ancient Martian civilizations, were a thing of the past. In 1965, the American-made Mariner 4 returned the first spacecraft views of the red planet's surface at a resolution of 1 km per pixel, revealing an ancient and cratered surface that looked much like our Moon. The Viking orbiters and landers in the 1970s returned a dataset that scientists mined for nearly thirty years until the Mars Global Surveyor (MGS) went into orbit in 1997, ushering in a new era of Mars exploration. The Mars Orbiter Camera [*Malin et al*., 1998] on board the MGS provided images with resolutions up to ~150 cm/pixel, as well as the first global topographic dataset from the Mars Orbiter Laser Altimeter [*Smith et al*., 1999]. Since 2006, the Mars Reconnaissance Orbiter with its Context (CTX) [*Malin et al*., 2007] and HiRISE (High Resolution Imaging Science Experiment) [*McEwen et al*., 2007] cameras have provided images with unprecedented coverage at unrivaled resolution.

We have also become accustomed to nearly daily "post cards" from our two functioning rovers on Mars: the Mars Exploration Rover (MER) *Opportunity* in Meridiani Planum and the Mars Science Laboratory (MSL) *Curiosity* rover in Gale crater. The rover ground operations are greatly facilitated by the coordinated efforts of orbital instruments such as

HiRISE, CTX and CRISM (Compact Reconnaissance Imaging Spectrometer for Mars) [*Murchie et al.*, 2007] that provide the contextual data to plan the daily activities for the rovers, which are ultimately paving the way for future human exploration. The instruments on the Mars Reconnaissance Orbiter not only chart our path, but also record the rovers' fleeting tracks – some of our first "footprints" on the dusty Martian surface. We are truly in the midst of a data deluge on Mars, with a collection of orbital and rover datasets that will be treasured for decades to come. The goal of exploring our solar system is to find evidence of life, to understand how life on Earth began, and to ultimately understand the origin of our universe. Scientists believe that life on Earth, and perhaps the formation of life more generally, is intimately associated with the presence of water. Therefore, Mars, due to its proximity and geomorphic evidence of past liquid water, has been a target for exploration. Detecting evidence of life on Mars or anywhere in our solar system would undoubtedly be the greatest discovery of humankind – and, if it is out there, I am certain we will find it.

One of the fundamental challenges in the field of planetary science is determining the age, or relative ages, of surfaces using orbital data. During the "period of heavy bombardment" that occurred early in the development of our solar system, there were more frequent, larger impacts. The occurrence of large impacts waned over time, and therefore surfaces that preserve more, larger craters are relatively older than surfaces with fewer larger craters. On Mars, geologic epochs are defined on the basis of geologic events and the size and frequency of craters preserved on the surface [*Carr and Head*, 2010]. The oldest surfaces on Mars are Noachian, named after Noachis Terra, a terrain that is characterized by both large and small impact craters. The Noachian period, from ~4.1 to

~3.7 Ga, experienced heavy bombardment and higher erosion rates relative to later periods on Mars [*Carr and Head,* 2010]. The Hesperian, named after the extensive lava plains of Hesperia Planum, dates to ~3.7 to 3.0 Ga. This period is characterized by flood volcanism and wrinkle ridge formation [*Carr and Head,* 2010]. The cold and arid Amazonian was named after the smooth and sparsely cratered northern plains, Amazonis Planitia. The Amazonian extends from ~3.0 Ga to present and is largely dominated by aeolian processes [*Carr and Head*, 2010].

Over the past twenty years, the suite of data collected by NASA and European space agencies has advanced our understanding of the hydrological and climatologic history of Mars, and is challenging the existing paradigms regarding the evolution of Mars. It is generally accepted that the early Noachian climate on Mars was capable of sustaining an active hydrological cycle, and that (possibly episodic) precipitation and runoff formed the low-to-mid latitude belt of valley networks [*Carr*, 2012; *Craddock and Howard*, 2002; *Grant*, 2000; *Howard et al.*, 2005; *Hynek and Phillips*, 2001; 2003; *Irwin and Howard*, 2002; *Irwin et al.*, 2005]. Age analyses from crater counts suggests a sudden decline in fluvial activity by the early Hesperian, presumably associated with the loss of the early denser atmosphere [*Fassett and Head*, 2008; *Hynek et al.*, 2010; *Fassett and Head*, 2011]. The climate in the Hesperian and Amazonian was always considered to be less favorable for precipitation (most likely snow) and runoff, with aqueous processes restricted to possible hydrothermal runoff on a few volcanic edifices and occasional Hesperian-aged outburst floods. This Viking-era view of a cold, arid post-Noachian Mars is being challenged by a growing inventory of well-preserved fluvial landforms, including fresh shallow valleys (FSVs), deltas, paleolakes and alluvial fans.

The objective of my dissertation, *"Fluvial Landforms and the Post-Noachian Environment on Mars,"* is to provide observations and interpretations about the climate evolution of Mars during the Hesperian and Amazonian by analyzing the geomorphology and distribution of fluvial landforms that formed during these epochs. Results of my work have improved our understanding of the geologic and hydrologic regimes that permitted the formation of these landforms in a post-Noachian climate, ultimately providing insight into the potential late-stage environment and habitability of Mars. Two regions on Mars, both located in the cratered highland terrain, were selected for geomorphic and geologic analyses: northern Arabia Terra (Chapter 2) and northwestern Noachis Terra (Chapters 3, 4 and 5).

Northern Arabia Terra

Northern Arabia Terra is an inherently interesting region due to its location on the margin of the Martian dichotomy, which is the topographic boundary between the cratered highlands and smooth northern lowlands. This region also has one of the highest concentrations of FSVs on Mars, which are smaller and presumably younger than the classic late Noachian valley networks [e.g., *Irwin et al.*, 2005; *Fassett and Head*, 2008; *Dickson et al.*, 2009; *Morgan and Head*, 2009; *Hynek et al.*, 2010; *Warner et al.*, 2010a, 2010b; *Fassett and Head*, 2011; *Howard and Moore,* 2011; *Adeli et al.*, 2016; *Salese et al.*, 2016]. These "young" valleys are morphologically distinct from both ancient valley networks and gullies [e.g., *Malin and Edgett*, 2000; *Dickson et al.*, 2009; *Fassett et al.*, 2010; *Howard and Moore*, 2011; *Hobley et al.*, 2014]. Chapter 2 maps the distribution of FSVs and their associated landforms including "pollywog" craters, deltas, and basin floor deposits. This investigation uses high-resolution image and topographic datasets to

characterize the morphology, occurrence, age, and the possible source(s), magnitudes and frequency of the formative flows responsible for FSV formation in northern Arabia Terra. A regional hydrologic routing model examines flow paths of water across the landscape and estimates the volume and area of filled depressions. Possible correlations between impact processes and valley formation were investigated by analyzing relationships between FSVs and crater ejecta, including their association with variables such as crater age, size, latitude and ejecta elevation and morphology. This research address the question of whether the FSVs formed as a result of a multiplicity of local mechanisms occurring as temporally scattered events (e.g., impact related) versus one or more episodes of widespread fluvial activity related to a global interval of favorable climate in the Hesperian to mid Amazonian.

Northwestern Noachis Terra

Images from the Mariner missions in the 1970s provided our first views of valleys and channels on Mars [*Schultz and Ingerson*, 1973], offering compelling evidence for a surface that was modified by liquid water. One of the most impressive valley systems on the planet is located in Margaritifer Terra and adjacent northwestern Noachis Terra. Overflow along the northern rim of the ~900 km-diameter Argyre basin created Uzboi Vallis, Ladon Valles and Morava Valles during the Noachian to Hesperian [e.g., *Saunders*, 1979; *Grant*, 1987; *Grant and Parker*, 2002; *Irwin and Grant*, 2013]. This meso-scale outflow system incised through the cratered highlands and debouched into the northern lowlands, preserving a long record of aqueous activity. Geologic mapping (1:1,000,000 scale) of four quadrangles in this region was undertaken to constrain the timing, source, duration and relative importance of aqueous versus other geomorphic processes (Chapter 3). The map area (17.5°S-32.5°S

between 320°E-325°E and 27.5°S-32.5°S between 325°E-330°E) encompasses Uzboi Vallis and surrounding terrain as well as the ancient Vinogradov basin, which is flanked by three craters that host alluvial fans (craters Roddy, Gringauz and Luba). The mapping was done using ArcGIS, a geographic information system (GIS) from the Environmental Systems Research Institute (ESRI). Standard mapping techniques were employed [*Tanaka et al.*, 2011] using a collection of projected base maps (image, thermal, topographic) at varying resolutions that were provided by the U.S. Geological Survey. The map results contributed directly to the observations and interpretations of the evolution of Uzboi Vallis presented in Chapter 4 and of the geomorphic effects of the Hale impact in Chapter 5. These findings provide insight into the climatic history and environmental conditions in the Late Hesperian and Early Amazonian, respectively.

The evolution of Uzboi Vallis (centered at ~28ºS, 323ºE), the southernmost segment of the Uzboi-Ladon-Morava (ULM) outflow system, is described in Chapter 4 in light of a recently recognized mound of material on Uzboi's floor at the mouth of Nirgal Vallis [*Wilson and Grant*, 2016a, 2016b, 2016c; *Wilson et al.*, 2017a, 2017b]. This study synthesizes image, topographic and spectral data to describe the morphology, structure, volume, and possible source(s) of the mound of material on the floor of Uzboi. The identification and characterization of the material on the floor of Uzboi is significant because it informs the timing of fluvial activity within Uzboi and possibly Nirgal Vallis, and may help constrain the source(s) of water for the Late Hesperian lake in Uzboi [*Grant et al.*, 2011]. This investigation also sheds light on the relationship between the late-stage evolution of Nirgal, Uzboi and the greater ULM outflow system, which in turn contributes

fundamental insight into the hydrologic environment, associated climate, and potential habitability during the Late Hesperian.

Hale crater is a 125 km by 150 km-diameter oblong impact that formed in the Early to Middle Amazonian [*Cabrol et al.*, 2001; *Jones et al.*, 2011] along the northern rim of the Argyre basin. The impact caused the emplacement of a variety of relatively fine-grained fluidized ejecta that incorporated significant amounts of water, as described in Chapter 5. Previous studies have shown that very large impact craters (>100 km in diameter) likely influenced the Noachian climate [e.g., *Segura et al.*, 2002], but the association between comparably sized Hesperian- and Amazonian-aged craters and sustained global or regional geomorphic activity has not been investigated and is less certain [*Irwin*, 2013]. Chapter 5 incorporates high resolution images and topographic data to characterize the emplacement, nature and distribution of the ejecta in order to understand the extent and duration of any regionally enhanced geomorphic activity that resulted from (or was sustained by) the young, large Hale impact. This study provides insight into the climate, environmental conditions, and degradational history of Amazonian Mars and constrains the timing of alluvial fan formation in this region [e.g., *Moore and Howard*, 2005; *Kraal et al.*, 2008; *Grant and Wilson*, 2011, 2012].

The Discussion (Chapter 6) summarizes the significance of the individual Chapters and provides a review of our current understanding of the post-Noachian environment on Mars. The extension of habitable conditions on Mars beyond the Noachian epoch is exciting from an astrobiological standpoint, as periods of warming that allowed liquid water to exist on the Martian surface may have provided favorable conditions for life to form or persist. This research will help inform potential future landing sites for robotic and eventual human

8

exploration, as they identify places on Mars that were modified by the latest episode(s) of widespread fluvial activity. Chapter 6 concludes with final thoughts about how this research contributes to the broader field of planetary geology, exploration of space, and our search for life beyond Earth.

1.1   References

Adeli, S., E. Hauber, M. Kleinhans, L. Le Deit, T. Platz, P. Fawdon and R. Jaumann (2016), Amazonian-aged fluvial system and associated ice-related features in Terra Cimmeria, Mars, *Icarus*, *288*, 286-299, http://dx.doi.org/10.1016,/j.icarus.2016.05.020.

Cabrol, N. A., D. D. Wynn-Williams, D. A. Crawford and E. A. Grin (2001), Recent aqueous environments in Martian impact craters: An astrobiological perspective, *Icarus*, *154*, (1), 98-112, doi:10.1006/icar.2001.6661.

Carr, M. H. (2012), *The fluvial history of Mars*, Philosophical Transactions of the Royal Society of London Series A, 370, 2193-2215.

Carr, M. H. and J. W. Head (2010), Geologic history of Mars, *Earth and Planetary Science Letters*, *294*(3-4), 185-203.

Craddock, R. A. and A. D. Howard (2002), The case for precipitation on a warm, wet early Mars, *J. Geophys. Res.*, *107* (E11), doi:10.1029/2001JE001505.

Dickson, J. L., C. I. Fassett and J. W. Head (2009), Amazonian-aged fluvial valley systems in a climatic microenvironment on Mars: Melting of ice deposits on the interior of Lyot Crater, *Geophys. Res. Lett.*, *36*, L08021, doi:10.1029/2009GL037472.

Fassett, C. I. and J. W Head (2008), Timing of martian valley network activity: Constraints from buffered crater counting, *Icarus*, *198*, 61-89.

Fassett, C. I. and J. W. Head (2011), Sequence and timing of conditions on early Mars, *Icarus*, *211*, 1204-1214.

Fassett, C. I., J. L. Dickson, J. W. Head, J. S. Levy and D. R. Marchant (2010), Supraglacial and proglacial valleys on Amazonian Mars, *Icarus*, *208*, 86-110.

Grant, J. A. (1987), The Geomorphic Evolution of Eastern Margaritifer Sinus, Mars, Advances in Planetary Geology, *NASA Tech. Memo*. 89871, pp. 1–268.

Grant, J. A. (2000), Valley formation in Margaritifer Sinus, Mars, by precipitation-recharged ground-water sapping, *Geology*, *28* (3), 223-226.

Grant, J. A. and T. J. Parker (2002), Drainage evolution of the Margaritifer Sinus region, Mars. *J. Geophys. Res*., 107. doi:10.1029/2001JE001678.

Grant, J. A. and S. A. Wilson (2011), Late alluvial fan formation in southern Margaritifer Terra, Mars, *Geophysical Res. Letts., 38*, L08201.

Grant, J. A. and S. A. Wilson (2012), A possible synoptic source of water for alluvial fan formation in southern Margaritifer Terra, Mars, *Planetary Space Sci*., *72*, 44-52.

Grant, J. A., R. P. Irwin III, S. A. Wilson, D. Buczkowski and K. Siebach (2011), A lake in Uzboi Vallis and implications for the Late Noachian-Early Hesperian climate on Mars, *Icarus*, *212* (1), 110–122, https://doi.org/10.1016/j.icarus.2010.11.024.

Hobley, D. E. J., A. D. Howard and J. M. Moore (2014), Fresh shallow valleys in the Martian midlatitudes as features formed by meltwater flow beneath ice, *J. Geophys. Res*., DOI: 10.1002/2013JE004396.

Howard, A. D. and J. M. Moore (2011), Late Hesperian to early Amazonian midlatitude Martian valleys: Evidence from Newton and Gorgonum basins, *J. Geophys. Res*., *116*, E05003, doi:10.1029/2010JE003782.

Howard, A. D., J. M. Moore and R. P. Irwin, III (2005), An intense terminal epoch of widespread fluvial activity on early Mars: 1. Valley network incision and associated deposits, *J. Geophys. Res*., *110* (D12S14), doi:10.1029/2005JE002459.

Hynek, B. M. and R .J. Phillips (2001), Evidence for extensive denudation of the Martian highlands, *Geology*, *29* (5), 407-410.

Hynek, B. M. and R. J. Phillips (2003), New data reveal mature, integrated drainage systems on Mars indicative of past precipitation, *Geology*, *31* (9), 757-760.

Hynek, B. M., M. Beach and M. R. T. Hoke (2010), Updated global map of Martian valley networks and implications for climate and hydrologic processes, *J. Geophys. Res*., *115*, E09008, doi:10.1029/2009JE003548.

Irwin, R. P. III (2013), Testing links between impacts and fluvial erosion on post-Noachian Mars, *Lunar and Planetary Science XXXXIV*, Abstract 2958.

Irwin, R. P., III and A. D. Howard (2002), Drainage basin evolution in Noachian Terra Cimmeria, Mars, *J. Geophys. Res*., *107* (E7), 10.1029/2001JE001818.

Irwin, R. P. and J. A. Grant (2013), Geologic map of MTM -15027, -20027, -25027, and -25032 Quadrangles, Margaritifer Terra Region of Mars, USGS Map I-3209.

Irwin, R. P., III, T. A. Maxwell, A. D. Howard, R. A. Craddock and J. M. Moore (2005), An intense terminal epoch of widespread fluvial activity on early Mars: 2. Increased runoff and paleolake development, *J. Geophys. Res*., *110*, E12S15, doi:10.1029/2005JE002460.

Jones A. P., A. S. McEwen, L. L. Tornabene, V. R. Baker, H. J. Melosh and D. C. Berman (2011), A geomorphic analysis of Hale crater, Mars: The effects of impact into ice-rich crust, *Icarus*, *211* (1), 259-272, doi:10.1016/j.icarus.2010.10.014.

Kraal, E.R., E. Asphaug, J. M. Moore, A. Howard and A. Bredt (2008), Catalogue of large alluvial fans in Martian impact craters, *Icarus, 194*, 101–110.

Malin, M. C. and K. S. Edgett (2000), Evidence for recent groundwater seepage and surface runoff on Mars, *Science*, *288*, 2330-2335.

Malin, M. C., M. H. Carr, G. E. Danielson, M. E. Davies, W. K. Hartmann, A. P. Ingersoll, P.B. James, H. Masursky, A. S. McEwen, L. A. Soderblom, P. Thomas, J. Veverka, M. A. Caplinger, M. A. Ravine, T. A. Soulanille and J. L. Warren (1998), Early views of the Martian surface from the Mars Orbiter Camera of Mars Global Surveyor, *Science, 279*(5357), 1681-1685, DOI: 10.1126/science.279.5357.1681.

Malin, M. C., et al. (2007), Context Camera Investigation on board the Mars Reconnaissance Orbiter, *J. Geophys. Res.*, *112*, E05S04, doi:10.1029/2006JE002808.

McEwen, A. S., et al. (2007), Mars Reconnaissance Orbiter's High Resolution Imaging Science Experiment (HiRISE), *J. Geophys. Res.*, *112*, E05S02, doi:10.1029/2005JE002605.

Miller, J. D. (2011), "Mars of Science, Mars of Dreams," in *Visions of Mars: Essays on the Red Planet in Fiction and Science*, Eds., H. V. Hendrix, G. Slusser, E. S. Rakin, McFarland & Company, North Carolina, USA.

Moore, J. M. and A. D. Howard (2005), Large alluvial fans on Mars, *J. Geophys. Res.*, *110*, E04005, doi:10.1029/2004JE002352.

Morgan, G. A. and J. W Head (2009), Sinton crater, Mars: Evidence for impact into a plateau icefield and melting to produce valley networks at the Hesperian-Amazonian boundary, *Icarus*, *202*, 39-59.

Murchie, S., et al. (2007), Compact Reconnaissance Imaging Spectrometer for Mars (CRISM) on Mars Reconnaissance Orbiter (MRO), *J. Geophys. Res.*, *112*, E05S03, doi:10.1029/2006JE002682.

Salese, F., G. Di Achille, A. Neesemann, G. G. Ori and E. Hauber (2016), Hydrological and sedimentary analyses of well-preserved paleofluvial-paleolacustrine systems at Moa Valles, Mars, *J. Geophys. Res. Planets*, 121, doi:10.1002/2015JE004891.

Saunders, S. R. (1979), Geologic Map of the Margaritifer Sinus Quadrangle of Mars, *U.S. Geol. Surv. Misc. Invest. Ser*. Map I-1144, Scale 1:5M.

Schultz, P. H. and F. E. Ingerson (1973), Martian lineaments from Mariner 6 and 7 images, *J. Geophys. Res*., 78(35), 8415–8427, doi:10.1029/JB078i035p08415.

Segura, T. L., O. B. Toon, A. Colaprete and K. Zahnle (2002), Environmental effects of large impacts on Mars, *Science*, 298(5600), 1977-1980, doi:10.1126/science.1073586.

Smith, D. E., and 18 others (1999), The global topography of Mars and implications for surface evolution, *Science*, *284*, 1495-1503.

Tanaka, K. L., J. A. Skinner and T. M. Hare (2011), *Planetary Geologic Mapping Handbook*, 24 pp., U.S. Geological Survey, Flagstaff, AZ.

Warner, N., S. Gupta, J-R. Kim, S.-Y Lin and J.-P. Muller (2010a), Hesperian equatorial thermokarst lakes in Ares Vallis as evidence for transient warm conditions on Mars, *Geology*, *38* (1), 71–74, doi:10.1130/G30579.1

Warner, N. S., S. Gupta, S-Y. Lin, J. –R. Kim, J.-P. Muller, and J. Morley (2010b), Late Noachian to Hesperian climate change on Mars: Evidence of episodic warming from transient crater lakes near Ares Vallis, *J. Geophys. Res*., *115*, E06013, doi:10.1029/2009JE003522.

Wilson, S. A. and J. A. Grant (2016a), Geologic mapping in Margaritifer Terra on Mars and a closer look at the confluence of Nirgal and Uzboi Valles, *47th Lunar and Planetary Science Conference*, Abstract 2505, Houston, TX.

Wilson, S. A. and J. A. Grant (2016b), Geologic Mapping in Southern Margaritifer Terra on Mars: Constraining the Timing of Fluvial Activity in Nirgal Vallis, *Annual Planetary Geologic Mappers Meeting*, Abstract 7034, Flagstaff, AZ.

Wilson, S. A. and J. A. Grant (2016c), Evidence for Late Hesperian fluvial activity in Nirgal Vallis on Mars*, Geol. Soc. of America Abstracts with Programs*, Abstract 283852, Denver, CO, September 24-28.

Wilson, S. A., J. A. Grant and D. L. Buczkowski (2017a), The evolution of Nirgal Vallis, Mars, *48th Lunar and Planetary Science Conference*, Houston, TX, Abstract 2663.

Wilson, S. A., J. A. Grant and D. L. Buczkowski (2017b), Geologic mapping in Southern Margaritifer Terra and the evolution of Nirgal Vallis on Mars, *Annual Planetary Geologic Mappers Meeting*, Flagstaff, AZ.

CHAPTER 2. Fresh Shallow Valleys in Northern Arabia Terra

Abstract

     The growing inventory of post-Noachian fluvial valleys may represent a late, widespread episode of aqueous activity on Mars, contrary to the paradigm that fluvial activity largely ceased around the Noachian-Hesperian boundary. Fresh shallow valleys (FSVs) are widespread from ~30-45° in both hemispheres with a high concentration in northern Arabia Terra. Valleys in northern Arabia Terra characteristically start abruptly on steeper slopes and terminate in topographic depressions at elevations corresponding to model-predicted lake levels. Longer valley systems flowed into and out of chains of paleolakes. Minimum discharges based on the dimensions of the incised channel assuming medium to coarse sand-size grains ranges from 10s to 100s m^3 s^{-1}, respectively, consistent with formation via snowmelt from surface or sub-ice flows. Hydrologic calculations indicate the valleys likely formed in hundreds of years or less, and crater statistics constrain the timing of fluvial activity to between the Hesperian and mid Amazonian. Several craters with channels extending radially outward supports evidence for overflow of interior crater lakes possibly fed by groundwater. Most FSVs occur away from young impact craters which makes an association with impact processes improbable. The widespread occurrence of FSVs along with their similar morphology and shared modest state of degradation is consistent with most forming during a global interval of favorable climate, perhaps contemporaneous with alluvial fan formation in equatorial and mid-latitudes. Evidence for a snowmelt based hydrology and considerable depths of water on the landscape in Arabia supports a cold, wet and possibly habitable environment late in Martian history.

2.1   Introduction

Several paradigm shifts have occurred over the past several decades as our understanding of the hydrological and climatologic history of Mars has evolved. It is generally accepted that the early climate on Mars was capable of sustaining an active hydrological cycle, and that (possibly episodic) precipitation and runoff formed the low-to-mid latitude belt of valley networks [*Grant*, 2000; *Hynek and Phillips*, 2001, *Craddock and Howard*, 2002; *Irwin and Howard*, 2002; *Hynek and Phillips*, 2003; *Howard et al.*, 2005; *Irwin et al.*, 2005a, *Carr*, 2012]. Age analyses from crater counts suggests a sudden decline in fluvial activity by the early Hesperian, presumably associated with the loss of the early denser atmosphere [*Fassett and Head*, 2008; *Hynek et al.*, 2010; *Fassett and Head*, 2011]. The climate in the Hesperian and Amazonian was generally considered to be less favorable for precipitation (most likely snow) and runoff, with aqueous processes restricted to possible hydrothermal runoff on a few volcanic edifices and occasional outburst floods. This view of a cold, arid post-Noachian Mars is being challenged by a growing inventory of well-preserved mid-latitude and equatorial fluvial valleys that are smaller and presumably younger than the classic late Noachian valley networks [e.g., *Irwin et al.*, 2005a; *Fassett and Head*, 2008; *Dickson et al.*, 2009; *Morgan and Head*, 2009; *Hynek et al.*, 2010; *Warner et al.*, 2010a, 2010b; *Fassett and Head*, 2011; *Howard and Moore,* 2011; *Adeli et al.*, 2016; *Salese et al.*, 2016].

These "young" valleys are morphologically distinct from both ancient valley networks and gullies [e.g., *Dickson et al.*, 2009; *Fassett et al.*, 2010; *Howard and Moore*, 2011; *Hobley et al.*, 2014]. The Noachian valley networks are deeply incised (50-250+ m), form strongly parallel to dendritic networks, and are heavily degraded. By contrast, gullies

16

[*Malin and Edgett*, 2000] are characterized by well-defined source areas, higher gradients, and are in general narrower and shorter in length [*Fassett et al.*, 2010] (Fig. 2.1). The "fresh shallow valleys" (FSVs), presented in this study, are defined by their morphology [*Hobley et al.*, 2014]. The term *fresh* implies the valleys lack significant overall degradation at the resolution of images from the Context Camera (CTX, ~6 m per pixel scale [*Malin et al.*, 2007]) and minimal modification of the valley sidewalls, which is consistent with their inferred post-Noachian age [e.g., *Howard and Moore*, 2011; *Hobley et al.*, 2014]. At a sub-meter to meter scale, however, FSVs in the mid latitudes are typically modified by mantling material likely related to periglacial processes [*Howard and Moore*, 2011; *Hobley et al.*, 2014]. FSVs are narrow (typically less than 500 m) and *shallow,* generally incising no more than a few decameters into the surrounding terrain.

This investigation uses high-resolution image and topographic datasets to characterize the morphology, occurrence, age, and the possible source(s), magnitudes and frequency of the formative flows responsible for FSV formation in northern Arabia Terra. A regional hydrologic routing model examines flow paths of water across the landscape and estimates the volume and area of filled depressions. Possible correlations between impact processes and valley formation were investigated by analyzing relationships between FSVs and crater ejecta including their association with variables such as crater age, size, latitude and ejecta elevation and morphology. We address the question of whether the FSVs formed as a result of a multiplicity of local mechanisms occurring as temporally scattered events (e.g., impact related) vs. one or more episodes of widespread fluvial activity related to a global interval of favorable climate. This distinction is important, as it provides insight into the geologic and climatic environments that permitted

the formation of FSVs in a post-Noachian climate with implications for potential late-stage

habitability on Mars.
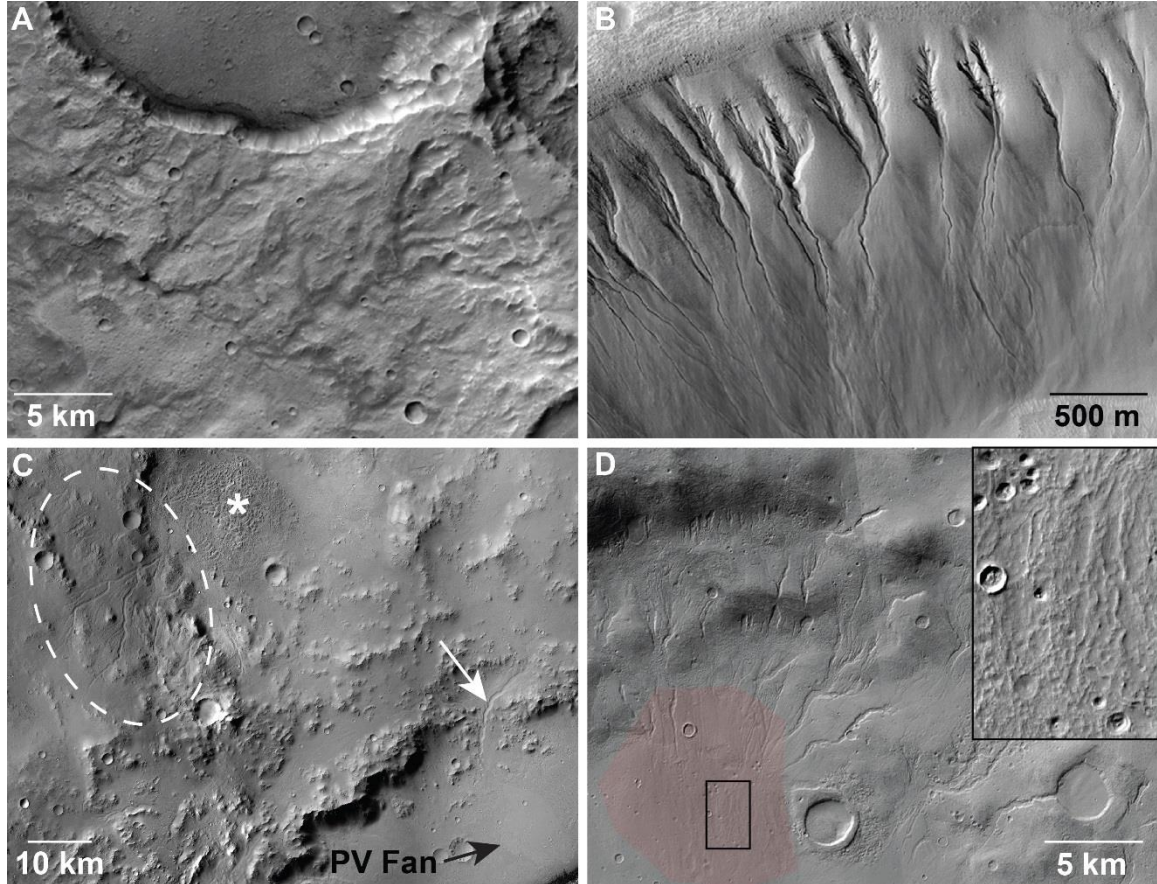
Figure 2.1   Morphology and characteristics of valleys on Mars

A) Noachian-Hesperian valley networks in the southern highlands of Mars are generally deeply incised, strongly dendritic and heavily degraded relative to fresh shallow valleys (FSVs). Example of a dissected outer crater rim near 25°S, 154°E. Subframe of CTX P11_005259_1541 (5.14 m scaled pixel width). **B**) Gullies [*Malin and Edgett*, 2000] have well-defined source areas, higher gradients, and are in general narrower and shorter in length relative to FSVs. Subframe of HiRISE PSP_003418_1335 (25 cm scaled pixel width) in Noachis Terra near 46ºS, 18.8°E. **C**) FSVs in the equatorial region commonly form on interior and exterior crater rims, such as Peace Vallis (white arrow) on the northern rim of Gale crater, which terminates in the Peace Vallis (PV) fan (black arrow). FSVs northwest of Gale (white dashed circle) are weakly dendritic, often with constant valley widths and indistinct headwater source, terminating in a fan-shaped deposit ("*"). Subframe of HRSC H5273 centered near 4.2°S, 136.8°E. **D**) FSVs are commonly incised into the latitude dependent mantle and flat valley floors can be modified ice-related processes [*Moore and Howard*, 2005]. FSVs originating on an interior crater rim of an unnamed crater (near 39.2°S, 19.3°E) terminate in a small fan deposit (shaded red); inset

(black box) shows inverted channels on fan surface [modified from *Howard et al*., 2014]. Subframes of CTX B17_016340_1402 (5.14 m scaled pixel width) and P16_007255_1411 (5.09 m scaled pixel width). North to top in all images.

2.2   Background

2.2.1   Morphology and Nature of FSVs

Previous studies have identified two morphological types of FSVs [*Hobley et al*., 2014] (Fig. 2.2A). Type 1 valleys are narrow, sinuous, entrenched valleys typically with sharp upper edges at scale of CTX images. They are generally 'V' to slightly 'U-shaped' with widths of 20–50+m, and may range from a few hundred meters to several kilometers in length [*Hobley et al*., 2014]. Type 1 valleys are often unbranched, start and terminate abruptly by narrowing and shallowing, and may lack obvious fluvial features upstream or downstream. Along relatively straight reaches, FSVs exhibit relatively constant widths and depths. Several Type 1 valleys may chain together and can be connected to (or interspersed with) Type 2 valleys. Type 2 valleys are generally wider with near-parallel borders and nearly flat floors that sometimes exhibit low longitudinal lineations that could be bedforms. These apparent bedforms, analogous to fluvial bars, low banks, or braiding, could have formed as a result of migrating flows within the floodplain (Figs. 2.2A and 2.9B).

FSVs can be locally integrated into dendritic patterns but are usually not space-filling networks. Individual FSVs often occur as scattered, isolated valleys or sparsely branched networks with individual valleys generally not extending more than a few tens of kilometers (Figs. 2.1 and 2.2). They are generally but not universally associated with high-relief surfaces, such as the interior and exterior slopes of impact craters. Some terminate in fans or deltas as seen in Xanthe Terra [*Hauber et al*., 2013], the sparse network feeding the

Eberswalde crater delta [*Howard et al.*, 2005], connecting fans to the interior rim of Bakhuysen crater [*Moore and Howard,* 2005] and on the rim and exterior of the Late Noachian to Hesperian-age Gale crater [e.g., *Grant et al.*, 2014; *Palucis et al.*, 2014] (Fig. 2.1).
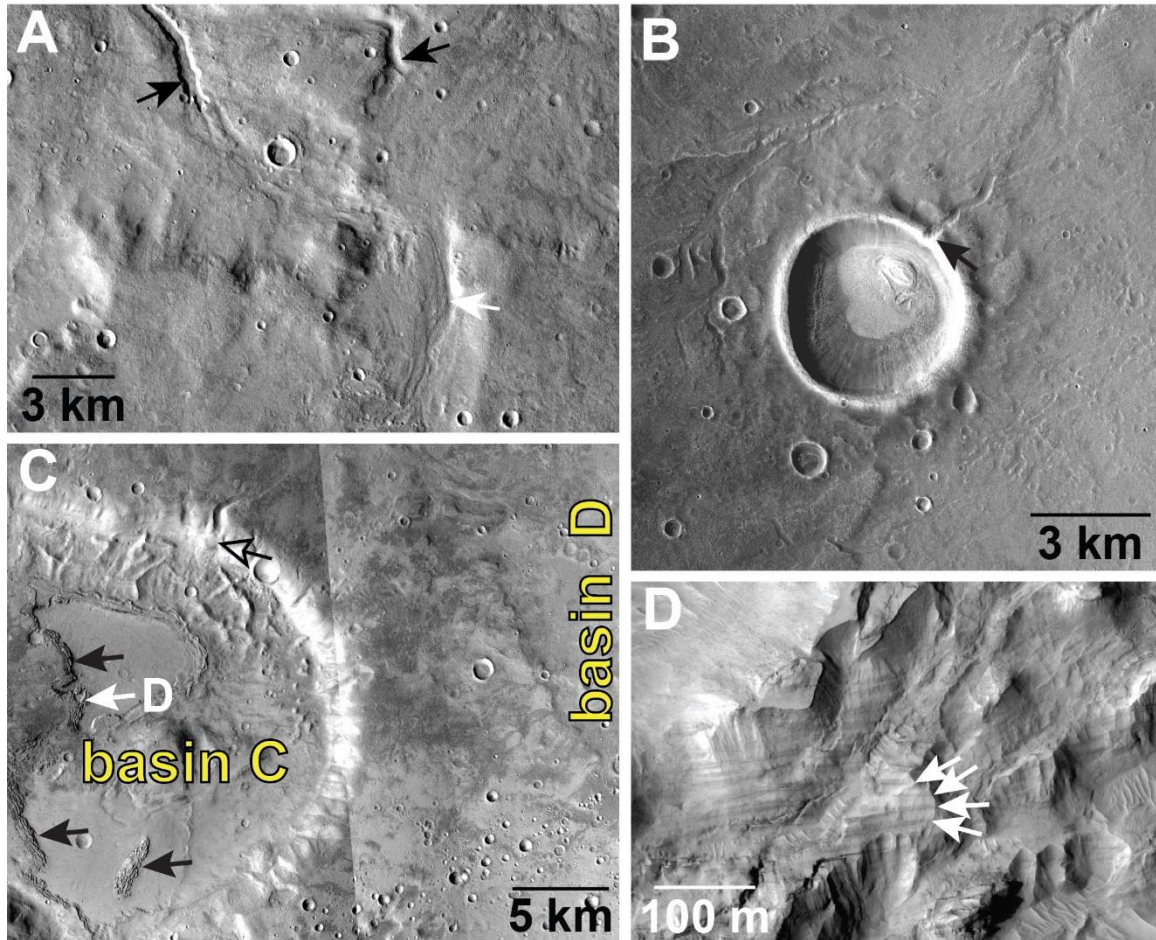
Figure 2.2   Examples of landforms discussed throughout text

A) *Morphological Types of FSVs* [after *Hobley et al.*, 2014]. Type 1 valleys (black arrows) are narrowly incised and Type 2 valleys (white arrow) are wider, shallower and sometimes have apparent bedforms (see Fig. 2.4 for context). Subframe of CTX P03_002284_2181 (5.88 m scaled pixel width). **B**) *Pollywogs*. "Pollywog" craters (black arrow) have a single channel that extends outward from their rim (see Fig. 2.4 for context). Crater is ~4.3 km diameter and is located near 35.0ºN, 8.0ºE. Subframe of CTX B16_015984_2149 (5.83 m scaled pixel width). **C**) *Deltas and Basin Floor Deposits*. Small lobe-shaped deposit (hollow black arrow) on northern interior rim of basin C inferred to be a sedimentary delta (see Fig 2.7A for context). The FSV and associated delta formed as water overflowed from

basin D into basin C (via a small water-filled depression in between). See Table 2.2 and additional deltas in Figs. 2.10 and 2.14C-E. *Basin floor deposits* (black arrows) occur on the lowest elevations of several model-predicted filled basins. The surface of these deposits have troughs oriented roughly parallel to the basin walls. These deposits can also occur as isolated mounds (see bottom black arrow and Fig. 2.8B). White arrow indicates location of Fig. 2.2D. Subframes of CTX images P01_001440_2174, P15_006807_2187 and P17_007809_2169 (~5.9 m scaled pixel width). **D**) *Detail of Basin Floor Deposits*. Horizontal, layers exposed in scarp of basin floor deposits. Deposit is fine-grained, massive, repetitive packages of ~10 m thick medium-toned layers separated by thinner dark toned layers. These deposits may consist of ice-rich sediment that was deposited in a standing water environment. Subframe of HiRISE PSP_001440_2175 (29.5 cm scaled pixel width). North to top in all images.

2.2.2   Occurrence and Global Distribution of FSVs

FSVs occur in a variety of settings including the flanks of volcanoes [*Gulick and Baker*, 1990; *Gulick*, 2001a; *Fassett and Head*, 2006; 2007], crater interiors [*Dickson et al.*, 2009; *Howard and Moore*, 2011; *Parsons et al.*, 2013; *Hobley et al.*, 2014;], intercrater plains and on the ejecta of young impact craters [*Morgan and Head*, 2009; *Jones et al.*, 2011; *Mangold*, 2012; *Mangold et al.*, 2012;]. These valleys are also commonly associated with Amazonian-age glacial features such as lobate debris aprons, concentric crater fills, viscous flow features, and lineated valley fills [*Fassett et al.*, 2010; *Adeli et al.*, 2016;], and in some cases the valleys may represent a period of reactivation of the Noachian-Hesperian aged valley networks that locally terminate as small deltas in Hesperian basins [*Irwin et al.*, 2005a].

FSVs are modified at the sub-meter to meter scale by "pasted on" deposits and hummocky topography related to "terrain softening," a non-fluvial process that modified Noachian to early Hesperian craters and may have continued into the late Amazonian in mid- to high-latitude locations [*Soderblom et al.*, 1973; *Mustard et al.*, 2001; *Berman et al.*, 2009; *Willmes et al.,* 2011] (Fig. 2.1D). This latitude dependent mantle may have

formed as a result of obliquity variations that mobilized water ice from the poles to the mid-latitude regions [e.g., *Head et al.*, 2003; *Laskar et al.*, 2004]. In most cases, much of the modification related to the latitude dependent mantle occurred prior to the formation of FSVs based on their superposition into the softened terrain and their largely fresh appearance at the resolution of CTX images (Fig. 2.1D).

A global survey of CTX images as of late 2012 that builds upon previous mapping [*Fassett et al.*, 2010; *Mangold,* 2012] reveals that FSVs are widely distributed (Fig. 2.3). The valleys occur in a latitude band between ~35-42º in the northern and southern hemispheres and are most easily recognized where they incise into the smooth latitude dependent mantle (which occurs poleward of ~35° in both hemispheres). Valleys in the northern hemisphere generally occur along the dichotomy boundary with clusters in Tempe Terra and northern Arabia Terra (Fig. 2.3). FSVs commonly occur in clusters that range from several valleys on the ejecta of a single impact crater to widely distributed valleys. FSVs also occur in the equatorial regions (e.g., Gale crater and surroundings, Fig. 2.1C) but are often hard to distinguish from Noachian valley networks.
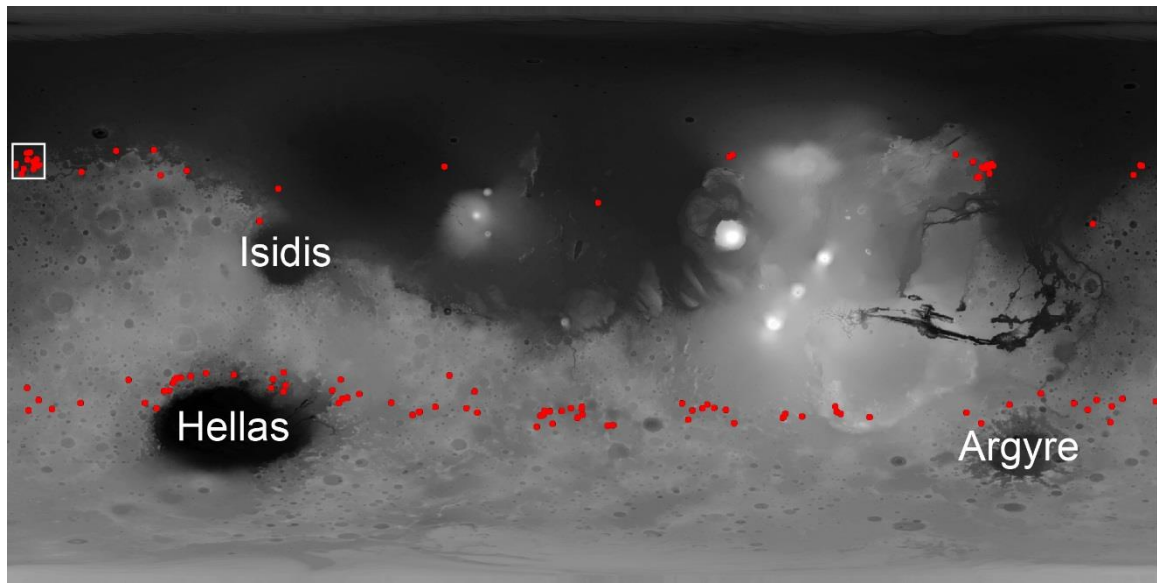
Figure 2.3   Global survey of fresh shallow valleys

Global survey of CTX data shows clusters of FSVs (red dots) that occur in a tight latitude band between ~35-42º in the northern and southern hemispheres. Northern Arabia Terra, roughly 30-40°N between 0-10ºE, has one of the highest concentrations of FSVs on Mars (white box, see Fig. 2.4). Global MGS MOLA Elevation Model (90°N to -90°N, -180°E to 180°E).

2.2.3   The Northern Arabia Terra Landscape and Associated Landforms

Northern Arabia Terra in USGS quadrangle Ismenius Lacus (Mars Chart 05) records a long history of aqueous activity from the Noachian through the Amazonian [*Mangold and Howard*, 2013]. Located south of the dichotomy boundary, the study region (30-40°N between 2°W-10ºE) is characterized by a low-lying (< -2 km relative to the MOLA datum) cratered landscape that contains putative ancient volcanic calderas mapped as Ismenia and Siloe Patera [*Michalski and Bleacher*, 2013] (Fig. 2.4). Several large depressions ~30 km wide and up to 1 km deep formed by deeply seated subsidence in the Noachian prior to the formation of the FSVs [*Mangold and Howard*, 2013]. Well-developed Noachian valley networks are notably absent from this terrain [e.g., *Luo and Stepinski*, 2009; *Hynek et al*., 2010] but the late Noachian-early Hesperian Okavango Vallis

outflow system is located on the eastern margin of the study area [*Mangold and Howard*, 2013] (Fig. 2.4).
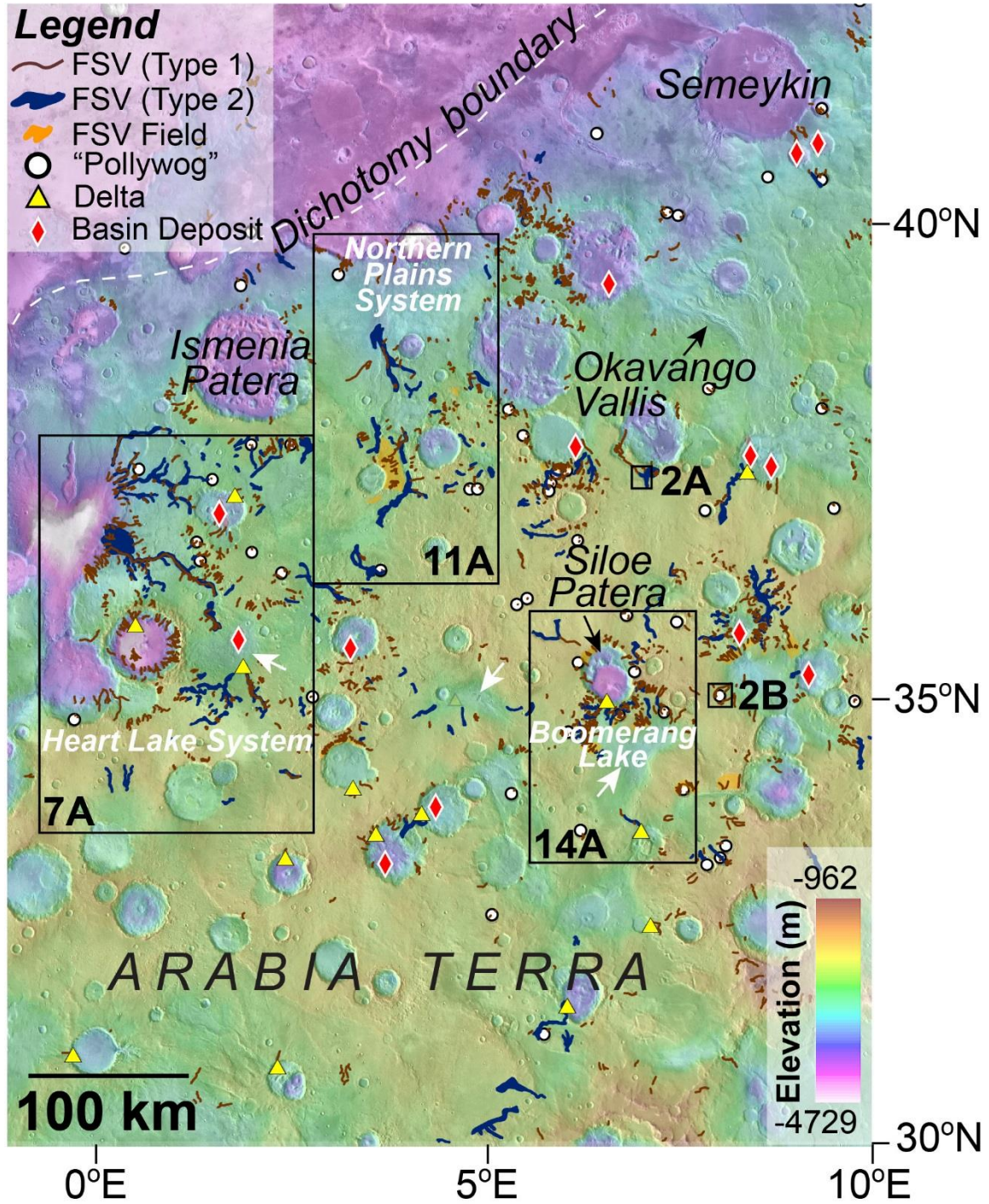
Figure 2.4   Study region in northern Arabia Terra in southwest Ismenius Lacus

Study region in Northern Arabia Terra in southwest Ismenius Lacus (see Fig. 2.3 for context) with major place names labeled for reference. South of the dichotomy boundary, this softened cratered landscape has many broad, Noachian-aged depressions (e.g., white arrows) and is dissected by FSVs (brown and blue lines are Types 1 and 2, respectively, see Fig. 2.2A). Some FSVs breach crater rims and terminate in small deltaic deposits (yellow triangles, see Fig. 2.2C) whereas other FSVs occur as single channels that extend outward from craters rim ("pollywogs") implying overflow of a crater lake (white circles, see Fig. 2.2B). A FSV "Field" indicates areas that are heavy dissected. Basin floor deposits are indicated by red diamonds (Figs. 2.2C-D, 2.8B). Black boxes show locations of Figs. 2.2A, 2.2B, 2.7A (Heart Lake valley system), 2.11A (Northern Plains valley system) and 2.14A (Boomerang Lake valley system). MOLA topography over subframe of THEMIS Day IR mosaic. The width of type 1 FSVs is exaggerated for clarity in regional maps (Figs. 2.4, 2.6, 2.7, 2.11 and 2.14).

This area contains a high concentration of FSVs, some of which incise crater rims. Craters with an outlet valley, characterized by a single valley extending outward from the rim and no inflowing valleys are informally named "pollywogs" (Fig. 2.2B). Pollywog craters most commonly have 1 valley but some craters have 2-3 valleys extending outward from their rims, with the channel generally oriented toward the nearest topographic low.

Lobe or fan-shaped deposits within craters at the mouth of inlet valleys are inferred to be sedimentary (Figs. 2.2C, 2.4 and 2.6) [e.g., *Goudge et al.*, 2015]. These landforms are consistent with a fluvial fan or deltaic origin based on their morphologic form (some of which have steep depositional fronts [e.g., *Di Achille and Hynek*, 2010]), hints of layering, and their position well above the crater floor that likely records deposition into standing bodies of water.

Landforms identified and mapped as "basin floor deposits" occur on the lowest floor elevation of some craters and depressions in the study region (Figs. 2.2C, 2.4 and 2.6). These deposits tend to be concentric to the edges of their respective host basin but also occur as isolated deposits. The margins and (or) surface of the basin floor deposits have

sub-parallel to parallel fractures. A scarp along the basin floor deposit adjacent to the deepest (> -3160 m) depression on the floor of basin C is characterized by fine-grained, massive, repetitive packages of ~10 m thick medium-toned layers separated by thinner darker-toned layers (Fig. 2.2D). The fine-grained, horizontal, layered nature of these deposits and their association with basin interiors is consistent with a lacustrine origin. The relative age and the relationship of these basin floor deposits with the timing of FSV activity is uncertain.

2.3   Data and Methods

2.3.1   Geomorphic Mapping

FSVs in northern Arabia Terra were mapped in ArcGIS utilizing processed and projected images from CTX and High Resolution Imaging Science Experiment (HiRISE, ~0.25 m pixel scale) [*McEwen et al*., 2007] on the Mars Reconnaissance Orbiter, images from the High Resolution Stereo Camera (HRSC, ~10 m pixel scale) [*Neukum et al*., 2004] on Mars Express, and topographic data from the Mars Orbiter Laser Altimeter (MOLA) on Mars Global Surveyor [*Smith et al*., 1999]. CTX and HiRISE digital terrain models (DTMs) were not available in the region at the time of publication, and the one HRSC DTM did not offer higher resolution data. We investigated a broader region but the final extent of the study area selected for detailed mapping, ~30-40°N between ~0-10ºE, was determined by the decreasing occurrence of FSVs and associated landforms outside of these bounds.

2.3.2   The Hydrological Routing Model

To constrain the hydrologic regime associated with the formation of FSVs in our study area, we utilized the hydrologic routing model after *Matsubara et al*. [2011, 2013] to 1)

estimate the flow of surface water across the landscape and 2) quantify the area and volume of any model-predicted water-filled depressions that have associated geomorphic evidence of valley incision. The model utilizes MOLA topography to route water and assumes a steady-state balance between evaporation and runoff over multi-year time periods. The model also assumes spatially uniform precipitation, runoff, and evaporation from standing water. Due to uncertainties associated with the absolute magnitudes of precipitation, runoff and evaporation, these variables are replaced by the "X-ratio," which serves as a proxy for climatic conditions [*Matsubara et al.*, 2011, 2013]. The X ratio is defined as:

$$X = \frac{(E-P)}{RP}$$

where E = evaporation from lakes, P = precipitation and R = fraction of precipitation resulting in runoff from non-submerged locations. Small X-ratio values (e.g., X = -1) correspond to an environment with total runoff and no evaporation. As the X-ratio increases, the corresponding climate becomes more arid, fewer basins overflow and drainage networks become more fragmented. As explained in *Matsubara et al.* [2013], the value of the X-ratio does not correspond to any one combination of precipitation, runoff and evaporation, such that that several combinations of values for these variables could result in the same X-ratio. For example, an X-ratio of ~2.2 could result from P=0.5 m yr^{-1}, R=0.45, and E=1 m yr^{-1} or P=1.45 m yr -1, R=0.17, E=2 m yr -1 [after *Matsubara et al.*, 2013]. Several simulations were run using a range of X ratio values from -1 (runoff-dominated) to 6 (evaporation-dominated with little runoff) to constrain how wet the environment had to be to match the location and morphology of FSVs preserved in the landscape, including overflow of inferred lakes embedded in long FSV systems.

For the deltas in our study area, the elevation of each upper delta platform (hereafter referred to as "platform") corresponding to the predicted water level at the time of active fan deposition was extracted from MOLA data overlaid on projected CTX images in *JMars* (an online geospatial information system developed by Arizona State University [*Christensen et al*., 2009], Table 2.2). The platform elevation represents the maximum water level associated with delta formation [e.g., *Di Achille and Hynek*, 2010]. In the cases where MOLA altimetry tracks intersected the delta platform, individual MOLA shot points were used to extract elevation data. In all other cases, gridded MOLA data was used to estimate the platform elevation. For 12 of the basins hosting deltas, the hydrologic model was queried to determine the X-ratio value that corresponds to the maximum lake level estimated from the elevation of the delta platform.

2.3.3 Crater Statistics and Relative Ages

The timing of fluvial activity was constrained by estimating the age of 22 craters (diameter range ~4-48 km) in the study region whose ejecta preserve a range of fluvial modification. We only considered craters with well-preserved ejecta and we determined the crater size-frequency distributions of smaller craters superimposed on the ejecta itself. The onset of fluvial activity is bound by the range in age of ejecta deposits incised by FSVs (based on the observation that valleys incise into the ejecta and are therefore younger), and the end of fluvial activity is derived from the age of the ejecta deposits that are fluvially unmodified. Uncertainties in individual derived ages due to relatively small counting areas associated with the crater ejecta deposits suggests FSV incision may have begun and ended somewhat earlier and later, respectively, but the collection of data provides meaningful insight into the timing of fluvial activity that formed the FSVs and associated landforms.

The craters superimposed on the continuous ejecta blankets were counted on projected CTX images (released as of July, 2014) using CraterTools software [*Kneissl et al.*, 2011] in ESRI's ArcGIS. Craterstats software was used to compile reverse cumulative histograms using pseudo log bins to interpret relative absolute ages [*Michael and Neukum*, 2010] based on the chronology function of *Hartmann and Neukum* [2001] and production function from *Ivanov* [2001]. Relative ages were verified using incremental plots based on the variable bin-size method of *Hartmann* [2005]. The maximum modeled absolute ages were estimated from the largest craters that provided the best fit for the expected production population. The linear density of Type 1 FSVs for each ejecta was determined by dividing the cumulative length of Type 1 FSVs incised into the ejecta by the area of the ejecta (Table 2.3). Each crater ejecta was classified as having a high linear density of FSVs (class 1, >0.04 km^{-1}), a low linear density of FSVs (class 2, $<\sim 0.03$ km^{-1}) or no FSVs (class 3).

2.4   Observations and Inferences

2.4.1   Distribution and Nature of FSVs and Associated Deposits

Mapping indicates FSVs in the study area are widespread and characteristically start abruptly on uplands and steeper slopes and terminate near the margins of numerous depressions in the landscape (Fig. 2.4). Most FSVs are relatively short and terminate on the flanks of local basins above the basin floor. Some FSV segments, however, are inferred to bridge depressions in the landscape to form long (> 150 km) valley systems (including the informally named "Heart Lake" and "Northern Plains" described in Sections 2.4.3 and 2.4.4, respectively). In such locations the intervening depression floors are undissected. These longer and more complex valley systems tend to have Type 1 valleys incised into Type 2 valleys (Fig. 2.4) and often have tributaries. The informally named "Boomerang

Lake" system is not a long, integrated system, but provides additional evidence for valley incision related to basin overflow (Section 5.4.5).

Several crater rims are incised by FSVs. Fifty-nine "pollywog" craters (Fig. 2.2B) identified in the study region have an average diameter of 3.9 km (diameter range 0.6-13.4 km) and the majority (61%) of pollywogs occur between 35ºN and 40ºN (Fig. 2.4). Approximately 31 craters have inlet valleys, of which 10 terminate in sedimentary deposits inferred to be deltaic in origin (Figs. 2.2C and 2.4). Three additional craters host deltas that originate from valleys along the interior rim of the host crater (i.e., the host crater rim is not breached). Craters hosting deltas have an average diameter of ~29 km (diameter range is 11-48 km) and occur between 31ºN and 37ºN (average 34ºN). Similar landforms associated with the older Okavango Vallis outflow system [*Mangold and Howard*, 2013] were not considered. The deltas are generally small (average < 3 km in length and < 2.5 km in width, Table 2.2). All of the deltas are located between ~200-850 m above the floor of their respective host craters (Table 2.2).

2.4.2   Hydrological Model

The output of the regional surface hydrology model, based on runoff vs. evaporation (X-ratio) [*Matsubara et al.*, 2011, 2013], shows inferred flow paths across the landscape and several submerged basins (Fig. 2.5). As the X-ratio increases, the predicted submerged regions decrease in volume and areal extent. At an X-ratio of ~2.2, the model-predicted location and extent of the submerged basins corresponds remarkably well to most downstream terminations of FSVs (Fig. 2.6).

All of the deltas occur along the interior walls of model-predicted submerged basins (Fig. 2.6). The X-ratio representing the modeled lake level corresponding to the platform

elevation of 12 deltas in the study region have average value of 2.5 (Table 2.2). This result is consistent with the X-ratio value of ~2.2 to 4 that corresponds to overflow of filled basins in the region (Table 2.1, Fig. 2.6).
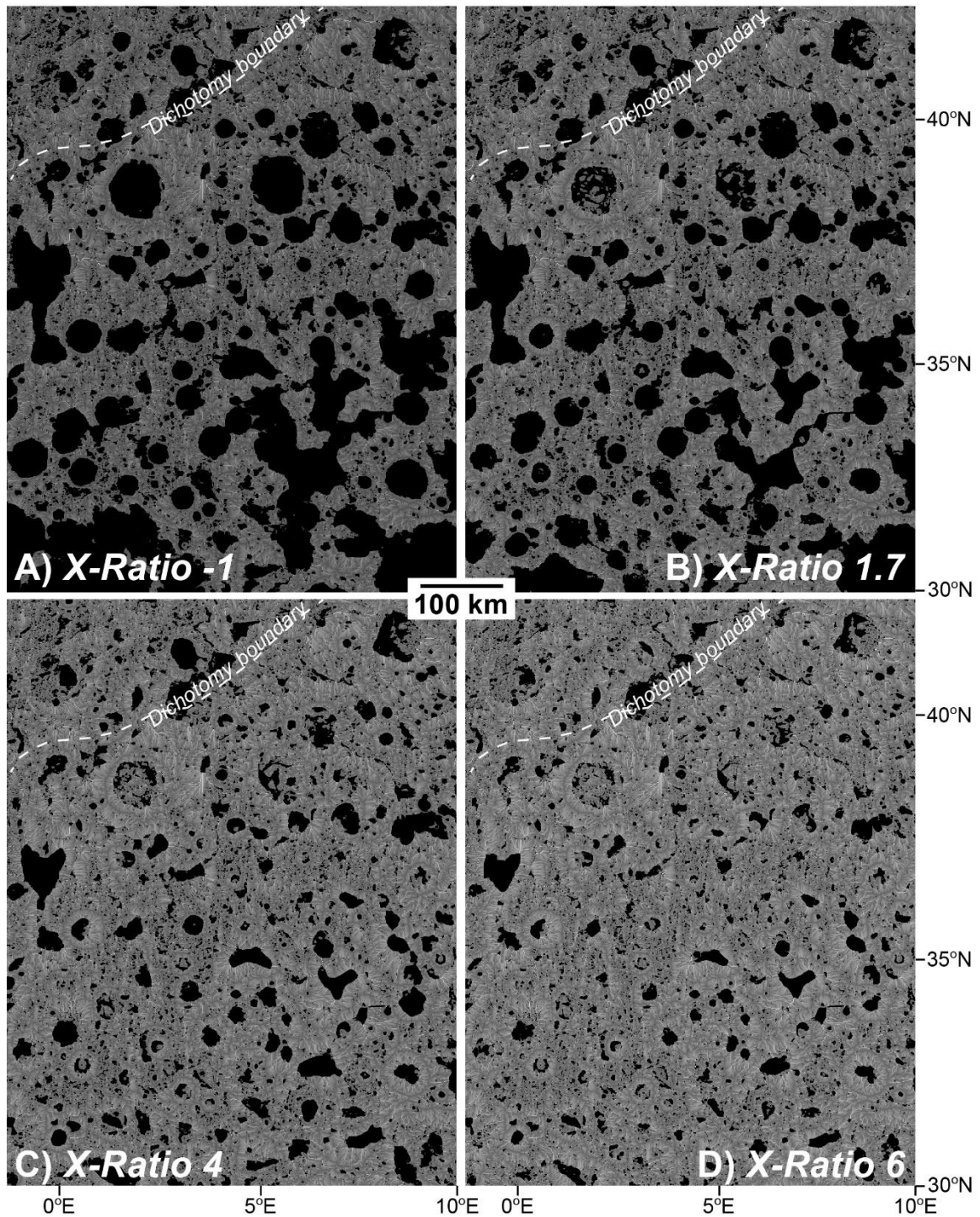
Figure 2.5   Regional surface hydrology model results

The regional surface hydrology model results for the study area (see Fig. 2.4 for context) for X-ratio [*Matsubara et al*., 2011, 2013] values equal to **A**) -1, **B**) 1.7, **C**) 4 and **D**) 6. Results of X-ratio ~2.2 shown in Fig. 2.6. White-gray lines are predicted annual surface flow with brightness proportional to the logarithm of discharge under spatially uniform annual precipitation, runoff, and evaporation. As evaporation becomes more important relative to other parameters, the environment becomes more arid and fewer basins will overflow and drainage networks become more fragmented [*Matsubara et al*., 2011]. Predicted submerged locations are black.
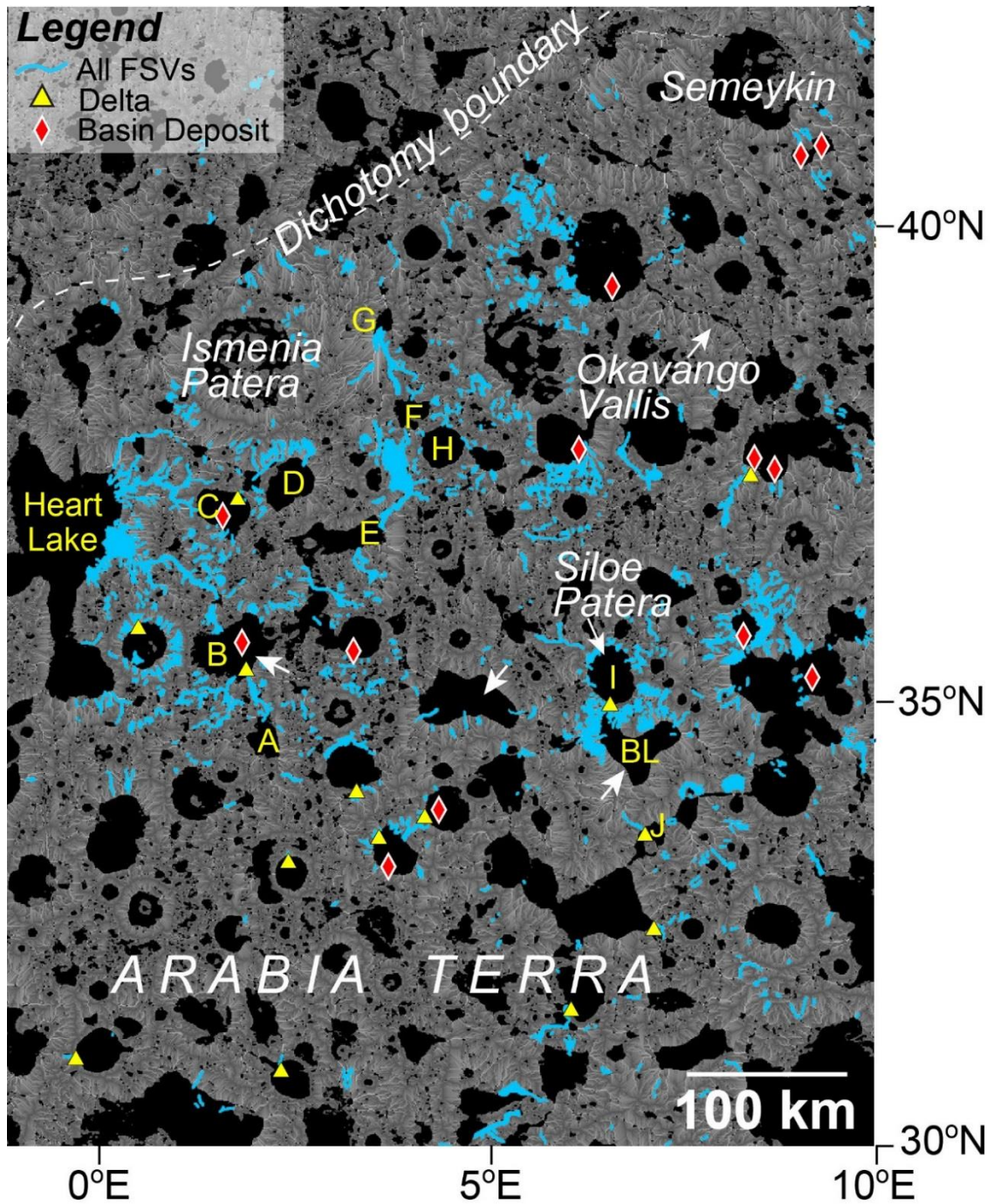
Figure 2.6   Correlation between FSVs and the hydrologic routing model results

All FSVs mapped on the basis of morphology (blue lines, see Fig. 2.4 for context) on top of the regional hydrologic routing model where the X-ratio is ~2.2 (see Fig. 2.5 for flow path and lake explanation). Most FSVs terminate at the margins of the model-predicted submerged basins and some valley segments connect to form longer systems consistent with connection by overflow across interspersed lakes. The width of FSVs is exaggerated

for recognition quality. White arrows indicate the same broad depressions labeled in Fig. 2.4 that would be submerged. Deltas (yellow triangles) and basin floor deposits (red diamonds) occur along lake margins and floors of submerged basins, respectively. Submerged basins discussed in the text are labeled as A-J, Boomerang Lake (BL) and Heart Lake (see Table 2.1).

Table 2.1   Characteristics of model predicted paleolakes in the Heart Lake, Northern Plains and Boomerang Lake valley systems based on hydrologic modeling results

Basin	Max. Lake Surface Elevation (m)	Max. Lake Volume (km^3)	Max. Lake Area (km^2)	Avg. Lake Depth (m) (vol/area)	Max. Lake Depth (m)	X-ratio at Lake Overflow
Heart Lake Valley System (Fig. 2.7)						
Basin A	-2369	12	366	30	310	≤ 4
Basin B	-2505	188	1409	130	401	≤ 2.25
Basin C	-2673	217	735	30	571	≤ 2.75
Basin D	-2663	29	654	40	166	≤ 4
Heart Lake	-3342	2790	7038	400	982	≤ 2.25
Northern Plains Valley System (Fig. 2.11)						
Basin E	-2528	1280	8643	150	783	≤ 2.5
Basin F	-2733	57	1195	50	139	≤ 4
Basin G	-3051	13	648	20	68	-1
Basin H	-2616	937	2152	440	842	≤ 2.75
Boomerang Lake Valley System (Fig. 2.14)						
Boomerang Lake (intact rim before overflow)	-2385	424	2334	182	571	≤ 1.25
Boomerang Lake (after overflow)	-2385	101	905	112	360	≤ 1.25
Basin I (intact rim before overflow)	-2385	1340	3563	376	1547	No overflow
Basin I (after overflow)	-2385	1350	3582	377	1547	No overflow

Table 2.2   Estimation of X-ratios and lake depths using elevation of delta platform

Delta Location	Delta length (km)	Delta width (km)	Elevation of Delta Platform (m)	X-ratio from Platform Elevation	Predicted Lake Depth (m)
31.3°N, 59.9°E	2.3	1.5	-2668 [a]	1.90	444
31.2°N, 2.4°E	4.7	3.5	-2704 [a]	3.25	222
31.8°N, 5.98°E	4	3	-2895 [b]	2.75	645
32.7°N, 7.02°E	2	2.58	-2489 [a]	2.12	264
33.7°N, 6.9°E (basin J, Fig. 2.14E)	2	1.3	-2446 [b]	1.38	368
35.0°N, 6.5°E (basin I, Fig. 2.14C)	2	2.8	-3075 [a]	3.92	857
33.4°N, 2.4°E	2.5	3.5	-2890 [a]	2.26	644
33.6°N, 3.6°E	1.7	3	-2836 [b]	2.21	625
33.9°N, 4.1°E	2.3	1.1	-2535 [b]	1.98	499
34.1°N, 3.3°E	2	1.2	-2527 [a]	3.11	322
35.8°N, 0.4°E (Fig. 2.10)	3.5	3.6	-3683 [b]	1.68	574
37.2°N, 1.65°E (basin C, Fig. 2.2C)	0.85	0.75	-3048 [b]	3.5	273

[a] Elevation estimated from MOLA shot point. [b] Elevation estimated from gridded MOLA data.

2.4.3   Heart Lake Valley System

The informally named "Heart Lake" valley system is ~150 km long and consists of two main FSV segments (Fig. 2.7). This system originates from a topographic depression (basin A) near 34.8ºN, 2.1ºE and incises northward for ~38 km before emptying into basin B. The valley is interpreted to reappear ~30 km to the northwest and flows west-northwest for ~100 km (average gradient ~0.005), terminating near 36.7ºN, 359.9ºE in a heart-shaped depression referred to as "Heart Lake" (Fig. 2.7).
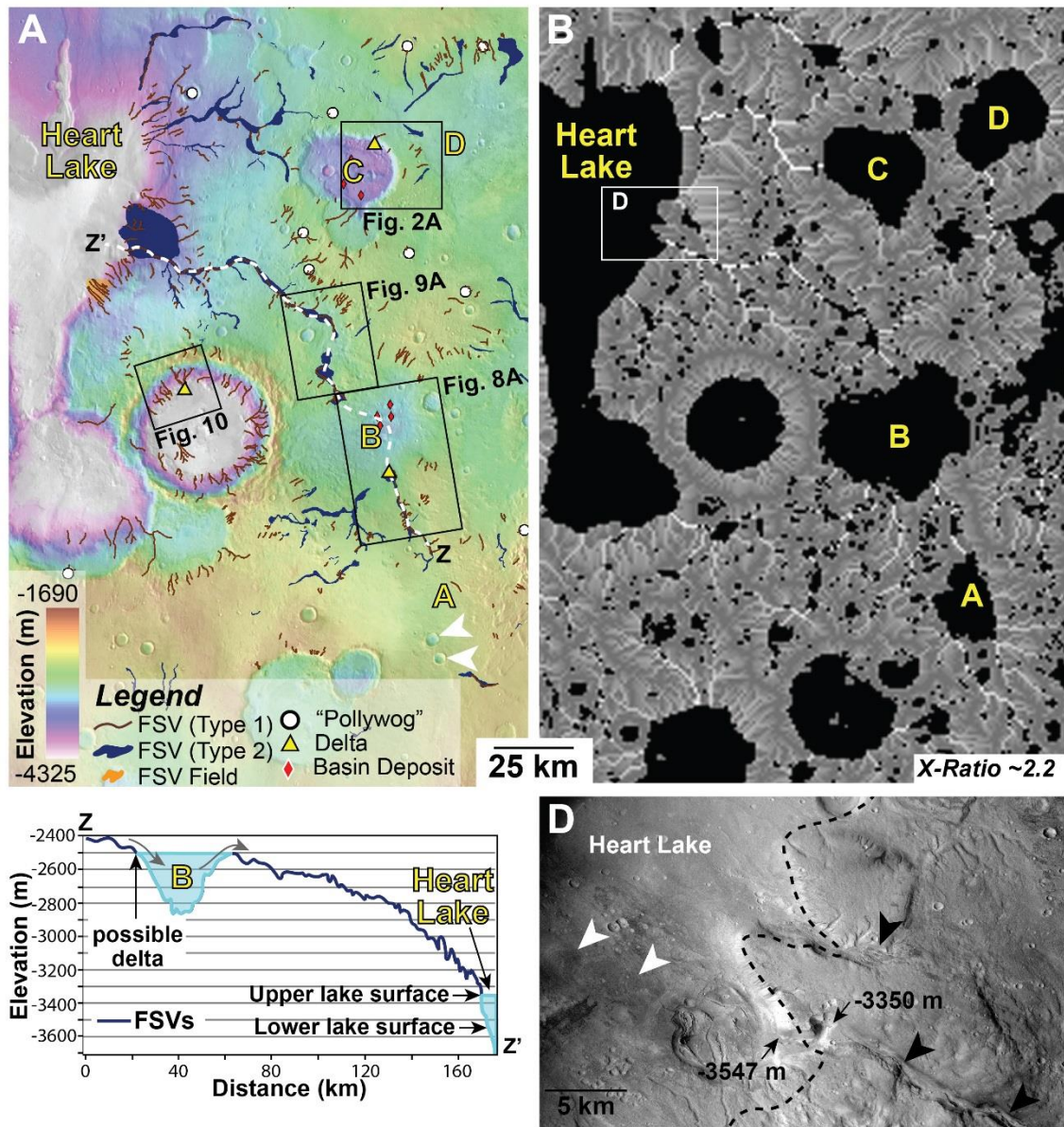
Figure 2.7   Overview of the Heart Lake valley system

A) Regional view (see Fig. 2.4 for context) of the informally-named "Heart Lake" valley system where two main FSV segments connect to make a 150+ km-long valley system (white dashed line). FSVs commonly disappear and reappear across depressions in the landscape (e.g., basin B) that were likely filled with (ice-covered?) lakes at the time of valley formation. Arrows indicate younger craters that obscure the amount of drainage entering basin A. Black boxes show locations of Figs. 2.2A, 2.8A, 2.9A and 2.10. MOLA over THEMIS Day IR, centered near 35.91º N, 1ºE. North to top. **B**) Regional hydrologic modeling predicts location, size and volume of filled depressions and flow paths across the landscape in the area of Fig. 2.7A (see Fig. 2.5 for flow path and lake explanation and Table 2.1). Model result equivalent to an X-ratio value of ~2.2 (see text), the point at which

basin B would have overflowed along its northern margin and transported sediment into Heart Lake. Submerged basins A, C and D likely contributed to the Heart Lake valley system although morphologic evidence of overflow from basin C is not convincing. The predicted extent and overflow of basin B is consistent with the preserved morphology (see Fig. 2.9). Box shows location of Fig. 2.7D. Centered near 35.91° N, 1ºE, North to top. **C**) Profile of transect Z to Z' in (A) indicating regional gradient toward Heart Lake. Valleys flowed into and out of basin B and terminate in Heart Lake. **D**) Valleys (black arrows) at the terminus of the Heart Lake valley system downcut ~200m to the floor of Heart Lake, consistent with a change in base level. Rounded lobes (white arrows) on the floor of Heart Lake. Predicted lake level at an X-ratio of ~2.2 (dashed line) corresponds well to the depth of valley incision. Subframe of CTX 17_007519_2147, 5.96 m scaled pixel scale. North to top.

The FSVs at the headwaters of this system originate at the northern margin of the model-predicted submerged basin A, but the extent of drainage entering this basin from the south is obscured by a subsequent impact crater (Fig. 2.7). The hydrologic routing model predicts a volume of ~12 km^3 for basin A, which would overflow at X-ratio values ≤ 4 (Table 2.1). The ~1 km wide valley emerging from the northern margin of basin A has a ~100 m wide interior valley and terminates near the southern boundary of the model-predicted margin of basin B (overflowing for X-ratio ~2.25), forming a low-relief fan shaped deposit (Fig. 2.8).
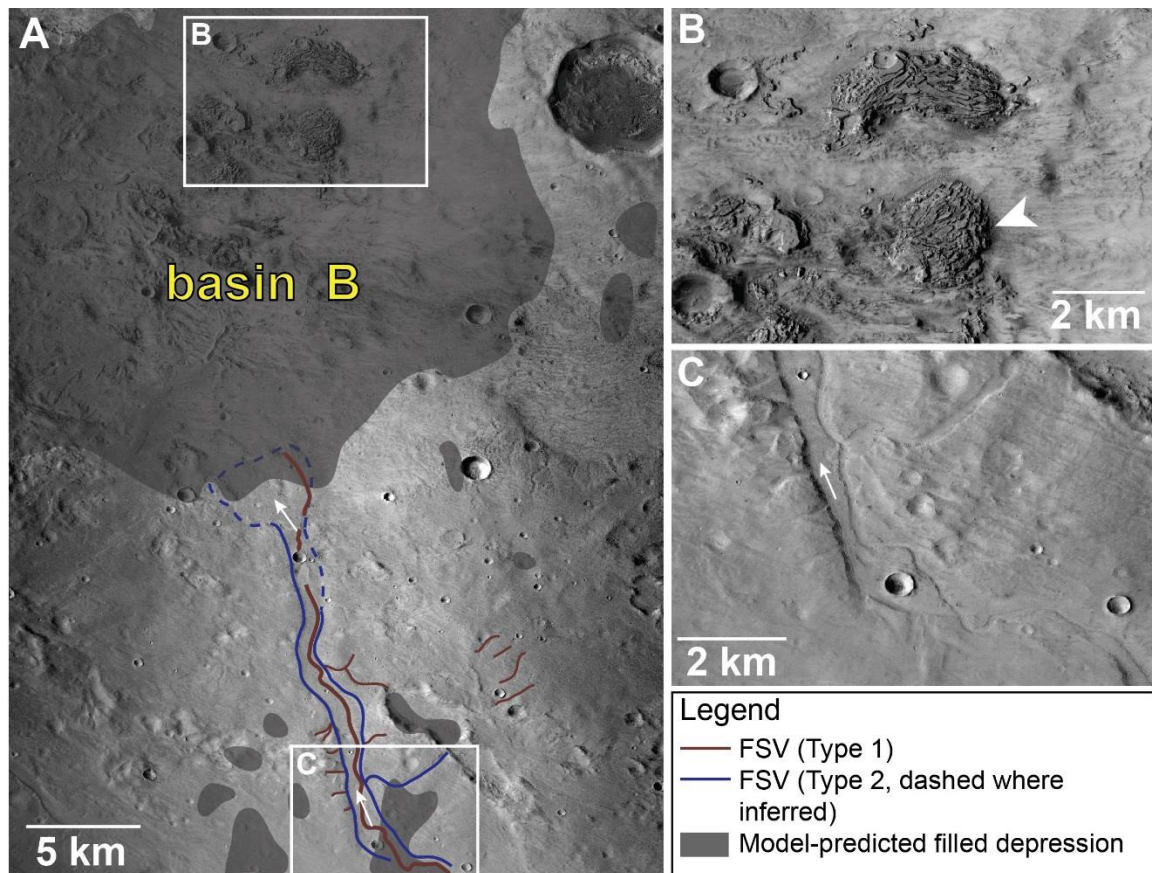
Figure 2.8   Inlet of the Heart Lake valley system

A) Geomorphic map of the southern inlet into basin B from basin A within the Heart Lake valley system (see Fig. 2.7A for context). The FSV disappears along the predicted margin of the submerged basin (shaded) at an X-ratio of ~2.2 (see Fig. 2.7B for context). Arrows indicate flow direction and boxes show location of Figs. 2.8B and 2.8C. Subframe of CTX P17_007809_2169 (5.89 m scaled pixel width) **B**) Dark-toned, possibly ice-rich layered sediment occurs along the deepest floor of Lake B, near an elevation of -2850 m relative to the MOLA datum. The rounded deposit (white arrow) is a few kilometers wide and rises about ~70 m from the lake floor and could be related to final stages of the lake that occupied this basin. These isolated deposits could be remnants of a larger deposit. Similar deposits occur in basin C (Fig. 2.2C-D) and elsewhere in the region (Figs. 2.4 and 2.6) along the floors of model-predicted submerged basins. **C**) Detail of ~17 km-long valley leading to southern margin of basin B, arrow indicates northward direction of flow. North to top in all images.

Basin B is an irregularly shaped depression with a maximum depth of ~400 m. The

southern margin of basin B received flow from basin A as well as other contributing valleys

(Fig. 2.7A). The basin has been slightly modified by the ejecta from the 48-km diameter

crater to the west and rounded deposits occur along the lowest elevations of the basin floor (Fig. 2.7B). These isolated deposits are a few kilometers in width and up to ~70 m in height. The relationship between these deposits and FSV formation is unclear; it is possible that these deposits are remnants related to the final waning stages of the lake that occupied this basin. These landforms are mapped as "basin floor deposits," and similar deposits occur in other model-predicted, water-filled basins in the study area (Figs. 2.2C-D, 2.4 and 2.6).

The steady state hydrologic model predicts overflow along the northern margin of basin B at a volume of 188 km^3 for all X-ratio values $\leq$ 2.25 (Table 2.1). The extent and elevation of this lake corresponds to morphologic evidence of overflow along the northern margin of basin B (Fig. 2.9). The mouth of the outlet valley is ~4 km wide and the channel appears deeply incised. Roughly ~10 km from the overflow breach a meander exhibits streamlined depositional bars within the valley (Fig. 2.9B). Locations along the valley where sidewalls are less defined, incised channels are absent, and possible fan-like depositional forms occur corresponds to model-predicted ponded water along the flow path (X-ratio ~2.2, Fig. 2.9A). The valley emerging from the southern margin of basin B continues ~100 km to the west-northwest and incises into the eastern margin of Heart Lake (Fig. 2.7).
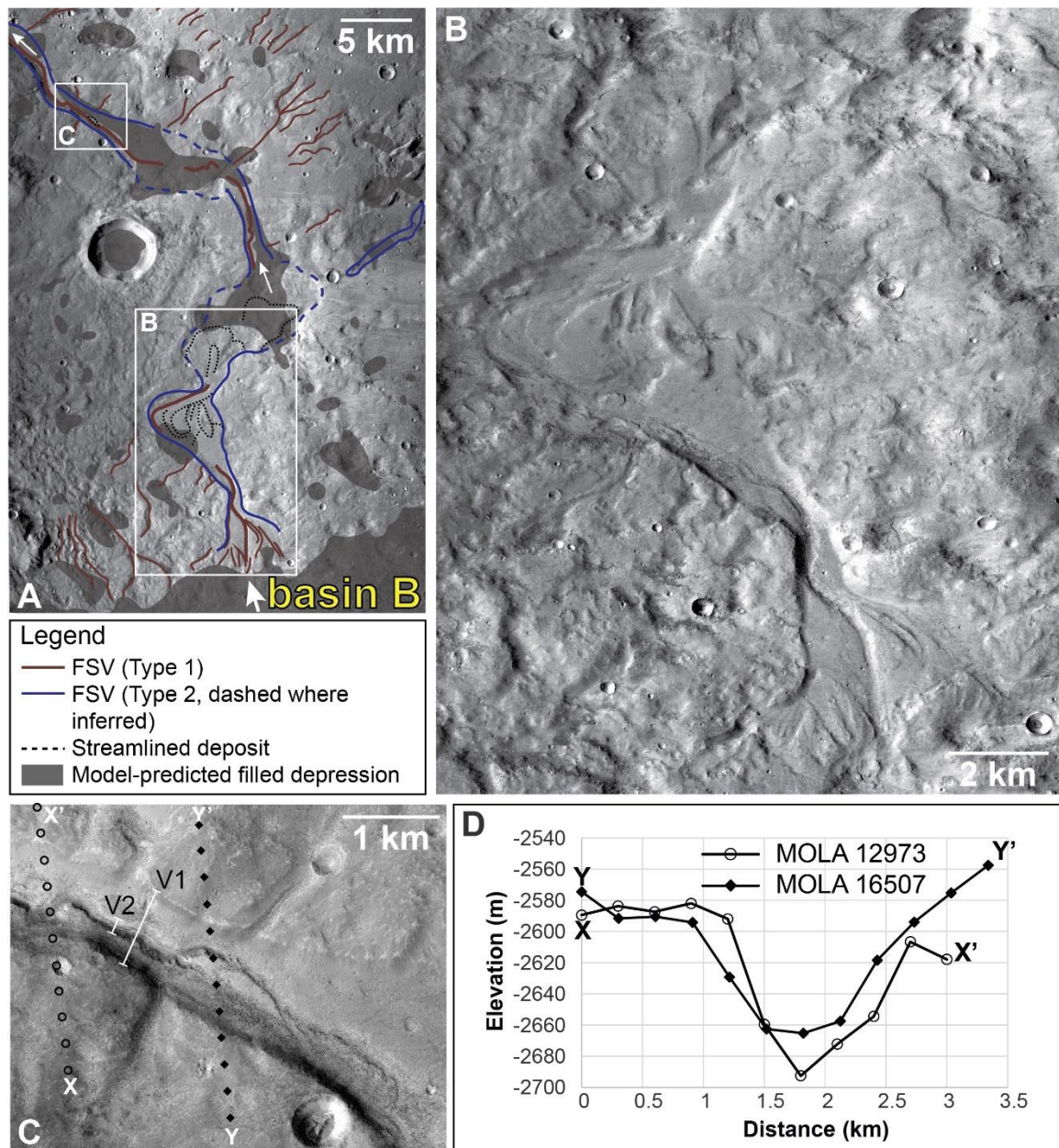
Figure 2.9   Outlet in the Heart Lake valley system

A) Geomorphic map of the outlet valley on the northern margin of basin B within the Heart Lake valley system (see Fig. 2.7A for context) detailing the FSVs and associated streamlined features (black dotted lines). The valley coincides with the model-predicted lake margin (shaded) at an X-ratio of ~2.2 (see Fig. 2.7B for context). Arrows indicate flow direction and boxes show location of Figs. 2.9B and 2.9C. Subframe of CTX B18_016815_2151 (5.8 m scaled pixel width). **B**) The FSV on the downstream side of basin B meanders and exhibits streamlined forms, scours and streamlined depositional channel bars. Subframe of CTX B18_016815_2151 (5.8 m scaled pixel width). **C**) Representative widths of the main valley (V1) and interior valley (V2) used to estimate

discharge rates (Section 2.5). Transect Y to Y' and X to X' from MOLA transects 16507 and 12973, respectively (see profiles in Fig. 9D). Subframe of HiRISE ESP_033245_2165 (59.7 cm scaled pixel width). **D**) Estimated from MOLA data, the main channel is roughly 1000 m wide and 70 m deep and the incised channel is ~90 m wide (assumed to be half of the channel wall-to-wall width) and ~2-8 m deep. North to top in all images.

The steady state hydrologic model predicts overflow along the northern margin of Heart Lake at a volume of 2790 km^3 for all X-ratio values ≤ 2.25 (Table 2.1). The predicted lake level in Heart Lake at an X-ratio of ~2.2 is -3342 m (dashed line in Fig. 2.7D), which corresponds well to the elevation of the broad, upper incised surface near the margin of Heart Lake. Near an elevation of -3350 m, a knick point in the profile likely corresponds to a change in base level in Heart Lake. The valley downcuts ~200 m to an elevation near -3547 m along the floor of Heart Lake, which corresponds to an X-ratio of ~2.7 that has a corresponding model-predicted lake surface of -3513 m. Between X-ratios of ~2.25 and ~2.7, the model predicts the volume and lake surface in Heart Lake would decrease by ~1110 km^3 and ~172 m, respectively, consistent with the amount of valley downcutting along the eastern margin of Heart Lake (Fig. 2.7D). The roughly circular deposit on the floor of Heart Lake at the valley terminus appears deflated and deformed with cracks and up-turned margins, perhaps indicative of sediment-ice interaction (Fig. 2.7D). A channel along the western margin of this enigmatic deposit is associated with rounded low-relief deposits that extend ~8 km onto the floor of Heart Lake (Fig. 2.7D). We interpret these landforms to be analogous to step deltas deposited during fluctuations in lake levels.

Several FSVs are incised between Heart Lake and basin C, located ~60 km to the east of the Heart Lake delta (Fig. 2.7). The model predicts basin C at its largest extent would hold ~217 km^3 of water, overflowing for X-ratio values of ≤ 2.75 (Table 2.1). Evidence indicative of overflow along the western margin of basin C is not convincing due to the

lack of a deeply incised channel as well as the absence of a fan at the valley terminus (Fig. 2.7). Morphologic evidence of water flowing from basin D to basin C (via a small depression in between basins C and D) is supported by the valley and associated delta on the northeastern rim of basin C (Fig. 2.2C). The X-ratio associated with a modeled lake surface of -3048 m (based on the elevation of the lobe surface) is ~3.5, implying the basin hosted a lake roughly 270 m deep. Basin D was small, with a model-predicted maximum volume and depth of 29 km^3 and 166 m, respectively, overflowing at X-ratio values ≤ 4 (Table 2.1).

One of the younger, large (48 km-diameter) craters in the study area is located between Heart Lake and basin B (35.6ºN, 0.55ºE, Fig. 2.7). The fresh-looking ejecta from this Amazonian- to Hesperian-aged [*Tanaka et al*., 2014] crater is dissected by the Heart Lake valley system (Fig. 2.7). The interior rim of this crater is dissected by FSVs that terminate in several fan-shaped deposits, including a steep-front step delta on the crater's northwestern rim (Fig. 2.10). This delta extends ~3.5 km from the apex (elevation of ~ -3683 m) to distal margin (elevation of -3930 m) with an overall gradient of ~0.07. The delta was fed by numerous incised valleys on the interior crater rim but distributary channels on the fan surface are not apparent. The fan surface at HiRISE scale has numerous small craters and is not heavily modified by mid-latitude mantling material. There are at least five steps on the delta front that decrease in elevation from the apex to the toe of the deposit, with elevations decreasing between ~20-80 m per step (average ~50 m, based on MOLA shot points). The steady-state hydrologic model predicts this 48 km-diameter crater would not host an overflowing lake unless the X-ratio dropped to the unrealistic value of -1 (Fig. 2.7B), consistent with the absence of a breach in the crater rim. The X-ratio

42

corresponding to the model predicted lake surface associated with the platform elevation

of the step delta is ~1.7, implying the crater hosted a ~575 m deep lake (Table 2.2).
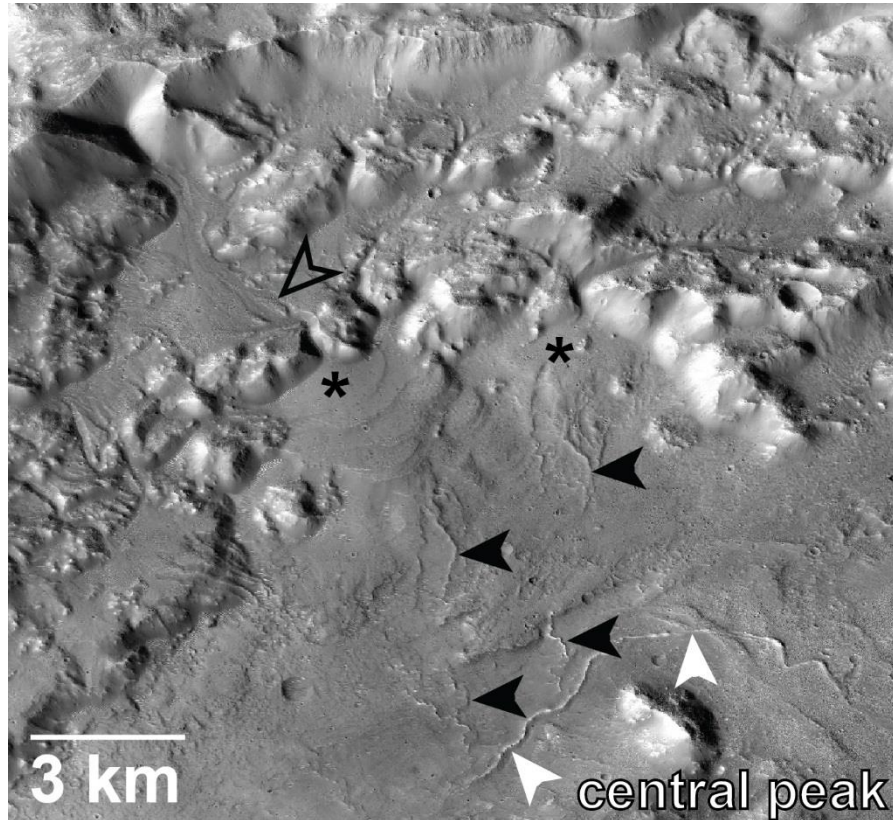
Figure 2.10 Fluvial landforms in an unnamed crater

The ~48 km-diameter crater near 35.6ºN, 0.55ºE preserves myriad fluvial landforms (see Fig. 2.7 for context) including FSVs (e.g., hollow black arrow) and deltas ("*"). Located between Heart Lake and basin B, the hydrologic model predicts this crater would have been submerged but did not overflow (Fig. 2.7B). The step delta on the northern rim supports evidence for fluctuating water levels within the crater. Sinuous ridges (white and black arrows) flow downhill into a local topographic depression along the western crater floor. Ridges appear to emerge from the base of the deltas (black arrows) and join the main ridge (white arrows) near the central peak of the crater. Subframe of CTX image D04_028841_2159 (5.86 m scaled pixel width). North to top.

Several light-toned, sinuous ridges appear to emerge from the distal end of the delta

and intersect a ~10 km long east-west oriented sinuous ridge with a gradient of 0.02. The

sinuous ridges at the delta front and the ridge on the crater floor begin near a common

43

elevation between -3890 and ~ -4000 m, correlating to the margin of the lowest part of the crater interior that occupies the western side of the crater floor. The origin of the sinuous ridges and their relationship to the delta on the northwestern rim remains unclear. The ridges could be inverted fluvial channels but if so, they would have to consist of much coarser grains relative to the adjacent delta so that the channels could erode and become inverted without significant observed modification of the delta. Alternatively, the channels could be related to flow beneath a now-absent ice cover, analogous to eskers [e.g., *Hobley et al.*, 2014]. Lastly, narrow channels could have eroded into the surface of an ice-covered lake, and subsequent "let down" of the channel during melting or sublimation of the ice could form landforms analogous to kames. This explanation has some deficiencies, however, as kame deposits are generally irregular due to the unevenness of ice melting and if the ice-covered lake were level, a fan or delta may be expected to form along the margin of the ice where the sediment-laden flows debouched.

2.4.4   Northern Plains Valley System

The informally named "Northern Plains" valley system is approximately 120 km northwest of basin B and originates near 36.9ºN, 3.56ºE (Fig. 2.11). This northward flowing, ~200 km long system consists of three main FSV segments separated by depressions in the landscape, ultimately terminating at the dichotomy boundary near 39.9ºN, 3.6ºE (Fig. 2.11).

The southernmost FSV segment in this system originates from the northeastern margin of basin E, which has a model-predicted volume of 1280 km^3 and would overflow for X-ratio values ≤ 2.5 (consistent to the X-ratio associated with the predicted overflow of basin B in the Heart Lake system, Table 2.1). The ~1 km wide outlet from basin E incises

northward with an average gradient of 0.003 for roughly 70 km before disappearing at the margin of a ~25 km wide depression, basin F (Fig. 2.11). The valley segment between basins E and F is predominantly a wider Type 2 valley that becomes incised with an interior valley just before debouching into the southern margin basin F (Fig. 2.12). Light-toned, possibly layered deposits occur along the northern margin of basin F where the basin is deepest (Fig. 2.13). The model-predicted volume and X-ratio where overflow would occur in basin F is 57 km^3 and ≤ 4, respectively (Table 2.1). A crater hosting basin H to the southwest of basin F (Fig. 2.11) may have stored a significant amount of water (~937 km^3) that would have overflowed at X-ratio values of ≤ 2.75 (Table 2.1). The northwestern, lowest portion of the rim of basin H is dissected by several FSVs, but the sense of flow into or out of basin H is unclear. No delta occurs in the crater interior where the FSVs erode the basin margin. One FSV on the northwestern crater rim, however, is associated with smooth, light toned material near the model predicated shoreline of basin F (see CTX D19_034669_2178) that might be a deltaic deposit from overflow of basin H.

From the northern margin of basin F, the valley incises ~40 km with an average gradient of 0.008 before disappearing at the model predicted margin of basin G. The model-predicted volume of basin G is only 13 km^3 and the model predicts overflow would only occur for negative X-ratio values. (Table 2.1). The ~60 km stretch from basin G to the system terminus has the steepest gradient of the entire Northern Plains valley system, ~0.013. A few incised valley segments are preserved along this path, and the channel transitions from incised to inverted as it crosses the dichotomy boundary (Fig. 2.11D).
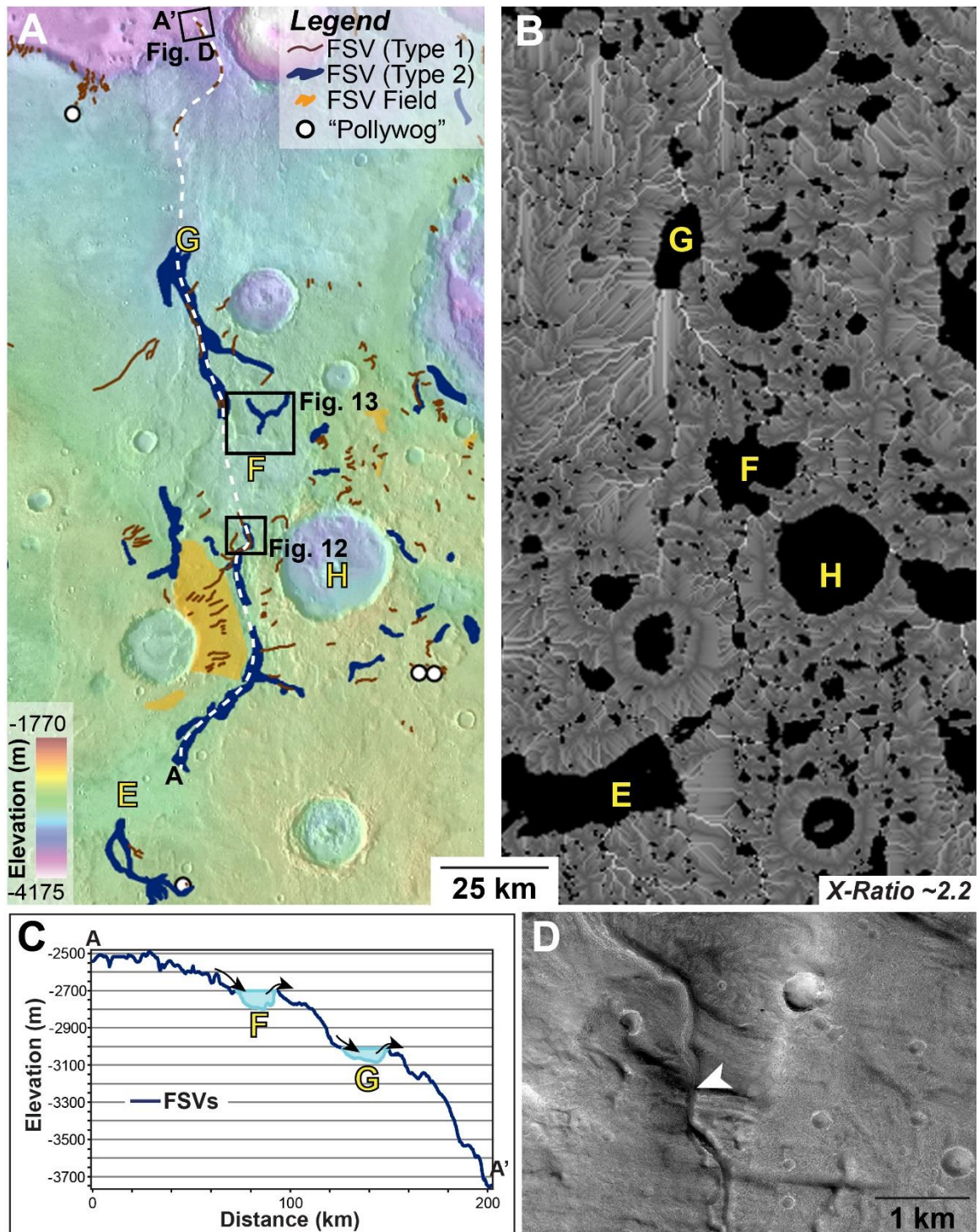
Figure 2.11 The Northern Plains valley system

A) Regional view (see Fig. 2.4 for context) of the informally named "Northern Plains" valley system where three main FSV segments connect through basins E, F and G to make a 200 km-long valley system (white dashed line). The depressions were likely filled with

(ice-covered?) lakes and were the source of water for valley formation. Boxes show locations of Figs. 2.12 and 2.13. MOLA over THEMIS Day IR. Centered near 38.2ºN, 3.8ºE, North to top. **B**) Regional hydrologic modeling predicts location, size and volume of filled depressions and flow paths across the landscape in the area of Fig. 2.11A (see Fig. 2.5 for flow path and lake explanation and Table 2.1). Model result equivalent to an X-ratio of ~2.2 (see text), consistent with the point at which Lake E would have overflowed toward Lake F, transporting sediment toward the northern plains. **C**) Profile of transect in Fig. 2.11A indicating regional gradient (0.006) toward the dichotomy boundary and location of proposed lakes that fed valley incision. FSVs are preserved in the morphology between depressions in the landscape (e.g., Lakes E, F and G) and terminate in the northern plains. **D**) The terminus of the Northern Plains valley system transitions from an incised to inverted channel along the dichotomy boundary, possibly suggesting flow continuing beneath an ice cover forming an esker. Subframe of HiRISE ESP_041144_2200 (59.8 cm scaled pixel width with illumination from upper left). North to top.
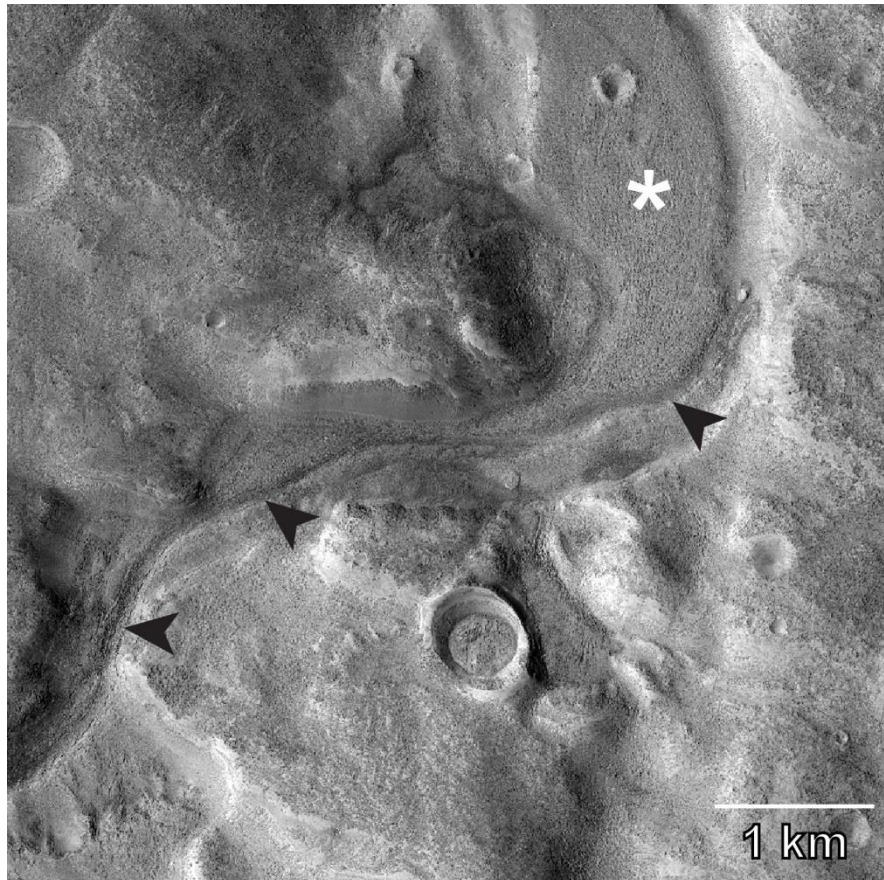
Figure 2.12   Inlet in the Northern Plains valley system

Northern Plains valley system showing inlet valley into basin F (see Fig. 2.11A for context). Black arrows show narrow incised (Type 1) channel within broader (Type 2) valley as system debouches into basin G. Possible broad depositional landform at margin

of basin F ("*") . Subframe of HiRISE ESP_042568_2180 (29.7 cm scaled pixel width). North to top.

Figure 2.13   Inverted channels in the Northern Plains valley system

The inverted channels (black arrows) flowing into the northern margin of basin F (see Fig. 2.11A for context) with associated light-toned deposits (white arrows) along the deepest part of the basin floor (-2850 m) are consist with the presence of a water-filled basin. Subframe of CTX G19_025676_2190 (6 m scaled pixel width). North to top.

2.4.5   Boomerang Lake Valley System

Approximately 200 km east-southeast of basin B (Fig. 2.4), the margins of a broadly-curved depression, informally named "Boomerang Lake," are heavily dissected by FSVs. Boomerang Lake breached the rim of basin I to the north and deposited a prominent steep-front delta (Fig. 2.14). The overflow channel into basin I is ~14 km in length and the width ranges from ~150 m up to 650 m near the delta front (Fig. 2.14C). There is no evidence for an incised interior channel. The fan surface is ~1 km long from apex to toe

and has a steep front with hints of layering at HiRISE scale (Fig. 2.14D). The platform of the delta is at an elevation of -3075 m, implying basin I was filled with water to a depth of over 850 m with a corresponding X-ratio of ~3.9. After the rim was incised, the hydrologic model suggests that during wet conditions (X-ratios up to ~3.5), both Boomerang Lake and basin I had common surface elevations and a combined volume of 1350 km^3. At an X-ratio of about 3, the two basins are barely connected, and have a combined volume of roughly 900 km^3. For higher X-ratios the basins would host separate lakes.

The overflow event from Boomerang Lake into basin I had to overcome an initially intact crater rim, suggesting Boomerang Lake had to reach a lake level of just above -2400 m (Table 2.1). This lake surface corresponds to an X-ratio value of roughly 1.5, implying humid conditions by Mars standards [*Matsubara et al*., 2013]. The southern margin of Boomerang Lake has an ~18 km long outlet valley that terminates in a small delta on the floor of basin J (Fig. 2.14). The X-ratio at which Boomerang Lake would have been connected to the outlet valley in the south is at ~1.7, comparable to the X-ratio required to breach the rim of lake I to the north. It is unusual for lakes to have stable overflows into two distinct outlet valleys, however. One possible explanation for the double outlet valley is an impact into a shallow Boomerang Lake that could have trigged a tsunami, resulting in overflow to the north and south forming deltas into basins I and J, respectively. There are several craters on the floor of Boomerang basin, and a few have well-preserved ejecta with radial morphologies that could be considered candidates for impact into a shallow lake (e.g., a 3 km-diameter crater along the eastern margin above the white arrow in Fig. 2.14A). Evidence for corresponding wave-related overflow features elsewhere around the margin of Boomerang basin, however, is lacking.

The deepest part of the basin has a few 4-5 km long sinuous ridges (Fig. 2.14, see CTX B01_009892__2148) similar in morphology to those seen in Fig. 2.10. If these ridges are analogous to eskers, which is consistent with their morphology, their presence could be consistent with flow beneath a thin ice cover. An inverted fluvial channel origin for the ridges cannot be definitively ruled out, however, due to the lack of topographic data on the basin floor (for example, if the ridges went uphill and downhill and did not obey regional variations in local topography the ridges would more analogous to eskers than inverted fluvial channels).
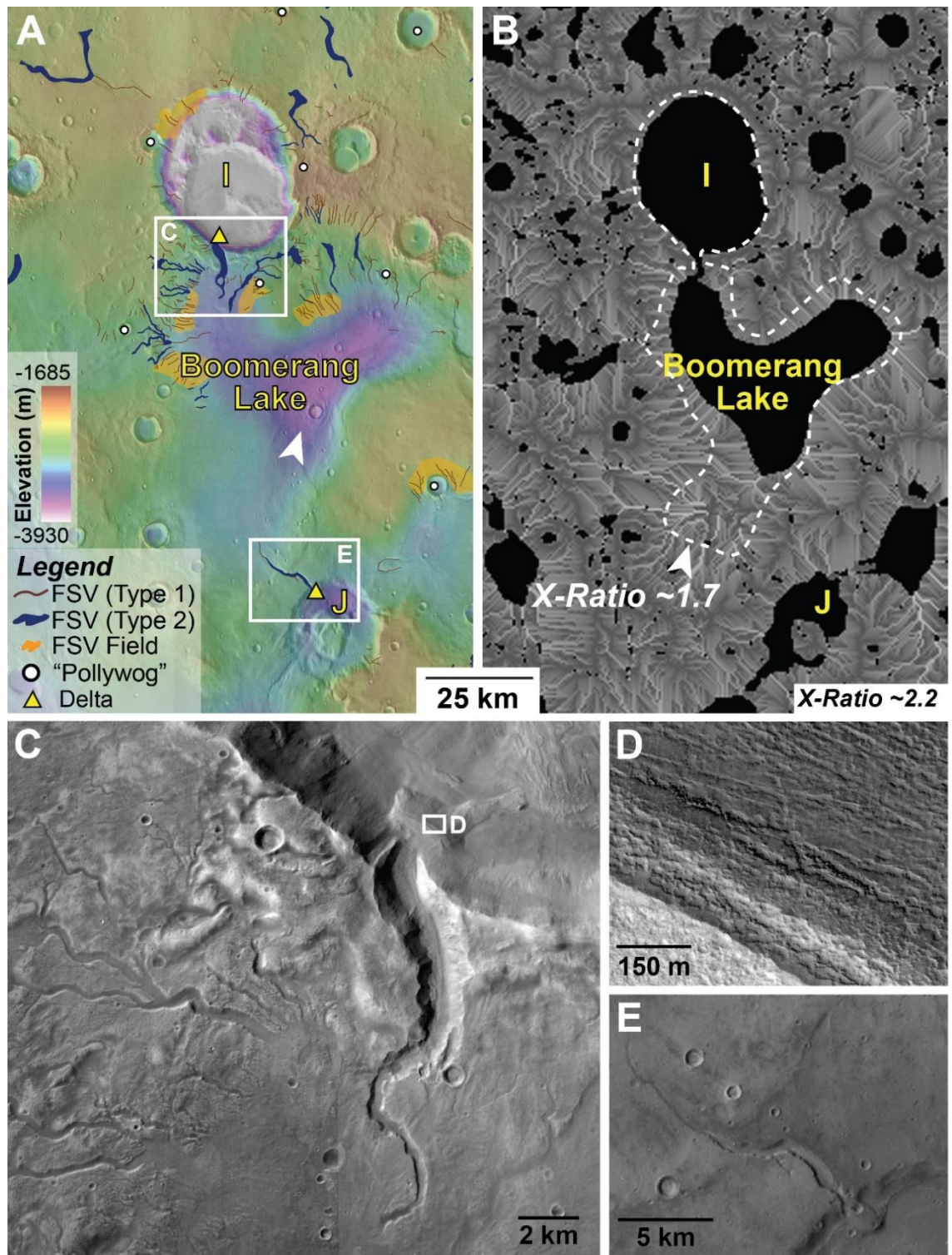
Figure 2.14   Boomerang Lake valley system

A) Regional view (see Fig. 2.4 for context) of the informally named "Boomerang Lake" valley system. This system has a high concentration of FSVs along the northern margin of

Boomerang Lake. White boxes location of Figs. 2.14C and 2.14E. Several sinuous ridges (e.g., white arrow) analogous to eskers occur on the deepest parts of the basin floor. MOLA over THEMIS Day IR. Centered near 34.4ºN, 6.5°E, North to top. **B**) Regional hydrologic modeling predicts location, size and volume of filled depressions and flow paths across the landscape in the area of Fig. 2.14A (see Fig. 2.5 for flow path and lake explanation and Table 2.1). At an X-ratio of ~2.2, basins I and Boomerang would be connected. Conditions would have to be more humid (X-ratio ~1.7, white dashed line) for Lake Boomerang to extend far enough south to overflow along its southern margin to form small delta in basin J. **C**) FSVs and lobe deposits on the floor of Lake I. Subframe of CTX D08_030344_2155 (5.94 m scaled pixel width). **D**) Subtle layers and blocks visible on delta front; delta surface at lower left. Subframe of HiRISE ESP_041223_2155 (29.7 cm scaled pixel width), North to top. **E**) The small (~2 km long) delta created by overflow from Boomerang Lake. Subframe of CTX B01_009892_2148 (5.88 m scaled pixel width).

2.5   FSV Discharge Estimates

To constrain the amount of runoff, we estimated discharge (Q) in the paleochannel of the Heart Lake FSV system (Fig. 2.9) from hydraulic relationships estimating velocities and flow depths based upon minimum conditions required to transport bed sediment. Discharges were calculated from the morphometry and local slopes of a representative reach using HiRISE and MOLA data (Fig. 2.9C and 2.9D). Discharge rates assume that active transport of bed sediment occurred, but due to the unknown nature of the channel bed, a range of possible grain sizes from medium sand (D~0.3 mm), very coarse sand (D~2 mm) and gravel (D~20 cm) were considered for both the main channel and incised channel.

The relatively straight valley segment between basin B and Heart Lake has a width and depth of ~1000 m and 70 m, respectively. The average bed width of the incised inner valley (assumed to be half of the wall-to-wall measurement) is approximately 90 m with an estimated depth of 3-10 m based on crude estimates from MOLA shot points with altimetry tracks oriented roughly perpendicular to the channel (Fig. 2.9C and 2.9D). These valley depths are probably a large overestimation of the effective depth of the flow because

the channels likely incised during flow events; that is, the flows probably never fully filled their valleys. Our approach using channel dimensions and estimated flow depth for sediment transport conditions representative of terrestrial rivers provides a conservative estimate of formative discharges.

Assuming medium sand bed river channels (D~0.3 mm) and an associated Shields number τ^* of roughly 2 dynes cm^{-2}, which is representative of transport conditions being about 10 times threshold conditions in such channels [e.g., *Talling*, 2000], the effective shear stress (τ) is given by:

$$\tau = \tau^*(\rho_{s}\text{-}\rho)g_{m}D$$

where sediment density (ρ_s) of basalt is approximately 3000 kg m^{-3}, fluid density (ρ) is 1000 kg m^{-3} and adjusted Mars gravity (g_m) is 3.71 m s^{-2}. With a τ ~3.67, the flow depth, z, can be solved by:

$$\tau = \rho g z S$$

where channel gradients (S) are 0.0045 for the Heart Lake system. The calculated flow depth to transport medium sand-sized grains is ~0.26 m. The Manning equation, corrected for Martian gravity, and the channel dimensions are used to estimate discharge (Q) within the channel [after *Mangold*, 2012; *Mangold and Howard*, 2013] by:

$$Q = A(g_{m}SR^{4/3} / g_{e}n^2)^{1/2}$$

where A is the cross-sectional area of the channel, S is the characteristic channel gradient (0.0045), R is the hydraulic radius (cross sectional area divided by wetted perimeter), g_m

and g_e are gravity for Mars (3.71 m s^{-2}) and Earth (9.8 m s^{-2}), respectively, and n is the Manning coefficient, assumed to equal 0.04.

The discharge in the main channel and incised channel for medium sand (D~0.3 mm) is approximately 177 m^3 s^{-1} and 16 m^3 s^{-1}, respectively. This result is of the same order of magnitude as earlier estimates of discharge in FSV systems [e.g., *Howard and Moore*, 2011; *Parsons et al.*, 2013; *Adeli et al.*, 2016; *Salese et al.*, 2016]. In the Heart Lake system, the minimum timescale for the hydrologic system to fill basin B (188 km^3) from overflow of basin A based on a discharge of 16 m^3 s^{-1} (from the incised interior channel dimensions) is 372 years. Based on the width of the main channel and associated discharge of 177 m^3 s^{-1}, the minimum timescale required to fill basin B is about 35 years.

Discharge estimates, however, vary as a function of grain size, which is a variable that cannot be determined from orbital data. For example, a channel bed consisting of very coarse sand (D~2 mm) would have an estimated minimum flow depth of roughly 1.7 m and associated discharges of 4,178 m^3 s^{-1} in the main channel and 376 m^3 s^{-1} in the incised channel. In the Heart Lake system, the minimum timescale for the hydrologic system to fill basin B from overflow of basin A based on a discharge of 376 m^3 s^{-1} (from the incised interior channel dimensions) is 16 years. Based on the width of the main channel and the associated discharge of 4,178 m^3 s^{-1}, the minimum timescale required to fill basin B is about 1.5 years.

Gravel in terrestrial channels is typically transported close to threshold conditions, with τ^*~0.06. For coarse gravel sized grains (D~20 cm), the minimum flow depth would be about 5 m with estimated discharges of 26,082 m^3 s^{-1} in the main channel and 2,347 m^3 s^{-1} in the incised channel. The minimum timescale for the hydrologic system to fill basin

B from overflow of basin A based on a discharge of 2347 m^3 s^{-1} (from the incised interior channel dimensions) is 2.5 years. Based on the width of the main channel and the associated discharge of 26,082 m^3 s^{-1}, basin B would fill up in about 3 months.

2.6   Estimate of FSV Age from Crater Statistics

Previous studies have shown that clusters of FSVs developed on or near the fluidized ejecta of relatively well-preserved and presumably young craters [e.g., *Morgan and Head*, 2009; *Mangold*, 2012; *Hobley et al.*, 2014]. The association of FSVs with young craters is not universal, however. In northern Arabia Terra, roughly 21% of Type 1 FSVs occur on well-preserved crater ejecta with the majority of FSVs forming between craters or near degraded craters (Fig. 2.15). In order to investigate possible relationships between ejecta and valley formation and to constrain the age of FSV formation and the timing of fluvial activity, we used crater statistics to estimate the age of craters with well-preserved ejecta that preserve a range of fluvial dissection (Fig. 2.16).
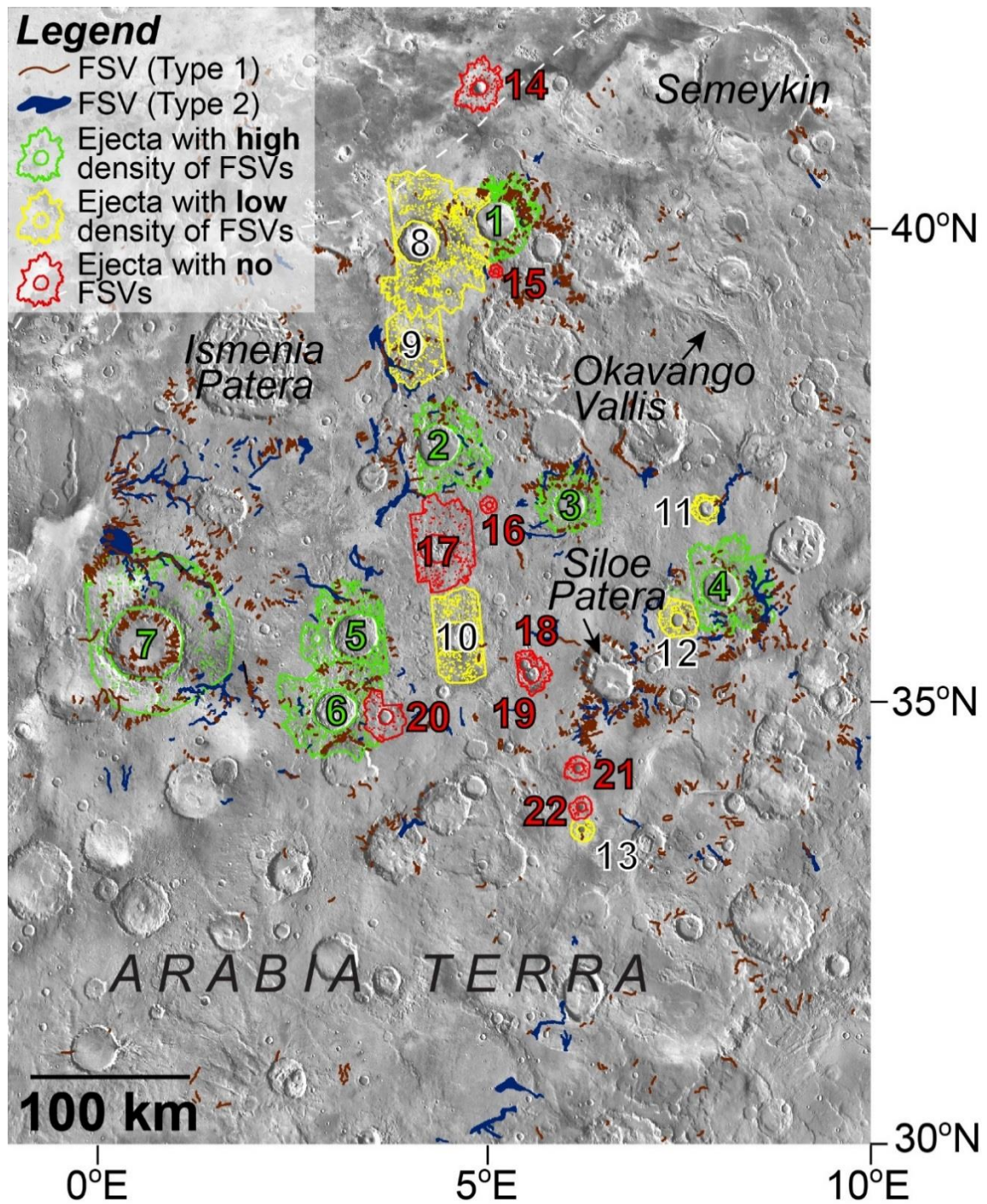
Figure 2.15   Association between fresh shallow valleys and crater ejecta

The majority of mapped FSVs are not associated with crater ejecta. All well-preserved ejecta deposits were mapped as having a 1) high linear density of Type 1 FSVs (Class 1, green), 2) low linear density of Type 1 FSVs (Class 2, yellow), or 3) no Type 1 FSVs (Class 3, red). Craters were counted using CTX data (some ejecta margins were mapped only to the extent of available data). White dashed line shows approximate location of the northern

dichotomy boundary. See Figures 2.16 and 2.17 for the results of the crater statistics and Table 2.3 for characteristics of the mapped craters.
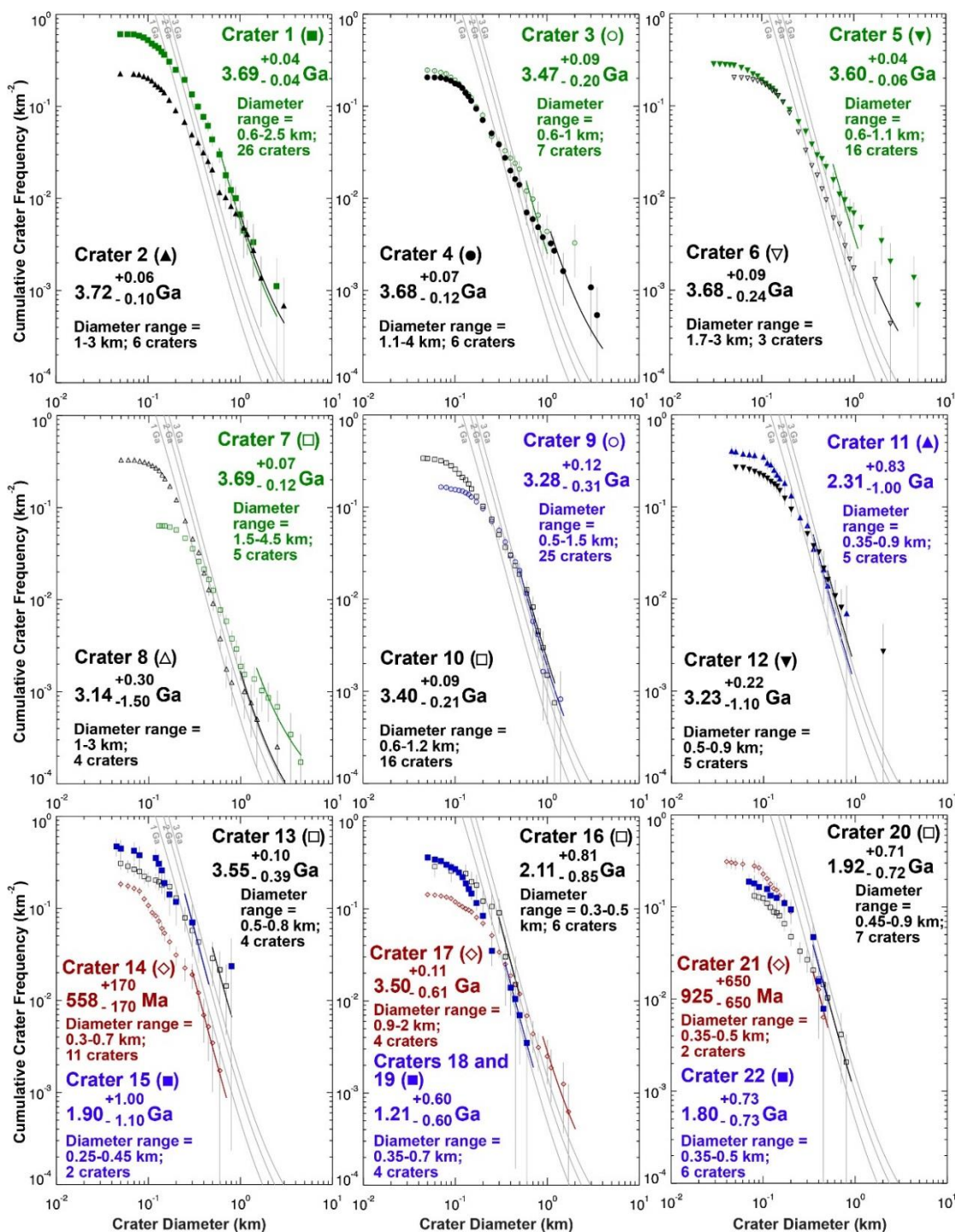
Figure 2.16   Cumulative crater statistics for well-preserved ejecta in the study region

Cumulative crater statistics for well-preserved ejecta mapped in Fig. 2.15 based on the chronology function production from *Hartmann and Neukum* [2001] and a production function from *Ivanov* [2001]. Example absolute ages estimated using Craterstats2 algorithm (error bars reflect +/- $1/N^{0.5}$) [*Michael and Neukum*, 2010] using the largest craters that provide the best fit to the expected production function (Table 2.3). The cumulative resurfacing correction of *Michael and Neukum* [2010] was not applied. The cumulative curves for craters 4, 6 and 7 have a break in slope parallel to the expected production function at crater diameters ranging between 700 m to 1 km that correspond to model ages of 3.39 Ga (+0.11/-0.36) based on 5 craters, 3.03 Ga (+0.29/-0.80) based on 8 craters and 3.28 Ga (+0.11/-0.24) based on 23 craters (see text for discussion).

We classified each ejecta as having a high linear density of FSVs (class 1, n=7), a low linear density of FSVs (class 2, n=6) or no evidence of FSVs (class 3, n=9) (Fig. 2.15, Table 2.3). The linear density of class 1 ejecta ranges from 0.042-0.24 km^{-1} (average 0.099 km^{-1}) and the linear density of class 2 ejecta ranges from 0.007-0.054 km^{-1} (average 0.023 km^{-1}, Table 2.3). A plot combining the estimated crater age vs. the degree of fluvial modification is shown in Fig. 2.17. The maximum estimated model age of craters whose ejecta have a high linear density of FSVs (class 1) are all greater than ~3.5 Ga, with relative ages corresponding to the Hesperian (Fig. 2.17, Table 2.3). The maximum estimated model age of craters whose ejecta have a low linear density of FSVs (class 2) are mostly older than 3 Ga (with the exception of crater 11 that is ~2.3 Ga (+0.83/-1)) with relative ages corresponding to the Hesperian to Amazonian/Hesperian (Fig. 2.17). By contrast, the majority of craters with well-preserved ejecta that are not dissected (class 3) are all less than 2.1 Ga with relative ages corresponding to the Amazonian. Crater 17 is the exception, as it has an approximate absolute age of 3.5 Ga (+0.11/-0.62) but remains fluvially unmodified (Fig. 2.17). The most likely period during which FSVs formed, therefore, was during a relatively short time interval between roughly 3.5 to 2 Ga, with 3 to 3.5 Ga likely representing the oldest period during which incision began.
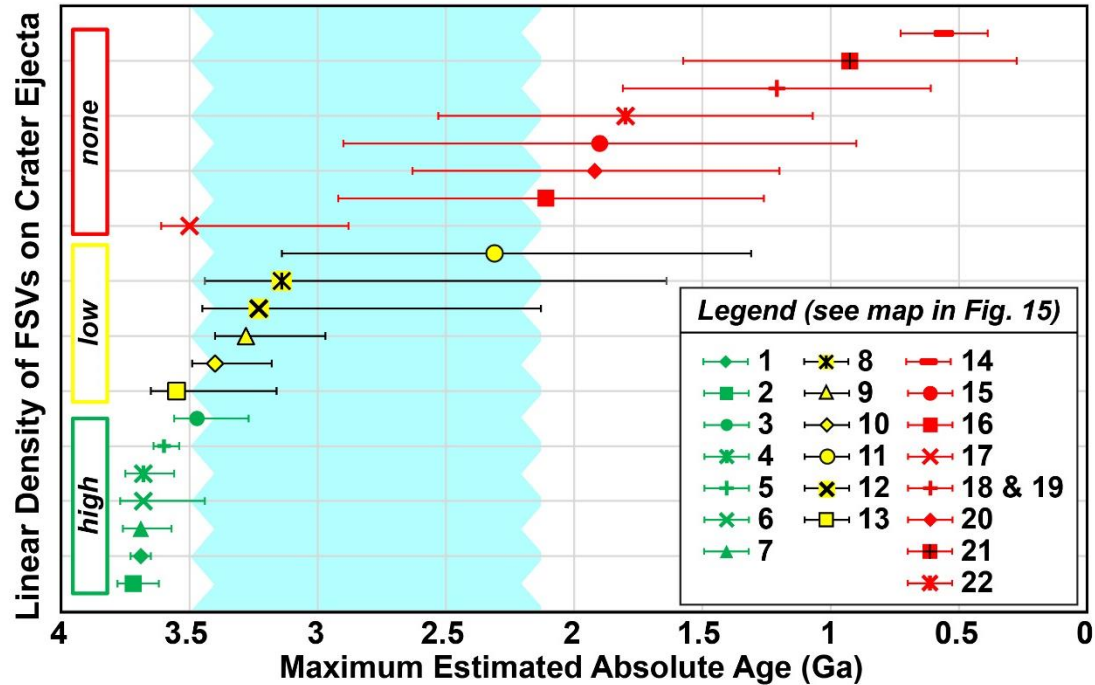
Figure 2.17   Age of well-preserved crater ejecta in the study region

Graph of the maximum estimate ages of the well-preserved crater ejecta in the study region (Fig. 2.16) categorized by their degree of fluvial dissection (Fig. 2.15). The well-preserved ejecta with a high linear density of valleys are relatively older than well-preserved ejecta that is not (or less) modified by fluvial activity. The most likely period during which FSVs formed (blue shaded region) was during a relatively short time interval between roughly 3.5 to 2 Ga, with 3 to 3.5 Ga likely representing the oldest period during which incision began.

     The cumulative curves for craters 4, 6 and 7 have an observed break in slope parallel

to the expected production function (crater diameter range of 0.7-1 km) that yield estimated

model ages of 3.39 Ga (+0.11/-0.36), 3.03 Ga (+0.29/-0.80) and 3.28 Ga (+0.11/-0.24),

respectively (Fig. 2.16). This putative break in slope could represent an erosional event

related to the formation of the FSVs themselves, which is consistent with the range of

possible ages indicated by the collection of statistics (Fig. 2.17). This conclusion is

tentative, however, because the break in slope could also be related to steady state erosion.

We recognize uncertainties introduced by using relatively small individual count areas [e.g., *Platz et al*., 2013; *Grant et al.,* 2014; *Warner et al*., 2015] (Fig. 2.16), but collectively these statistics suggest that 1) well-preserved ejecta with a high linear density of valleys are relatively older than well-preserved ejecta that is not (or less) modified by fluvial activity and 2) most FSV formation likely occurred in a relatively short-lived event sometime around the Amazonian/Hesperian transition to approximately the middle Amazonian (Fig. 2.17).

This dataset also allows us to consider relationships between FSVs and crater variables such as size, latitude, and ejecta elevation and morphology. The class 1 ejecta typically have lobate ejecta and more degraded crater interiors (Table 2.3) that could reflect modification by multiple processes in addition to formation of the FSVs. By contrast, class 2 and 3 ejecta have a less modified crater interior and a strong radial pattern on their ejecta. The crater age, composition of surface materials or substrate, and (or) the topography could influence the ejecta morphology. On average, class 1 ejecta are associated with larger craters (Table 2.3), which is expected from the impact flux that predicts a decrease in crater size population over time. The elevation of the crater ejecta and the latitude do not seem to have a significant role in the distribution of FSVs.

Table 2.3   Characteristics of craters with well-preserved ejecta in the study region

Ejecta Class	Label[1]	D (km)	Lat. (°N)	Approx. Elevation of crater ejecta[2] (m)	Cumulative length of FSVs[3] on ejecta (km)	Area (km2)	Linear Density (km-1) FSVs[3]	Ejecta Morph-Ology	Estimated Maximum Model Age[5]	RA
Class 1: High Linear Density of FSVs	1	25.8	40	-2975	217.8	894	0.24	Lobate	3.69 Ga (+0.04/-0.04)	H
	2	27.7	37.7	-2500	69.37	1451	0.048	Lobate	3.72 Ga (+0.6/-0.10)	H
	3	18.9	37.1	-2100	100.2	917	0.11	Lobate	3.47 Ga (+0.09/-0.20)	H
	4	23.9	36.2	-2250	119.67	1855	0.065	Lobate	3.68 Ga (+0.07/-0.12)	H
	5	29.4	35.7	-2250	61.1	1467	0.042	Lobate	3.60 Ga (+0.04/-0.06)	H
	6	27	34.9	-2100	192.3	2308	0.083	Lobate	3.68 Ga (+0.09/-0.24)	H
	7	48	35.6	-2475	307.8	5822	0.053	Lobate	3.69 Ga (+0.07/-0.12)	H
	Avg.	28.7	36.7	-2380	152.6	2102	0.099	Lobate	--	H
Class 2: Low Linear Density of FSVs	8	25.4	39.8	-3350	63.01	3965	0.016	Radial	3.14 Ga (+0.30/-1.50)	A/H
	9	17	38.8	-2850	17.37	1215	0.014	Radial	3.28 Ga (+0.12/-0.31)	A/H
	10	18.5	35.6	-2150	9.552	1335	0.0072	Radial	3.40 Ga (+0.09/-0.21)	H
	11	11.5	37	-2150	7.754	143	0.054[4]	Lobate	2.31 Ga (+0.83/-1.00)	A/H
	12	9.4	35.8	-2100	6.4	373	0.017	Radial	3.23 Ga (+0.22/-1.10)	A/H
	13	5.7	33.6	-2220	3.8	139	0.028	Radial	3.55 Ga (+0.10/-0.39)	A/H
	Avg.	14.6	36.8	-1753	17.98	1195	0.023	Radial	--	A/H
Class 3: No FSVs	14	9.2	41.5	-3650	0	579	0	Lobate	558 Ma (+170/-170)	A
	15	3.4	39.5	-2825	0	42	0	Radial	1.90 Ga (+1.0/-1.1)	A
	16	4.1	37.1	-2100	0	66	0	Radial	2.11 Ga (+0.81/-0.85)	A
	17	17.5	36.6	-2275	0	1596	0	Lobate	3.5 Ga (+0.11/-0.61)	A/H
	18	7.3	35.4	-2000	0	286	0	Radial	1.21 Ga (+0.60/-0.60)	A
	19	10.4	35.3	-2050	0		0	Radial		
	20	9.2	34.8	-2200	0	571	0	Radial	1.92 Ga (+0.71/-0.72)	A
	21	6.6	34.3	-2160	0	157	0	Radial	925 Ma (+650/-650)	A
	22	5.9	33.8	-2325	0	127	0	Radial	1.80 Ga (+0.73/-0.73)	A
	Avg.	8.2	36.5	-2398	0	428	0	Radial	--	A

[1]See Fig. 2.15. [2]Relative to MOLA. [3] Type 1 FSVs. [4]Only one valley segment. [5]See Figs. 2.16 and 2.17. RA is "relative age" were H is "Hesperian" and "A" is Amazonian, based on estimated model ages including error bars. "D" is crater diameter.

2.7   Discussion

2.7.1   Mechanisms for Fluvial Activity and Sources of Water

A variety of mechanisms have been proposed to account for the formation of post-Noachian valleys including hydrothermal circulation on volcanoes [*Gulick and Baker*, 1990; *Gulick*, 2001b], melting of a snowpack from volcanic heating [*Fassett and Head*, 2006, 2007], melting of ice-rich deposits due to a favorable microclimate at low relative elevations [*Dickson et al.*, 2009], glaciofluvial [*Fassett et al.*, 2010] and flow beneath thin, regionally extensive ice cover [*Hobley et al.*, 2014]. *Carr and Head* [2003] suggest that snow and ice accumulations hundreds of meters thick might melt at their base leading to discharge that excavates fluvial channels. Other research suggests that valley formation is linked to impact cratering, either directly, such that the heat generated from the impact would melt the ice-rich subsurface beneath the ejecta [*Segura et al.*, 2002, 2008; *Williams and Malin*, 2008; *Morgan and Head*, 2009; *Toon et al.*, 2010; *Jones et al.*, 2011; *Mangold*, 2012; *Mangold et al.*, 2012; *Salese et al.*, 2016], or indirectly, where the impact would inject water vapor into atmosphere that would result in regional snow accumulation and subsequent melting [*Kite et al.*, 2011; *Goddard et al.*, 2013].

The aforementioned studies attribute valley formation to local environmental conditions and (or) localized melting of ice from endogenic heat sources, which is not consistent with the nature and distribution of FSVs in northern Arabia Terra. Some investigations, however, suggest valleys required at least regionally extensive precipitation, either producing direct runoff or melting of accumulated snow and ice [*Ansan and Mangold*, 2006; *Mangold et al.*, 2004, 2008; *Burr et al.*, 2010; *Howard and Moore*, 2011; *Adeli et al.*, 2016;]. At present, evidence for Amazonian-Hesperian paleolakes that

are contemporaneous with fluvial valley formation is limited, but previous studies include examples from Tempe Terra along the dichotomy boundary (35.6°N 305.3°E) [*Salese et al.*, 2016], the region near Ares Vallis (0-17°N, 330-350°E) [*Warner et al.*, 2010b], Eberswalde crater [e.g., as summarized in *Irwin et al.*, 2015] and Gorgonum basin (37°S, 189°E) [*Howard and Moore*, 2011].

2.7.2   Evidence for Paleolakes

Regional mapping reveals that the majority of valleys occur far from young impact craters, making a direct and (or) indirect association with impact processes less probable (Fig. 2.15). Instead, the valleys characteristically start abruptly on uplands and terminate along the flanks of numerous depressions at elevations that correspond remarkably well to model-predicted lake surfaces at an X-ratio of ~2.2 (Fig. 2.6). We propose some FSV segments flowed both into and out of paleolakes to form 150-200 km long valley systems. The morphological evidence supporting the continuity of FSVs across intra-valley depressions such as basin B in the Heart Lake system (Section 2.4.3) and basins F and G in the Northern Plains system (Section 2.4.4) includes 1) consistent widths of the basin inlet and outlet, including an incised channel within a larger channel, 2) equal elevation for the termination and origin of the level of the incoming and outgoing channels, respectively 3) absence of FSVs on the inferred paleolake floor below level of the valley inlet and outlet, 4) overall continuity of profile of FSV system above and below inferred lake, after accounting for the intervening flat lake surface, and 5) the modeled lake would have overflowed for the X-ratio value that correlates best with the regional occurrence and distribution of FSVs (particularly their downstream terminations).

Morphological evidence consistent with the location and extent of the modeled paleolakes includes 1) equal elevation for the termination and origin of the level of the incoming and outgoing FSVs at the modeled margins of the basins, 2) inferred sedimentary fan deltas occur along the interior margins of some model-predicted lakes, 3) fans, if deltaic in origin, would imply deposition into deep bodies of standing water, which is consistent with the observation that the fans are located hundreds of meters above the floors of their respective host basins (Table 2.2), 4) some fan deltas preserve evidence of fluctuating lake levels (Figs. 2.7D and 2.10), and 5) basin floor deposits inferred to be sedimentary in origin (Figs. 2.2D and 2.8B) are associated with model-predicted filled basins (Fig. 2.6).

2.7.3   Discharge Estimates and Style of Erosion

The wide and strongly incised channel immediately downstream from the outlet of basin B is exceptional for FSVs in the study region and is indicative of high-discharge flow (Fig. 2.9B). This system could have formed from 1) multiple, sustained flows or 2) a single overflow event with a complex history of widening and valley incision that lead to the abandonment of depositional bars related to peak flow stages, similar to the Noachian-Hesperian Okavango Valles [*Mangold and Howard*, 2013]. The down-cutting of the outflow valley (Fig. 2.9B) supports formation by a single overflow event, but the comparable width of the basin B inlet valley (Fig. 2.8) is more consistent with relatively high runoff throughout the entire system. If the outlet from basin B (Fig. 2.9) experienced rapid breaching and downcutting of the lake outlet, discharge rates may have greatly exceeded the estimates stated in Section 2.5 for a short period of time [e.g., *Mangold and Howard*, 2013].

Most of the FSVs in Arabia Terra do not have incised channels and could have formed in a single episode of erosion. The presence of incised interior channels as in the Heart Lake and Northern Plains systems, however, supports formation via progressive erosion [e.g., *Irwin et al.*, 2005b]. The interior channel could have formed as water levels decreased and the channel became entrenched, perhaps in response to a change in hydrologic regime toward increasing aridity. Alternatively, the incised channels could be related to smaller lake-overflow events that occurred subsequent to a main overflow event or as a response to changes in local base level.

Estimated discharges vary considerably as a function of grain size as well as assumptions about the nature of the flow within the channel. As discussed in Section 2.5, discharge estimates based on the dimensions of the incised interior channel ranges from ~10s to 100s to 1000s m^3 s^{-1} based on the active transport of medium sand, very coarse sand and gravel, respectively. Likewise, discharge estimates based on the dimensions of the main channel ranges from 100s to 1000s to tens of thousands m^3 s^{-1} for a medium sand, very coarse sand and gravel bed, respectively. We calculated similar estimated discharges using empirical roughness coefficients based upon sediment size, channel gradient, Shields stress, and sediment density [e.g. *Morgan et al.*, 2014]. *Mangold* [2012] estimated much higher discharge rates (500-10,000s m^3 s^{-1}) for valleys on ejecta in northern Arabia Terra area based on greater flow depths using a range of estimated channel depths. We consider our discharge estimates to be conservative and they are commensurate with runoff yields from snowmelt on Mars [e.g., *Moore et al.*, 2003; *Howard and Moore*, 2011; *McKnight*, 2011; *Kite et al.*, 2013; *Parsons et al.*, 2013; *Salese et al.*, 2016]. Terrestrial analogues would include snowmelt-fed streams at high elevation or high latitude such as in

65

Cornwallis Island in the Canadian Arctic or the Tibetan Plateau, where valleys are characterized by low drainage densities and incised channels that serve as traps for windblown snow.

2.7.4 The Role of Groundwater

The formation of a thick cryosphere in the Hesperian and Amazonian makes a groundwater-related source (e.g., groundwater seeps) for the formation of valleys less likely [*Clifford et al*., 2010]. This is consistent with our observations that 1) the majority of FSVs occur well away from impact craters (Fig. 2.15), 2) many young crater ejecta lack FSVs and 3) the presence of long valley systems (e.g., Heart Lake and Northern Plains) are not consistent with impact-generated sources and (or) groundwater seeps. Numerous single-exit-breach craters (pollywogs) that imply overflow of a deep interior crater lake, however, may argue for connection to groundwater, which could be related to groundwater upwelling previously predicted in Arabia Terra from hydrological modeling on early Mars [*Andrews-Hanna et al*., 2010].

The overflow of pollywogs in northern Arabia Terra seem to integrate into the local FSV systems, suggesting their formation was contemporaneous. If the region experienced large accumulations of snow and ice across the landscape, eventual overflow of craters with smaller diameters may occur. Although the nature of the permafrost and the groundwater table is unknown, pollywogs may be indicative of the involvement of artesian groundwater flow filling the lakes to overflow. Seasonally-unfrozen lakes in terrestrial permafrost regions develop unfrozen depressions in the permafrost (taliks) which, if the lakes are sufficiently large and the permafrost sufficiently thin, can extend to the base of the permafrost (through taliks) [e.g. *Burn*, 2002]. If there is an upward hydraulic gradient

in the sub-permafrost aquifer, thermal advection can enhance and maintain through taliks [*Scheidegger and Bense*, 2014]. We have noted pollywog craters elsewhere located on regional slopes [e.g., *Parsons et al.*, 2013] where artesian pressures beneath the permafrost might be involved, and, because of the low elevation of the northern Arabia region, might be connected to a global artesian sub-permafrost aquifer [*Clifford and Parker*, 2001; *Andrews-Hanna et al.*, 2010]. Pollywogs are only seen in craters with diameters between 0.6-13 km, perhaps suggesting that this diameter range is capable of depressing the permafrost to access groundwater via fractures along the crater floor to form seasonally ice-covered lakes. Larger, deeper craters may access the permafrost layer along the crater walls and smaller craters ($< \sim 0.5$ km in diameter) have insufficient depths to access groundwater.

2.7.5 The Timing and Duration of Fluvial Activity and Implications for Climate

The hydrologic routing model utilized in this study provides basic insight into the flow of water across a surface based on the assumed ratio of runoff to lake evaporation. The model and resulting X-ratio values assumes 1) precipitation (or melting) is uniform across the landscape, 2) spatial properties of the surface are uniform, and 3) the resulting lake levels correspond to a yearly average of precipitation to evaporation. Although the model provides a simplified view of the regional hydrology, it is particularly useful for predicting the level at which lake overflow would occur.

In the Heart Lake system, there is clear morphologic evidence of overflow from basins A, B and D where the model-predicted X-Ratio values corresponding to overflow are ≤ 4, $\leq \sim 2.2$ and ≤ 4, respectively (Table 2.1). X-ratios for overflow of Heart Lake and

basin C corresponds to values of ≤2.25 and ≤2.75, respectively. The lack of convincing morphologic evidence for overflow from basin C along with the higher X-Ratio value predicted for overflow may indicate the hydrologic system was not in a steady state with respect to an X-ratio value of ~2.2. This X-ratio of 2.75 for basin C could reflect issues not accounted for by the model, such as non-uniform precipitation or time-limited infilling of basins (such that there was not enough time or available water to infill basin C but enough to infill basin B). The surface elevation of the fan delta platform in basin C (formed by overflow of basin D) corresponds to a modeled lake level with X-ratio of 3.5, which is in the range for this Heart Lake system (Table 2.2). In the Northern Plains system, morphologic evidence of overflow from basins E and F correspond to model-predicted X-Ratios of ≤ 2.5 and ≤ 4, respectively. The X-ratios necessary to provide lake levels consistent with 12 within-crater deltas range from 1.4 to 3.5, averaging 2.5 (Table 2.2).

The degree to which we get reasonable agreement of X-ratio values that are consistent with the distribution of FSVs and deltas deposited into paleolakes across the region is indicative of a relatively stable climate over the timescale that the FSVs were active. As explained by *Matsubara et al.* [2013], the value of the X-ratio does not correspond to any one combination of precipitation, runoff and evaporation - several combinations of values for these variables could result in the same X-ratio. For example, an X-ratio of ~2.2 could result from P=0.5 m yr $^{-1}$, R=0.45, and E=1 m yr $^{-1}$ or P=1.45 m yr -1, R=0.17, E=2 m yr -1 [after *Matsubara et al*., 2013]. In terrestrial systems with through-flowing drainage, corresponding X-ratios would be in the range of -1 to 0, whereas in terrestrial deserts the X-ratio may exceed 20 [*Matsubara et al*., 2013]. *Matsubara et al*., [2011] found X-ratio values in the range of 3-7 for the late Noachian climate on Mars,

which would be comparable to the evaporation and precipitation regime during the late Pleistocene epoch in the Great Basin region when lakes Lahontan and Bonneville were at their greatest extent [*Matsubara and Howard*, 2009].

The widespread distribution of FSVs (Fig. 2.3), their similar morphology and modest state of degradation is consistent with formation during a global interval of favorable climate. The climate suggested by the landforms and modeling in Arabia Terra was capable of sustaining a considerable volume of water on the landscape, with basin B alone containing a volume of water greater than the present-day Lake Tahoe in California (Table 2.2). Given the presumed cold temperatures in Hesperian and Amazonian, it is likely that larger bodies of water remained frozen for most of the time and valleys formed during intermittent melting events. The presence of ice-covered lakes is consistent with the sinuous ridges on some basin floors that could be eskers. The proposed Hesperian-Amazonian snowmelt-based hydrology likely continued seasonally or episodically over hundreds of years although shorter time scales are possible. Lake levels are interpreted to be an average response to longer-term climate conditions.

The increased coverage of high resolution images has facilitated the identification and analysis of post-Noachian fluvial landforms that further our understanding of the climate evolution of Mars. These landforms, including valleys in the mid-latitude regions of both hemispheres [e.g., *Dickson et al.*, 2009; *Fassett and Head*, 2008, 2011; *Hynek et al.*, 2010; *Warner et al.*, 2010a, 2010b; *Howard and Moore,* 2011; *Hauber et al.*, 2013; *Adeli et al.*, 2016; *Salese et al.*, 2016] as well as alluvial fans at the equator to mid-latitudes [e.g., *Moore and Howard*, 2005; *Grant and Wilson*, 2011, 2012; *Wilson et. al.*, 2013; *Grant et al.*, 2014; *Morgan et al.*, 2014;], challenge the paradigm that fluvial activity ceased at

the Noachian-Hesperian boundary. The trigger for climatic warming could be related to obliquity-driven changes in insulation [e.g., *Laskar et al*., 2004] or warming from ephemeral atmospheric changes [*Hobley et al*., 2014]. Evidence supporting the existence of an active hydrologic cycle during the Hesperian to Amazonian is intriguing, as the associated (ice-covered?) lakes may have provided habitable environments for microbial life to form and (or) persist on Mars.

2.8   Summary

Modification by water and ice on a paleo-landscape is one of the most unambiguous markers of past climate. The widespread distribution of FSVs in the mid-latitudes, their similar morphology, and modest state of degradation is consistent with most forming during a global interval of favorable climate, likely through snowmelt from surface or sub-ice flows. The distribution and morphology of the FSVs in northern Arabia Terra is consistent with an active hydrological system near the Hesperian-Amazonian boundary during a time period on Mars that was always thought to be less favorable for precipitation (in the form of snow) and runoff. The modeled paleolakes in northern Arabia Terra imply a considerable depth of water on the landscape late in Mars history, possibly extending habitable conditions well into the Amazonian. Similar FSVs occur at the equator but they are often harder to distinguish from older valley networks and in some cases they may reactivate older channels. The transient warming that formed FSVs in the mid-latitudes may be contemporaneous with alluvial fan and delta formation in equatorial to mid-latitudes.

2.9   Citation

Wilson, S. A., A. D. Howard, J. M. Moore, and J. A. Grant (2016), A cold-wet middle-latitude environment on Mars during the Hesperian-Amazonian transition: Evidence from Northern Arabia Valleys and Paleolakes, *J. Geophys. Res. Planets*, 121, doi:10.1002/2016JE005052.

2.10   References

Adeli, S., E. Hauber, M. Kleinhans, L. Le Deit, T. Platz, P. Fawdon and R. Jaumann (2016), Amazonian-aged fluvial system and associated ice-related features in Terra Cimmeria, Mars, *Icarus*, *288*, 286-299, http://dx.doi.org/10.1016,/j.icarus.2016.05.020.

Andrews-Hanna, J. C., M. T. Zuber, R. E. Arvidson and S. M. Wiseman (2010), Early Mars hydrology: Meridiani playa deposits and the sedimentary record of Arabia Terra, *J. Geophys. Res. Planets*, *115*, E06002, doi:10.1029/2009JE003485.

Ansan, V. and N. Mangold (2006), New observations of Warrego Valles, Mars: Evidence for precipitation and surface runoff, *Planet. Space Sci*. *54*, 219–242.

Berman, D. C., D. A. Crown and L. F. I. Bleamaster (2009), Degradation of mid-latitude craters on Mars, *Icarus*, *200*, 77-99.

Burn, C. R. (2002), Tundra lakes and permafrost, Richards Island, western Arctic coast, Canada, *Canadian Journal of Earth Science*, *39*(8), 1281-1298, doi:10.1139/E02-035

Burr, D. M., R. M .E. Williams, K .D. Wendell, M. Chojnacki and J. P. Emery (2010), Inverted fluvial features in the Aeolis/Zephyria Plana region, Mars: Formation mechanism and initial paleodischarge estimates, *J. Geophys. Res*., *115*, E07011, doi:10.1029/2009JE003496.

Carr, M. H. (2012), *The fluvial history of Mars*, Philosophical Transactions of the Royal Society of London Series A, 370, 2193-2215.

Carr, M. H. and J. W. Head (2003), Basal melting of snow on early Mars: A possible origin of some valley networks, *Geophys. Res. Lett. 30*, 2245. doi:10.1029/2003GL018575.

Christensen, P. R., E. Engle, S. Anwar, S. Dickenshied, D. Noss, N. Gorelick, M. Weiss-Malik (2009), JMARS – A Planetary GIS, http://adsabs.harvard.edu/abs/2009AGUFMIN22A..06C.

Clifford, S. M., and Parker, T. J. (2001), The evolution of the martian hydrosphere: Implications for the fate of a primordial ocean and the current state of the Northern Plains, *Icarus*, *154*, 40-79, doi:10.1006/icar.2001.6671.

Clifford, S. M., J. Lasue, E. Heggy, J. Boisson, P. McGovern, and M. D. Max (2010), Depth of the Martian cryosphere: Revised estimates and implications for the existence and detection of subpermafrost groundwater, *J. Geophys. Res.*, *115*, E07001, doi:10.1029/2009JE003462.

Craddock, R.A., and A.D. Howard (2002), The case for precipitation on a warm, wet early Mars, *J. Geophys. Res.*, *107* (E11), doi:10.1029/2001JE001505.

Di Achille, G., and B. M. Hynek (2010), Ancient ocean on Mars supported by global distribution of deltas and valleys, *Nature Geoscience, 3*, 459 – 463.

Dickson, J.L., C.I. Fassett, and J.W. Head (2009), Amazonian-aged fluvial valley systems in a climatic microenvironment on Mars: Melting of ice deposits on the interior of Lyot Crater, *Geophys. Res. Lett.*, *36*, L08021, doi:10.1029/2009GL037472.

Fassett, C.I., and J.W. Head, III (2006), Valleys on Hecates Tholus, Mars: origin by basal melting of summit snowpack*, Planetary and Space Science*, *54*, 370-378.

Fassett, C. I. and J. W. Head (2007), Valley formation on martian volcanoes in the Hesperian: Evidence for melting of summit snowpack, caldera lake formation, drainage and erosion on Ceraunius Tholus, *Icarus*, *189*, 118-135.

Fassett, C. I. and J. W Head (2008), Timing of martian valley network activity: Constraints from buffered crater counting, *Icarus*, *198*, 61-89.

Fassett, C. I. and J. W. Head (2011), Sequence and timing of conditions on early Mars, *Icarus*, *211*, 1204-1214.

Fassett, C.I., J. L. Dickson, J. W. Head, J. S. Levy and D. R. Marchant (2010), Supraglacial and proglacial valleys on Amazonian Mars, *Icarus*, *208*, 86-110.

Goddard, K., N. H. Warner, S. Gupta and J.-R. Kim (2014), Mechanisms and timescales of fluvial activity at Mojave and other young Martian craters, *J. Geophys. Res. Planets*, *119*, 604–634, doi:10.1002/2013JE004564.

Goudge, T. A., K. L. Aureli, J. W. Heaad, C. I Fassett and J. F. Mustard (2015), Classification and analysis of candidate impact crater-hosted closed-basin lakes on Mars, *Icarus*, *260*, 349-367, doi:10.1016/j.icarus.2015.07.026.

Grant, J. A. (2000), Valley formation in Margaritifer Sinus, Mars, by precipitation-recharged ground-water sapping, *Geology*, *28* (3), 223-226.

Grant, J. A. and S. A. Wilson (2011), Late alluvial fan formation in southern Margaritifer Terra, Mars, *Geophys. Res. Letts*., *38*, L08201, doi:10.1029/2011GL046844.

Grant, J. A. and S. A. Wilson (2012), A possible synoptic source of water for alluvial fan formation in southern Margaritifer Terra, Mars, *Planet. Space Sci*., *72*, 44-52, 10.1016/j.pss.2012.05.020.

Grant, J. A. S., A. Wilson, N. Mangold, Fred Calef III, and J. P. Grotzinger (2014), The timing of alluvial activity in Gale crater, Mars, *Geophys. Res. Lett*., *41*, 1142-1149.

Grant, J. A., S. A. Wilson, N. Mangold and F. Calef III (2014), The timing of alluvial activity in Gale crater, Mars, *Geophys. Res. Letts*., *41* (4), 1142-1149, DOI: 10.1002/2013GL058909.

Gulick, V. C. (2001a), Some ground water considerations regarding the formation of small Martian gullies, *Lunar and Planet. Sci. Conf.*, Abstract 2193.

Gulick, V. C. (2001b), Origin of the valley networks on Mars: A hydrological perspective, *Geomorphology*, *37*, 241-268.

Gulick, V. C. and V. R. Baker (1990), Origin and evolution of valleys on Martian volcanoes, *J. Geophys. Res*., *95*, 14325-14344.

Hauber, E., T. Platz, D. Reiss, L. Le Deit, M. G. Kleinhans, W. A. Marra, T. de Haas and P. Carbonneau (2013), Asynchronous formation of Hesperian and Amazonian-aged deltas on Mars and implications for climate, *J. Geophys. Res. Planets*, *118*, 1529–1544, doi:10.1002/jgre.20107.

Hartmann, W. K. (2005), Martian cratering 8: Isochron refinement and the chronology of Mars, *Icarus*, *174*, 294-320.

Hartmann, W. K. and G. Neukum (2001), Cratering chronology and the evolution of Mars, *Space Science Reviews*, *96*, 165–194.

Head, J. W., G. Neukum, R. Jaumann, H. Hiesinger, E. Hauber, M. Carr, P. Masson, B. Foing, H. Hoffmann, M. Kreslavsky, S. Werner, S. Milkovich, S. van Gasselt, and the HRSC Co-Investigator Team (2003), Tropical to mid-latitude snow and ice

accumulation, flow and glaciation on Mars, *Nature*, *434*, 346-351, doi:10.1038/nature03359.

Hobley, D. E. J., A. D. Howard and J. M. Moore (2014), Fresh shallow valleys in the Martian midlatitudes as features formed by meltwater flow beneath ice, *J. Geophys. Res.*, DOI: 10.1002/2013JE004396.

Howard, A. D. and J. M. Moore (2011), Late Hesperian to early Amazonian midlatitude Martian valleys: Evidence from Newton and Gorgonum basins, *J. Geophys. Res.*, *116*, E05003, doi:10.1029/2010JE003782.

Howard, A. D., J. M. Moore and R. P. Irwin, III (2005), An intense terminal epoch of widespread fluvial activity on early Mars: 1. Valley network incision and associated deposits, *J. Geophys. Res.*, *110* (D12S14), doi:10.1029/2005JE002459.

Howard, A.D., J. M. Moore and S. A. Wilson (2014), Fresh Shallow Valleys (FSVs) on Mars, 8th Mars conference, July 14-18, Pasadena, CA.

Hynek, B. M. and R. J. Phillips (2001), Evidence for extensive denudation of the Martian highlands, *Geology*, *29* (5), 407-410.

Hynek, B. M., and R. J. Phillips (2003), New data reveal mature, integrated drainage systems on Mars indicative of past precipitation, *Geology*, *31* (9), 757-760.

Hynek, B. M., M. Beach and M. R. T. Hoke (2010), Updated global map of Martian valley networks and implications for climate and hydrologic processes, *J. Geophys. Res.*, *115*, E09008, doi:10.1029/2009JE003548.

Irwin, R. P. III and A. D. Howard (2002), Drainage basin evolution in Noachian Terra Cimmeria, Mars, *J. Geophys. Res.*, *107* (E7), 10.1029/2001JE001818.

Irwin, R. P., III, T. A. Maxwell, A. D. Howard, R. A. Craddock, and J. M. Moore (2005a), An intense terminal epoch of widespread fluvial activity on early Mars: 2. Increased runoff and paleolake development, *J. Geophys. Res.*, *110*, E12S15, doi:10.1029/2005JE002460.

Irwin, R. P., III, R. A. Craddock and A. D. Howard (2005b), Interior channels in Martian valley networks: Discharge and runoff production, *Geology*, *33*, 489-492.

Irwin, R. P., III, K. W. Lewis, A. D. Howard and J. A. Grant (2015), Paleohydrology of Eberswalde crater, Mars, *Geomorphology*, *240*, 83-101.

Ivanov, B. A. (2001), Mars/Moon cratering ratio estimates, *Space Science Review*, *96*, 87–104.

Jones, A. P., A. S. McEwen, L. L. Tornabene, V. R. Baker, H. J. Melosh and D. C. Berman (2011), A geomorphic analysis of Hale crater, Mars: the effects of inpact into ice-rich crust, *Icarus*, *211*, 259-272.

Kite, E. S., T. I Michaels, S. Rafkin, M. Manga, and W. E. Dietrich (2011), Localized precipitation and runoff on Mars, *J. Geophys. Res.*, *116*, E07002, doi:10.1029/2010JE003783.

Kite, E. S., I. Halevy, M. A. Kahre, M. J. Wolff and M. Manga (2013), Seasonal melting and the formation of sedimentary rocks on Mars, with predictions for the Gale Crater mound, *Icarus*, *223*, 181-210.

Kneissl, T., S. van Gasselt and G. Neukum (2011), Map-projection-independent crater size-frequency determination in GIS environments—New software tool for ArcGIS, *Planet. Space Sci.*, *59*, 1243-1254, doi:10.1016/j.pss.2010.03.015.

Laskar, J., A. C. M. Correia, M. Gastineau, F. Joutel, B. Levrard and P. Robutel (2004), Long term evolution and chaotic diffusion of the insolation quantities of Mars, *Icarus*, *170*, 2, 343-364, Doi 10.1016/J.Icarus.2004.04.005.

Luo, W. and T. F. Stepinski (2009), Computer-generated global map of valley networks on Mars, *J. Geophys. Res.*, *114*, E11010. http://dx.doi.org/10.1029/2009JE003357.

Malin, M. C. and K. S. Edgett (2000), Evidence for recent groundwater seepage and surface runoff on Mars, *Science*, *288*, 2330-2335.

Malin, M. C., et al. (2007), Context Camera Investigation on board the Mars Reconnaissance Orbiter, *J. Geophys. Res.*, *112*, E05S04, doi:10.1029/2006JE002808.

Mangold, N. (2012), Fluvial landforms on fresh impact ejecta on Mars, *Planet. Space Sci.*, *62*, 69-85.

Mangold, N. and A. D. Howard (2013), Outflow channels with deltaic deposits in Ismenius Lucas, Mars, *Icarus*, *226*, 385-401, http://dx.doi.org/10.1016/j.icarus.2013.05.040.

Mangold, N., C. Quantin, V. Ansan, C. Delacourt and P. Allemand (2004), Evidence for precipitation on Mars from dendritic valleys in the Valles Marineris area, *Science*, *305*, 78-81.

Mangold, N., V. Ansan, P. Masson, C. Quantin and G. Neukum (2008), Geomorphic study of fluvial landforms on the northern Valles Marineris plateau, *J. Geophys. Res.*, *113*, E08009, doi:10.1029/2007JE002985.

Mangold, N., E. S. Kite, M. G. Kleinhans, H. Newsom, V. Ansan, E. Hauber, E. Kraal, C. Quantin and K. Tanaka (2012), The origin and timing of fluvial activity at Eberswalde crater, Mars, *Icarus*, *220*, 530-551.

Matsubara, Y. and A. D. Howard (2009), A spatially-explicit model of runoff, evaporation and lake extent: Application to modern and late Pleistocene lakes in the Great Basin region, western United States, *Water Resour. Res*., *45*, W06425, doi:10.1029/2007WR005953.

Matsubara, Y., A. D. Howard and S. A. Drummond (2011), Hydrology of early Mars: Lake basins, *J. Geophys. Res*., *116*, E04001, doi:10.1029/2010JE003739.

Matsubara, Y., A. D. Howard and J. P. Gochenour (2013), Hydrology of early Mars: Valley network incision, *J. Geophys. Res*., *118*, doi:10.1002/jgre.20081.

McEwen, A. S., et al. (2007), Mars Reconnaissance Orbiter's High Resolution Imaging Science Experiment (HiRISE), *J. Geophys. Res*., *112*, E05S02, doi:10.1029/2005JE002605.

McKnight, D. (2011), Onyx River at Vanda Gauge Measurements. National Science Foundation McMurdo Dry Valleys Long Term Ecological Research Signature Datasets. knb-lter-mcm.9022.4.

Michael, G. G. and G. Neukum (2010), Planetary surface dating from crater size-frequency distribution measurements: Partial resurfacing events and statistical age uncertainty, *Earth and Planet. Sci. Letts*., doi:10.1016/j.epsl.2009.12.041.

Michalski, J. R. and J. E. Bleacher (2013), Supervolcanoes within an ancient volcanic province in Arabia Terra, Mars, *Nature*, *502*, 47–52, doi:10.1038/nature12482.

Moore, J. M. and A. D. Howard (2005), Large alluvial fans on Mars, *J. Geophys. Res*., *110*, E04005.

Moore, J. M., A. D. Howard, W. E. Dietrich and P. M. Schenk (2003), Martian layered fluvial deposits: Implications for Noachian climate scenarios, *Geophys. Res. Letts.*, *30*, 2292.

Morgan, A. M., A. D. Howard, D. E. J. Hobley, J. M. Moore, W. E. Dietrich, R. M. E. Williams, D. M. Burr, J. A. Grant, S. A. Wilson and Y. Matsubara (2014), Sedimentology and climatic environment of alluvial fans in the martian Saheki crater and a comparison with terrestrial fans in the Atacama Desert, *Icarus*, *229*, 131-156.

Morgan, G. A. and J. W Head (2009), Sinton crater, Mars: Evidence for impact into a plateau icefield and melting to produce valley networks at the Hesperian-Amazonian boundary, *Icarus*, *202*, 39-59.

Mustard, J. F., C. D. Cooper and M. K. Rifkin (2001), Evidence for recent climate change on Mars from the identification of youthful near-surface ground ice, *Nature*, *412*, 4111-4114.

Neukum, G., Jaumann, R., and the HRSC Co-Investigator and Experiment Team (2004), HRSC: the high resolution stereo camera of Mars Express, *ESA Spec. Publ. 1240*, 1–19.

Palucis, M. C., W. E. Dietrich, A. G. Hayes, R. M. E. Williams, S. Gupta, N. Mangold, H. Newsom, C. Hardgrove, F. Calef III and D Y. Sumner (2014), The origin and evolution of the Peace Vallis fan system that drains to the *Curiosity* landing area, Gale crater, Mars, *J. Geophys. Res.*, *119* (4), 705-728, DOI: 10.1002/2013JE004583.

Parsons, R.A., J. M. Moore and A. D. Howard (2013), Evidence for a short period of hydrologic activity in Newton crater, Mars, near the Hesperian-Amazonian transition, *J. Geophys. Res.*, *118* (5), 1082-1093, DOI: 10.1002/jgre.20088.

Platz, T. G. Michael, K. L. Tanaka, J. A. Skinner, Jr. and C. M. Fortezzo (2013), Crater-based dating of geological units on Mars: Methods and application for the new global geological map, *Icarus*, *225*(1), 806-827, doi:10.1016/j.icarus.2013.04.021.

Salese, F., G. Di Achille, A. Neesemann, G. G. Ori and E. Hauber (2016), Hydrological and sedimentary analyses of well-preserved paleofluvial-paleolacustrine systems at Moa Valles, Mars, *J. Geophys. Res. Planets*, *121*, doi:10.1002/2015JE004891.

Scheidegger, J. M. and V. F. Bense (2014), Impacts of glacially recharged groundwater flow systems on talik evolution, *J. Geophys. Res.: Earth Surface*, *119*, 758-778, doi:10.1002/2013JF002894.

Segura, T. L., O. B. Toon, A. Colaprete and K. Zahnle (2002), Environmental effects of large impacts on Mars, *Science*, 298(5600), 1977-1980, doi:10.1126/science.1073586.

Segura, T. L., O. B. Toon and A. Colaprete (2008), Modeling the environmental effects of moderate-sized impacts on Mars, *J. Geophys. Res.*, *113*, E11007, doi:10.1029/2008JE003147.

Smith, D. E., and 18 others (1999), The global topography of Mars and implications for surface evolution, *Science*, *284*, 1495-1503.

Soderblom, L. A., T. J. Kreidler and H. Masursky (1973), Latitudinal Distribution of a Debris Mantle on the Martian Surface, *J. Geophys. Res.*, *78* (20), 4117-4122.

Talling, P. J. (2000), Self-organization of river networks to threshold states, *Water Resources Research*, *36*, 4, 1119-1128.

Tanaka, K. L., J. A. Skinner Jr., J. M. Dohm, R. P. Irwin III, E. J. Kolb, C. M. Fortezzo, T. Platz, G. G. Michael and T. M. Hare (2014), Geologic map of Mars, *U.S. Geological*

Survey Scientific Investigations Map 3292, scale 1:20,000,000, pamphlet 43 p., http://dx.doi.org/10.3133/sim3292.

Toon, O. B. T. Segura and K. Zahnle (2010), The Formation of Martian River Valleys by Impacts, *Annual Review of Earth and Planetary Sciences*, 38, 303-322, https://doi.org/10.1146/annurev-earth-040809-152354.

Warner, N., S. Gupta, J-R. Kim, S.-Y Lin and J.-P. Muller (2010a), Hesperian equatorial thermokarst lakes in Ares Vallis as evidence for transient warm conditions on Mars, *Geology*, *38* (1), 71–74, doi:10.1130/G30579.1

Warner, N. S., S. Gupta, S-Y. Lin, J. –R. Kim, J.-P. Muller and J. Morley (2010b), Late Noachian to Hesperian climate change on Mars: Evidence of episodic warming from transient crater lakes near Ares Vallis, *J. Geophys. Res*., *115*, E06013, doi:10.1029/2009JE003522.

Warner, N. S., S. Guputa, F. Calef, P. Grindrod, N. Boll and K. Goddard (2015), Minimum effective area for high resolution crater counting of martian terrains, *Icarus*, *245*, 198-240, doi:10.1016/j.icarus.2014.09.024.

Williams, R. M. E. and M. C. Malin (2008), Sub-kilometer fans in Mojave Crater, Mars, *Icarus*, *198*, 365–383.

Willmes, M., D. Reiss, H. Hiesinger and M. Zanetti (2011), Surface age of the ice-dust mantle deposit in Malea Planum, Mars, *Planet. Space Sci*., doi:10.1016/j.pss.2011.08.006.

Wilson, S. A., J. A. Grant and A. D. Howard (2013), Inventory of equatorial alluvial fans and deltas on Mars, *Lunar and Planet. Sci. Conf.*, Abstract 2710.

2.11   JPL Press Release

https://www.jpl.nasa.gov/news/news.php?feature=6619

Jet Propulsion Laboratory
California Institute of Technology

Some Ancient Mars Lakes Came Long After Others
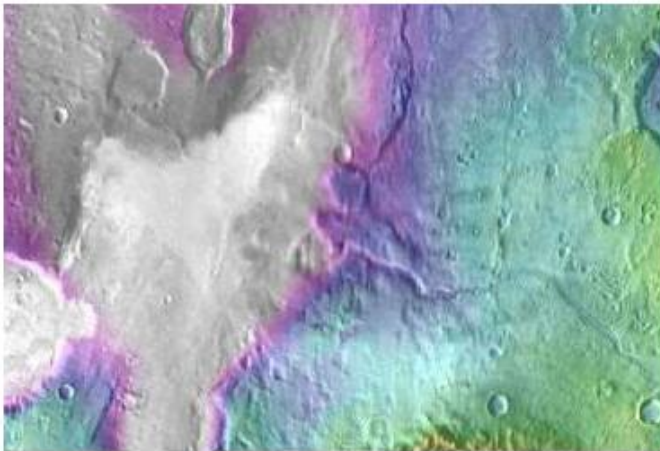
Valleys much younger than well-known ancient valley networks on Mars are evident near the informally named "Heart Lake" on Mars. Image credit: NASA/JPL–Caltech/ASU
› Full image and caption

Lakes and snowmelt-fed streams on Mars formed much later than previously thought possible, according to new findings using data primarily from NASA's Mars Reconnaissance Orbiter.

The recently discovered lakes and streams appeared roughly a billion years after a well-documented, earlier era of wet conditions on ancient Mars. These results provide insight into the climate history of the Red Planet and suggest the surface conditions at this later time may also have been suitable for microbial life.

"We discovered valleys that carried water into lake basins," said Sharon Wilson of the Smithsonian Institution, Washington, and the University of Virginia, Charlottesville. "Several lake basins filled and overflowed, indicating there was a considerable amount of water on the landscape during this time."

Wilson and colleagues found evidence of these features in Mars' northern Arabia Terra region by analyzing images from the Context Camera and High Resolution Imaging Science

Experiment camera on the Mars Reconnaissance Orbiter and additional data from NASA's Mars Global Surveyor and the European Space Agency's Mars Express.

"One of the lakes in this region was comparable in volume to Lake Tahoe," Wilson said, referring to a California-Nevada lake that holds about 45 cubic miles (188 cubic kilometers) of water, "This particular Martian lake was fed by an inlet valley on its southern edge and overflowed along its northern margin, carrying water downstream into a very large, water-filled basin we nicknamed 'Heart Lake.'"

The chain of lakes and valleys that are part of the Heart Lake valley system extends about 90 miles (about 150 kilometers). Researchers calculate Heart Lake held about 670 cubic miles of water (2,790 cubic kilometers), more than in Lake Ontario of North America's Great Lakes.

Wilson and co-authors of the report in the Journal of Geophysical Research, Planets, map the extent of stream-flow in "fresh shallow valleys" and their associated former lakes, They suggest that the runoff that formed the valleys may have been seasonal.

To bracket the time period when the fresh shallow valleys in Arabia Terra formed, scientists started with age estimates for 22 impact craters in the area, They assessed whether or not the valleys carved into the blankets of surrounding debris ejected from the craters, as an indicator of whether the valleys are older or younger than the craters, They concluded that this fairly wet period on Mars likely occurred between two and three billion years ago, long after it is generally thought that most of Mars' original atmosphere had been lost and most of the remaining water on the planet had frozen.

The characteristics of the valleys support the interpretation that the climate was cold: "The rate at which water flowed through these valleys is consistent with runoff from melting snow," Wilson said, "These weren't rushing rivers. They have simple drainage patterns and did not form deep or complex systems like the ancient valley networks from early Mars."

They note that similar valleys occur elsewhere on Mars between about 35 and 42 degrees latitude, both north and south of the equator. The similar appearance and widespread nature of these fresh, shallow valleys on Mars suggest they formed on a global scale rather than a local or regional scale.

"A key goal for Mars exploration is to understand when and where liquid water was present in sufficient volume to alter the Martian surface and perhaps provide habitable environments,"

said Mars Reconnaissance Orbiter Project Scientist Rich Zurek of NASA's Jet Propulsion Laboratory, Pasadena, California, "This paper presents evidence for episodes of water modifying the surface on early Mars for possibly several hundred million years later than previously thought, with some implication that the water was emplaced by snow, not rain."

The findings will likely prompt more studies to understand how conditions warmed enough on the frozen planet to allow an interval with flowing water. One possibility could be an extreme change in the planet's tilt, with more direct illumination of polar ice.

Wilson's co-authors are Alan Howard of the University of Virginia; Jeffrey Moore of the NASA Ames Research Center, Moffett Field, California; and John Grant of the Smithsonian.

NASA's Mars orbiter missions are advancing understanding about the Red Planet that serves in preparation for human-crew missions to Mars beginning in the 2030s. For more about NASA's Journey to Mars, visit:

http://www.nasa.gov/content/nasas-journey-to-mars

News Media Contact

Guy Webster
Jet Propulsion Laboratory, Pasadena, Calif.
818-354-6278
guy.webster@jpl.nasa.gov

Dwayne Brown / Laurie Cantillo
NASA Headquarters, Washington
202-358-1726 / 202-358-1077
dwayne.c.brown@nasa.gov / laura.l.cantillo@nasa.gov

2016-241

Site Manager: Jon Nelson
Webmasters: Tony Greicius, Martin Perez, Luis Espinoza

2.12   AGU Earth & Space Science News: EOS Research Spotlight

https://eos.org/research-spotlights/marss-climate-may-have-been-wet-much-later-than-thought

NEWS ▾   NEWS FROM AGU JOURNALS ▾   TOPICS & DISCIPLINES ▾   OPINIONS ▾   BLOGS   JOBS & RESOURCES

HYDROLOGY, CRYOSPHERE & EARTH SURFACE   📋 Research Spotlight

By Sarah Stanley   ⏱ 30 September 2016

Mars's Climate May Have Been Wet Much Later Than Thought

Water-carved valleys may be relatively young, challenging assumptions about the history of the Red Planet's climate.

SOURCE: *Journal of Geophysical Research: Planets*

Scientists believe that ancient Mars had a relatively warm, wet climate. Running water carved deep and complex networks of valleys and collected in lake beds, the remains of which are still visible in satellite images today. About 3.5 billion years ago, the Red Planet became colder and drier, and valley formation slowed as precipitation dwindled—or so scientists thought.

New research from *Wilson et al.* suggests that flowing water, perhaps from snowmelt, formed midlatitude valleys between 2 billion and 3 billion years ago, near the transition between Mars's Hesperian and Amazonian periods. This could be evidence that Mars had a cold, wet climate during the transition and possibly well into the Amazonian.

These findings arose from efforts to uncover the history of distinctive, water-carved features known as fresh shallow valleys, which are found in midlatitude regions across Mars. Fresh shallow valleys are narrower, shallower, and less degraded than other ancient valleys, suggesting that they might also be younger.

Wilson's team used high-resolution images and topographic data collected by satellites to examine the size, shape, age, and distribution of fresh shallow valleys in Arabia Terra, a large region just north of the Martian equator. They also used a computer model to simulate water flow and recreate rivers and lakes that may have existed in the Red Planet's past.

The results suggest that fresh shallow valleys in Arabia Terra formed between the late Hesperian period, which ended 3 billion years ago, and the mid-Amazonian, about 2 billion years ago. The shape and shallow depths of the valleys indicate that they were likely active for a geologically short period of time, probably carved by seasonal melting of snow that flowed across the surface.

Other researchers have speculated that volcanic activity, asteroid impacts, or other local heat sources could have melted enough water to form relatively young valleys on Mars. However, these hypotheses are inconsistent with the authors' findings. Instead, the researchers say the appearance and wide distribution of the valleys in the midlatitudes point to a global Martian climate that was wet—and potentially habitable—much later than has been assumed. (*Journal of Geophysical Research: Planets*, doi:10.1002/2016JE005052, 2016)

—Sarah Stanley, Freelance Writer

A channel on the surface of northern Arabia Terra, a region north of Mars's equator. New research suggests that some water-carved valleys in this area are relatively young, indicating that the climate on Mars was wet much later than scientists previously thought. Credit: NASA/JPL-Caltech/Malin Space Science Systems

CHAPTER 3. Geologic Mapping in Northwestern Noachis Terra

3.1   Introduction

Mars Transverse Mercator (MTM) quadrangles -20037, -25037, -30037 and -30032 (17.5°S-32.5°S, 320°E-325°E and 27.5°S-32.5°S, 325°E-330°E) (Fig. 3.1) in northwestern Noachis Terra near the southern margin of Margaritifer Terra record a long geomorphic and geologic history. The northeastern regional slope is defined by the ancient Chryse trough and the informally named Holden and Ladon impact basin structures that formed in the Middle Noachian or earlier [*Schultz and Glicken*, 1979; *Schultz et al*., 1982]. Uzboi Vallis, Ladon Valles and Morava Valles (ULM) formed a meso-scale outflow system in the Noachian to Hesperian, alternately incising channels into the southern highlands and infilling the formerly closed Holden and Ladon impact basins [*Saunders*, 1979; *Schultz et al*., 1982; *Grant*, 1987; *Frey et al*., 2003; *Irwin and Grant*, 2013]. Argyre basin sourced the water for the ULM system, which eventually flowed through the informally named Margaritifer basin, located northeast of Morava Valles, reaching the northern plains via Ares Valles [*Rotto and Tanaka*, 1995; *Grant and Parker*, 2002; *Irwin and Grant*, 2009].

This map encompasses Uzboi Vallis, the terminus of Nirgal Vallis, and surrounding terrain including the ancient Vinogradov basin (Fig. 3.2). The area includes well-preserved examples of alluvial fans and related aqueous landforms in craters Gringauz, Roddy and Luba [*Moore and Howard*, 2005; *Wilson et al*., 2014, 2017], as well as paleolakes, [*Grant et al*., 2011], fan deltas (Chapter 4), dissected crater rims, and light-toned layered deposits. The southern portion of the map was modified by aqueous-rich ejecta deposits from the Hale impact crater (Chapter 5). Structural features include Hesperian wrinkle ridges, floor-

fractured impact craters, and grabens associated with the Tharsis volcanic complex to the west (Fig. 3.1, inset). The diversity of landforms in this area provide a unique location to constrain the timing, source, duration and relative importance of aqueous versus other geomorphic processes. Putting these deposits in a broader framework helps further our understanding of the climate and associated habitability through a significant portion of the Martian geologic record.
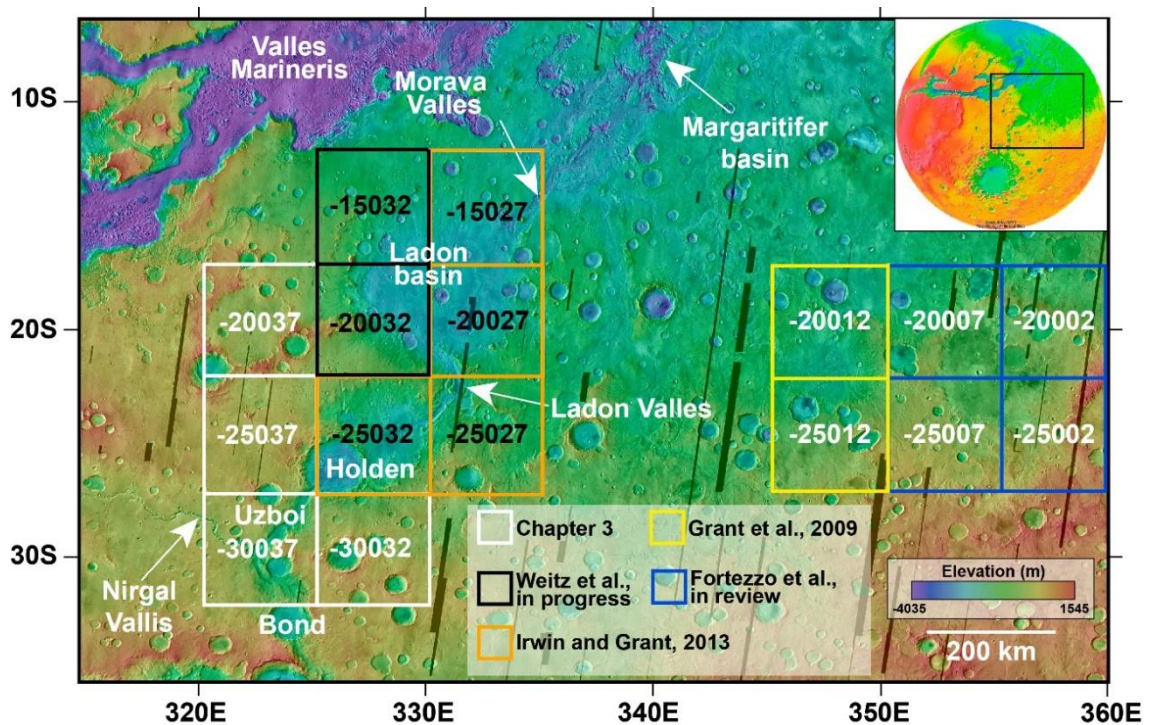
Figure 3.1   Status of geologic mapping in Margaritifer Terra and Noachis Terra

Geologic mapping in MTM quadrangles -20037, -25037, -30037 and -30037 (white boxes) is part of a series of 1:500,000 to 1:1,000,000 scale maps in Margaritifer Terra and Noachis Terra. Neighboring quadrangles are published (orange and yellow), in preparation (black) or in review (blue). MOLA over global THEMIS day IR mosaic. Inset in upper right provides global context, with Tharsis complex along western limb in red. North is to the top.
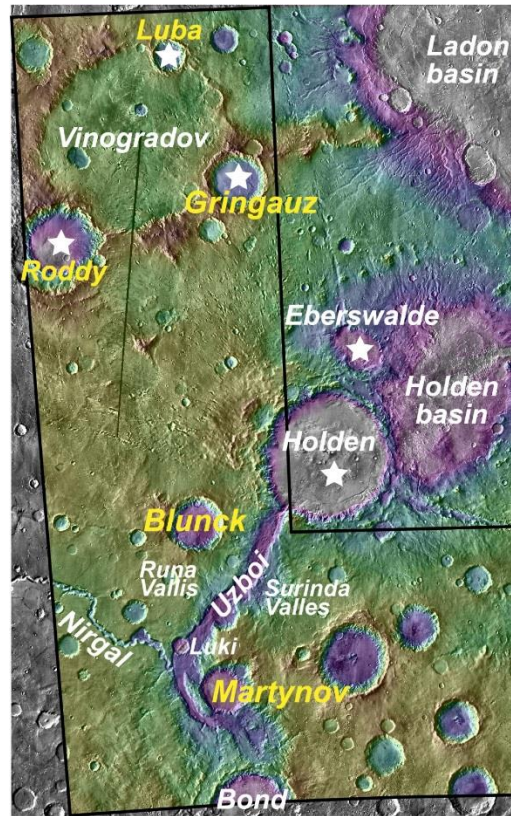
Figure 3.2   Names of features in the map area

Official place names in the map area (outlined in black, see Fig. 3.1 for context). Five unnamed craters in the map area were submitted to, and approved by, the International Astronomical Union (IAU) Working Group for Planetary System Nomenclature for this mapping project: Luba, Roddy, Gringauz, Blunck and Martynov. Several alluvial fans and fluvial features occur in craters within the map area (white stars, e.g., *Moore and Howard* [2005]). Vertical distance along western edge is ~912 km, horizontal distance across southern edge is ~512 km. North is to the top.

3.2   Background

Previous geologic mapping of the area at smaller map scales includes a 1:5,000,000 map based on Mariner 9 data by *Saunders* [1979], a 1:1,000,000 map [*Grant,* 1987], a 1:15,000,000 map based on Viking Orbiter data [*Scott and Tanaka* 1986], and the 1:20,000,000 map based Mars Orbiter Laser Altimeter (MOLA) data [*Smith et al.,* 2001] and the Thermal Emission Imaging System (THEMIS) daytime infrared (IR) image mosaic

[*Christensen et al*., 2004] by *Tanaka et al.* [2014]. The four MTM quadrangles mapped in Chapter 3 are part of a series of 1:500,000 to 1:1,000,000 scale maps in the Margaritifer Terra and Noachis Terra regions [*Grant et al*., 2009; *Irwin and Grant,* 2013; *Fortezzo,* 2017; *Weitz et al*., 2017] (Fig. 3.1).

Several investigations have focused on this region due to its water-rich history. *Grant* [1987] investigated the geomorphic history of the broader Margaritifer Sinus Quadrangle by analyzing the relationship between degraded craters and the development of fluvial landforms. The ULM system, including its source, timing of formation, and association with other deposits, has been studied for decades [*Irwin and Grant,* 2013, *and references therein*].

Uzboi Vallis formed from multiple discharge events originating from Argyre [*Grant and Parker*, 2002] but Bond crater, and the younger Early to Middle Amazonian-aged Hale crater [*Cabrol et al*., 2001; *Jones et al.*, 2011] destroyed evidence of the original outlet. The northern end of Uzboi was modified by the large (154 km-diameter) Holden crater [*Grant and Parker*, 2002] in the mid- to Late Hesperian [*Irwin and Grant*, 2013]. After Holden formed, the closed basin in Uzboi Vallis between craters Holden and Bond hosted a geologically short-lived lake [*Grant et al*., 2008, 2011] (Fig. 4.2A) before the impounded water breached Holden's rim in a Hesperian-aged flood event [*Grant et al*., 2008, 2011; *Irwin and Grant*, 2013].

Moore and Howard [2005] identified and described the alluvial fans in the map area using THEMIS Visible (VIS) images (craters "A," "C" and "D" in *Moore and Howard* [2005] were later officially named Roddy, Gringauz and Luba, respectively). Subsequent

investigations constrained the timing of alluvial fan activity in Margaritifer Terra to the Late Hesperian or into the Amazonian [e.g., *Grant and Wilson*, 2011, 2012].

3.3   Mapping Methods and Data

Photogeologic mapping was completed using standard mapping methods [*Tanaka et al*., 2011] in ArcGIS 10.3, a geographic information system (GIS) from the Environmental Systems Research Institute (ESRI). The U.S. Geological Survey provided several base maps (Fig. 3.3) including a Viking Mars Digital Image Mosaic 2.1 (231 m per pixel), THEMIS daytime and nighttime IR mosaics (100 m per pixel), and MOLA topography (color and hillshade, 128 pixel per degree). Detailed mapping was done using the mosaic of images from the Context Camera (CTX, ~6 m per pixel) [*Malin et al.*, 2007], which was amended to add CTX images as data became available over the course of the project. Images from the High Resolution Imaging Science Experiment (HiRISE, ~0.25 m per pixel) [*McEwen et al*., 2007] were consulted where available. The map base uses a transverse Mercator projection with a central meridian of 325ºE.   Topographic measurements were based on gridded 128 pixel per degree MOLA data. A scale of 1:250,000 was used to draft linework for the expected 1:1,000,000 publication scale. Unit contacts have a stream-digitized vertex spacing of roughly 500 m, which are attributed as certain (solid) or approximate (dashed). Linear features include faults, ridges, grabens, troughs, crater rim crests, buried craters, and fluvial channels.

Crater statistics were compiled in ArcGIS using available CTX data at the time of analysis and CraterTools software [*Kneissl et al*., 2011] were used to estimate surface ages (Section 3.4). The resolution of CTX data (~6 m/pixel scale) enables confident definition of craters >20 m in diameter, and counts excluded obvious secondary clusters. Counts were

completed on individual CTX images to minimize variable lighting and image quality effects. To further reduce effects of image resolution, craters with D <50 m were counted but excluded from interpretation of ages. Interpreted ages for each count were derived from segments of the plots for each unit that best match the expected production population using "pseudo-log" binned reverse cumulative histograms and Craterstats2 software [*Michael and Neukum*, 2010]. Absolute ages are based on the chronology function of *Hartmann and Neukum* [2001] and production function from *Ivanov* [2001].
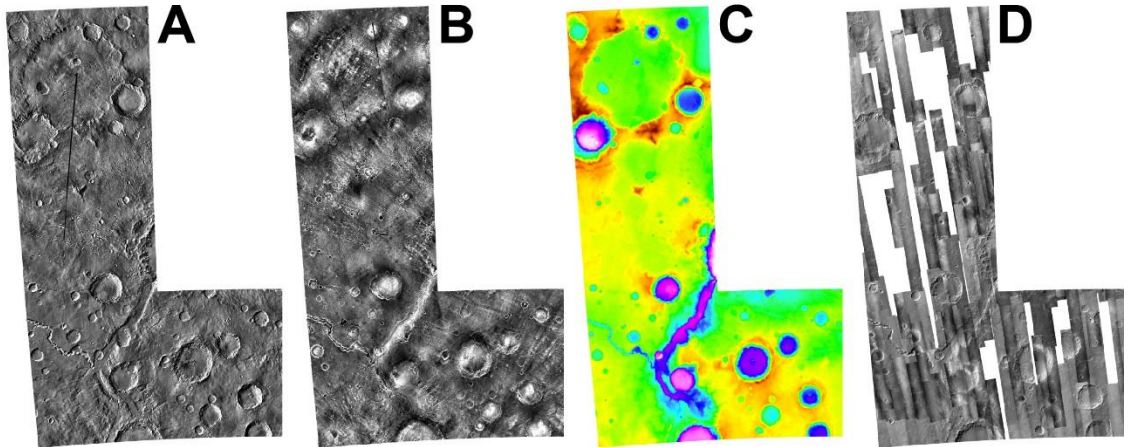
Figure 3.3   Data used as base maps for geologic mapping

Base maps used for geologic mapping of MTM quadrangles -20037, -25037, -30037 and -30032 between 17.5°S-32.5°S, 320°E-325°E and 27.5°S-32.5°S, 325°E-330°E (see Fig. 3.1 and 3.2 for context). **A)** THEMIS daytime IR, **B)** THEMIS nighttime IR, **C)** Gridded MOLA color topography, and **D)** mosaic of CTX images. Vertical distance along western edge is ~912 km, horizontal distance across southern edge is ~512 km. North is to top in all images.

3.4   Age Determinations

Previous studies and maps have dated the Plateau and Highland units in the map area [e.g., *Scott and Tanaka*, 1986; *Irwin and Grant*, 2013], which will be confirmed for

the final map and supporting pamphlet. Therefore, efforts presented here focus on constraining the ages of some Basin, Crater and Channel Fill units including the fan-bearing craters and their interior deposits.

Luba is ~39 km-diameter crater on the northern rim of the Vinogradov basin (see Fig. 3.2 for context). The fluidized or lobate ejecta from Luba is consistent with the presence of subsurface liquid water. The craters preserved on Luba's ejecta suggest Luba formed in the mid- to Late Hesperian (Fig. 3.4A-B). Luba is contemporary with Holden, but is relatively younger based on the observation that Luba ejecta embays secondaries from Holden crater. Fans in Luba encompass the entire crater floor, fill the central depression, and have inverted channels on their surfaces. The craters preserved on Luba's fan surface yield an Amazonian age (Fig. 3.4A-B) [*Wilson et al.*, 2014], consistent with the ages of other fans in this region [e.g., *Grant and Wilson*, 2011].

Roddy is an ~86 km-diameter crater on the southwestern rim of Vinogradov (Fig. 3.4C, see Fig. 3.2 for context). Preliminary crater counts on Roddy's ejecta yield an Early Hesperian age for the crater (Fig. 3.4D). The eastern rim of Roddy is modified by a ~15 km-diameter, unnamed, younger (mid-Hesperian to Early Amazonian) crater, whose fluidized ejecta mantles the fluvial fan deposits on Roddy's interior floor. The fluidized ejecta that overlies some fan surfaces has preserved at least ~60 m of layered fans relative to adjacent, unarmored fan surfaces. The relationship between the fans in Roddy and the ejecta from this ~15 km-diameter crater suggests the fans in Roddy were emplaced before the ~15 km-diameter crater formed. Thus, the ages of Roddy and the ~15 km-diameter crater provide lower and upper limits on fan formation, respectively.
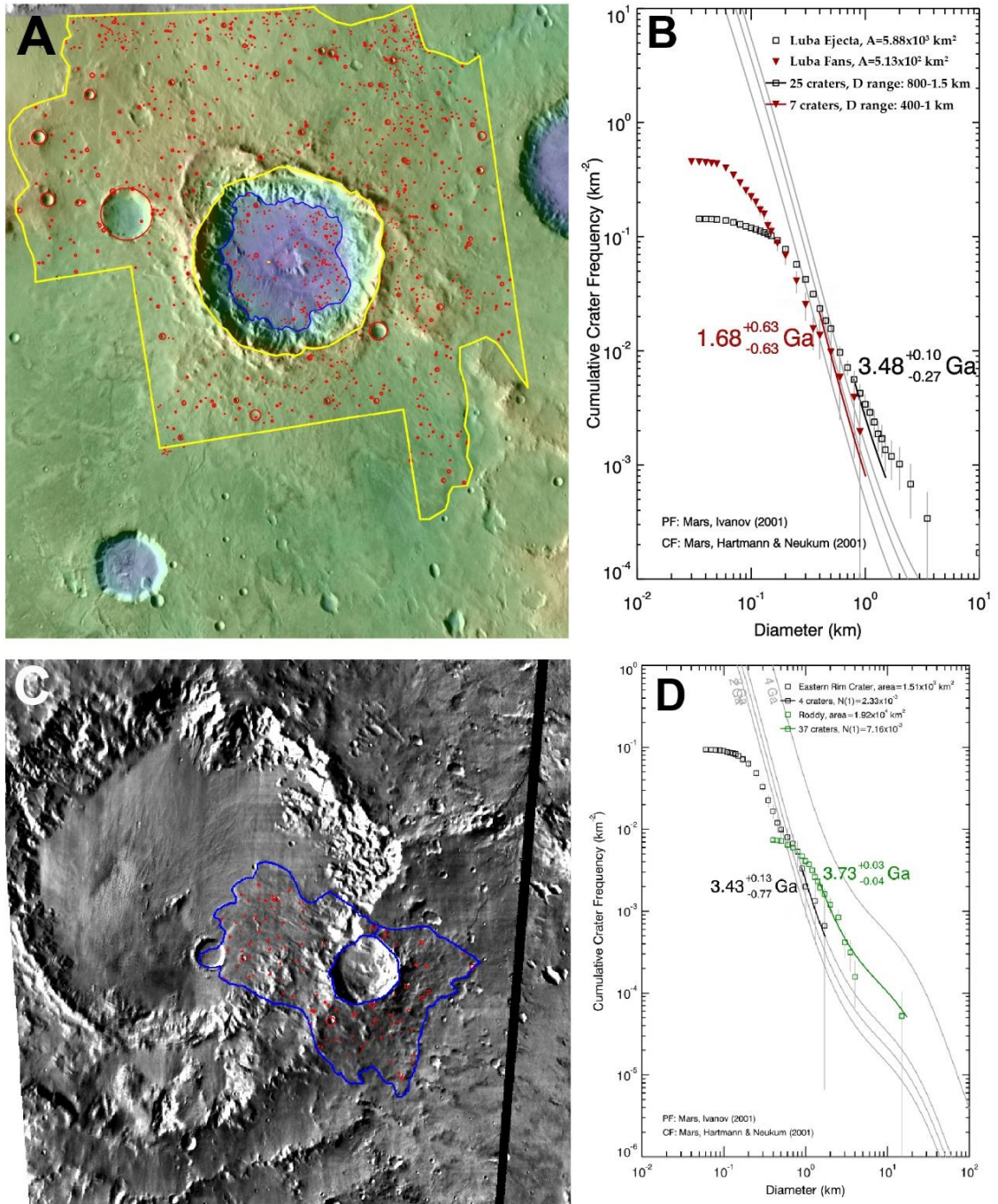
Figure 3.4 Estimated ages of craters Luba and Roddy and their interior deposits

A) Luba is ~39 km-diameter crater on the northern rim of the Vinogradov basin (see Fig. 3.2 for context). Craters (red circles) were mapped on a portion of continuous ejecta (yellow line) and the alluvial deposits on the crater floor (blue line). MOLA over THEMIS day IR. North is to the top. **B)** Cumulative crater statistics from Luba's continuous ejecta (black squares, yellow area in (A)) indicate that it is contemporary with Holden, yielding

a mid- to Late Hesperian age (estimated absolute age based on a crater diameter range of ~0.8-1.5 km). Luba's fan surface (red triangles, blue area in (A)) yield an Amazonian age (estimated absolute age based on a crater diameter range of ~0.4-1 km). **C)** Crater Roddy is an ~86 km diameter crater on the southwestern rim of the Vinogradov basin (see Fig. 3.2 for context). Craters (red circles) were mapped on Roddy's continuous ejecta the fluidized ejecta of a ~15 km diameter crater that modifies Roddy's eastern rim (blue line). THEMIS daytime IR data, north is to the top. **D)** Cumulative crater statistics from Roddy's ejecta suggest the crater likely formed in the Early Hesperian (green squares, estimated absolute age based on a crater diameter range of ~1.5 to 15 km). The age of the 15 km-diameter crater, which formed after the bulk of the fans in Roddy were deposited, yields a mid-Hesperian to Early Amazonian age (black squares, blue area in (C); estimated absolute age based on a crater diameter range of ~0.9-1.5 km).

3.5   Stratigraphy

The geologic map contains several units that date to the Noachian, Hesperian and Amazonian Epochs (Fig. 3.5). The correlation of map units (Fig. 3.6), schematic cross section (Fig. 3.7), and description of the map units (Table 3.1) accompanies the map. The unit descriptions and interpretations (Table 3.1) are based on morphology, albedo, brightness temperature, stratigraphic position, and superimposed crater population as seen in available orbital imaging and topography. Image data include Mars Odyssey THEMIS IR and Mars Reconnaissance Orbiter (MRO) HiRISE and CTX images, and 128 pixel per degree gridded MOLA Mission Experiment Gridded Data Record (MEGDR) on board the Mars Global Surveyor (MGS). Derived products from CRISM were analyzed where available to identify mineralogical differences within and between mapped geologic units.

Legend

Units

Ad	Hf	Nm
As1	He	Mm
As2	HNch1	Ac3
AHf	HNt	Hc2
AHl	Nh	Nc1

Contacts

— certain

– – – approximate

LinearFeatures

——— channel (fluvial)

– – – – Ladon and Holden basins

–·–·– crest of buried crater

⊣⊣⊣⊣ crest of crater rim

—•— graben trace, approx.

—◇— ridge on fluidized ejecta

—◆— wrinkle ridge

⊤⊤⊤⊤ scarp base

——▲— scarp crest

—I— trough

SurfaceFeatures

▓ secondary crater chain

Km
0 25 50   100   150   200
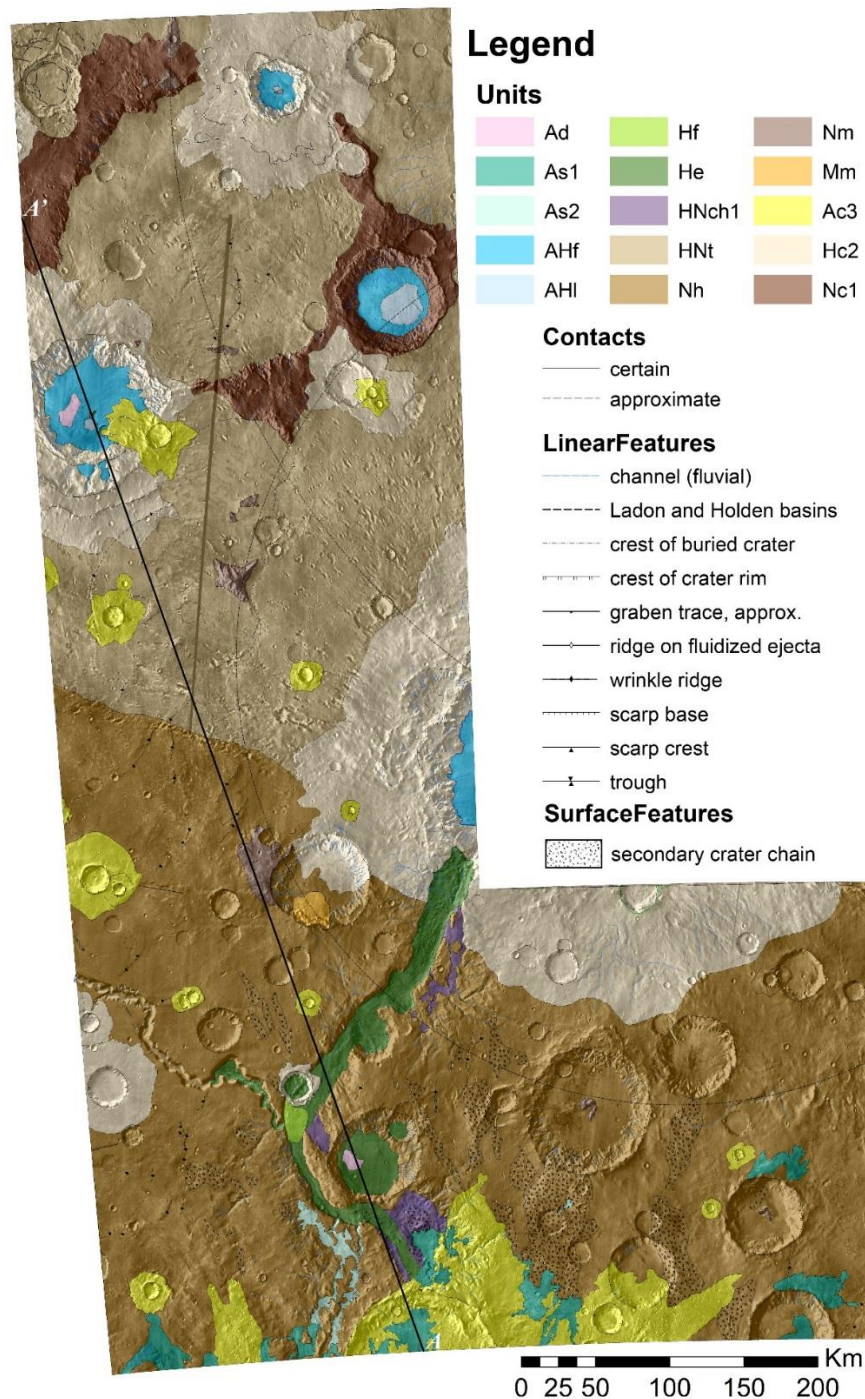
Figure 3.5   Geologic map of MTM quadrangles -20037, -25037, -30037 and -30032

Geologic map of MTM quadrangles -20037, -25037, -30037 and -30032 (17.5°S-32.5°S, 320°E-325°E and 27.5°S-32.5°S, 325°E-330°E) (see Figs. 3.1 and 3.2 for context and the correlation of map units (Fig. 3.6) and description of map units (Table 3.1) for more detail). The transect (black line, A to A') corresponds to schematic profile in Fig. 3.7.

95
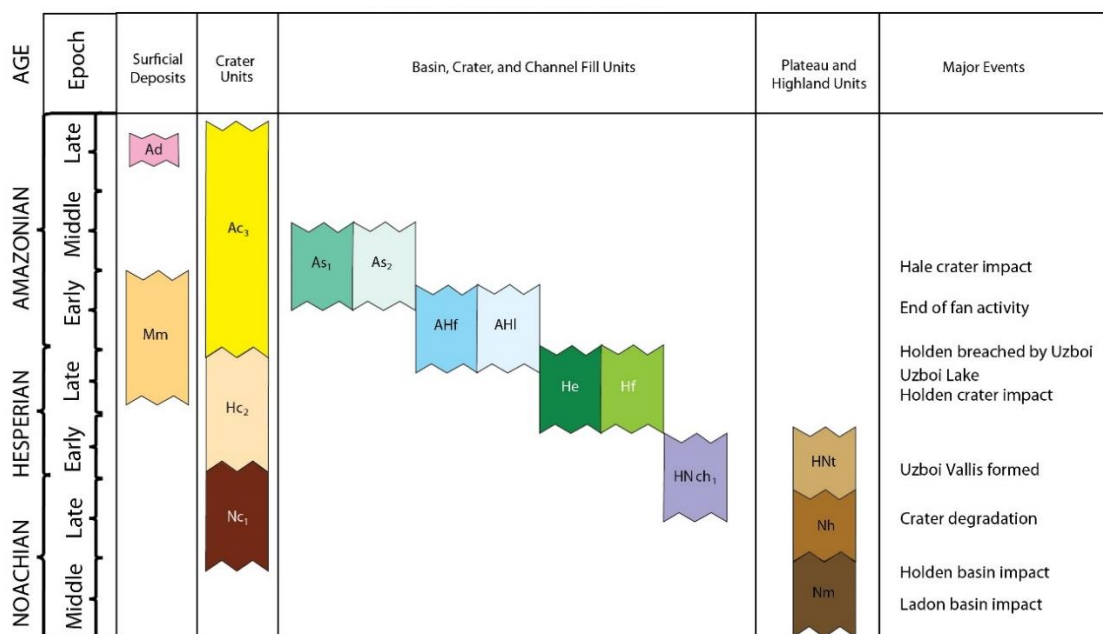
Figure 3.6   Correlation of map units

Correlation of map units (see geologic map in Fig. 3.5 and description of map units in Table 3.1).
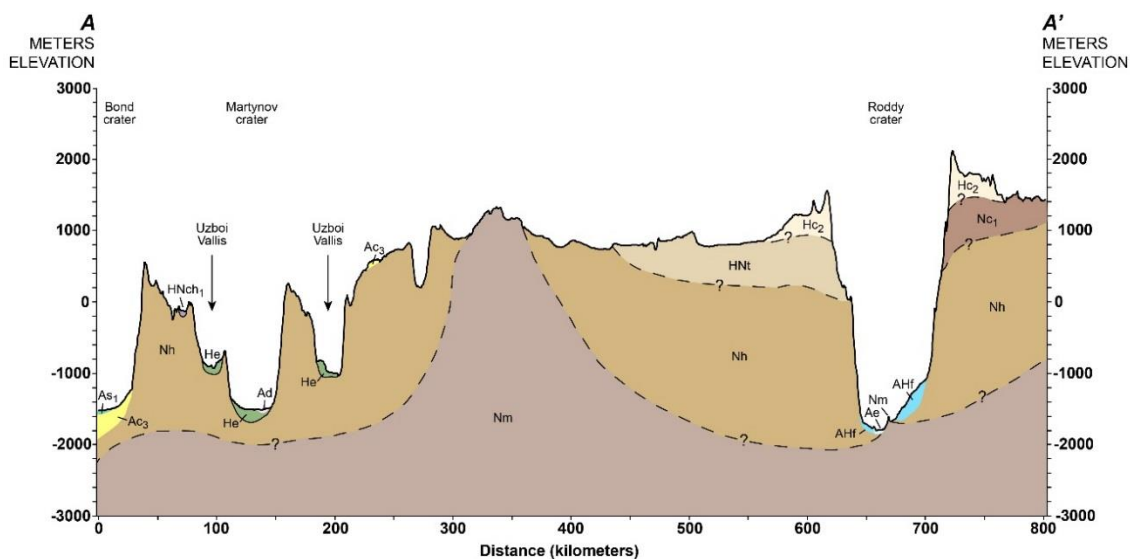
Figure 3.7   Schematic cross section

Schematic cross section from A to A' that correlates to transect in Fig. 3.5. The vertical scale is significantly exaggerated and the subsurface contacts are conceptual. Unit thickness are unknown. See Table 3.1 for full description of map units and Fig. 3.6 for the correlation of map units.

96

3.5.1   Noachian Period

The oldest map unit is the Middle Noachian (or perhaps older) mountainous unit (Nm). This unit has been mapped by others [e.g., *Schultz et al.*, 1982; *Grant*, 1987] to represent isolated bedrock promontories with Noachian or older crystallization ages that were exposed as fractured ring structures during the ancient Ladon and Holden basin impacts [e.g., *Schultz et al.*, 1982]. Small outcrops of the mountainous unit occur on the western margin of crater Blunck and between craters Blunck and Vinogradov (Fig. 3.5). The mountainous unit also includes central peaks in craters Roddy and two unnamed craters east of crater Martynov in quadrangle -30032, which are interpreted to similarly expose deep crustal rocks (Fig. 3.5).

The Highland unit (Nh) is Late Noachian in age and occurs primarily in quadrangles -30037 and -30032. This unit, previously mapped as Noachian plains (Npl_1) [*Scott and Tanaka*, 1986], is heavily cratered, differentially mantled, contains older valley networks, grabens, and wrinkle ridges. The phyllosilicate layer exposed in the walls of Nirgal and in the terrain to the northwest [*Buczkowski et al.*, 2010; *LeDeit et al.*, 2012; *Buczkowski et al.*, 2013] is not evident in the Highland unit east of Uzboi Vallis [*Wilson and Grant,* 2014]. Unit Nh embays unit Nm and underlies all other units.

The Late Noachian to Early Hesperian Terra unit (HNt) is characterized by widespread, smooth to rolling, cratered and variably dissected surfaces between degraded impact craters [*Irwin and Grant*, 2013]. The Terra unit primarily occurs in quadrangles -30037 and -30032, beneath the continuous Holden ejecta (unit Hc_2) and on the floor of crater Vinogradov. The Terra unit in the map was modified by secondary craters from the Holden crater impact.

3.5.2 Hesperian Period

The Late Noachian to Early Hesperian Channel unit ($NHch_1$) is equivalent to the surface mapped in *Irwin and Grant* [2013], interpreted to be fluvially eroded surfaces related to the initial incision of Uzboi Vallis, which formed from multiple flow events [*Grant and Parker*, 2002].

The floor of Uzboi Vallis is mapped as Early to Late Hesperian Etched unit (He), characterized by erosionally resistant material exposed where aeolian deflation has selectively removed either light-toned material that is locally layered [*Irwin and Grant*, 2013] or dark-toned material. The Hesperian Etched unit corresponds to surfaces that were formed or modified by aqueous processes related to a short-lived lake that occupied Uzboi [*Grant et al.*, 2011] in the mid- to Late Hesperian [*Irwin and Grant*, 2013]. MOLA data reveals a large mound of material on the floor of Uzboi Vallis at the confluence of Nirgal Vallis that consists of an upper and lower unit (Chapter 4). The upper unit is triangular and symmetrical to the mouth of Nirgal Vallis and consists of horizontal layers that dip to the southeast along its southern margin. This upper unit is mapped as a Hesperian fan unit (Hf), interpreted to be a fan delta that formed in a mid- to Late Hesperian lacustrine environment in Uzboi [*Grant et al.,* 2011]. The lower unit of the Uzboi floor deposit is mapped as the Hesperian Etched unit (He) due to uncertainties related to its origin and age (Chapter 4).

The Late Hesperian to Early Amazonian Fan unit (AHf) are sloping or cone-shaped deposits (sometimes coalesced into a bajada) that occur on the interior slopes of craters [after *Irwin and Grant*, 2013]. Distributary paleo-channel networks are preserved in negative and (more commonly) positive relief. Some inverted channels are layered. Cone-

shaped deposits derived from deeply dissected impact crater walls coalesced into fans in craters Luba, Roddy, Gringauz and Holden. Bright in THEMIS nighttime IR. We interpret AHf as alluvial deposits composed primarily of gravel and fines due to efficient stripping of much of the surface that leaves presumably coarser channel deposits standing in relief [e.g. *Moore and Howard*, 2005; *Morgan et al*., 2014]. Hence, the fans were emplaced by fluvial sediment transport with little to no evident contributions from debris flows. Boulders, where observed in HiRISE images, tend to be associated with fluvial bars (Fig. 3.8).

The Late Hesperian to Early Amazonian Etched unit (AHe) is rough, scabby, light-toned material that is confined to low-lying crater interiors in Roddy, Gringauz and Luba, at the terminus of alluvial fans (unit AHf). The material can be knobby and (or) polygonally fractured and is not obviously layered. This unit is interpreted to be material deposited in a playa-like environment contemporaneous with alluvial fan (AHf) formation.
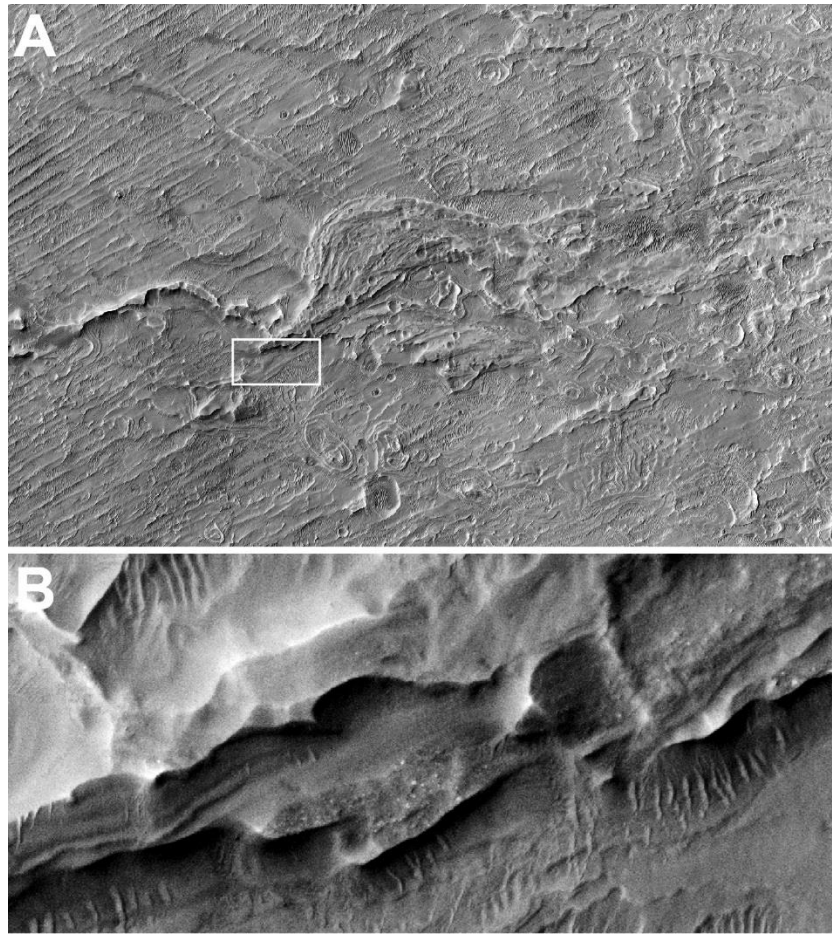
Figure 3.8 Distributary morphology of alluvial fans in crater Roddy

A) Strong aeolian deflation of the fan surfaces in Roddy suggests the fans are primarily fine-grained, but the fan distributaries consisting of coarser material are left in positive relief. Box shows location of (B). Subframe of HiRISE image ESP_033471_1580 (25 cm pixel resolution) from fan surface east of Roddy's central peak. Image is ~3.8 km across, north is to the top. **B)** White, meter-scale blocks are incorporated into some layers within the deposit (see (A) for context). Further work will examine the nature and spatial distribution of the blocks. Image is ~300 meters across.

3.5.3   Amazonian Period

The formation of crater Hale south of the map region in the Early to Middle

Amazonian [*Cabrol et al*., 2009; *Jones et al*., 2011] greatly modified MTM quadrangles -

30037 and -30032. The Amazonian Smooth units (As$_1$ and As$_2$) are dark-toned, smooth at

scales of 10s to 100s of m, typically bright in THEMIS day IR with variable thickness (Chapter 5). Units As_1 and As_2 occur in pre-existing valleys and (or) topographic depressions, and As_1 locally forms lobes with distinct margins (Figs. 5.5 and 5.6). Light-toned, meter-scale boulders, aeolian bedforms and extensive cracks are common on lobe surfaces, and layering is not evident. Deposits of unit As_1 embay secondary craters from Hale and generally thin with distance from Hale (Figs. 5.9 and 5.10). Unit As_2 (Fig. 5.7) may have formed from de-watering of unit As_1. We interpret the Smooth units to be aqueous deposits related to the emplacement and subsequent dewatering of ejecta associated with the formation of crater Hale.

The upper limit of alluvial fan formation in the map area may extend into the Early Amazonian [e.g., *Grant and Wilson*, 2011]. The last unit that may be Amazonian (or older) is unit Mm, which occurs on the floor of crater Blunck. This unit has broadly rounded margins and is sourced from an interior wall of Blunck crater that exhibits large, rotated blocks consistent with slumping and backwasting of the crater wall. The surface of this unit has parallel lineations that are oriented in the presumed direction of flow. Unit Mm is interpreted to be a landslide that may have been triggered by impact cratering.

The crater units in the map area are Noachian, Hesperian and Amazonian. The Noachian Crater 1 unit (Nc_1) has heavily modified rims with little to no preserved ejecta (e.g., Vinogradov). Late to Early Hesperian Crater 2 unit (Hc_2) is characterized by moderately degraded crater rims with relatively continuous ejecta (e.g., Luba). Late Hesperian to Late Amazonian Crater 3 Unit (Ac_3) are "fresh" craters with relatively sharp rims and well-preserved ejecta (e.g., Hale).

Table 3.1   Description of Map Units

Label	Unit name, Age, Description	Additional Characteristics	Interpretation
Plateau and Highland Units			
HNt	**Terra unit** (Early Hesperian to Late Noachian) – Widespread, smooth to rolling, cratered, and variably dissected surface between degraded impact craters.	Overlies mountainous unit (Nm) and highland unit (Nh). Underlies all other units. Equivalent to smooth undifferentiated plans (Sp_u) unit [*Grant*, 1987] and unit HNt [*Irwin and Grant*, 2013]; wrinkle ridges. Modified by secondaries from Holden crater.	Noachian to Hesperian geomorphic surface resulting from impact cratering, ejecta emplacement, prolonged weathering, and erosion primarily by water and wind.
Nh	**Highland unit** (Late Noachian) Heavily cratered, differentially mantled. Contains older valley networks, grabens, few wrinkle ridges.	Phyllosilicate-bearing layer exposed in walls of Nirgal Vallis but not observed east of Uzboi. Overlies mountainous unit (Nm) and underlies all other units.	Noachian geomorphic surface resulting from impact cratering, ejecta emplacement, prolonged weathering, and erosion primarily by water and wind.
Nm	**Mountainous unit** (Middle Noachian) – Bedrock promontories including impact crater central peaks and mountain chains along impact basin rings. Mountains typically steep and variably eroded depending on age.	Oldest unit in map area.	Deeper Noachian bedrock outcrops exposed during impacts and overlain by highland and (or) terra units.
Crater and Channel Fill Units			
As_2	**Smooth unit 2** (Middle to Early Amazonian) – smooth (at scales of 10s to 100s of meters), dark-toned deposit. Occurs at margins of As_1 unit in pre-existing valleys, topographic depressions, craters, and embays secondary craters from Hale. Thins with increasing distance from Hale.	Bright in THEMIS day IR. Variable thickness.	Deposits post-date the initial formation of Hale and formed by de-watering of smooth unit 1 (As_1).
As_1	**Smooth unit 1** (Middle to Early Amazonian) – smooth (at scales of 10s to 100s of meters), dark-toned deposit. Channels and streamlined deposits common close to Hale crater. Occurs in pre-existing valleys, topographic depressions, craters, and embays secondary	Bright in THEMIS day IR. Locally forms lobes w/ distinct margins. Some flow lobe surfaces characterized by roughly parallel ridges, oriented perpendicular to the presumed direction of flow. Light-toned, meter-	Relatively fine-grained fluidized material emplaced as ground-hugging or ballistic ejecta hours to a day or so after Hale impact. Variable thickness.

	craters from Hale. Thins with increasing distance from Hale.	scale boulders, aeolian bedforms and extensive cracks (some that cross-cut ridges) are common on lobe surfaces, and layering is not evident.	
AHe	**Etched unit** (Early Amazonian to Late Hesperian) – Rough, knobby, scabby, light-toned material in low-lying crater floors, polygonal fracturing and block present.	Occurs in low-lying crater interiors of Roddy, Luba, Gringauz at terminus of alluvial fans (unit AHf). Dark in THEMIS day IR.	Possible remnant playas that were contemporaneous with alluvial fan formation (unit AHf)
AHf	**Fan unit** (Early Amazonian to Late Hesperian) – sloping or cone-shaped deposits. Distributary paleochannel networks preserved in negative or (more commonly) positive relief.	Cone-shaped deposits derived from deeply dissected impact crater walls coalesced into fans in craters Luba, Roddy, Gringauz and Holden. Bright in THEMIS nighttime IR.	Alluvial deposits composed primarily of gravel and fines, emplaced by fluvial sediment transport with little to no evident contribution from debris flows. Low abundance of boulders at HiRISE scale.
Hf	**Fan unit** (mid- to Late Hesperian) – Degraded material on the floor of Uzboi Valles at the mouth of Nirgal Vallis. Light-toned material, layered.	Upper fan-shaped deposit is symmetric to mouth of Nirgal. Some boulders incorporated but upper section is layered.	Fan delta deposited in a lacustrine environment when a lake filled Uzboi Vallis after Holden crater formed.
He	**Etched unit** (Early to Late Hesperian) – Variably erosionally resistant material in Uzboi Vallis. Massive in places, some light-toned knobs and boulders.	Light- to medium toned material, knobs, blocks. Variable layered.	Deflated crater-fill deposits overlying Hesperian Holden crater ejecta. Includes fine-grained, phyllosilicate-bearing, lacustrine, distal alluvial and (or) mass wasting deposits overlain by coarse-grained alluvial sediments in some places.
NHch₁	**Channel unit** (Early Hesperian to Late Noachian) – Eroded surfaces related to early incision of Uzboi Vallis. Streamlined outcrops of HNt and Nm common.	Overlies HNt. Equivalent to HNch₁ in *Irwin and Grant* [2013].	Surfaces eroded by Late Noachian to Early Hesperian catastrophic flooding and things veneered by coarse fluvial sediments during waning flow.
Surficial Deposits			
Ad	**Dune unit** (Late Amazonian) – concentration of typically dark-toned bedforms.	Dark in THEMIS nighttime IR.	Recent aeolian dunes, likely composed of chemically unaltered basaltic sand.

Mm	**Mass movement** (Amazonian to Hesperian) – landform with broadly rounded margins. Surface has parallel lineations in the presumed direction of flow.	Slumping of head-scarp is common. Located in interior of crater Blunck.	Landslide deposit; movement may have been triggered by nearby impact cratering events.
Crater Units			
Ac_3	**Crater 3 unit** (Late Amazonian to Late Hesperian) – floor, rim and continuous ejecta of morphologically fresh impact craters little modified by rim erosion and (or) infilling. Hale crater.	Locally overlies HNt, Nh. Underlies As_1 and As_2.	Impact material, fractured rim and continuous ejecta of Hesperian and Amazonian impact craters.
Hc_2	**Crater 2 unit** (Late to Early Hesperian) – rims of Holden and Luba and adjacent areas mantled by their continuous ejecta.	Overlies HNt. Underlies unit AHf.	Moderately degraded crater rim and impact ejecta from Hesperian Holden and Luba (and other unnamed craters)
Nc_1	**Crater 1 unit** (Late Noachian) – Remnant eroded rims from heavily modified craters such as Vinogradov and Gringauz.	Little to no ejecta blanket preserved.	Highly degraded crater rims from the Noachian.

3.6   Conclusions and Future Work

The mapping at 1:1,000,000 scale (Fig. 3.5) directly contributed to the understanding the evolution of Uzboi Vallis (Chapters 4) and the geomorphic effects of the Hale impact (Chapter 5) that affected the southern portion of the map. Larger scale mapping is underway in crater Roddy (Fig. 3.9), which hosts some of the largest and best-exposed alluvial fans on Mars (with the exception of Saheki crater [*Morgan et al.*, 2014]). The relationship between these large, alluvial fans and other landforms in the crater including fluidized ejecta, rugged topography, and aeolian deposits (Fig. 3.9) provides insight into the processes affecting fan development, and thus make Roddy a prime location for detailed mapping and analysis [*Wilson et al.*, 2017].
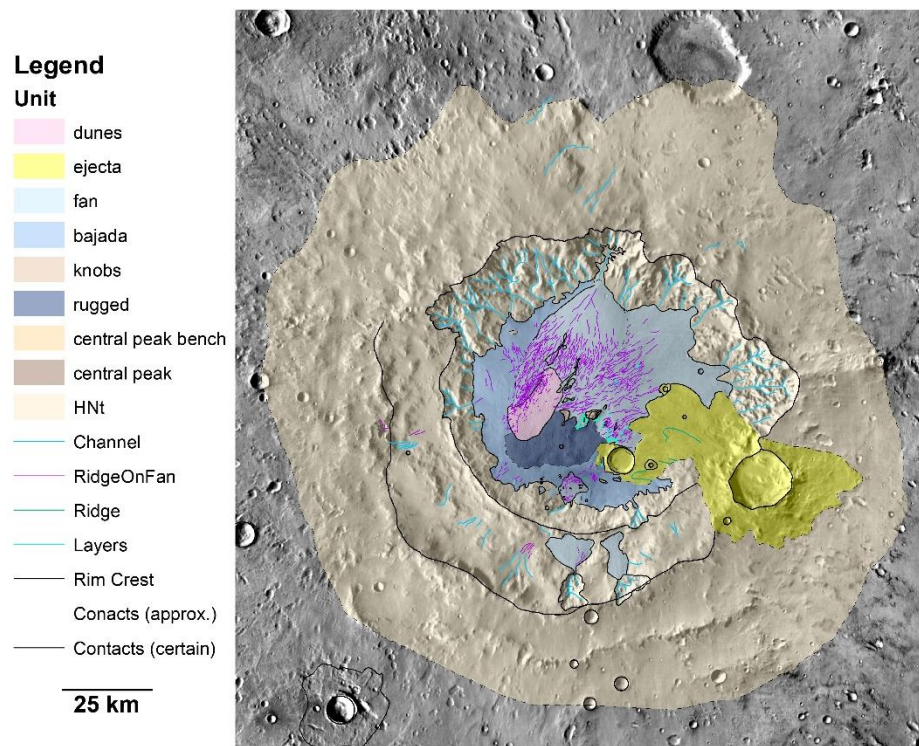
Figure 3.9   Geomorphic map of crater Roddy

Preliminary geomorphic mapping in crater Roddy at ~1:25,000 scale (see Fig. 3.2 for context). Roddy contains large, well-exposed alluvial fans as well as many other landforms that should prove helpful in understanding the timing and processes that affected fan formation.

3.7   References

Buczkowski, D., K. D. Seelos, S. L. Murchie, F. P. Seelos, E. Malaret, C. Hash and the CRISM team (2010), Extensive Phyllosilicate-bearing Layer Exposed by Valley Systems in Northwest Noachis Terra, *Lunar Planet. Sci., XLI*, Abstract 1458.

Buczkowski, D., K. D. Seelos, S. L. Murchie, F. P. Seelos, E. Malaret, C. Hash and the CRISM team (2013), Evidence for multiple widespread buried phyllosilicate-bearing layers between Argyre and Vallis Marineris, *Lunar Planet. Sci., XLIV*, Abstract 2331.

Cabrol, N. A., D. D. Wynn-Williams, D. A. Crawford and E. A. Grin (2001), Recent aqueous environments in Martian impact craters: An astrobiological perspective, *Icarus*, *154*, (1), 98-112, doi:10.1006/icar.2001.6661.

Christensen, P. R. et al., (2004), The Thermal Emission Imaging System (THEMIS) for the Mars 2001 Odyssey Mission, *Space Sci. Reviews*, *110* (1), 85-130.

Frey, H. V., E. L. Frey, W. K. Hartmann and K. L. T. Tanaka (2003), Evidence for buried "pre-Noachian" crust pre-dating the oldest observed surface units on Mars, *Lunar Planet. Sci. XXXIV*, Abstract 1848.

Fortezzo, C. M. (2017), Dollfus crater quadrangles, Mars, *U. S. Geol. Sur., Scientific Investigations* Map, scale 1:1,000,000, *in review*.

Grant, J. A. (1987), The geomorphic evolution of eastern Margaritifer Sinus, Mars, in Advances in planetary geology: Washington, D.C., *National Aeronautics and Space Administration Technical Memorandum 89871*, p. 1–268.

Grant, J. A. and T. J. Parker (2002), Drainage evolution in the Margaritifer Sinus region, Mars, *J. Geophys. Res.*, *107*, E9, 5066, doi:10.1029/2001JE001678.

Grant, J. A. and S. A. Wilson (2011), Late alluvial fan formation in southern Margaritifer Terra, Mars, *Geophys. Res. Lett.*, *38*, L08201, doi:10.1029/2011GL046844.

Grant, J. A. and S. A. Wilson (2012), A possible synoptic source of water for alluvial fan formation in southern Margaritifer Terra, Mars, *Planet. Space Sci.*, *72*, 44, doi:10.1016/j.pss.2012.05.020.

Grant, J. A., R. P. Irwin, III, J. P. Grotzinger, R. E. Milliken, L. L. Tornabene, A. S. McEwen, C. M. Weitz, S.W., Squyres, T. D. Glotch and B.J. Thomson (2008), HiRISE

imaging of impact megabreccia and sub-meter aqueous strata in Holden Crater, Mars, *Geology*, *36*, 195-198, doi:10.1130/G24340A.

Grant, J. A., S. A. Wilson, C. M. Fortezzo and D. A. Clark (2009), Geologic map of MTM -20012 and -25012 quadrangles, Margaritifer Terra region of Mars, *U. S. Geol. Sur., Scientific Investigations* Map 3041, scale 1:1,000,000.

Grant, J. A., R. P. Irwin III, S. A. Wilson, D. Buczkowski and K. Siebach (2011), A lake in Uzboi Vallis and implications for the Late Noachian-Early Hesperian climate on Mars, *Icarus*, *212* (1), 110–122, https://doi.org/10.1016/j.icarus.2010.11.024.

Hartmann, W. K. and G. Neukum (2001), Cratering chronology and the evolution of Mars, *Space Sci. Re*v., *96*, 165–194.

Irwin, R.P., III and J. A. Grant (2009), Large basin overflow floods on Mars, in Burr, D.M., Baker, V.R., and Carling, P.A., eds., *Megaflooding on Earth and Mars*: Cambridge, U.K., Cambridge University Press, p. 209–224.

Irwin, R. P. and J. A. Grant (2013), Geologic map of MTM -15027, -20027, -25027, and -25032 Quadrangles, Margaritifer Terra Region of Mars, *U.S. Geol. Surv. Misc. Invest. Ser.* Map I-3209.

Ivanov, B. A. (2001), Mars/Moon cratering ratio estimates, *Space Sci. Rev*., 96, 87–104.

Jones A. P., A. S. McEwen, L. L. Tornabene, V. R. Baker, H. J. Melosh and D. C. Berman (2011), A geomorphic analysis of Hale crater, Mars: The effects of impact into ice-rich crust, *Icarus*, *211* (1), 259-272, doi:10.1016/j.icarus.2010.10.014.

Kneissl, T., S. van Gasselt and G. Neukum (2011), Map-projection-independent crater size-frequency determination in GIS environments—New software tool for ArcGIS, *Planet. Space Sci*., *59*, 1243–1254, doi:10.1016/j.pss.2010.03.015.

Le Deit, L., J. Flahaut, C. Quantin, E. Hauber, D. Mège, O. Bourgeois, J. Gurgurewicz, M. Massé and R. Jaumann (2012), Extensive surface pedogenic alteration of the Martian Noachian crust suggested by plateau phyllosilicates around Valles Marineris, *J. Geophys. Res., 117*, E00J05, doi:10.1029/2011JE003983.

Malin, M. C., et al. (2007), Context Camera Investigation on board the Mars Reconnaissance Orbiter, *J. Geophys. Res*., *112*, E05S04, doi:10.1029/2006JE002808.

McEwen, A. S., et al. (2007), Mars Reconnaissance Orbiter's High Resolution Imaging Science Experiment (HiRISE), *J. Geophys. Res.*, 112, E05S02, doi:10.1029/2005JE002605.

Michael, G. G. and G. Neukum (2010), Planetary surface dating from crater size-frequency distribution measurements: Partial resurfacing events and statistical age uncertainty, *Earth Planet. Sci. Lett*., *226*, 885–890, doi:10.1016/j.epsl.2009.12.041.

Moore, J. M. and A. D. Howard (2005), Large alluvial fans on Mars, J. Geophys. Res., 110, E04005, doi:10.1029/2004JE002352.

Morgan, A. M., A. D. Howard, D. E. J. Hobley, J. M. Moore, W. E. Dietrich, R. M. E. Williams, D.M. Burr, J. A. Grant, S. A. Wilson and Y. Matsubara (2014), Sedimentology and climatic environment of alluvial fans in a Martian Saheki crater and a comparison with terrestrial fans in the Atacama Desert, *Icarus*, *229*, 131-156.

Rotto, S. and K. L. Tanaka (1995), Geologic/geomorphic map of the Chryse Planitia region of Mars, *U.S. Geological Survey Miscellaneous Investigations Series* Map I–2441, scale 1:5,000,000.

Saunders, S. R. (1979), Geologic Map of the Margaritifer Sinus Quadrangle of Mars, *U.S. Geol. Surv. Misc. Invest. Ser*. Map I-1144, Scale 1:5M.

Schultz, P. H. and H. Glicken (1979), Impact crater and basin control of igneous processes on Mars, *J. Geophys. Res.*, *84*, 8033–8047.

Schultz, P. H., R. A. Schultz and J. Rogers (1982), The structure and evolution of ancient impact basins on Mars, *J. Geophys. Res.*, *87*, 9803–9820.

Scott, D. H. and K. L. Tanaka (1986), Geologic map of the western equatorial region of Mars: U.S. Geological Survey Miscellaneous Investigations Series Map I–1802–A, scale 1:15,000,000.

Smith, D.E., M. T. Zuber H. V. Frey and 21 others (2001), Mars Orbiter Laser Altimeter Experiment summary after the first year of global mapping of Mars, *J. Geophys. Res.*, *106*, E10, p. 23,689–23,722.

Tanaka, K. L., J. A. Skinner and T. M. Hare (2011), Planetary Geologic Mapping Handbook, 24 pp., U.S. Geological Survey, Flagstaff, AZ.

Tanaka, K. L., J. A. Skinner, Jr., J. M. Dohm, R. P. Irwin III, E. J. Kolb, C. M. Fortezzo, T. Platz, G. G. Michael and T. Hare (2014), Geologic map of Mars, USGS Scientific Investigations Map 3292.

Weitz, C. M., S. A. Wilson, R. P. Irwin III and J. A. Grant (2017), Geologic mapping to constrain the sources and timing of fluvial activity in western Ladon basin, Mars, *Annual Planetary Geologic Mappers Meeting*, Flagstaff, AZ

Wilson, S. A. and J. A. Grant (2014), Geologic mapping in MTM quadrangles -20037, -25037, -30037, -30032 in southern Margaritifer Terra, Mars, *Annual Planetary Geologic Mappers Meeting*.

Wilson, S. A., J. A. Grant, C. M. Weitz, R. P. Irwin (2014), Geologic Mapping of Vinogradov Crater on Mars: Ancient Phyllosilicates to Alluvial Fans, *LPS XXXXV*, Abstract 2382.

Wilson, S. A., A. D. Howard and J. A. Grant (2017), Geologic mapping and stratigraphic analysis of alluvial fans in Roddy crater on Mars, *Geol. Soc. of America*, Abstract 319-7.

CHAPTER 4. The Evolution of Uzboi Vallis

Abstract

The ~400 km-long Uzboi Vallis is the southernmost segment of the Noachian to Hesperian-aged Uzboi-Ladon-Morava (ULM) mesoscale outflow system that dominates regional drainage in northwestern Noachis Terra and southwestern Margaritifer Terra. Recently acquired HiRISE images and MOLA topography help identify and characterize the nature and origin of a previously unrecognized deposit on the floor of Uzboi Vallis at the confluence of Nirgal Vallis. The Uzboi floor deposit consists of an upper unit (~34 km^3) and a lower unit (~255 km^3). The upper unit is relatively symmetric in planform and its topographic apex occurs at the mouth of Nirgal Vallis. The southern margin of the upper unit exposes sequences of light- and medium-toned, fine-grained layers that dip to the southeast. The upper unit of the Uzboi floor deposit is morphologically consistent with a sedimentary fan delta originating from Nirgal that is likely contemporaneous with a short-lived lake that occupied Uzboi Vallis after Holden crater formed in the mid- to Late Hesperian. The origin and timing of the lower unit is less constrained, and may have formed by a combination of fluvial and (or) mass wasting processes. The volume of material eroded from Nirgal Vallis is ~5.5 more than the total volume of the Uzboi floor deposit, suggesting most of the material eroded by Nirgal was transported some unknown distance downstream before Holden crater formed. The upper unit of the Uzboi floor deposit, interpreted to be a fan delta, is one of the largest on Mars and provides insight into the evolution of the ULM system, and is also indicative of a mid- to Late Hesperian climate that was capable of supporting an active hydrological cycle. The fan delta in Uzboi is likely contemporaneous with the Eberswalde delta and alluvial fans in the region as well as fresh

shallow valley elsewhere on Mars, contributing to a growing inventory of fluvial and alluvial landforms that are consistent with a habitable surface environment relatively late in Martian history.

4.1   Introduction

The first images of valleys and channels on Mars returned from the Mariner missions in the 1970s [e.g., *Schultz and Ingerson*, 1973] provided compelling geomorphic evidence for a landscape modified by liquid water. Understanding the process(es) responsible for the formation of such landforms, including the role, timing and duration of water, provides important information about past environmental conditions on Mars. One of the most impressive valley systems on Mars was formed by overflow along the northern rim of the ~900 km-diameter [*Tanaka et al*., 2014] Argyre impact basin, which created Uzboi Vallis, Ladon Valles, and Morava Valles, a segmented meso-scale outflow system [*Saunders*, 1979; *Grant*, 1987; *Grant and Parker*, 2002; *Irwin and Grant*, 2013] (Fig. 4.1). The Noachian-Hesperian age [*Grant*, 1987] Uzboi-Ladon-Morava (ULM) system alternately incised the southern highlands and infilled the intervening Early to Middle Noachian-aged Holden and Ladon impact basins [*Saunders*, 1979; *Schultz et al*., 1982; *Frey et al*., 2003], eventually reaching the northern plains via Ares Valles (Fig. 4.1). The ULM outflow system dominates the regional drainage in northwestern Noachis Terra and Margaritifer Terra, and is unique in that it records aqueous processes throughout a significant portion of Martian history.
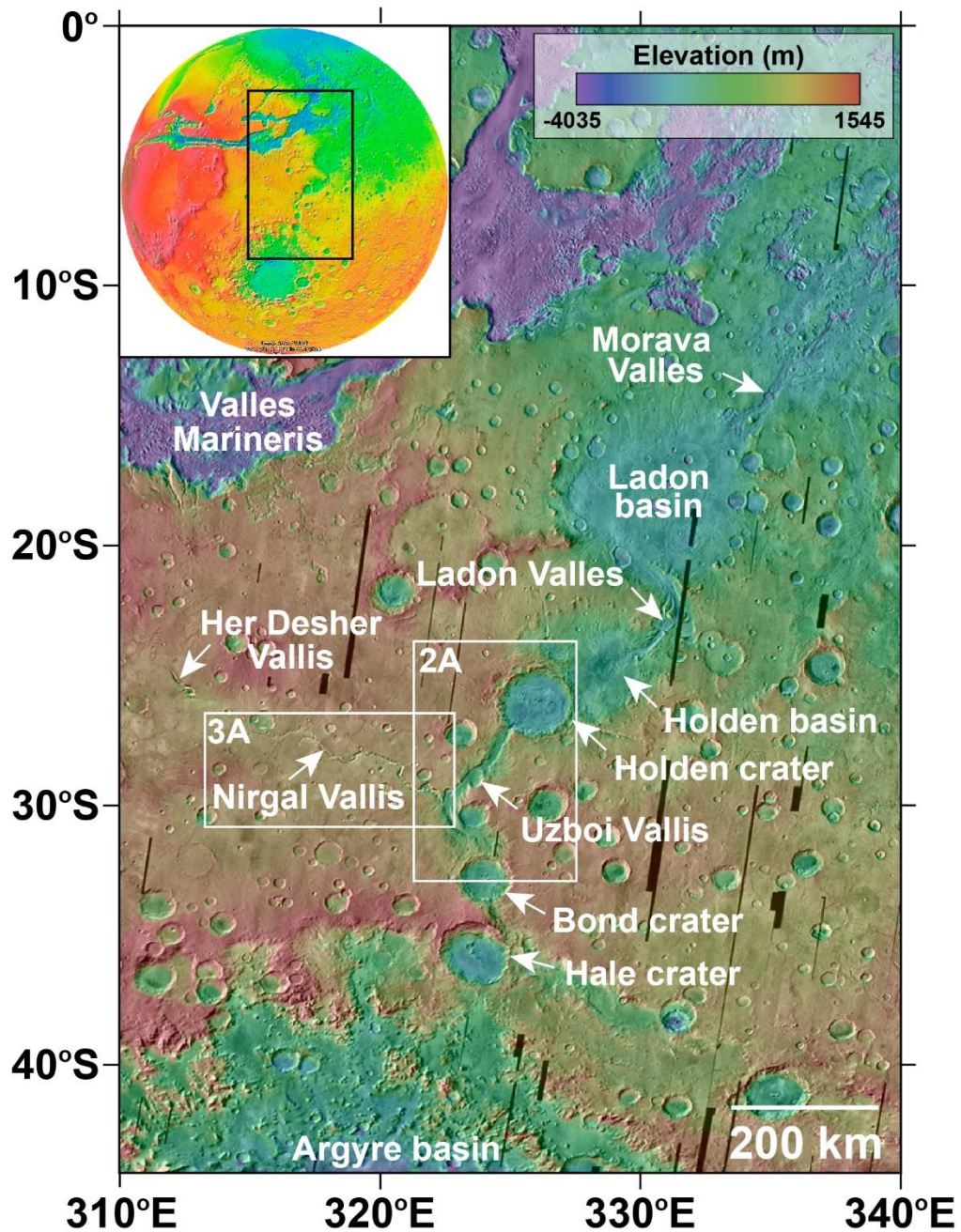
Figure 4.1   Northwestern Noachis Terra and southern Margaritifer Terra

The northwestern Noachis and southern Margaritifer Terra region on Mars (see inset for context) is characterized by the once through-flowing Uzboi-Ladon-Morava (ULM) outflow system that extends from Argyre toward the northern plains. Boxes show location of Figs. 4.2A and 4.3A and major place names referred to in the text are indicated (note terraces in Ladon Valles just north of associated arrowhead). MOLA over THEMIS day IR mosaic. Modified from *Grant et al*. [2011]. North is to the top.

Recent investigation of Uzboi Vallis (centered at ~28ºS, 323ºE), the southernmost segment of the ULM system, revealed a previously unrecognized mound of material on the valley floor that extends across the width of Uzboi and ~50-70 km to the south and north of the Nirgal-Uzboi confluence [*Wilson and Grant*, 2016a, 2016b, 2016c; *Wilson et al.*, 2017a, 2017b]. This study describes the morphology, structure, volume, and possible source(s) of the mound of material on Uzboi's valley floor using a combination of high-resolution images, topographic and spectral data. The identification and characterization of the material on the floor of Uzboi is significant because it informs the timing, duration and relative importance of fluvial versus other geomorphic processes within Uzboi and possibly Nirgal Vallis, and may help constrain the source(s) of water for the Late Hesperian lake in Uzboi [*Grant et al.*, 2011]. Furthermore, the relationship between the late-stage evolution of Nirgal, Uzboi and the greater ULM outflow system provides fundamental insight into the hydrologic environment, associated climate, and potential habitability of Mars during the mid- to Late Hesperian.

4.2   Background and Geologic Setting

4.2.1   Uzboi Vallis

Uzboi Vallis is a ~400 km long, typically ~7-15 km wide (up to ~25 km at widest), arcuate channel that incises Noachian-age plains [*Tanaka et al.*, 2014]. Uzboi formed from multiple discharge events originating from Argyre [*Grant and Parker*, 2002] and debouched into the degraded, ancient multi-ringed Holden basin [*Sanders*, 1979; *Schultz et al.*, 1982; *Frey et al.*, 2003] (Fig. 4.1). The formation of Bond crater and the Early to Middle Amazonian-aged Hale crater [*Cabrol et al.*, 2001; *Jones et al.*, 2011] destroyed evidence of the original Uzboi outlet from Argyre. The northern end of Uzboi was

significantly modified by the formation of the 154 km-diameter Holden crater in the mid- to Late Hesperian [*Grant and Parker*, 2002; *Irwin and Grant*, 2013].

When Holden crater formed, its southern rim damned Uzboi Vallis, forming an enclosed drainage basin that filled with ~4000 km^3 of water between craters Holden and Bond [*Grant et al.*, 2008, 2011] (Fig. 4.2A). The short-lived [*Grant et al.*, 2011] lake in Uzboi eventually breached Holden's southern rim in a Hesperian-aged flood event [*Grant et al.*, 2008, 2011; *Irwin and Grant*, 2013]. Water catastrophically drained into Holden crater, transporting flood deposits on top of pre-existing lacustrine and alluvial deposits in the crater [*Moore and Howard*, 2005; *Grant et al.*, 2008; *Irwin and Grant*, 2013]. *Grant et al.* [2011] suggested the source of water for the lake in Uzboi was most likely precipitation due to the paucity of morphological evidence supporting contributions from groundwater or overflow from Argyre. Nirgal Vallis, Uzboi's largest tributary, was considered a potential source of water for the lake in Uzboi but previous investigations were inconclusive due to the lack of evidence for an associated deposit [*Grant et al.*, 2011].

4.2.2   Nirgal Vallis

Nirgal is a striking, ~670 km-long [*Baker*, 1982; *Reiss et al.*, 2004], longitudinal valley system that was first recognized in Mariner 9 data [e.g., *Sharp and Malin*, 1975]. The valley, centered approximately 29°S, 320°E (Fig. 4.3A), debouches into Uzboi just south of crater Luki near 29.93°S, 322.43°E (Figs. 4.2A and 4.3A). Nirgal incises into a smooth, relatively low-lying, broad surface that lacks a well-defined contributing area, and there is little to no evidence of fluvial incision from overland flow on surfaces adjacent to the valley (Fig. 4.3). Most of Nirgal incises Noachian-aged plains, interpreted to be lava flows, pyroclastic material and impact breccia (unit Npl$_1$), and thin interbedded lava and

aeolian material (unit Npl$_2$) respectively [*Scott and Tanaka*, 1986]. The westernmost reaches of Nirgal, however, incise Hesperian aged lava flows [*Scott and Tanaka*, 1986]. The age of Nirgal is disputed, with some studies designating a Noachian-age for the valley [e.g., *Carr and Clow*, 1981; *Reiss et al.*, 2004; *Irwin et al.*, 2005] despite its relatively fresh appearance and incision into what others designate as Hesperian terrain [*Carr*, 2006].

The morphology of Nirgal is unique in that it changes from upstream to downstream [*Milton*, 1973; *Sharp and Malin*, 1975; *Baker*, 1982]: the western, upstream section of Nirgal Vallis is relatively shallow (~200 m deep [*Reiss*, 2001]) and characterized by stubby, alcove-like tributaries, whereas the eastern, downstream section of the valley is sinuous and deeply entrenched (up to ~1200 m deep [*Reiss*, 2001]) (Fig. 4.3A). The width of Nirgal Vallis ranges from 2 km upstream to 10–12 km downstream [*Reiss*, 2001] and the valley is "U"-shaped in cross section with a linear longitudinal profile [e.g., *Baker*, 1982; *Carr*, 1996; *Jaumann and Reiss*, 2002]. The overall east-west orientation of Nirgal, which mirrors the trend of Her Desher Vallis and Vallis Marineris to the north, is consistent with a strong structural control from Tharsis [*Carr*, 1996; *Jaumann and Reiss*, 2002] (Fig. 4.1). The uneven distribution and orientation of the tributaries in the upstream section of Nirgal provide additional evidence for structural influence on valley form [*Jaumann and Reiss*, 2002; *Glines and Fassett*, 2013] (Fig. 4.3A).
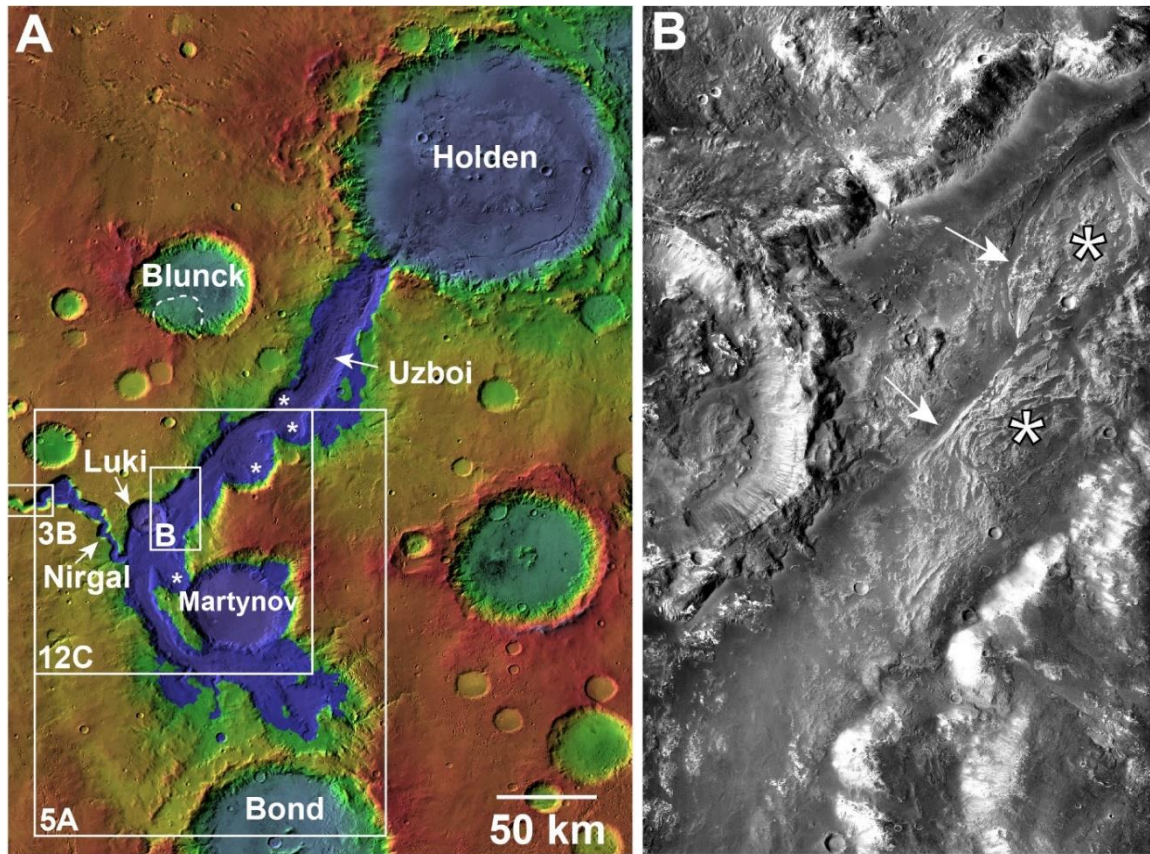
Figure 4.2   Uzboi Vallis and the extent of the Uzboi lake

A) The impact that formed Holden crater at the northern end of Uzboi Vallis blocked the northward-flowing system [*Grant and Parker*, 2002], creating a ~4000 km^3 lake in Uzboi (shaded blue) that filled to ~ -350 m [*Grant et al*., 2011] (see Fig. 4.1 for context). Several alcoves along the length of Uzboi ("*") may be regressive landslides. Dashed line in crater Blunck indicates margin of a landslide. Boxes shows location of (B) and Figs. 4.3B, 4.5A and 4.12C. MOLA over THEMIS daytime IR. **B**) Channels (white arrows) in lower unit of the Uzboi floor deposit and example of possible landslides/slumps ("*") originating from Uzboi walls. Subframe of CTX image D10_031137_1502 (5.15 m scaled pixel width). Image is ~25 km across. North is to the top in both images.
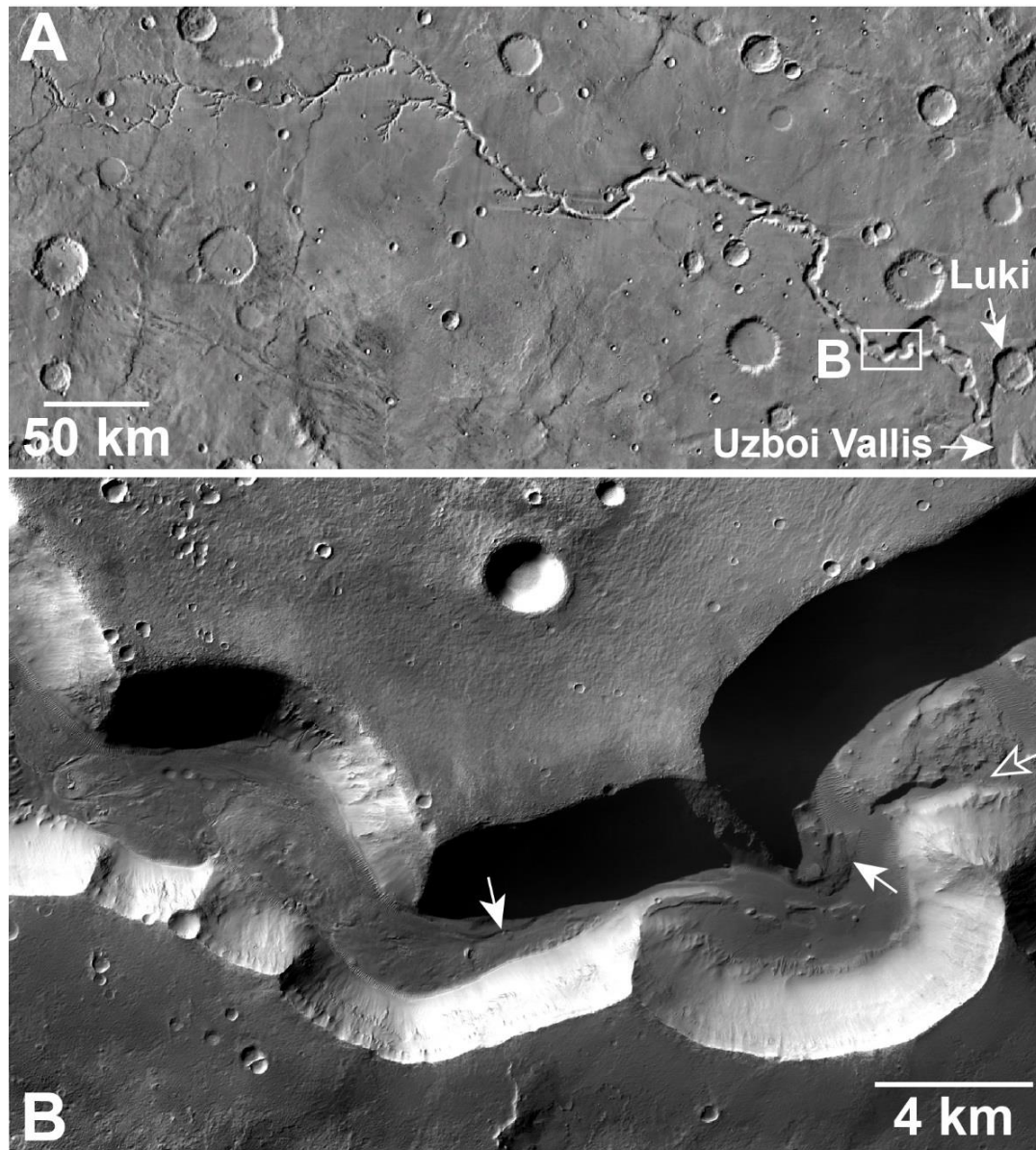
Figure 4.3   Nirgal Vallis

A) Nirgal Vallis is a longitudinal valley that debouches into Uzboi Vallis south of crater Luki. Box shows location of (B). Subframe of THEMIS daytime IR mosaic (see Fig. 4.1 for context). **B**) Possible meander cut off (hollow arrow after *Irwin et al*. [2005], *Malin and Edgett*, [2001]), incised channel (left solid arrow) and streamlined forms (right solid arrow) occur on the floor of Nirgal (also see Fig. 4.2A for context). Subframe of CTX B01_010039_505 (5.14 m scaled pixel width). North is to the top in both images.

4.3   Data and Methods

This study utilizes a variety of datasets including global daytime infrared mosaics from the Thermal Emission Imaging System (THEMIS, ~100 m per pixel resolution) [*Christensen et al.*, 2004], topographic data from the Mars Orbiter Laser Altimeter (MOLA, 128 pixel per degree resolution) [*Smith et al.*, 1999], and spectral information from the Compact Reconnaissance Imaging Spectrometer for Mars (CRISM Full Resolution Target (FRT), ~20 m pixel resolution) [*Murchie et al.*, 2007]. Images and digital terrain models (DTMs) from the Mars Context Camera (CTX, ~6 m pixel resolution) [*Malin et al.*, 2007] and the High Resolution Imaging Science Experiment (HiRISE, ~0.25 m pixel resolution) [*McEwen et al.*, 2007] provide the coverage and resolution to analyze the fine-scale features and orientations of the material in Uzboi and its surroundings.

Geologic and geomorphic mapping of the region bounding the confluence of Nirgal and Uzboi Vallis was completed using standard methods [*Tanaka et al.*, 2011] in ArcGIS, a geographic information system (GIS) from the Environmental Systems Research Institute (ESRI). ESRI's ArcScene was used for three-dimensional renderings of the available HiRISE DTM [*Kirk et al.*, 2008]. The Layer Tools extension [*Kneissl et al.*, 2010] in ArcGIS was used to estimate the orientation of layers exposed in Uzboi Vallis. Contour maps of Uzboi Vallis were produced from gridded MOLA data in the commercial program SURFER®.

Two of the three available CRISM Map-projected Targeted Reduced Data Record (MTRDR) images, FRTs 1C9ED and 16554, were mosaicked to analyze the mineralogy of the mouth of Nirgal Vallis and the adjacent Uzboi floor. The MTRDRs standardize CRISM targeted observations to what they would be if each scene were viewed at a single viewing

geometry, as close to nadir as possible, and without the influence of atmospheric gases [*Seelos et al.*, 2012]. Spectral parameter images overlie corrected I/F imagery to show occurrences of olivine (OLINDEX: red), low-calcium pyroxene (LCPINDEX: green) and Fe/Mg phyllosilicates (D2300: blue). The quality of the other CRISM image covering this area that was available at the time of publication, FRT 1B5F2, was too poor to analyze. There were no available CRISM Multispectral (MSP) strips that covered our region of interest.

The volume of material eroded to form Nirgal Vallis was estimated to be ~1600 km^3 by comparing a "pre-Nirgal" surface digital elevation model (DEM) to the present day DEM (Fig. 4.4). In ArcGIS, a reconstructed "pre-Nirgal" surface was created by clipping the gridded 128 pixel per degree MOLA data to encompass ~632 km of Nirgal Vallis. The DEM raster was converted to individual elevation points, and the points within Nirgal Vallis, plus a 1.5 km buffer around the margin of Nirgal, were removed (Fig. 4.4A). A triangular irregular network (TIN) was generated from the remaining elevations points, which creates a surface by connecting straight lines across the elevation points in Nirgal that was removed in the previous step (Fig. 4.4B). The TIN was converted to a raster DEM with a cell size of 463 to correspond to the original resolution of the 128 pixel per degree gridded MOLA data using the nearest neighbor interpolation method (Fig. 4.4C). The ArcGIS "Cut/Fill" tool calculated the difference in volume between the "pre-Nirgal" DEM and the present day topography (Fig. 4.4D).
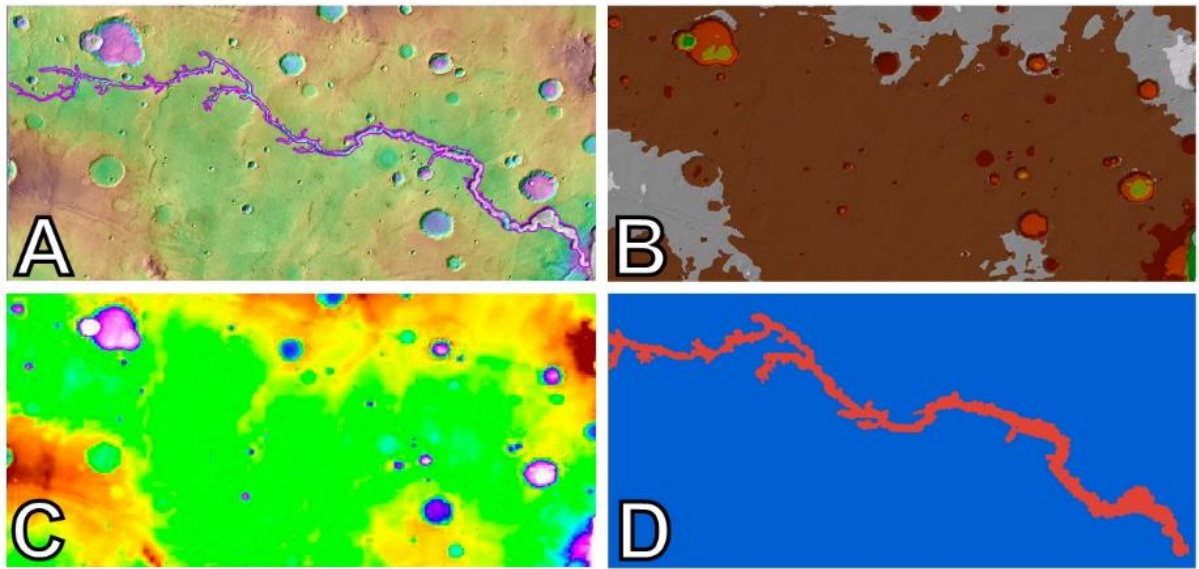
Figure 4.4   Volume estimation of material eroded from Nirgal Vallis

A) MOLA data was clipped to encompass Nirgal Vallis and its margins were outlined (purple line), forming a polygon. The MOLA elevation points within this polygon were removed. **B**) A triangular irregular network (TIN) was created from the remaining elevation points. **C**) The TIN was converted to a raster DTM and, **D**) the difference in volume was calculated between the DTMs of the present day Nirgal surface (A) and the "pre-Nirgal surface" (C). The estimated volume of material removed by Nirgal Vallis provides an order of magnitude estimate, as the actual valley profile (and thus resulting volume) is approximated using a DEM generated from coarsely spaced (~½ km) MOLA elevation shot points (Section 4.3). This is sufficient, however, because the net difference in volume between the Uzboi floor deposit relative to the total volume of material eroded from Nirgal Vallis is significant (see text for discussion). North is to the top in all images and each scene is ~450 km across.

4.4   Observations and Inferences

4.4.1   Topography of the Uzboi Vallis Floor: Evidence for the Uzboi Floor Deposit

Elevations between approximately -1400 m and -300 m emphasize the topography of the Uzboi Vallis floor (Fig. 4.5A). Transects along the length of Uzboi (Fig. 4.5B) indicate the lowest elevation in Uzboi between craters Bond and Holden within ~75 km of the Nirgal confluence is approximately -1160 m and -1300 south and north of Nirgal's mouth, respectively (Fig. 4.5C). In the ~120 km stretch between these points, the elevation

on the valley floor increases to roughly -720 m, with the highest elevation at the mouth of Nirgal Vallis (Fig. 4.5C). The elevation of Nirgal's valley floor at the mouth of Nirgal is graded to the elevation of the Uzboi floor, approximately -720 m. The overall slope south and north of the Nirgal-Uzboi confluence is 0.0075 and 0.0039, respectively. The change in elevation along Uzboi floor, which extends ~50 km and 70 km to the south and north of the Nirgal-Uzboi confluence, respectively (Fig. 4.5A), provides evidence for a mound of material in Uzboi hereafter referred to as the "Uzboi floor deposit" (Section 4.4.2). Based on the morphology, proximity to the Uzboi-Nirgal confluence and the slope, the Uzboi floor deposit is divided into a smaller, *upper unit* (Section 4.4.2.1) and a larger, *lower unit* (Section 4.4.2.2) (Fig. 4.5C).
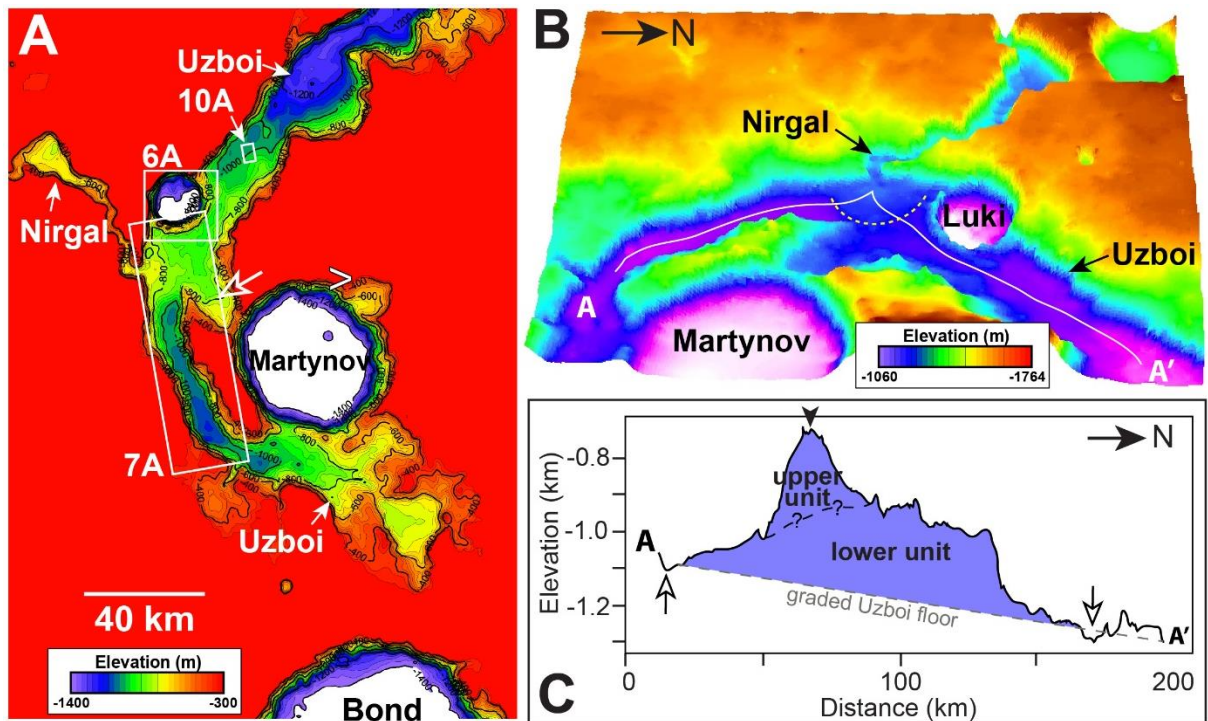
Figure 4.5   Topography of the Uzboi floor

A) MOLA data below -300 m highlights the topography along the floor of Uzboi Vallis and the location and extent of the Uzboi floor deposit at the mouth of Nirgal Vallis (see

Fig. 4.2A for context). "V" shows perspective view shown in (B) and boxes show location of Figs. 4.6A, 4.7A and 4.10A. Hollow white arrow indicates the alcove in the Uzboi wall that extends southeast toward Martynov that is a possible source of material for the lower unit (see text Section 4.5.2). Contour map generated using SURFER® software. North is to the top. **B**) Perspective eastward-looking view of deposit in Uzboi at confluence of Nirgal Vallis (MOLA 8X vertical exaggeration. For scale, Luki crater is 20.8 km in diameter. Transect (white line) corresponds to profile in (C). Dashed yellow line approximates the upper unit that is symmetric relative to the mouth of Nirgal. North is to the right. **C**) MOLA profile of Uzboi floor (see (B) for context) shows location and extent of the Uzboi floor deposit (upper and lower units, shaded blue area). Dashed gray line shows projected elevation of Uzboi beneath the Uzboi floor deposit. The upper unit (~34 km^3) at the mouth of Nirgal is fairly symmetric whereas the lower unit (~255 km^3) is offset to the north towards Holden. Black arrow approximates mouth of Nirgal Vallis and the hollow arrows indicate low elevation points on Uzboi floor north and south of Nirgal. North is to the right.

The rim and ejecta from Luki, a 20.8 km-diameter crater in Uzboi Vallis just north of the Uzboi-Nirgal confluence, may also contribute to the topography associated with the Uzboi floor deposit (Fig. 4.6). Although an absolute age from crater statistics cannot be estimated (due to the lack a continuous ejecta surface), the stratigraphic position and degree of degradation helps constrain the relative timing of emplacement of Luki crater. Luki modifies the wall and floor of Uzboi Vallis (Fig. 4.2A), and is therefore interpreted to be relatively younger than Uzboi. Luki pre-dates some, if not all, of the emplacement of the Uzboi floor deposit because the flanks of Luki within Uzboi Vallis have been modified and (or) buried by the Uzboi floor deposit (Section 4.4.2). If Luki pre-dates the Uzboi lake stage, its interior would have been inundated. The embayment of the flanks of Luki coupled with the elevation of its southern rim (-600 m), which is 250 m lower than the predicted elevation of the Uzboi lake, provides evidence to support infilling of Luki (Figs. 4.2A and 4.6B) [*Grant et al.*, 2011].

Luki's interior is asymmetric, with the northwestern half ~350 m higher than the adjacent southeastern floor (Fig. 4.6B). This asymmetry could be related to pre-existing structure along the wall of Uzboi Vallis or evidence for a landslide originating from its northwestern rim. Standing water in Luki, the sudden change in base level due to the catastrophic draining of the Uzboi lake, or seismic activity related to large impacts in the area (e.g., Holden) could have destabilized Luki's northwestern interior rim, triggering a landslide. The relatively circular appearance of the crater, and lack of elongation of the crater rim that is typically associated with landslides, disfavors this process. Exposures of light-toned massive material occur in Luki, but there is no obvious evidence of light-toned layered deposits. The intriguing bench-like forms in the lower-lying portions of the crater interior (Fig. 4.6A) may provide support for formation or modification by standing water.
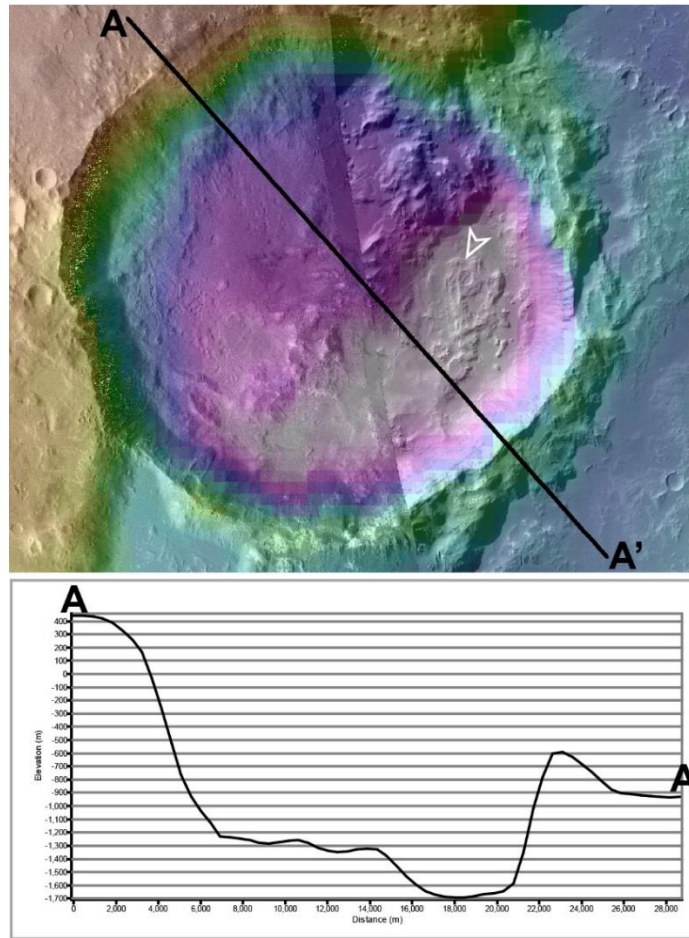
Figure 4.6   Crater Luki

A) Crater Luki is a 20.8 km diameter crater on the western margin of Uzboi Vallis (see Fig. 5A for context). This exterior rim of this heavily modified crater that is within Uzboi Vallis has been buried by the Uzboi floor deposit. White arrow indicates flat-lying benches in the lower portion of the crater floor. Transect corresponds to profile in B). MOLA over CTX mosaic; elevation ranges from -1761 to 517 m. **B**) Profile of Luki showing asymmetric nature of the crater fill. This crater, with the lower rim at -600 m in elevation, would have been infilled by the lake in Uzboi (see Fig. 4.2A for context).

4.4.2   The Uzboi Floor Deposit

The Uzboi floor deposit covers an area of approximately 1260 km^2 (Fig. 4.5). The

southern, upstream margin of the Uzboi floor deposit coincides with where the valley width

begins to increase by a factor of 2-3X, and the northern margin occurs downstream of Luki,

a crater that constricts Uzboi's valley width by roughly a factor of two (Fig. 4.5). The thickness of the Uzboi floor deposit, as estimated from the elevation difference between the surface of the deposit and the projected elevation of Uzboi's floor beneath the deposit, varies along its length but it appears thickest (up to ~400 m) at the mouth of Nirgal (Fig. 4.5C). The transect along the floor of Uzboi Vallis suggests the gradient was continuous upstream and downstream of the floor deposit, but the actual gradient of the Uzboi floor beneath the overlying Uzboi floor deposits is unknown.

The upper unit of the Uzboi floor deposit appears to be stratigraphically on top of the lower unit of the Uzboi floor deposit, but the location and type of contact (e.g., unconformable, gradational, etc.) between these units is difficult to discern due to lack of diagnostic exposures and (or) availability of HiRISE data. The thickness and volume estimates of the upper and lower units of the Uzboi floor deposit presented below do not account for relief (e.g., ejecta from craters Luki and (or) Martynov) that may be buried by the younger floor deposits. Therefore, the volume estimates below should be viewed as maximum approximations.

The surface area of the upper unit is ~300 km^2, with a maximum estimated thickness of ~225 m (Fig. 4.5C). Using an average unit thickness, the resulting volume is ~34 km^3. A similar volume is calculated using the volume of a cone, $V = \frac{1}{3} r^2 h$, where h ~225 m and r~12 km. The volume of the lower unit upstream, beneath and downstream of the upper unit is ~6 km^3 (95 km^2 area x 60 m average thickness), 60 km^3 (300 km^2 area x 200 m average thickness) and 189 km^3 (840 km^2 area x 225 m average thickness) respectively, for a total volume of ~255 km^3. The total estimated volume of the Uzboi floor deposit (upper and lower units combined) is ~289 km^3, which is ~5.5 times less than

the estimated total volume of material (~1600 km^3) eroded to form most of Nirgal Vallis (Section 4.3, Fig. 4.4).

4.4.2.1 The Nature of the Upper Unit of the Uzboi Floor Deposit

The upper unit of the Uzboi floor deposit is fairly symmetric relative to the mouth of Nirgal with slopes of 0.028 and 0.018 to the south and north, respectively (Figs. 4.5 and 4.7). The upper unit is triangular in planform, extending ~18 km in length and ~20 km in width (Fig. 4.7A). The surface of the upper unit is moderately cratered and degraded (e.g., eroded crater rims, infilling by aeolian material, rough and fluted textures) (Fig. 4.7). Linear, streamlined, shallow depressions on the fan surface, now infilled with smooth dark-toned and (or) aeolian material, may be evidence of degraded fluvial channels on the surface of the upper unit (Fig. 4.7A). The upper unit's surface directly north of Nirgal's mouth has 2-3 concentric ridges oriented perpendicular to the presumed northward direction of flow (Fig. 4.7A). Adjacent to these ridges, the upper unit surface consists of light-toned material that incorporates light-toned, meter-scale blocks and layering that ranges from fine (meter-scale) to massive (10s of meter scale) beds at the base of the deposit (Fig. 4.7B). Approximately east and east-southeast of the Nirgal-Uzboi confluence, evidence of both massive light-toned material in some locations and hints of layering and (or) bedding in others are present on the surface of the upper unit, and the variations in color and texture as seen in HiRISE color is consistent with the presence of different rock types (Figs. 4.7C-D).
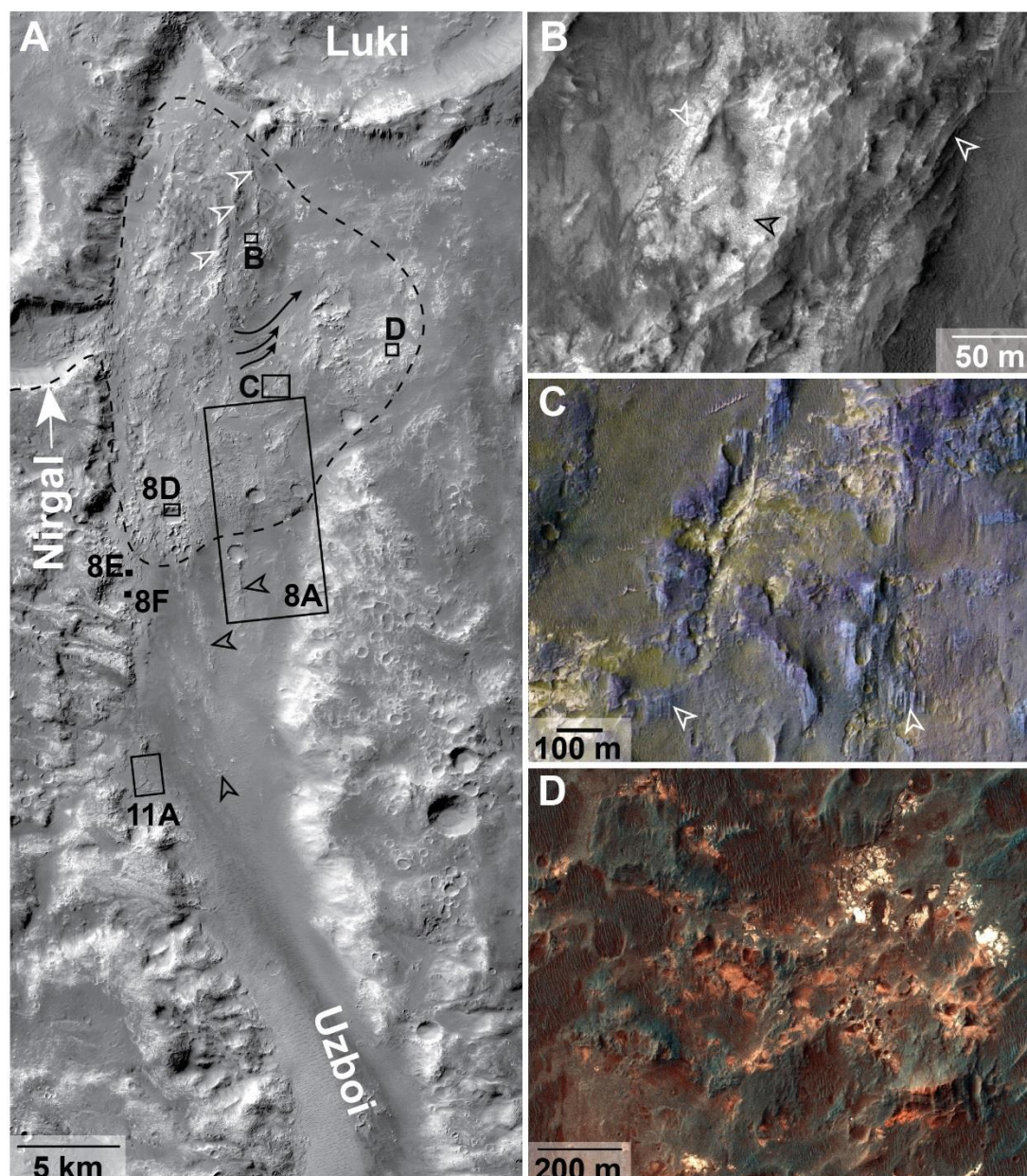
Figure 4.7   Nature of the upper unit of the Uzboi floor deposit

A) The upper unit of the Uzboi floor deposit in Uzboi Vallis at the confluence of Nirgal Vallis (black dashed line, see Fig. 4.6A for context) with lower unit to the south. The surface of the upper unit is degraded with shallow channels indicating downstream flow towards Holden (black arrows). Hollow white arrows indicate concentric ridges. Black hollow arrows indicate scabby, possibly layered remnants distal deposits associated with the lower unit of the Uzboi floor deposit. Boxes show location of (B), (C), (D), and Figs. 4.8A, 4.8D-8F and 4.11A. Subframe of CTX F16_042082_1494 (5.62 m scaled pixel width). **B**) Surface of the upper unit ~11 km from the mouth of Nirgal consists of light-toned massive material that may incorporate light-toned boulder-sized rocks (black arrow).

Possible layering is evident (e.g., white arrows). Subframe of HiRISE PSP_003565_1495 (25.9 cm scaled pixel width). **C**) Variations in color and texture ~ 9 km from the Nirgal mouth suggests different rock types that have hints of layering (white hollow arrows). Subframe of HiRISE PSP_ 003565_1495 (25 cm scaled pixel width). **D**) Bright, light-toned rock under a darker toned-surface with no obvious layering, ~14 km from the mouth of Nirgal. Subframe of HiRISE ESP_049941_1500. North is to the top in all images.

A few ~1 km-diameter craters on the southern margin of the upper unit reveal sequences of light- and medium-toned layers that are presumably fine-grained due to the paucity of recognizable blocks within the layers or on adjacent slopes (Fig. 4.8A-B, 4.8D). Layers, where exposed, are continuous in most cases for tens to hundreds of meters. A light-toned layer nearly 85 m in length lower in the depositional sequence (near an elevation of approximately -940 m) appears to be dipping ~6° (±2.6°) to the southeast (128±19°; R^2=98.14%) (Fig. 4.8C, Table 4.1).

The two high-resolution CRISM MTRDR FRTs of Nirgal Vallis and adjacent Uzboi show evidence of mafic deposits on the western flank of Uzboi north of Nirgal that include a large olivine deposit and smaller outcrops of low-calcium pyroxene (Fig. 4.9). Smaller mafic deposits occur on the western flank of Uzboi south of Nirgal. Hints of the phyllosilicate-bearing layer are present in the walls of Nirgal near its mouth, but not as recognizable as exposures upstream [*Buczkowski et al.*, 2010, 2013] or in the plains to the northwest [*LeDeit et al.*, 2012]. There are no obvious phyllosilicates exposed in the upper unit of the Uzboi floor deposit, but the low quality of the CRISM spectra makes this observation tentative.
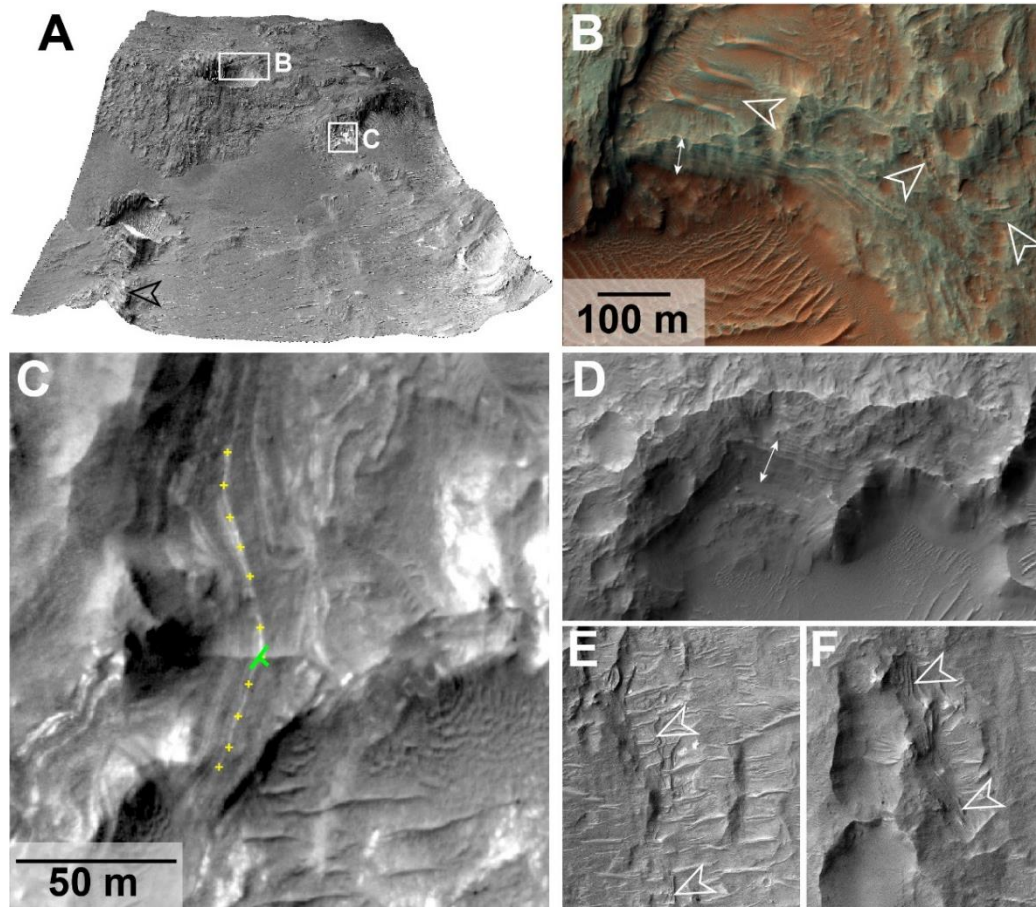
Figure 4.8   Light-toned layers in the Uzboi floor deposit

A) 3-D view of southern margin of Uzboi floor deposit ~15 km from the mouth of Nirgal (5X vertical exaggeration, see Fig. 4.7A for context). Possibly layered ridges extend to the south from the upper unit (black arrow). Boxes show location of (B) and (C). HiRISE DTM from stereo pair ESP_042082_1495 and ESP_042016_1495 (25.8 cm scaled pixel width). Image is ~6 km across. **B**) Light-toned, fine-grained layers in the upper unit exposed along the northern rim of a ~0.9 km-diameter crater. Subframe of HiRISE ESP_042082_1495 (25.8 cm scaled pixel width). **C**) A layer in the upper unit dips 6° ($\pm 2.5°$) to the south-south east ($126° \pm 17°$) (green symbol; $R^2 = 98.26\%$, R = 0.99, RMS Error = 0.21, Max Dev. = 0.39) based on eleven points (yellow "+") (Table 4.1). Subframe of HiRISE ESP_042082_1495 (25.8 cm scaled pixel width). **D**) Sequence of layers exposed in a 1 km-diameter crater on the surface of the upper unit (see Fig. 4.6A for context). Subframe of HiRISE ESP_046249_1495 (25.9 cm scaled pixel width). Image is ~720 m across. **E**) and **F**) Examples of fine, horizontal layers exposed along the wall of Uzboi near the presumed contact between the upper and lower units (see Fig. 4.7A for context). (E) and (F) are ~400 m and ~365 m across, respectively. Subframes of HiRISE ESP_046249_1495 (25.9 cm scaled pixel width). North is to the top in all images.

Table 4.1   Strike and Dip Measurements of Layer in Upper Unit

Points measured along layer exposed in Fig. 4.7C to estimate dip and direction of the Uzboi floor deposit (points were collected from south to north, see Fig. 4.8C for context). HiRISE DTM ESP_042016_1495 and ESP_042082_1495 (produced by the University of Arizona).

Point	Point Location		Elevation (m)	Deviation
	X	Y		
1	811.3352	-1781174.6865	-936.849	0.31
2	810.2769	-1781183.1532	-937.503	0.13
3	812.1819	-1781191.1965	-938.727	-0.38
4	814.7219	-1781198.6049	-939.084	-0.02
5	816.8385	-1781206.0132	-940.026	-0.28
6	819.5902	-1781218.9249	-941.035	-0.18
7	819.8019	-1781226.5449	-941	0.39
8	816.4858	-1781233.3095	-941.466	0.11
9	813.8399	-1781241.247	-942.098	-0.23
10	811.591	-1781249.1845	-941.934	0.27
11	808.9451	-1781253.947	-942.415	-0.11
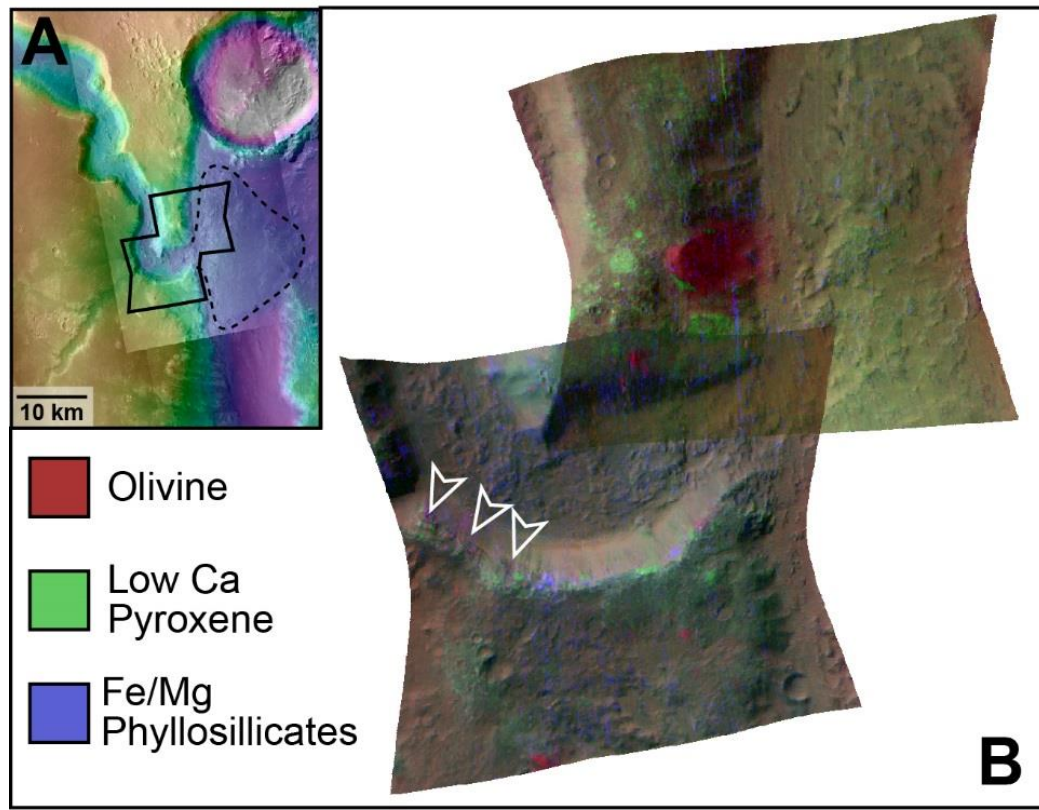
Figure 4.9   CRISM data of the upper unit of the Uzboi floor deposit

A) Regional context for the location of the CRISM image mosaic (solid line) in (B) with approximate boundary of the upper unit of the Uzboi floor deposit (dashed line). MOLA over CTX.   **B**) Mosaic of CRISM Map-projected Targeted Reduced Data Record (MTRDR) images near the mouth of Nirgal Vallis and part of the Uzboi floor deposit from FRT 1C9ED (upper) and FRT 16554 (lower), see (A) for context. Spectral parameter images overlie corrected I/F imagery to show the location of olivine (OLINDEX: red), low-calcium pyroxene (LCPINDEX: green) and Fe/Mg phyllosilicates (D2300: blue). Arrows indicate a phyllosilicate-bearing layer exposed in the wall of Nirgal. North is to the top in both images.

4.2.2.2 The Nature of the Lower Unit of the Uzboi Floor Deposit

The lower unit of the Uzboi floor deposit appears offset to the north relative to the

mouth of Nirgal, or downstream toward Holden crater (Fig. 4.5C). North of Nirgal Vallis,

the lower unit is heavily degraded, mostly massive and is easily sculpted by the wind (Fig.

4.10A). The material is predominantly light-toned, contains light-toned blocks in places,

and lacks obvious layering (Fig. 4.10B). The surface is incised by a few poorly integrated channels downstream of crater Luki [*Grant et al.*, 2008] (Fig. 4.10A). North of Nirgal Vallis, the transition and nature of the contact between upper and lower units is difficult to discern given the available HiRISE coverage and degraded state of the constituent material.

The topographic expression of the lower unit in Uzboi south of Nirgal Vallis extends approximately ~15 km beyond the southern margin of the upper unit (Fig. 4.7A). Although the majority of the Uzboi Vallis floor between crater Bond and Nirgal Vallis is largely obscured by dark-toned material and (or) superposing aeolian bedforms, surfaces along steeper slopes expose discontinuous, north-south oriented ridge segments (hollow black arrows in Figs. 4.7A and 4.8A). The ridges appear scabby, cratered, light-toned and layered in some places (Fig. 4.8A). Light-toned, fine-scale horizontal layers oriented parallel to the walls of Uzboi are exposed near the probable contact between the upper and lower units, adjacent to a section of the Uzboi valley wall that is strongly dissected by channels (Figs. 4.8E-F, and HiRISE ESP_042082_1495). Further south, the lower unit exhibits broad layered surfaces as well as ridges that extend east-northeast into Uzboi Vallis (Fig. 4.11). The ridges consist of interbedded light- and dark-toned layers (~30.36°S, 322.54°E, elevation ~ -890 m) and are similar in morphology to inverted fluvial channels in Saheki crater [*Morgan et al.*, 2014] and elsewhere on Mars.
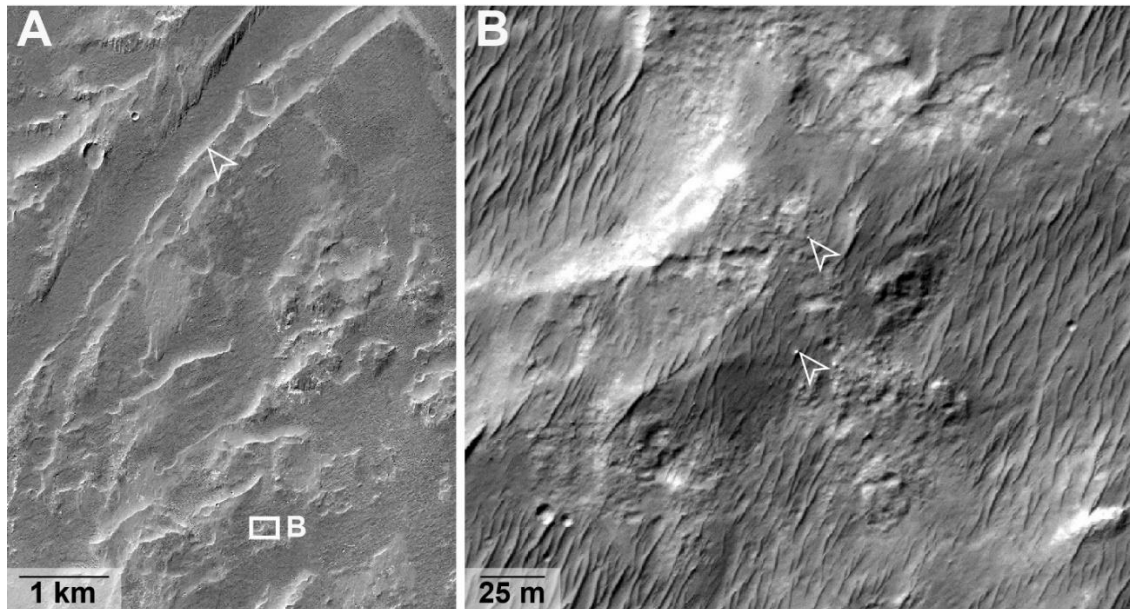
Figure 4.10 Nature of the lower unit of the Uzboi floor deposit

A) The lower unit of the Uzboi floor deposit downstream of Nirgal Vallis is degraded and easily erodes into yardangs (see Fig. 4.5A for context). Possible channels (white arrow) incise the surface. Box shows location of B). **B**) The material is light-toned and massive and lacks obvious layering. Meter-scale boulders are present (white arrows). Subframes of HiRISE image ESP_043717_1505 (25 cm scaled pixel width). North is to the top in both images.
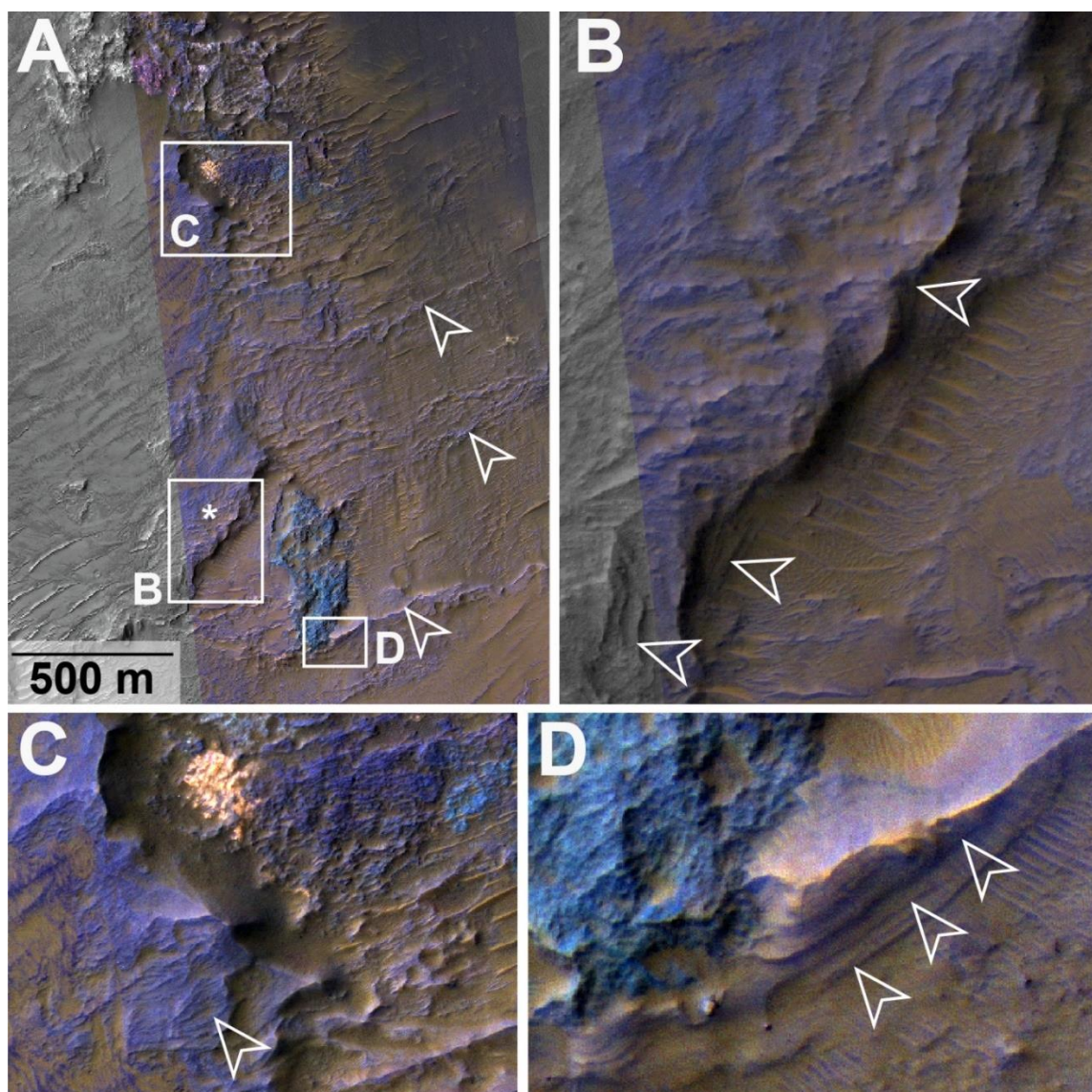
Figure 4.11   Fluvial features in the lower unit of the Uzboi floor deposit

A) The floor of Uzboi Vallis south of Nirgal Vallis has several ridges (white arrows) oriented approximately perpendicular to Uzboi's western wall, as well as possible layered, remnant fan surfaces ("*") (see Fig. 4.7A for context). Boxes indicate locations of (B), (C) and (D). **B**) A possible degraded fan surface has horizontal layers visible at HiRISE scale (white arrows). Image is ~300 m across. **C**) The edge of another possible fan surface has fine layers. The diversity of colors on the floor adjacent to the fan surface suggests multiple rock types may be present. Image is ~467 m across. **D**) Some ridges expose multiple fine-grained, light toned layers. Image is ~210 m across. A)-D) are subframes of merged IRB map projected HiRISE ESP_050376_1495 (25 cm scaled pixel width). North is up in all images.

4.4.3   Crater Martynov

Martynov is one of the larger (~61 km-diameter), degraded impact craters in the area (Figs. 4.2 and 4.12). The timing of formation of crater Martynov relative to the formation of the ULM outflow system is unknown. High standing topography related to the Martynov rim and ejecta may have diverted flow from Argyre around Martynov, perhaps contributing to the broadly arcuate nature of the channel along this section of the valley. Alternatively, the formation of Martynov may post-date the initial incision of Uzboi, and thus the broad depression along its northwestern rim may be a segment of a remnant terrace, analogous to the high-standing terraces preserved in Ladon Valles (Fig. 4.1) [*Grant and Parker*, 2002; *Irwin and Grant*, 2013]. During the lake stage in Uzboi that post-dates the mid- to Late Hesperian Holden crater, Martynov would have likely been filled with water (Fig. 4.2A) [*Grant et al*., 2011]. The floor of Martynov is infilled, and deposits weathering along blocky fractures may be indicative of lacustrine material (Fig. 4.12A), sourced from a small inlet on Martynov's southwestern rim (Fig. 4.12B). The southern rim of Martynov exhibits topographic irregularities, some of which may indicate transport of water into Martynov. Layered beds adjacent to a possible inlet along Marytnov's southern rim consists of boulder-sized blocks and possibly gravel sized grains that appear to be dipping to the northwest. Along the northwestern rim of Martynov, however, there is no geomorphic evidence (e.g., breached rim) that supports overflow of water out of Martynov into the adjacent low-lying Uzboi Vallis (Figs. 4.12B and 4.12C). This would be expected if there was significant amounts of water in Uzboi when crater Bond formed or if discharge from Argyre had been routed through crater Martynov. The

surface of the broad depression forming an alcove on Martynov's northwestern rim, that extends into Uzboi Vallis, exhibits sculpting supportive of flow-like forms (Fig. 4.12B).
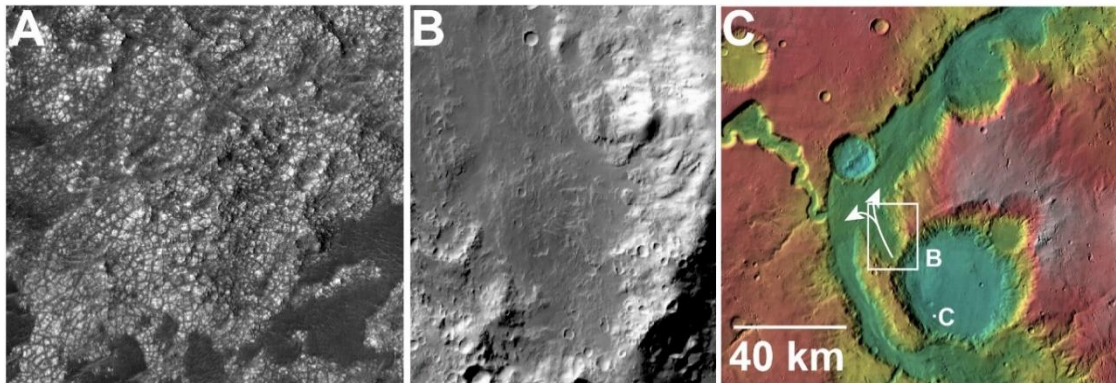
Figure 4.12   Crater Martynov

A) Light-toned blocky nature on floor of Martynov crater (see (C) for context). Image is ~595 m across. Subframe of HiRISE ESP_021722_1490 (~50 cm pixel scale resolution). **B**) Broad depression adjacent to NW Martynov rim that leads to Uzboi Vallis could be the site of a landslide that contributed material to the lower unit of the Uzboi floor deposit via mass wasting, or it could be a remnant terrace (see (C) for context).   Note rim of Martynov is not breached. **C)** Mass wasting and associated flow from the broad depression (white arrows) may have contributed material to the lower unit (see Fig. 4.2A for context). The flow of material both upstream and downstream (white arrows) could account for the asymmetry of the lower unit (Fig. 4.5C). MOLA over THEMIS Day IR data.

4.5   Discussion

The topography along the floor of Uzboi Vallis between craters Bond and Holden provides evidence for a previously unrecognized deposit on the floor of Uzboi Vallis at the confluence of Nirgal Vallis (Section 4.4.1, Fig. 4.5). The varied geologic history of the region suggests the Uzboi floor deposit could have formed from a combination of spatially and temporally varying geomorphic processes, perhaps in response to changes in environmental conditions over time.

The Uzboi floor deposit consists of material that could have been produced in a variety of ways ranging from physical and (or) chemical weathering, pyroclastic eruptions,

impact cratering, chemical precipitation, and (or) comminution during transport [e.g.,

Wilson et al., 2007]. Transportation of the material that comprises the Uzboi floor deposit

could have occurred by mass wasting, impact, volcanic, airfall deposition from myriad

sources (e.g., wind erosion, volcanic ash), and (or) or fluvial, alluvial and lacustrine

processes. The mechanism by which Uzboi floor deposit was deposited could be the same

as the aforementioned transport mechanisms, or it could have been subject to subsequent

reworking by wind, ice, fluvial, lacustrine or mass wasting processes. The nature of the

Uzboi floor deposit, including its volume, morphology and orientation, helps constrain the

source(s) of the material, the mode of transport, and the final depositional mechanism

responsible for the formation of the upper and lower units.

4.5.1   Nature and Origin of the Upper Unit of the Uzboi Floor Deposit

Analysis of the characteristics of the upper unit of the Uzboi floor deposit in Section

4.4.2.1 provides the following critical observations:

1) The upper unit is fan-shaped, relatively symmetric, and triangular in planform.

2) The topographic apex of the upper unit is located at the mouth of Nirgal Vallis
   (Fig. 4.5).

3) The southern margin of the upper unit exposes sequences of alternating light-
   and medium-toned layers (Fig. 4.8).

   a. The layers are meter- to multi-meter scale in thickness and laterally
      continuous at a minimum of tens to hundreds of meters.

   b. The lack of boulders and ease of erosion suggests the layers are
      primarily composed of partially indurated sediment finer than sand.

c. The ~6° (±2.6°) southeast dip of the layers is indicative of deposition from the northwest.

Based on the form, location, and the nature and dip of the layers in the upper unit (outlined in observations 1-3 above), we conclude that the upper unit of the Uzboi floor deposit is consistent with a fan delta origin that was sourced from Nirgal, deposited via traction and suspension. The regular, fine-grained nature of the layered sequences is not consistent with other depositional mechanisms such as mass wasting. The light-toned layers and their ease of erosion dismiss origins such as volcanic lava flows or volcanic intrusions. The layers appear to be too regular to be dunes and the lack of cross-bedding disfavors aeolian processes. Glacial processes can form layers but they tend to consist of a large range of sediment sizes, which is not observed, in addition to the lack of regional geomorphic evidence indicating the presence of a past ice sheet. The repetitive and fine-grained nature of the layers is not consistent morphologically with impact-related deposits. Lastly, the light-toned nature of the layers and their ease of erosion could be consistent with volcanic ash or loess, but the lack of a proximal source makes this process less likely.

The dip and direction of the layers exposed in the lower portions of the upper unit (Fig. 4.8) are consistent with delta foreset beds in prograding sedimentary fan deposits [*Rich*, 1951; *Mitchum et al.*, 1977; *Orton and Reading*, 1993]. A fan delta origin and deposition in a lacustrine environment is consistent with evidence for a short-lived lake in Uzboi (Fig. 4.2A) [*Grant et al.*, 2011]. Fluvial activity in Nirgal Vallis that sourced the fan delta, therefore, is thought to be contemporaneous with the Uzboi lake. The predicted lake margin in Uzboi at its maximum extent, which would have back-flooded the lower reaches of Nirgal Vallis for some distance (Fig. 4.2A) [*Grant et al.*, 2011], corresponds to

the location of a possible meander cut-off [*Irwin et. al*., 2005], incised channels and streamlined forms on the floor of Nirgal (Fig. 4.3C). The location and relatively preserved nature of these fluvial landforms in Nirgal Vallis provides further evidence for aqueous processes that are likely contemporaneous with the formation of the upper unit (fan delta) and consistent with the presence of a lacustrine environment in Uzboi Vallis.

Although the surface of the upper unit is degraded, it differs morphologically compared to the fine layers observed lower in the upper unit. There are hints of light-toned beds near the surface of the upper unit, yet they typically appear more massive (Fig. 4.6B) and incorporate meter-scale blocks (Fig. 4.7A-D). This morphology is more consistent with deposition via shear flows such as fluvial bedload or mass flows rather than deposition via traction and suspension. This observation could be a function of limited diagnostic exposures and (or) data, or the surface of the upper unit may represent a different depositional environment. The geologic record in Holden supports a catastrophic draining of the lake in Uzboi when the impounded water overtopped and breached Holden's rim [*Grant et al*., 2008, 2011; *Irwin and Grant*, 2013]. This rapid change in depositional environment and associated base level may be related to the nature of the upper unit's surface. The km-long, blocky, concentric ridges oriented in the downstream direction of flow (Fig. 4.7A) are reminiscent of surge deposits that may have been emplaced during the rapid removal of water that back-flooded into the lower reaches of Nirgal Vallis (Fig. 4.2A). The unusual widening near the terminus of Nirgal noted by *Baker* [1982] may have been caused by slumping triggered by the sudden drawdown of the water impounded in Uzboi.

4.5.2 Nature and Origin of the Lower Unit of the Uzboi Floor Deposit

The nature and origin of the lower unit is less certain, as is the timing of its formation relative to other landforms and geologic events (Table 4.2). The lower unit has fewer diagnostic characteristics (due to gentler slopes that limit relief) as well as less HiRISE and CRISM coverage. The analysis of the characteristics of the lower unit (Section 4.4.2.2) provides the following observations:

1) The lower unit is stratigraphically below the upper fan-shaped deposit and is therefore is relatively older.

2) The lower unit is asymmetric in profile, and is offset to the north relative to the mouth of Nirgal Vallis (Fig. 4.5C).

3) The southern, upstream margin of the lower unit coincides with a 2-3X widening of Uzboi near the mouth of Nirgal. The northern margin of the lower unit is located just downstream of crater Luki, which constricts Uzboi's valley width by roughly a factor of two (Fig. 4.5).

4) North of Nirgal Vallis, the lower unit consists of sediment that is light- to medium-toned, contains variable occurrences of meter-scale blocks, and is readily eroded by the wind. No obvious fine-scale layering is observed (Fig. 4.10).

5) South of Nirgal Vallis, the lower unit is also light- to medium-toned and has evidence of fine layers oriented parallel to the Uzboi walls, layered fan-like surfaces, and east-west oriented layered ridges that extend toward the center of the valley (Fig. 4.11).

In general, the variation in the size of the materials and lack of layering in the lower unit north of Nirgal Vallis is more consistent with deposition via shear flows such as fluvial

bedload, mass flows or glacial till, rather than deposition from traction and suspension as suggested for (at least the lower portion of) the upper unit. The light-toned nature of the lower unit and its ease of erosion could be consistent with airfall deposits, but dismiss origins such as volcanic lava flows, volcanic intrusions, or impact material. As discussed earlier, glacial processes could deliver a range of sediment sizes as observed, but there is no regional evidence of extant ice.

The location of the lower unit on the floor of Uzboi at the mouth of Nirgal Vallis limits the probable sources of material to one or a combination of the following: 1) Nirgal Vallis, 2) Argyre or points upstream, 3) locally derived from adjacent Uzboi valley walls, 4) fluvial or wind transported material from adjacent upland terrain, or 5) impact-related material. Each source and the supporting evidence is described below.

Nirgal Vallis: The location of the lower mound on the floor of Uzboi Vallis centered near the mouth of Nirgal, in addition to the observation that the upper unit is consistent with fluvial deposition from Nirgal, makes Nirgal Vallis an intriguing source for the lower unit as well. The asymmetrical nature of the lower unit relative to the mouth of Nirgal could be evidence of downstream transport of material from Nirgal into Uzboi, when there was active flow through the ULM system (e.g., before the lake in Uzboi formed). The sharp southern margin of the lower unit could have been subsequently enhanced by wind erosion.

Argyre or points upstream: Alternatively, the lower unit could have been sourced from flows from Argyre, possibly well before Nirgal Vallis formed. In this scenario, large, high-velocity flows would have readily transported material through Uzboi, and the widening of the valley at the present-day mouth of Nirgal would have encouraged

deposition in this location. Waning or later flows through Uzboi could have carved into the deposit and created a prograding delta downstream from crater Luki, which could explain the sharp topographic edge of the lower unit along its northern margin (although associated layering has not yet been observed).

Another significant geologic event that occurred upstream of the lower unit deposit is the formation of crater Bond. Although the absolute age of Bond is unknown, it formed after Uzboi Vallis but prior to Holden crater and the lake in Uzboi (Fig. 4.2A). If there was active flow or ponded water in Uzboi Vallis when Bond formed, the impact could have triggered flows that formed (or modified) the lower unit of the Uzboi floor deposit.

Locally derived material: The broad depression on the northwestern rim of crater Martynov that extends into Uzboi, if formed by mass wasting processes, is another possible source of material for the lower unit (Figs. 4.5A and 4.12). The rim of Martynov adjacent to this broad alcove is not breached, suggesting the depression was not likely formed by overflow (Fig. 4.12B). The lineations on the surface of the broad alcove are consistent with flow (Fig. 4.12B), and this landform is analogous to other pronounced alcoves along Uzboi's valley walls between Martynov and Holden crater (Fig. 4.2A). These alcoves (some of which may be remnant crater rims) may have formed by mass wasting, effectively widening the valley walls and depositing material into the channel. Flows or slumps originating from the northwestern rim of Martynov, depositing some material to the north and south of Nirgal (Fig. 4.12C), could account for the asymmetry observed in the lower unit (Fig. 4.5C).

The "beheaded" nature of the terminus of Nirgal Vallis is consistent with possible backwasting of the Uzboi wall, as well as the parallel orientation of nature of the possible

143

slump deposits relative to the Uzboi channel wall (Fig. 4.2B). The degraded nature of the bedrock incised by Uzboi Vallis appears to consist of soft, friable material such as fine volcanic or aeolian dust that would be readily transported and reworked. If correct, material derived by widening of the Uzboi valley walls could have transported significant amounts of material into Uzboi that may account for some or all of the volume of the lower unit of the Uzboi floor deposit.

Failure and transport of material into Uzboi may have been triggered by the saturation and destabilization of slopes when water was impounded in the valley or shortly thereafter. Another possible trigger for landslides and widening of Uzboi, which could have pre-dated the lake in Uzboi, is seismic energy generated during impact events. In this scenario, craters Luki, Bond and (or) Holden are possible local candidates. Because crater Luki likely pre-dates the period of major excavation within Nirgal (given the paucity of Luki's ejecta the lack of Luki secondaries in Nirgal Vallis or surrounding terrain), any landslides in Uzboi generated by crater Luki would have likely been subsequently modified and transported downstream by flows from Nirgal. The energy generated by craters Bond and (or) Holden could have triggered mass movements in Uzboi and formed landslide deposits in craters Blunck (Fig. 4.2A) or possibly Luki (Fig. 4.6).

Fluvial or wind transported material from adjacent upland terrain: The lack of deep incision into the surrounding uplands adjacent to the lower unit makes fluvial processes on the plains inherently less favorable as the dominant source for the lower unit, although smaller contributions cannot be completely ruled out. Transport by wind is not favored because this process cannot account for the observed meter-scale blocks.

Impact-related material: Due to lack of data and (or) diagnostic exposures, contributions of ejecta, or ejecta that has been subsequently reworked and modified, including that from Luki crater, cannot be definitely ruled out.

In summary, many of the aforementioned sources and associated processes, such as impact and aeolian, are less favored for the origin of the lower unit relative to fluvial and (or) mass wasting processes. Both fluvial and mass wasting can account for the asymmetry of the lower unit, which is offset to the north relative to the mouth of Nirgal Vallis, as well as the observed morphology of the deposit. Although the volume of the lower unit is commensurate with the volume of the indentation of the Uzboi valley wall extending southeast toward Martynov crater (Figs. 4.2A, 4.5A, 4.12C), the lack of a head scarp or other features indicative of mass wasting along the outer northwestern rim and flank of Martynov make this interpretation tentative. The enigmatic depression extending from the northwestern rim of Martynov is morphologically similar to terraces in Ladon Vallis to the north (Fig. 4.1). If the depression along the northwestern rim of Martynov is a terrace related to the development of Uzboi, this would indicate Martynov post-dates the period of major incision that formed Uzboi Vallis.

4.5.3   The Timing of Fluvial Activity in Nirgal Vallis

Despite the fact that Nirgal is Uzboi's largest tributary, the relative age and timing of fluvial activity between the two valleys is not well understood. This relationship is further hampered by prior lack of evidence for material at the confluence of Uzboi and Nirgal, which made it was unclear whether discharge from Nirgal contributed to the lake in Uzboi, or if fluvial activity in Nirgal terminated prior to, or persisted after the filling and draining of the Uzboi basin [*Grant et al.*, 2011].   The volume of material eroded from

Nirgal is ~5.5 times greater than the total volume of the Uzboi floor deposit, indicating most of the "missing" material eroded by Nirgal was likely deposited into Uzboi and transported some unknown distance downstream when there was still active flow through the system (e.g., before craters Bond and Holden formed, Table 2). Some of the material could have been eroded and transported during and after the final drawdown of the lake in Uzboi, as supported by the shallow channels on the surface of the upper and lower units of the Uzboi floor deposit (Figs. 4.2C, 4.7A, 4.10A). The role of Nirgal in the formation of the lower unit is less certain, but the nature of the upper unit suggests that at least the latest period of fluvial activity in Nirgal was contemporary with the formation of the impounded lake in Uzboi that formed when Holden crater blocked the through-flow of water in the mid- to Late Hesperian.

4.5.4   Implications for the mid- to Late Hesperian Climate

Deltas provide geomorphic evidence for paleolakes, and thus their stratigraphy provides a link to the paleohydrology and associated paleoclimate. Numerous deltas have been identified on Mars [e.g., *Cabrol and Grin*, 1999; *Irwin et al.*, 2005; *Mangold and Ansan*, 2006; *DiAchille and Hynek*, 2010; *Goudge et al.*, 2012; *Wilson et al.,* 2013, 2016]. The largest, best exposed deltas on Mars occur in craters Jezero [e.g., *Fassett and Head*, 2005; *Ehlmann et al.*, 2008; *Schon et al.*, 2012; *Goudge et al.*, 2017] and Eberswalde [e.g., *Malin and Edgett,* 2003; *Moore et al.*, 2003; *Rice et al.*, 2013; *Jerolmack et al.*, 2004; *Lewis and Aharonson*, 2006; *Pondrelli et al.*, 2008; *Irwin et al.*, 2015], and have been the subject of numerous investigations and forwarded as potential targets for future landing sites. The volume of the Late Noachian Jezero delta is on the order of 5 km^3 [*Fassett and Head*, 2005]. Estimates of the volume of the Late Hesperian [*Irwin et al.*, 2015] Eberswalde delta

ranges from ~6 km^3 [*Malin and Edgett,* 2003; *Jerolmack et al.*, 2004; *Mangold et al.*, 2012]

to ~13 km^3 [*Moore et al.*, 2003] to 20-30 km^3 [*Bhattacharya et al.*, 2005]. By comparison,

the volume of the fan delta in Uzboi Vallis, ~34 km^3 (uncertainty in thickness makes this

a maximum estimate), is therefore one of the largest fan deltas preserved on the surface of

Mars. *Irwin et al.* [2005] estimated discharges from Nirgal on the order of 4800 m^3 s^{-1}

based on the dimensions of its interior incised channel (Fig. 4.3C), which could have filled

the enclosed basin in Uzboi (Fig. 4.2A) in as little as 20–30 years [*Grant et al.*, 2011].

These discharges suggest that the entire Uzboi floor deposit (~289 km^3), if formed by

fluvial processes from Nirgal, could have formed in as little as ~2 years. Significantly less

time would be required for Nirgal to deposit only the material in the upper unit associated

with the fan delta.

The evolution of Uzboi Vallis and the identification of a relatively large fan delta

offers a unique opportunity to constrain the origin, timing and duration of fluvial and

lacustrine activity, which formed subsequent to the Holden impact in the mid- to Late

Hesperian [*Irwin and Grant*, 2013]. Widespread, synoptic precipitation (either rainfall or

snowfall that later melted) is a mechanism that has been forwarded to explain the formation

of other fluvial landforms of similar age in Margaritifer Terra, including alluvial and

lacustrine deposition in Holden crater [*Grant et al.*, 2008], the Eberswalde delta [e.g.,

Moore et al., 2003], and the formation of alluvial fans [e.g., *Moore and Howard*, 2005;

Kraal et al., 2008; *Grant and Wilson*, 2011, 2012; *Kite et al.*, 2017]. Evidence for an active

hydrologic cycle is also supported by Hesperian to middle Amazonian valleys in the

midlatitude of both hemispheres [e.g., *Fassett and Head*, 2008; *Dickson et al.*, 2009; *Hynek

et al.*, 2010; *Warner et al.*, 2010a, 2010b; *Fassett and Head*, 2011; *Howard and Moore*,

2011; *Hauber et al.*, 2013; *Adeli et al.*, 2016; *Salese et al.*, 2016; *Wilson et al.*, 2016]. The catalyst for the climatic optimum that created warming is not known, but could be related to variations in the insulation triggered by changes in obliquity [e.g., *Laskar et al.*, 2004] or warming from ephemeral atmospheric changes [*Hobley et al.*, 2014]. Regardless, the growing geomorphic evidence for a post-Noachian climate that was capable of supporting an active hydrologic cycle is intriguing in terms of conditions that were favorable for habitable surface conditions.

The stratigraphic record in Holden crater indicates only limited fluvial activity persisted after the main flood event that drained the lake in Uzboi [*Grant et al.*, 2008, 2011; *Irwin and Grant*, 2013]. This scenario is consistent with the nature and state of preservation of the fan delta, as we do not see evidence for multiple episodes of deposition separated by gaps in time. It is also consistent with the lack of evidence for dense dissection on the terrain adjacent to Uzboi Vallis, which may be expected for longer or more intense periods of sustained runoff. After Holden's rim was breached and the impounded water in Uzboi largely drained, water in low-lying areas such as the floor of craters Luki (Fig. 4.6A) and Martynov, and in Uzboi upstream of the fan delta (Fig. 4.11) may have persisted for a geologically short time.

4.6   Summary

The provisional geologic timeline for the Uzboi Vallis region (with major events summarized below in relative sequence designated Stages "A" through "N," see Table 4.2) supports a long and dynamic history of aqueous and other geomorphic processes.

Uzboi formed in the Noachian to Hesperian from multiple discharge events originating from Argyre. Possible terraces formed and water debouched into the ancient

multi-ringed Holden basin (Stages A-D). Crater Luki formed along the western margin of Uzboi, depositing ejecta on the floor of Uzboi and surroundings, and may have triggered landslides along the interior Uzboi walls (Stage E). Both of these events may have produced material that contributed to the present day topography of the Uzboi floor deposit, the extent of which is unknown (between stages E and F). Discharge from Argyre and (or) Nirgal may have modified Uzboi Vallis after Luki formed, and flows though this part of the valley could have eroded, transported and (or) buried Luki ejecta or Luki-related landslide deposits downstream. The size and position of Luki would have constricted flows through this section of Uzboi, encouraging deposition of material upstream that may have contributed to the formation of the lower unit (between Stages E and F).

The relative timing of emplacement of crater Luki (Stage E), crater Bond (Stage F) and Nirgal Vallis (Stage G) is not well constrained due to the lack of defining age relationships and broadly similar states of degradation. If Bond is older than Luki, we infer that flows from Argyre and associated deposition did not contribute to the formation of the lower unit because the rim of Bond lacks evidence of entrance or exit breaches that would be expected if flow persisted from Argyre after Bond crater formed. Crater Bond (Stage F) is younger than Uzboi Vallis (Stage D) and older than crater Holden (Stage H). If water occupied Uzboi when crater Bond formed, flooding induced by impact may have contributed to the formation lower unit deposit downstream of Bond, possibly enhanced by the preferential deposition related to the constriction in Uzboi due to Luki. Seismic activity related to the impact of this 104 km-diameter crater may have also triggered landslides along the walls of Uzboi that may have contributed material to the lower unit (between stages F and G).

The timing of formation of Nirgal Vallis is not well constrained but it post-dates the incision of Uzboi Vallis. This study indicates that most of the major excavation of Nirgal (even if the lower unit was entirely sourced from Nirgal Vallis) occurred when there was active flow through the system, (e.g., before Holden crater formed in Stage H). The latest period of fluvial activity that occurred within Nirgal Vallis (Stage G) that formed the upper unit is younger than crater Luki, but the relationship between the age of the lower unit of the Uzboi floor deposit and crater Luki (Stage E) is less certain. Discharge from Nirgal may have formed, contributed to, or modified the lower unit (between stages G and H). Seismic activity related to the large, mid- to Late Hesperian Holden impact (Stage H) could have destabilized slopes that contributed material to the lower unit (between stages H and I), possibly simultaneously triggering landslides in craters Blunck (Fig. 4.2A) and maybe Luki (Fig. 4.6). Saturation of the valley walls during or shortly after the Uzboi lake (Stage I) could have triggered failure and slumping within Uzboi that contributed to the lower unit (between stages I and J). The last period of fluvial activity in Nirgal, which formed the fan delta associated with the upper unit of the Uzboi floor deposit (Stage J), likely occurred in the Late Hesperian and pre-dates the breach of the Holden rim that drained the lake in Uzboi (Stage K).

Shallow pools of water may have persisted for a short time in low-lying areas (Stage L) after the lake in Uzboi drained, before water infiltrated and (or) evaporated. Finally, the Early to Middle Amazonian Hale impact (Stage M) emplaced fluidized ejecta and secondaries in Nirgal and across the region, followed by aeolian activity (Stage N) that was ongoing throughout Amazonian.

Table 4.2   Provisional Geologic Timeline for the Uzboi Vallis Region

Stage	Description of Events	Probable Time Correlation
A	Formation of the ancient Holden and Ladon impact basins	Middle Noachian or older [*Frey et al.*, 2003; *Irwin and Grant*, 2013; *Saunders*, 1979; *Schultz et al.*, 1982]
B	Argyre basin and the cratered highland plains form	Middle Noachian [*Tanaka et al.*, 2014; *Scott and Tanaka*, 1986]
C	Variable dissection of the highland plains	Early Hesperian to Late Noachian [unit HNt of *Irwin and Grant*, 2013]. Martynov crater may pre-date the formation of the ULM system
D	Overflow from Argyre creates the Uzboi Vallis, Ladon Valles and Morava Valles (ULM) meso-scale outflow system	Noachian to Hesperian [*Grant*, 1987; *Grant and Parker*, 2002]. Martynov crater may post-date period of Uzboi incision
E*	Luki crater forms	Post-dates formation of Uzboi Vallis and pre-dates some, if not all, of incision of Nirgal Vallis
?	Formation (or contribution/modification) of the lower unit of Uzboi floor deposit: A) Possible contributions from Luki ejecta or widening of Uzboi related to landslides triggered by formation of Luki B) Subsequent flows from Argyre would have preferentially deposited sediment due to the constriction of the Uzboi	A) Post-dates formation of crater Luki B) Post-dates formation of crater Luki, only occurred if pre-dates formation of crater Bond
F*	Bond crater forms	Post-dates Uzboi Vallis, pre-dates Holden crater. Formative flows from Argyre end before emplacement of Bond crater. Bond could post-date formation of Nirgal Vallis
?	Formation (or contribution/modification) of the lower unit of Uzboi floor deposit: A) Possible sedimentation related to flooding triggered by Bond if there was water in Uzboi Vallis B) Possible contributions from widening of Uzboi related to landslides triggered by formation of Bond	A) Post-dates formation of crater Bond B) Post-dates formation of crater Bond

G*	Nirgal Vallis forms	Post-dates formation of Uzboi. Initial formation is unknown, Late Noachian (?) to Early to mid- (?) Hesperian [*Carr*, 2006]. Most of material removed from Nirgal was transported downstream before Holden crater formed. Nirgal may pre-date Bond and (or) Luki.
?	Formation (or contribution/modification) of the lower unit of Uzboi floor deposit related to fluvial activity from Nirgal	Post-dates incision of Nirgal Vallis
H	Holden crater forms, destroys northern end of Uzboi Vallis	Mid to Late Hesperian [*Irwin and Grant*, 2013]
?	Formation (or contribution/modification) of the lower unit of Uzboi floor deposit related to widening of Uzboi from landslides triggered by formation of Holden	Post-dates formation of crater Holden
I	Water impounded in Uzboi Vallis forms a lake between craters Bond and Holden [*Grant et al.*, 2011]	Mid to Late Hesperian
?	Formation (or contribution/modification) of the lower unit of Uzboi floor deposit related to widening of Uzboi from landslides triggered by saturation and destabilization related to impounded water	Mid to Late Hesperian
J	Formation of upper unit interpreted to be a fan delta sourced from Nirgal, contemporaneous with Eberswalde delta [*Irwin et al.*, 2015 and references therein]. Formation of alluvial fans in Holden and elsewhere in Margaritifer Terra [e.g., *Grant and Wilson*, 2012]	Mid to Late Hesperian
K	Holden rim is breached, lake in Uzboi drains, massive flood emplaced in Holden crater	Mid to Late Hesperian
L	Water ponds in low-lying areas (e.g., Uzboi upstream of Nirgal and crater Luki) forming possible fluvial channels (Fig. 4.11) and bench like	Mid to Late Hesperian (or later)

	landforms (Fig. 4.6). Regional fluvial activity wanes.	
M	Hale crater forms	Early to Middle Amazonian [*Cabrol et al.*, 2001; *Jones et al.*, 2011]
N	Ongoing aeolian activity	Amazonian

The origin and timing of the formation of the lower unit of the Uzboi floor deposit is unknown and depending on the process, could have formed between Stages E and F, F and G, G and H and (or) I and J, see text for further details. *The relative timing of formation between craters Luki (E) and Bond (F) and Nirgal Vallis (G) cannot be definitively constrained (e.g., Nirgal could have formed before Bond crater).

4.7   References

Adeli, S., E. Hauber, M. Kleinhans, L. Le Deit, T. Platz, P. Fawdon and R. Jaumann (2016), Amazonian-aged fluvial system and associated ice-related features in Terra Cimmeria, Mars, *Icarus*, *288*, 286, doi:10.1016/j.icarus.2016.05.020.

Baker, V. R. (1982), *The Channels of Mars*, 198 pp., Univ. of Tex. Press, Austin.

Bhattacharya, J. P., T. H. D. Payenberg, S. C. Lang, M. Bourke (2005), Dynamic river channels suggest a long-lived Noachian crater lake on Mars, *Geophys. Res. Lett*. 32, L10201.http://dx.doi.org/10.1029/2005GL022747.

Buczkowski, D., K. D. Seelos, S. L. Murchie, F. P. Seelos, E. Malaret, C. Hash and the CRISM team (2010), Extensive Phyllosilicate-bearing Layer Exposed by Valley Systems in Northwest Noachis Terra, *Lunar Planet. Sci., XLI*, Abstract 1458.

Buczkowski, D., K. D. Seelos, S. L. Murchie, F. P. Seelos, E. Malaret, C. Hash and the CRISM team (2013), Evidence for multiple widespread buried phyllosilicate-bearing layers between Argyre and Vallis Marineris, *Lunar Planet. Sci., XLIV*, Abstract 2331.

Cabrol, N.A. and E. A. Grin (1999), Distribution, classification, and ages of martian impact crater lakes, *Icarus* 142, 160–172.

Cabrol, N. A., D. D. Wynn-Williams, D. A. Crawford and E. A. Grin (2001), Recent aqueous environments in Martian impact craters: An astrobiological perspective, *Icarus*, *154*, (1), 98-112, doi:10.1006/icar.2001.6661.

Carr, M. H. (1996), *Water on Mars*, 229 pp., Oxford Univ. Press, New York.

Carr, M. H. (2006), *The Surface of Mars*, 307 pp., Cambridge Univ. Press, New York.

Carr, M. H. and G. D. Clow (1981), Martian channels and valleys—Their characteristics, distribution, and age, *Icarus*, *48*, 91– 117.

Christensen, P. R. et al., (2004), The Thermal Emission Imaging System (THEMIS) for the Mars 2001 Odyssey Mission, *Space Sci. Reviews*, *110* (1), 85-130.

Di Achille, G., and B. Hynek (2010), Deltas and valley networks on Mars: Implications for a global hydrosphere. In: Cabrol, N., Grin, E. (Eds.), *Lakes on Mars*. Elsevier, Amsterdam, pp. 223–248.

Dickson, J. L., C. I. Fassett and J. W. Head (2009), Amazonian-aged fluvial valley systems in a climatic microenvironment on Mars: Melting of ice deposits on the interior of Lyot Crater, *Geophys. Res. Lett*., *36*, L08021, doi:10.1029/2009GL037472.

Ehlmann, B.L., et al. (2008), Clay minerals in delta deposits and organic preservation potential on Mars. *Nat. Geosci.* 1, 355–358 .

Fassett, C. and J. Head (2005), Fluvial sedimentary deposits on Mars: Ancient deltas in a crater lake in the Nili Fossae region. *Geophys. Res. Lett*., *32*, L14201.

Fassett, C. I. and J. W. Head (2008), Timing of Martian valley network activity: Constraints from buffered crater counting, *Icarus*, *198*, 61.

Fassett, C. I. and J. W. Head (2011), Sequence and timing of conditions on early Mars, *Icarus*, *211*, 1204.

Frey, H. V., E. L. Frey, W. K. Hartmann and K. L. T. Tanaka (2003), Evidence for buried "pre- Noachian" crust pre-dating the oldest observed surface units on Mars. *Lunar Planet. Sci. XXXIV*. Abstract 1848.

Glines, N. H. and C. I. Fassett (2013), Evidence for groundwater sapping on Mars from junction angles of Nirgal Vallis tributaries, *Lunar Planet. Sci., XLIV*, Abstract 2011.

Goudge , T. A, J. W. Head, J. F. Mustard and C. I Fassett (2012), An analysis of open-basin lake deposits on Mars: Evidence for the nature of associated lacustrine deposits and post-lacustrine modification processes, *Icarus*, *219*, 211-229.

Goudge, T. A., D. Mohrig, B. T. Cardenas, C. M. Hughes, C. I. Fassett (2017), Stratigraphy and paleohydrology of delta channel deposits, Jezero crater, Mars, *Icarus* https://doi.org/10.1016/j.icarus.2017.09.034.

Grant, J. A. (1987), The Geomorphic Evolution of Eastern Margaritifer Sinus, Mars. Advances in Planetary Geology, NASA Tech. Memo. 89871, pp. 1–268.

Grant, J.A. and T. J. Parker (2002), Drainage evolution of the Margaritifer Sinus region, Mars. *J. Geophys. Res*., *107*. doi:10.1029/2001JE001678.

Grant, J. A. and S. A. Wilson (2011), Late alluvial fan formation in southern Margaritifer Terra, Mars, *Geophys. Res. Lett*., 38, L08201, doi:10.1029/2011GL046844.

Grant, J. A. and S. A. Wilson (2012), A possible synoptic source of water for alluvial fan formation in southern Margaritifer Terra, Mars, *Planet. Space Sci*., *72*, 44, doi:10.1016/j.pss.2012.05.020.

Grant, J. A., R. P. Irwin III, J. P. Grotzinger, R. E. Milliken, L. L. Tornabene, A. S. McEwen, C. M. Weitz, S. W. Squyres, T. D. Glotch and B. J. Thomson (2008), HiRISE imaging

of impact megabreccia and sub-meter aqueous strata in Holden Crater, Mars, *Geology 36*, 195–198, doi:10.1130/G24340.

Grant, J.A., R. P. Irwin III, S. A. Wilson, D. Buczkowski and K. Siebach (2011), A lake in Uzboi Vallis and implications for the Late Noachian-Early Hesperian climate on Mars, *Icarus*, *212* (1), 110–122, https://doi.org/10.1016/j.icarus.2010.11.024.

Hauber, E., T. Platz, D. Reiss, L. Le Deit, M. G. Kleinhans, W. A. Marra, T. de Haas, and P. Carbonneau (2013), Asynchronous formation of Hesperian and Amazonian-aged deltas on Mars and implications for climate, *J. Geophys. Res. Planets*, *118*, 1529–1544, doi:10.1002/jgre.20107.

Hobley, D. E. J., A. D. Howard and J. M. Moore (2014), Fresh shallow valleys in the Martian midlatitudes as features formed by meltwater flow beneath ice, *J. Geophys. Res.*, DOI: 10.1002/2013JE004396.

Howard, A. D. and J. M. Moore (2011), Late Hesperian to early Amazonian midlatitude Martian valleys: Evidence from Newton and Gorgonum basins, *J. Geophys. Res.*, *116*, E05003, doi:10.1029/2010JE003782.

Hynek, B. M., M. Beach and M. R. T. Hoke (2010), Updated global map of Martian valley networks and implications for climate and hydrologic processes, *J. Geophys. Res.*, *115*, E09008, doi:10.1029/2009JE003548.

Irwin III, R.P., R. A. Craddock and A. D. Howard (2005), Interior channels in Martian valley networks: Discharge and runoff production. *Geology 33*, 489–492.

Irwin, R. P. and J. A. Grant (2013), Geologic map of MTM -15027, -20027, -25027, and -25032 Quadrangles, Margaritifer Terra Region of Mars, USGS Map I-3209.

Irwin, R. P. III, K. W. Lewis, A. D. Howard and J. A. Grant (2015), Paeleohydrology of Eberswalde crater, Mars, *Geomorphology,* 240, 83-101.

Jaumann R. and D. Reiss (2002), Nirgal Vallis: Evidence for extensive sapping, *Lunar Planet. Sci., XXXIII*, Abstract 1579.

Jerolmack, D.J., D. Mohrig, M. T. Zuber, S. Byrne (2004), A minimum time for the formation of Holden Northeast fan, Mars. *Geophys. Res. Lett*., *31*, L21701. http://dx.doi.org/10.1029/2004GL021326.

Jones A. P., A. S. McEwen, L. L. Tornabene, V. R. Baker, H. J. Melosh and D. C. Berman (2011), A geomorphic analysis of Hale crater, Mars: The effects of impact into ice-rich crust, *Icarus*, *211* (1), 259-272, doi:10.1016/j.icarus.2010.10.014.

Laskar, J., A. C. M. Correia, M. Gastineau, F. Joutel, B. Levrard and P. Robutel (2004), Long term evolution and chaotic diffusion of the insolation quantities of Mars, *Icarus*, *170*, 2, 343-364, Doi 10.1016/J.Icarus.2004.04.005.

Lewis, K. W. and O. Aharonson (2006), Stratigraphic analysis of the distributary fan in Eberswalde crater using stereo imagery. *J. Geophys. Res*., *111*, E06001. http://dx.doi.org/10.1029/2005JE002558.

Kirk, R. L., et al. (2008), Ultrahigh resolution topographic mapping of Mars with MRO HiRISE stereo images: Meter-scale slopes of candidate Phoenix landing sites, *J. Geophys. Res*., *113*, E00A24, doi:10.1029/2007JE003000.

Kite, E. S., J. Sneed, D. P. Mayer and S. A. Wilson (2017), Persistent or repeated surface habitability on Mars during the late Hesperian - Amazonian, *Geophys. Res. Lett*., 44, doi:10.1002.2017GL072660.

Kneissel, T., S. van Gasselt and G. Neukum (2010), Measurement of strike and dip of geologic layers from remote sensing data – new software tool for ArcGIS, *Lunar Planet. Sci., XXXXI*, Abstract 1640.

Kraal, E.R., E. Asphaug, J. M. Moore, A. Howard, A. Bredt (2008), Catalogue of large alluvial fans in martian impact craters, *Icarus*, *194*, 101–110.

Le Deit, L., J. Flahaut, C. Quantin, E. Hauber, D. Mège, O. Bourgeois, J. Gurgurewicz, M. Massé, and R. Jaumann (2012), Extensive surface pedogenic alteration of the Martian Noachian crust suggested by plateau phyllosilicates around Valles Marineris, *J. Geophys. Res., 117*, E00J05, doi:10.1029/2011JE003983.

Malin, M.C. and K. S. Edgett (2001), Mars Global Surveyor Mars Orbiter Camera: Interplanetary cruise through primary mission*: Journal of Geophysical Research*, *106*, 23,429–23,570.

Malin, M.C. and K. S. Edgett (2003), Evidence for persistent flow and aqueous sedimentation on Mars. *Science 302*, 1931–1934, doi:10.1126/science.1090544.

Malin, M. C., et al. (2007), Context Camera Investigation on board the Mars Reconnaissance Orbiter, *J. Geophys. Res.*, *112*, E05S04, doi:10.1029/2006JE002808.

Mangold, N. and V. Ansan (2006), Detailed study of an hydrological system of valleys, a delta, and lakes in Southwest Thaumasia region, Mars. *Icarus 180*, 75–87.

Mangold, N., E. S. Kite, M. G. Kleinhans, H. Newsom, V. Ansan, E. Hauber, E. Kraal, C. Quantin, K. Tanaka (2012), The origin and timing of fluvial activity at Eberswalde crater, Mars, *Icarus 220*, 530–551. http://dx.doi.org/10.1016/j.icarus.2012.05.026.

McEwen, A. S., et al. (2007), Mars Reconnaissance Orbiter's High Resolution Imaging Science Experiment (HiRISE), *J. Geophys. Res.*, 112, E05S02, doi:10.1029/2005JE002605.

Milton, D. J. (1973), Water and processes of degradation in the Martian landscape, *J. Geophys. Res.*, 78 (20), 4037-4047.

Mitchum, R. M., P. R. Vail, J. B. Sangree (1977), Seismic stratigraphy and global changes of sea level, part 6: stratigraphic interpretation of seismic reflection patters in depositional sequences. In : Payton, C. E. (Ed.), Seismic stratigraphy – Applications to Hydrocarbon Exploration, AAPG, Tulsa, USA, pp. 117-133.

Moore, J. M., A. D. Howard, W. E. Dietrich and P. M. Schenk (2003), Martian layered fluvial deposits: Implications for Noachian climate scenarios. *Geophys. Res. Lett.* 30(24), 2292, doi:10.1029/2003GL019002.

Moore, J. M. and A. D. Howard (2005), Large alluvial fans on Mars, *J. Geophys. Res.*, *110*, E04005, doi:10.1029/2004JE002352.

Morgan, A.M., A. D. Howard, D. E. J. Hobley, J. M. Moore, W. E. Dietrich, R. M. E. Williams, D.M. Burr, J. A. Grant, S. A. Wilson and Y. Matsubara (2014), Sedimentology and climatic environment of alluvial fans in a Martian Seheki crater and a comparison with terrestrial fans in the Atacama Desert, *Icarus*, *229*, 131-156.

Murchie, S., et al. (2007), Compact Reconnaissance Imaging Spectrometer for Mars (CRISM) on Mars Reconnaissance Orbiter (MRO), *J. Geophys. Res.*, *112*, E05S03, doi:10.1029/2006JE002682.

Orton, G. J. and H. G. Reading (1993), Variability in deltaic processes in terms of sediment supply, with particular emphasis on grain size, *Sedimentology*, *40*, pp. 475-512.

Pondrelli, M., Rossi, A.P., Marinangeli, L., Hauber, E., Gwinner, K., Baliva, A., Di Lorenzo, S. (2008), Evolution and depositional environments of the Eberswalde fan delta, Mars, *Icarus, 197*, 429–451. http://dx.doi.org/10.1016/j.icarus.2008.05.018.

Reiss, D. (2001), Untersuchungen zur Morphologie des Nirgal Vallis, Mars, Master's thesis, 94 pp., Georg-August-Univ. Göttingen, Göttingen, Germany.

Reiss, D., S. van Gasselt, G. Neukum, and R. Jaumann (2004), Absolute dune ages and implications for the time of formation of gullies in Nirgal Vallis, Mars, *J. Geophys. Res*., *109*, E06007, doi:10.1029/2004JE002251.

Rice, M. S., J. F. Bell III, S. Gupta, N. H. Warner, K. Goddard, R. B. Anderson (2013), A detailed geologic characterization of Eberswalde crater, Mars. Mars 8, 15–59. http://dx.doi.org/10.1555/mars.2013.0002.

Rich, J. L. (1951), Three critical environments of deposition and criteria for recognition of rocks deposited in each of them, *Geol. Soc. Am Bull*., *62*, 1-19.

Saunders, S. R. (1979), Geologic Map of the Margaritifer Sinus Quadrangle of Mars. U.S. Geol. Surv. Misc. Invest. Ser. Map I-1144, Scale 1:5M.

Salese, F., G. Di Achille, A. Neesemann, G. G. Ori, and E. Hauber (2016), Hydrological and sedimentary analyses of well-preserved paleofluvial-paleolacustrine systems at Moa Valles, Mars, *J. Geophys. Res. Plan*ets, *121*, 194–232, doi:10.1002/2015JE004891.

Schon, S. C., J. W. Head and C. I Fassett (2012), An overfilled lacustrine system and progradational delta in Jezero crater, Mars: Implications for Noachian climate, *Planet. Space Sci*. 67, 28–45.

Schultz, P. H. and F. E. Ingerson (1973), Martian lineaments from Mariner 6 and 7 images, *J. Geophys. Res.*, *78*(35), 8415–8427, doi:10.1029/JB078i035p08415.

Schultz, P. H., R. A. Schultz and J. Rogers (1982), The structure and evolution of ancient impact basins on Mars, *J. Geophys. Res.*, *87*, 9803–9820.

Scott, D. H. and K. L. Tanaka (1986), Geologic map of the western equatorial region of Mars: U.S. Geological Survey Miscellaneous Investigations Series Map I–1802–A, scale 1:15,000,000.

Seelos, F. P., M. F. Morgan, H. W. Taylor, S. L. Murchie, D. C. Humm, K. D. Seelos, O. S. Barnouin, C. E. Viviano, and CRISM Team (2012), CRISM Map Projected Targeted Reduced Data Records (MTRDRs) – High level analysis and visualization data products, in Planetary Data: A Workshop for Users and Software Developers, U.S. Geological Survey, Reston, Va.

Sharp, R. P. and M. C. Malin (1975), Channels on Mars, *Geol. Soc. Am. Bull.*, 86, 593-609.

Smith, D. E. et al. (1999), The global topography of Mars and implications for surface evolution, *Science*, *284*, 1495-1503.

Tanaka, K. L., J. A. Skinner and T. M. Hare (2011), Planetary Geologic Mapping Handbook, 24 pp., U.S. Geological Survey, Flagstaff, AZ.

Tanaka, K. L., J. A. Skinner, Jr., J. M. Dohm, R. P. Irwin III, E. J. Kolb, C. M. Fortezzo, T. Platz, G. G. Michael, and T. Hare (2014), Geologic map of Mars, USGS Scientific Investigations Map 3292.

Warner, N., S. Gupta, S.-Y. Lin, J.-R. Kim, J.-P. Muller, and J. Morley (2010a), Late Noachian to Hesperian climate change on Mars: Evidence of episodic warming from

transient crater lakes near Ares Vallis, *J. Geophys. Res*., *115*, E06013, doi:10.1029/2009JE003522.

Warner, N., S. Gupta, J.-R. Kim, S.-Y. Lin, and J.-P. Muller (2010b), Hesperian equatorial thermokarst lakes in Ares Vallis as evidence for transient warm conditions on Mars, *Geology*, 38*(1)*, 71, doi:10.1130/G30579.1.

Wilson, S. A., J. A. Grant and A. D. Howard (2013), Inventory of equatorial alluvial fans and deltas on Mars, *Lunar and Planet. Sci. Conf*., Abstract 2710.

Wilson, S. A. and J. A. Grant (2016a), Geologic mapping in Margaritifer Terra on Mars and a closer look at the confluence of Nirgal and Uzboi Valles, *47th Lunar and Planetary Science Conference*, Abstract 2505, Houston, TX.

Wilson, S. A. and J. A. Grant (2016b), Geologic Mapping in Southern Margaritifer Terra on Mars: Constraining the Timing of Fluvial Activity in Nirgal Vallis, *Annual Planetary Geologic Mappers Meeting*, Abstract 7034, Flagstaff, AZ.

Wilson, S. A. and J. A. Grant (2016c), Evidence for Late Hesperian fluvial activity in Nirgal Vallis on Mars, *Geol. Soc. of America Abstracts with Programs*, Abstract 283852, Denver, CO, September 24-28.

Wilson, S. A., A. D. Howard, J. M. Moore, and J. A. Grant (2007), Geomorphic and stratigraphic analysis of Crater Terby and layered deposits north of Hellas basin, Mars, *J. Geophys. Res*., *112*, E08009, doi:10.1029/2006JE002830.

Wilson, S. A., A. D. Howard, J. M. Moore, and J. A. Grant (2016), A cold-wet middle-latitude environment on Mars during the Hesperian-Amazonian transition: Evidence from northern Arabia valleys and paleolakes, *J. Geophys. Res. Planets*, *121*, 1667–1694, doi:10.1002/ 2016JE005052.

Wilson, S. A., J. A. Grant and D. L. Buczkowski (2017a), The evolution of Nirgal Vallis, Mars, *48th Lunar and Planetary Science Conference*, Houston, TX, Abstract 2663.

Wilson, S. A., J. A. Grant and D. L. Buczkowski (2017b), Geologic mapping in Southern Margaritifer Terra and the evolution of Nirgal Vallis on Mars, *Annual Planetary Geologic Mappers Meeting*, Flagstaff, AZ.

CHAPTER 5. Distal Aqueous-Rich Ejecta Deposits from Hale Crater

Abstract

Hale crater (125 km by 150 km-diameter, 35.69ºS, 323.64ºE) formed in the Early to Middle Amazonian and is one of the best preserved large craters on Mars. We focus on emplacement of the previously mapped and more mobile distal continuous ejecta as well as newly recognized discontinuous distal ejecta deposits that extend up to 450 km northeast of Hale. Where examined, the distal continuous ejecta deposits are up to 10s of meters thick, but two large craters east of Hale are mostly filled. The deposits were likely water-rich and subsequent dewatering of some deposits resulted in flow along gradients of 10m/km for distances of 10s of km, possibly reaching Uzboi Vallis. The discontinuous distal ejecta are typically <10 m thick with volumes generally <0.5 km^3 and embay Hale secondaries, which occur up to ~600 km from the Hale rim. Both continuous and discontinuous distal ejecta deposits are typically smooth at scales of tens to hundreds of meters, relatively dark-toned, devoid of superposing eolian bedforms, inferred to be mostly fine-grained and were likely emplaced within hours to a day or two after the Hale impact. The occurrence of well-preserved discontinuous distal ejecta at Hale is unusual compared to other similar sized Martian craters and could be the result of impact into an ice-rich substrate that enabled their formation and (or) their survival after only limited post-impact degradation relative to older craters. The remarkably pristine nature of distal continuous and discontinuous distal deposits at Hale and the widespread preservation of associated secondaries imply 1) erosion rates were low after the Hale impact and comparable to those estimated elsewhere during the Amazonian; 2) the impact did not significantly influence

global or regional scale geomorphic activity or climate; and 3) the Hale impact occurred after late alluvial fan activity in southern Margaritifer Terra.

5.1   Introduction

Impact craters are the most widely occurring and common landform on Mars, ranging in size from meter-scale structures observed *in situ* in Meridiani Planum (*Golombek et al*., 2010) to the enormous ~2300 km-diameter Hellas basin impact structure (*Tanaka et al*., 2014). Craters form during the collision of both primary and secondary impactors (*Melosh*, 1989) and take on a range of primary and erosional morphologies, both in terms of their interior structure (e.g., *Carr*, 2006), surrounding ejecta deposits (e.g., *Mouginis-Mark*, 1979; *Schultz and Gault,* 1990*; Grant and Shultz*, 1993; *Barlow*, 2005; *Kadish et al*., 2008), and overall shape (e.g., *Schultz and Lutz-Garihan*, 1982). The target properties of the surface (e.g., subsurface volatiles) may influence the morphological form of craters (e.g., *Barlow and Perez*, 2003) and recent investigations suggest the geomorphic effects of large impacts (craters >100 km in diameter) may extend far beyond the limit of the ejecta deposits in some instances (e.g., *Schultz and Wrobel*, 2012).

Very large impacts likely influenced the past Martian climate (e.g., *Segura et al*., 2002) but the link between the formation of large (>100 km in diameter) post-Noachian craters and sustained global or regional geomorphic activity in the Hesperian and Amazonian is less certain (*Irwin*, 2013). Some studies suggest post-Noachian impact cratering may cause regional fluvial activity, either directly by melting ice in the subsurface (e.g., *Mangold*, 2012; *Mangold et al*., 2012), or indirectly by injecting water vapor into the atmosphere resulting in regional snow accumulation and subsequent melting (*Kite et al*., 2011). The

Amazonian-aged Hale crater provides a unique opportunity to characterize the nature and distribution of the impact deposits to constrain the magnitude and duration of geomorphic activity triggered by large impacts, thereby providing insight into the post-Noachian climate, environmental conditions, and degradational history of Mars.

5.2   Background

Hale crater is a 125 km by 150 km-diameter oblong impact structure on the northern margin of the larger Argyre basin in Nereidum Montes (centered at 35.69ºS, 323.64ºE, Fig. 5.1). The crater formed during an oblique impact (*Schultz and Wrobel*, 2012) into water-ice-rich target materials (~10% ice by volume, see *Jones et al.,* 2011; *El-Maarry et al.,* 2013) during the Early to Middle Amazonian (*Cabrol et al.*, 2001; *Jones et al.*, 2011). Hale is one of the best preserved large craters on Mars and the continuous ejecta deposits were mapped by *Jones et al.*, (2011) into two units: a more proximal, rougher unit (He1) and a more distal, smoother, thinner unit (He2). The He1 unit was interpreted as a combination of ballistic and ground-hugging ejecta, whereas He2 occurs as a thinner, more mobile unit that "emanates" from He1 and extends for more than a crater diameter to both the northeast and southwest before grading into the surrounding terrain (Fig. 5.2). Based on this description, emplacement of the He1 unit would largely precede the He2 unit and is roughly consistent with the sequence described for ejecta emplacement at Bamburg crater on Mars (*Mouginis-Mark*, 1979).

A number of channels are sourced from He1 and continue into He2. In many locations, these ejecta units show evidence of incision and ponding of material as a result of secondary flow of ejecta mixed with water-ice-rich basin materials that were excavated and melted during crater formation (*Jones et al.*, 2011; *El-Maarry et al.*, 2013) (Fig. 5.3).

Dewatering of some of the He2 deposits described by *El-Maarry et al*. (2013) and *Jones et al*. (2011) quantify the resultant flows as slurries of slushy water-rich (>40%) debris.
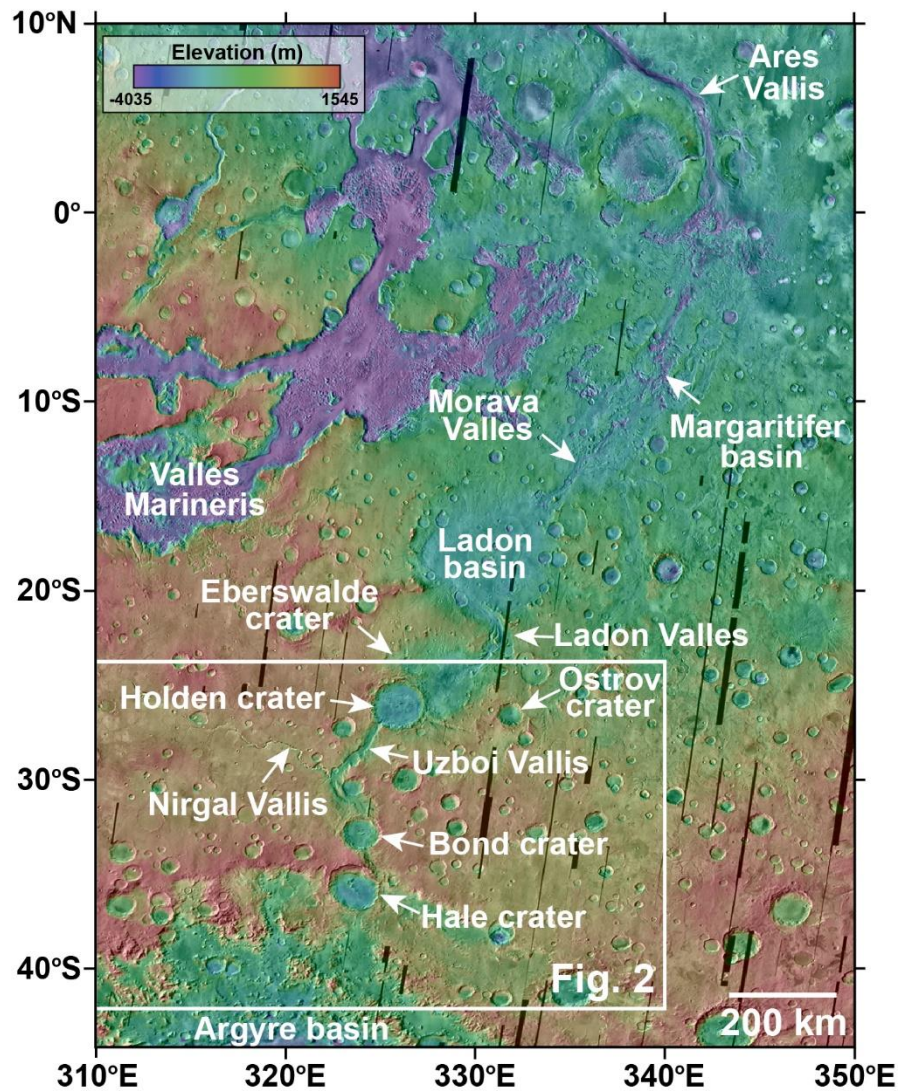
Figure 5.1 Southern Margaritifer Terra region

The Hale impact crater is located on the northern rim of Argyre basin just south of Margaritifer Terra. The once through-flowing Uzboi-Ladon-Morava meso-scale outflow system was interrupted by the formation of Hale, Bond, and Holden craters. Box shows location of Fig. 5.2. MOLA over subframe of global THEMIS daytime IR mosaic. North towards the top. Modified from *Grant et al*. (2011).
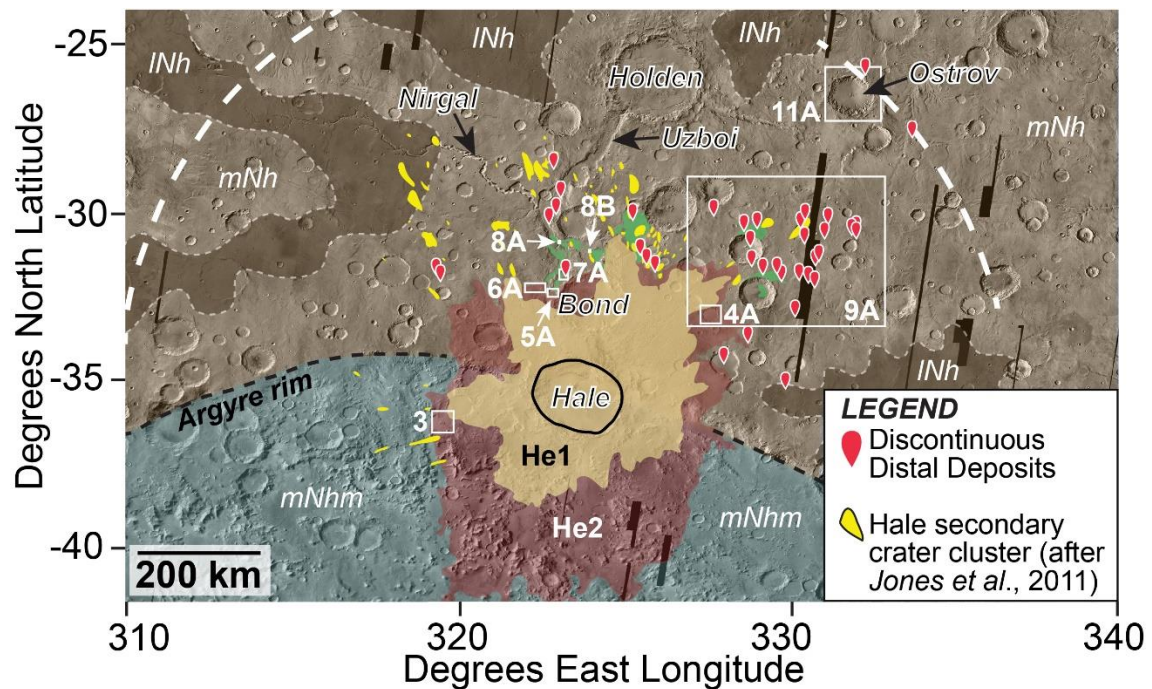
Figure 5.2   Hale related ejecta and associated deposits

Hale related ejecta and associated deposits (see Fig. 5.1 for context). Continuous Hale ejecta mapped as proximal (He1) and distal (He2) after *Jones et al*. (2011) extends ~275 km from Hale's northeastern rim. Major secondary crater clusters (yellow) occur up to ~435 km from Hale's northwestern rim (after *Jones et al*., 2011). Discontinuous distal Hale deposits identified in this study (e.g., red pins) as well as deposits and channels derived from the continuous (He2) Hale ejecta north and east of crater Bond (e.g., green units after *Wilson and Grant,* 2016) occur as far as 450 km from the northeastern rim of Hale. The discontinuous distal deposits correlate well to the location and extent of the wind streaks (white dashed line) that resulted from the Hale blast (*Shultz and Wrobel*, 2012). The late Noachian highland unit (lNh), middle Noachian highland unit (mNh), and middle Noachian highland massif unit (mNhm) are geologic units modified after *Tanaka et al*. (2014). Black dashed line shows approximate rim of Argyre. Boxes show location of Figs. 5.3, 5.4A, 5.5A, 5.6A, 5.7A, 5.8A, 5.8B, 5.9A and 5.11A. Subframe of global THEMIS daytime IR mosaic, gaps in data are filled with black. North towards the top.
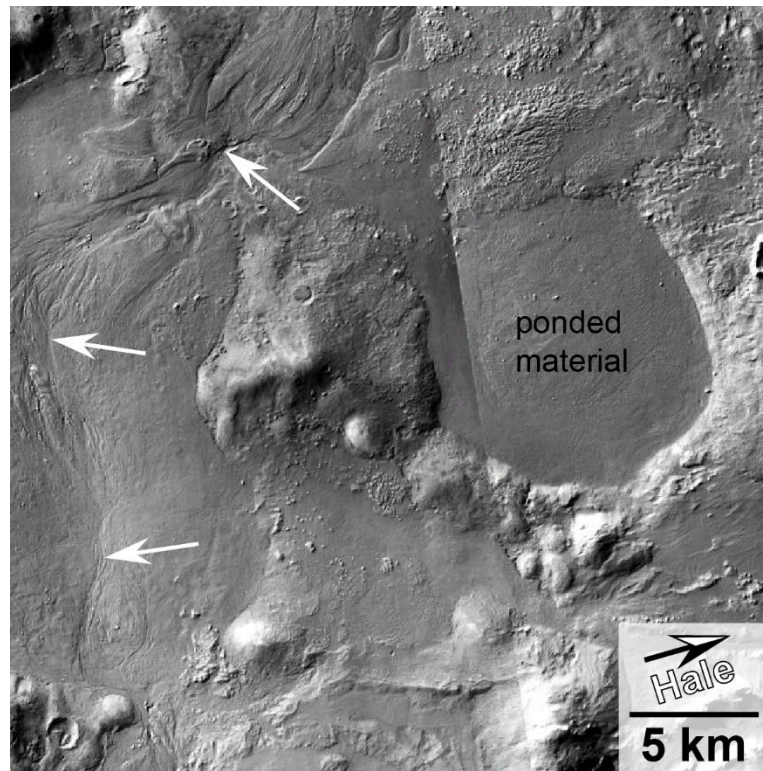
Figure 5.3   Nature of the distal continuous ejecta west of Hale

Incision (arrows) and deposition (e.g., "ponded material") related to the fluidized flows associated with Hale's distal continuous (He2) ejecta (near 36.4°S, 319.6°E, see Fig. 5.2 for context). Black and white arrow indicates direction to center of Hale crater. Subframe of CTX P22_009749_1456 and P15_007099_1434 (~5.2 m scaled pixel width). North towards the top.

Mapping in and near USGS Mars Transverse Mercator quadrangles -30037 and -30032 to the north and northeast of Hale (e.g., *Schultz and Wrobel*, 2012; *Wilson and Grant*, 2014, 2016; *Wilson et al.,* 2015; *Grant and Wilson*, 2016) reveals possibly thicker accumulations of continuous ejecta ponded within craters as well as accumulations of He2 ejecta located downstream of local topographic obstructions that appear to have dewatered (*El-Maarry et al*., 2013) with subsequent drainage to the north.

A suite of Hale-related features and landforms is also recognized well beyond the distal continuous ejecta mapped by *Jones et al.* (2011) (Fig. 5.2). These include previously mapped wind streaks (*Jones et al.*, 2011; *Schultz and Wrobel*, 2012), irregular clusters of secondary craters (*Jones et al.*, 2011; *El-Maarry et al.*, 2013), and newly identified discontinuous distal deposits inferred to have flowed upon emplacement. These discontinuous distal deposits are likely the furthest occurrences of Hale ejecta and their morphology and preservation can directly inform the local geomorphic effects of the Hale impact. This investigation characterizes the emplacement and nature of some of the He2 distal continuous deposits as well as the more distal, discontinuous deposits to understand the extent and duration of any regional enhanced geomorphic activity that resulted from (or was sustained by) the Hale impact.

5.3   Methods and Data

Mapping in ArcGIS utilized a variety of datasets including the global nighttime and daytime infrared mosaics from the Thermal Emission Imaging System (THEMIS, ~100 m per pixel resolution) (*Christensen et al.*, 2004), topographic data from the Mars Orbiter Laser Altimeter (MOLA, 128 pixel per degree resolution) (*Smith et al.*, 1999), high resolution images from the Mars Context Camera (CTX, ~6 m pixel resolution) (*Malin et al.*, 2007), and the High Resolution Imaging Science Experiment (HiRISE, ~0.25 m pixel resolution) (*McEwen et al.*, 2007). In addition, the web-based Geographic Information Systems application MarsSI (MARS Système d'Information) was used to generate 2 CTX Digital Terrain Models (DTMs). ArcScene was used for three dimensional renderings of CTX DTMs.

CTX images up to ~600 km to the north, northwest and northeast of Hale were systematically searched for discontinuous distal Hale ejecta deposits (Fig. 5.2). The region to the northeast of Hale is presented in this study as a type locality because of the high concentration of discontinuous distal deposits although similar deposits also occur to the north and northwest and perhaps elsewhere around the crater.

5.4   Occurrence and Morphology of the Hale-Related Features and Deposits

5.4.1   Thick Accumulations of Distal Continuous (He2) Ejecta Deposits

Accumulations of distal continuous (He2) ejecta are observed partially filling an unnamed 22 km-diameter crater located ~170 km to the east-northeast of Hale (*Jones et al.*, 2011) (Fig. 5.4) and an unnamed 44 km-diameter crater roughly 60 km to its south, approximately ~130 km to the east-northeast of Hale (see Fig. 5.2 for context). Both craters have degraded rims with evidence of breaches related to past incision. The He2 deposits within the craters are sometimes bound by low, outward facing scarps near crater walls, but appear to merge smoothly with walls in other locations (Fig. 5.4). The surfaces of the deposits are fairly smooth at 100-meter length scales, but are marked by small (meters to ~20 m across), irregularly spaced mounds (Fig. 5.4B). Subtle lineations on the surface bears evidence that the material in these craters once flowed (Fig. 5.4A).

The 22 km-diameter crater is currently ~200 m deep (Fig. 5.4), whereas the 44 km-diameter crater is currently ~750 m deep. Various crater diameter-to-depth relationships (e.g., summarized in *Grant et al.*, 2015) predict original depths of 1.5-2.2 km and 2-4 km for the 22 km- and 44 km-diameter craters, respectively, yet the current depths are only ~10% and 20-30% of that. The amount of pre-Hale infilling is unknown, and therefore it is possible that pre-Hale degradation destroyed the crater rim and resulted in nearly complete

infilling to the level seen today. However, the valley entering the northeast corner of the 22-km diameter crater is graded to a level below what is at least 10s of m of backfilling by He2 deposits and all topography on the floor of both craters is completely buried by the deposits (Fig. 5.4). Nearby craters lacking Hale materials are not as shallow, suggesting Hale contributions to the crater infilling were significant. Hence, at least 10s of meters to perhaps up to a km or more of Hale-related fill may be present in one or both craters. This equates to 10s of km^3 at a minimum if the deposits are only 10s of meters thick to perhaps 100-200 km^3 or more for considerably thicker He2 infill in the 44 km-diameter crater.
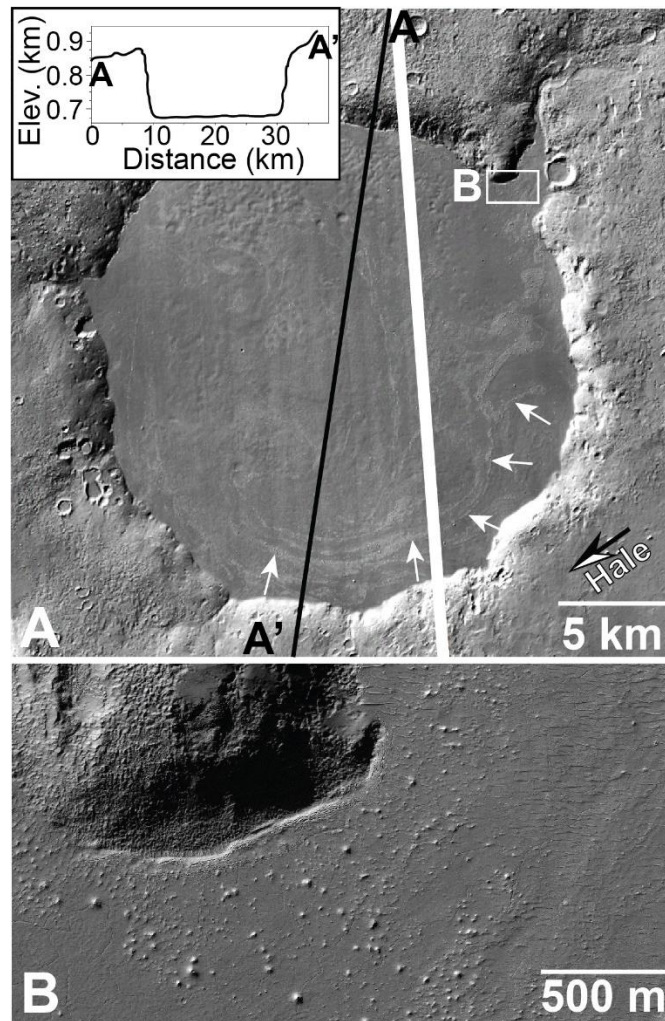
Figure 5.4   Nature of the distal continuous ejecta northeast of Hale

A) A 22 km-diameter crater ~170 km northeast of Hale (see Fig. 5.2 for context) is filled with distal continuous (He2) Hale ejecta. Black line shows transect A to A' from MOLA profile 8582 with corresponding profile in inset. Subtle surface lineations (white arrows) are consistent with evidence of flow. Black and white arrow indicates direction to center of Hale crater. Box shows location of (B). Subframes of CTX B19_017133_1471 and B18_016777_1461 (5.1 m scaled pixel width), gap in data is filled with white. **B)** Surface of the crater fill contains meter-scale relief but is smooth at length scales of 10s to 100s of meters. Subframe of HiRISE ESP_034908_1465 (51 cm scaled pixel width). North towards the top in both images.

The surface of He2 ejecta deposits outside of craters are varied and include locations where the fluidized debris incises and ponds (*Jones et al*., 2011; *El-Maarry et al*., 2013). Water-related features associated with the ejecta mapped by *Jones et al.* (2011) occur up to ~200 km north of the Hale crater rim, often emerging from thicker He1 ejecta accumulations that occur downstream of topographic constrictions (Figs. 5.5 and 5.6A). Locally, these thicker deposits form lobes of He2 ejecta up to 20-50 m thick that are capped by ridges approximately perpendicular to the flow direction (Figs. 5.5 and 5.6) and are bound by digitate margins (Fig. 5.5). The surfaces of these thicker accumulations are commonly fractured (Fig. 5.6F) and, in places, erosion has isolated small segments of the digitate margin with minimal debris remaining as evidence of a past connection to the main deposit (Fig. 5.5C).
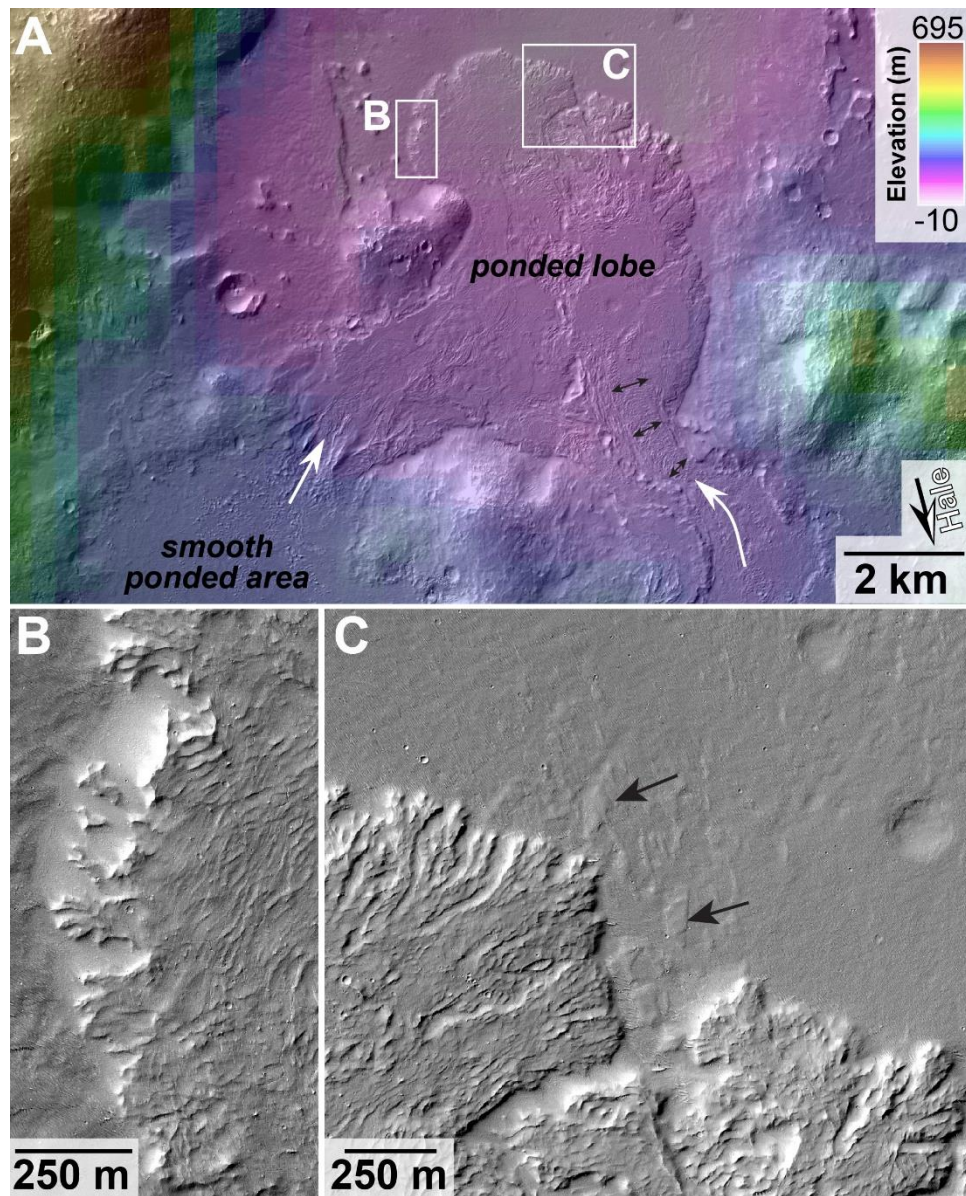
Figure 5.5   Nature of a ponded fluidized debris lobe from distal continuous Hale ejecta

A) Distal continuous (He2) ejecta from Hale west of crater Bond (see Fig. 5.2 for context) Material ponded to south and flowed (white arrows) into low-lying topography forming a large, ponded debris lobe.   Linear ridges (between black arrows) on lobe surface are perpendicular to flow direction (white arrow). Ponded lobe has distinct margins and is ~20-50 m thick at the northern edge. Black and white arrow indicates direction to center of Hale crater. Boxes show location of (B) and (C).   MOLA over subframe of CTX B22_018254_1472 (5.2 m scaled pixel width). North towards the top in all images. **B)** Local erosion of digitate distal margins produces minimal blocky debris that implies a significant fine-grained component. Subframe of HiRISE PSP_008259_1470 (50 cm scaled pixel width).   **C)** Valleys emerging from the margin of the lobe and associated

streamlined forms (e.g., arrows) along the surface beyond the lobes indicates possible de-watering of the deposit along its margin. Subframe of HiRISE PSP_008259_1470 (50 cm scaled pixel width).
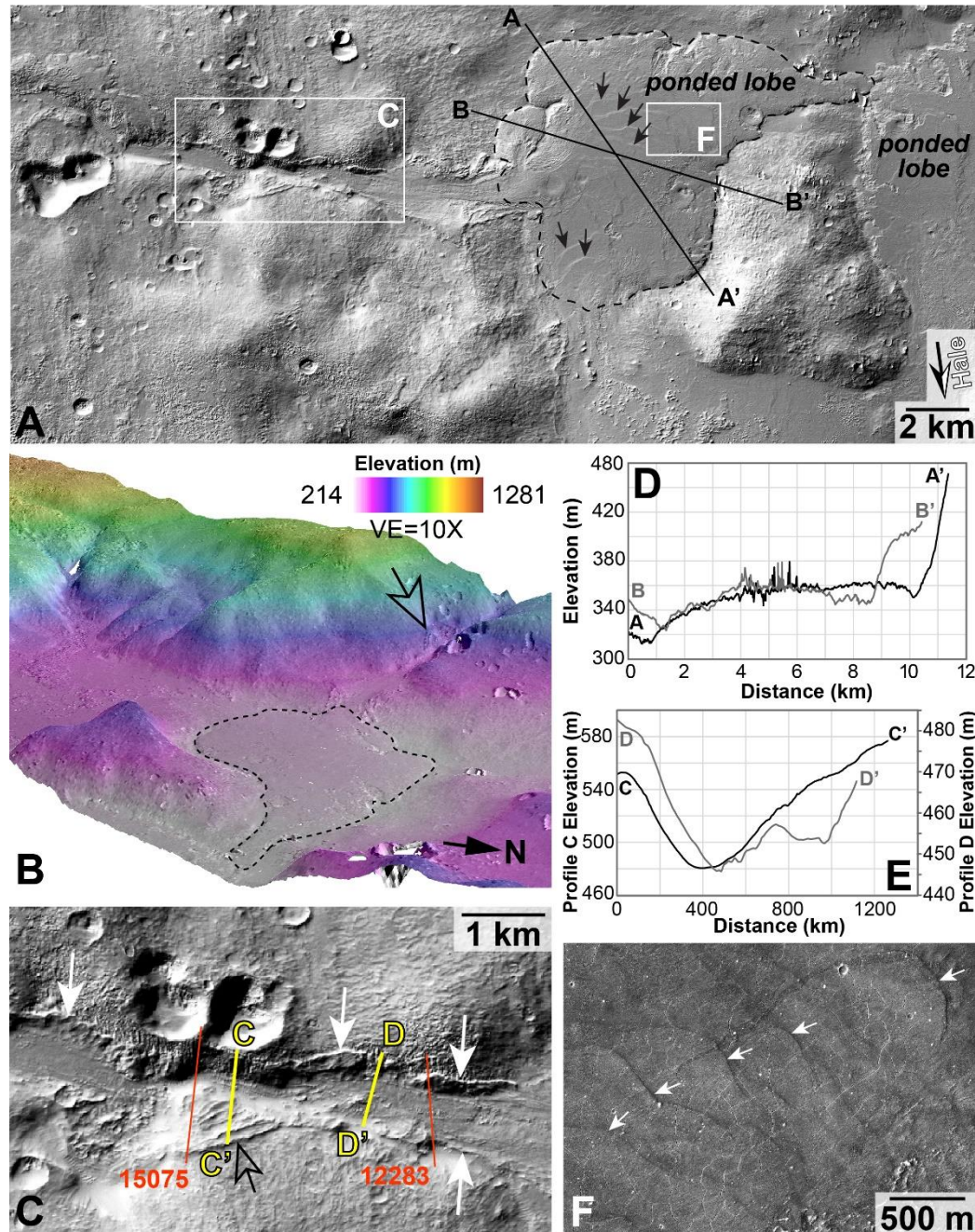
**Figure 5.6**   Fluidized debris flows through channel and forms lobe

A) Distal continuous (He2) ejecta west of crater Bond, (~ 25 km northwest of Fig. 5.5, see Fig. 5.2 for context). Ejecta flowed through a confined channel and formed a ponded lobe with an area of ~63.5 km² (dashed line). Multiple arcuate ridges (arrows) on the surface of

the deposit suggest emplacement occurred in several surges. Transects A and B (black lines) were used to estimate deposit thickness (see profiles in D). Black and white arrow indicates direction to center of Hale crater. Boxes show location of (C) and (F). Subframe of CTX image F01_036161_1466 (~6 m scaled pixel width). North towards the top. **B)** Three dimensional rendering of ponded lobe (dashed line) in (A) looking southwest with a vertical exaggeration (VE) of 10X. Ejecta flowed through the channel and accumulated in a local topographic low. Hollow arrow points to run-up deposit preserved on southern valley wall used to estimate the flow dynamics of emplacement (see hollow arrow in C and Section 4.7). CTX DTM from P21_0090250_1472 and F01_036161_1466. **C)** Detail of channel that confined the flow (see (A) for context) with high-stands of the flow preserved on valley walls (arrows) caused by a constriction and downstream bend in the channel. Hollow arrow indicates a run-up of material on the valley wall (B). Location of transects C and D used to estimate flow velocity based on topography from the CTX DTM (B) are indicated (profiles in E). Topography from segments of MOLA tracks 15075 and 12283 (red lines) across the channel provide consistent results (MOLA track 19243 is in the same location as transect 'D'). Subframe of CTX F01_036161_1466 (~6 m scaled pixel width). North towards the top. **D)** Thickness of the ponded lobe is ~ 20m to 40m based on example profiles across the deposit (using topography from the CTX DTM in B, see (A) for context). **E)** Profiles of transects C and D from the CTX DTM used to estimate local run-up heights to constrain the velocity and duration of flow. **F)** The surface of the ponded lobe has numerous polygonal cracks and the arcuate ridges (arrows) are consistent with the flow to the east-northeast (see (A) for context). A few bright blocks have been incorporated into the surface of the lobe. Subframe of HiRISE PSP_004053_1475 (25 cm scaled pixel width).

5.4.2   Evidence for De-watering of Distal Continuous (He2) Ejecta Deposits

Features downstream from the thicker lobes (e.g., Fig. 5.5) occur mostly as relatively dark-toned incisional landforms (Fig. 5.7). The transition to channelized forms with increasing distance from Hale can be subtle and sometimes occur where streamlined forms emerge from between the digitate margins of thicker lobes and continue further to the north (Fig. 5.5C). Incised surfaces are discontinuous, follow topography, and are interrupted by surfaces where evidence of past flow is poor or small depositional forms occur in local lows (e.g., where emerging from small craters, Fig. 5.7C). Some reaches just west of Bond crater are up to ~100 km long and characterized by average gradients of only 10 m/km and channels within them may extend to the upper reaches of Uzboi Vallis (Figs. 5.2 and 5.8).

Local occurrences of darker-toned, smooth materials with distinct margins are observed on the floor of Uzboi below the entry of tributaries inferred to have been modified by drainage from the distal Hale deposits (Fig. 5.8A). These putative distal Hale deposits in Uzboi are topped by transverse aeolian ridges (Fig. 5.8A), thereby making them somewhat distinct from the deposits mapped elsewhere to the north and northeast of Hale. In another location just upstream of a constriction in an Uzboi tributary channel, materials appear to form elongated bedforms oriented across local slopes (Fig. 5.8B).
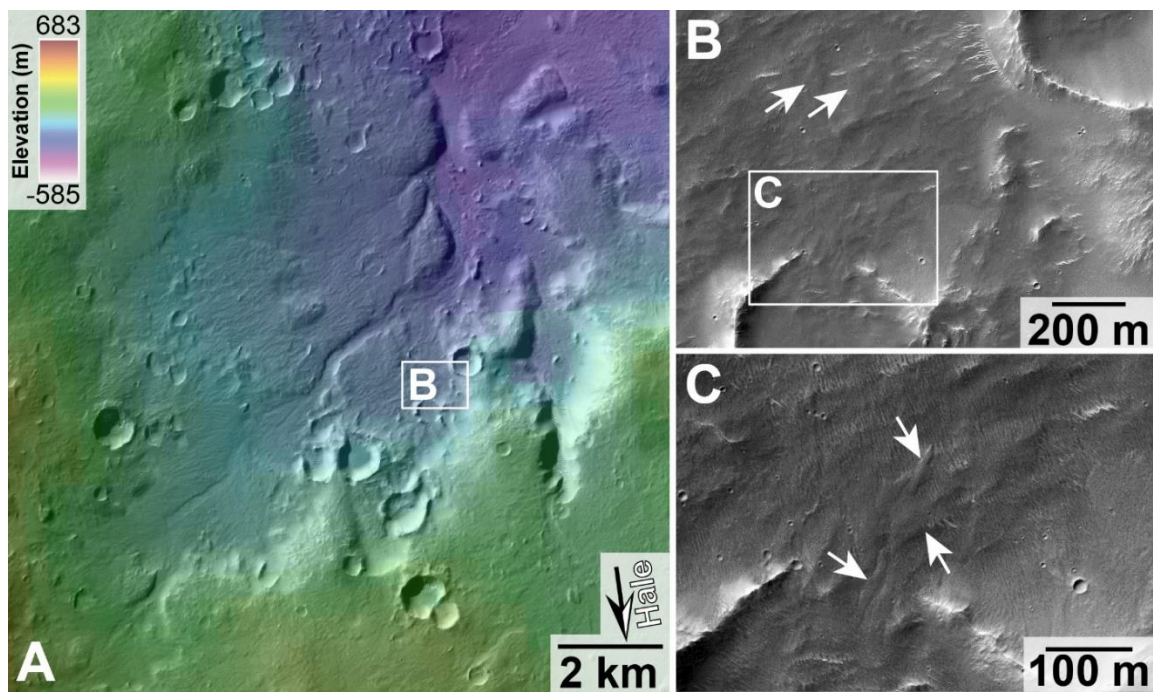
Figure 5.7   Possible de-watering of fluidized lobes of distal continuous ejecta

A) Fluidized lobes of the distal continuous (He2) ejecta west of crater Bond (e.g., Fig. 5.5) may have de-watered, depositing dark-toned material further north toward Uzboi Vallis (see Fig. 5.2 for context). Black and white arrow indicates direction to center of Hale crater. Box shows location of (B). MOLA over subframe of CTX P20_008694_1480 (5.3 m scaled pixel width). North towards the top in all images. **B)** Detail of dark-toned deposits adjacent to incised valleys west of crater Bond, some of which may have superposed lighter-toned transverse aeolian ridges (e.g., arrows). Subframe of ESP_042227_1480 (25 cm scaled pixel width). Box shows location of (C). **C)** Dark-toned deposits with lobes and possible incised channels on deposit surface (arrows). Subframe of ESP_042227_1480 (25 cm scaled pixel width).

177
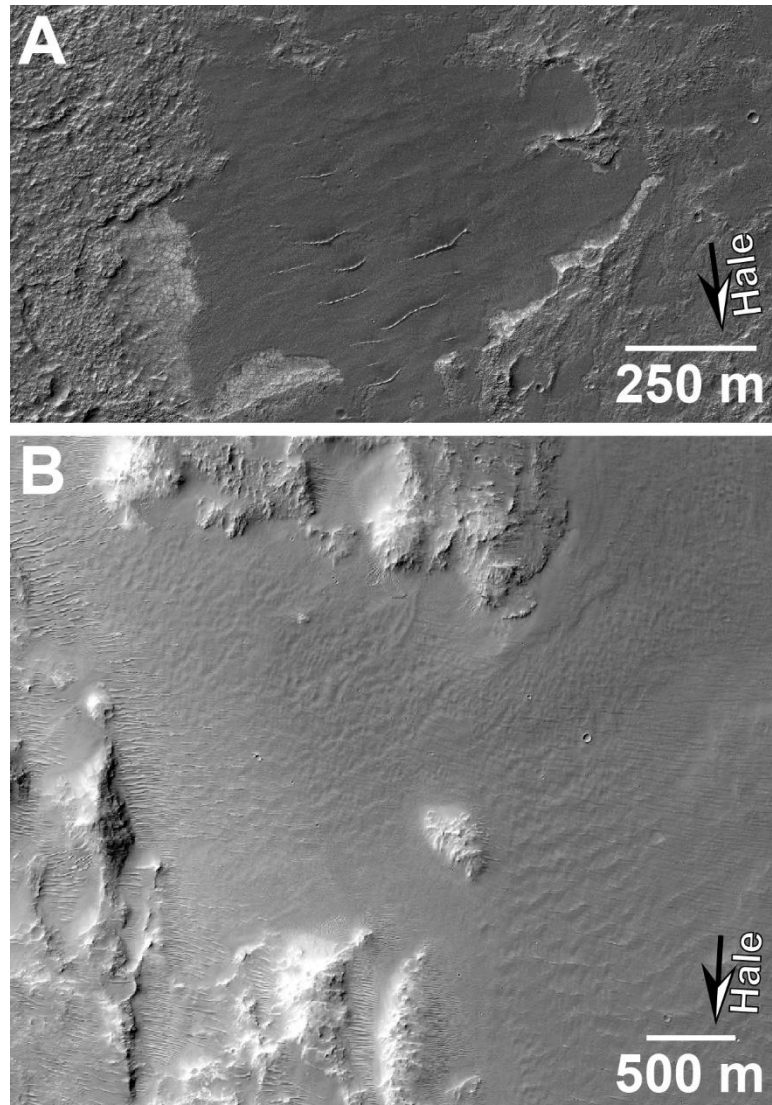
Figure 5.8   Possible Hale deposits in Uzboi Vallis

Possible deposits in Uzboi Vallis (see Fig. 5.2 for context) related to de-watering of distal continuous (He2) ejecta lobes to the south (Fig. 5.5). Black and white arrows indicate direction to center of Hale crater. North towards the top in both images. **A)** Smooth, dark-toned deposit on floor of Uzboi Vallis that embays topographic lows, forms distinct margins, and has apparent superposing transverse eolian ridges. At mouth of Uzboi tributary north of crater Bond near 31ºS, 323ºE. Subframe of HiRISE ESP_034328_1485 (~26 cm scaled pixel width). **B)** Possible bedforms on the floor of Uzboi Vallis near the outlet of the tributary basin near 31.3°S, 324°E. If aqueous in origin, these bedforms suggest appreciable discharge was associated with their formation. Subframe of HiRISE ESP_015920_1485 (52 cm scaled pixel width). Modified from Fig. 5.13D of *Grant et al.* (2011).

5.4.3 Wind Streaks and Secondary Craters

To the northeast and northwest of Hale, prominent wind streaks are visible in THEMIS nighttime images up to ~600 km radially from the crater (*Jones et al.*, 2011) and are interpreted to be related to the impact (*Schultz and Wrobel*, 2012) (Figs. 5.2 and 5.9A). In addition, secondary craters associated with Hale crater are widespread throughout the region and occur in both compact and irregular to elongated clusters (Fig. 5.2, *Jones et al.*, 2011), generally aligned with the orientation of impact-related wind streaks (*Jones et al.*, 2011; *Schultz and Wrobel*, 2012). Individual secondaries are up to 100s of meters across, typically retain raised rims, and are circular to somewhat irregular in plan view (e.g., Figs. 5.9D-F, 5.10B, C, and F, 5.11B-C). Hale secondary craters are observed in Ostrov crater more than 600 km beyond the rim of Hale (Fig. 5.11), but comparable examples of secondaries are not as obvious in Holden crater ~400 km north of Hale's rim (Fig. 5.2).

5.4.4 Discontinuous Distal Ejecta Deposits

Previously unrecognized discontinuous distal deposits have been identified beyond the limit of the distal continuous ejecta (He2) north of Hale, and their occurrence is associated with Hale-related wind streaks and secondary craters (Figs. 5.2 and 5.9A). The highest concentration of discontinuous distal deposits occurs northeast of Hale (Fig. 5.9A) and they have no direct connection to the continuous Hale ejecta mapped by *Jones et al.* (2011). The discontinuous deposits occur up to 450 km northeast of Hale (Figs. 5.9 and 5.10) and individual occurrences are up to 20-25 km long and oriented approximately radial to Hale, consistent with Hale-related wind streaks (*Schultz and Wrobel*, 2012) (Figs. 5.9 and 5.10). Deposits often originate on elevated surfaces (e.g., on the northeastern rims of craters) and flow downslope, sometimes forming shallow channels (Figs. 5.9 and 5.10). These distal

Hale deposits appear to mostly mantle rather than excavate the surface where they originate and are often channelized by topography to produce streamlined forms (Fig. 5.9C). The surface of the deposits are typically smooth at scales of tens to hundreds of meters, darker-toned relative to bounding materials, and largely devoid of eolian bedforms. The deposits always embay and never originate from Hale secondary craters when present. They have distinct, occasionally leveed lateral margins in medial to distal sections and terminate in both single and multi-lobate forms that lack terminal ramparts and often pool in low lying topography or pre-existing craters (Figs. 5.9 and 5.10). MOLA tracks crossing the deposits indicate they are often only meters up to ~10 m thick towards their downstream ends, but the elevation of the laterally bounding surfaces adjacent to the deposits are generally comparable and confirms the deposits form a thin veneer on the surface. The volume of most occurrences of the distal ejecta deposits is relatively small, with individual lobes typically representing ~0.5 km^3 or less material, much less relative to accumulations of He2 ejecta materials occurring within craters closer to Hale (Figs. 5.5 and 5.6).

THEMIS Nighttime IR data indicates the discontinuous distal deposits are generally darker-toned than their adjacent surfaces, but there are examples where they are brighter-toned (Fig. 5.12). Interestingly, Hale-related wind streaks northeast of a brighter-toned distal deposit are sometimes brighter than the discontinuous distal deposits themselves (*Schultz and Wrobel*, 2012) (Fig. 5.9A), thereby suggesting winds associated with their formation removed fines mantling the surface.
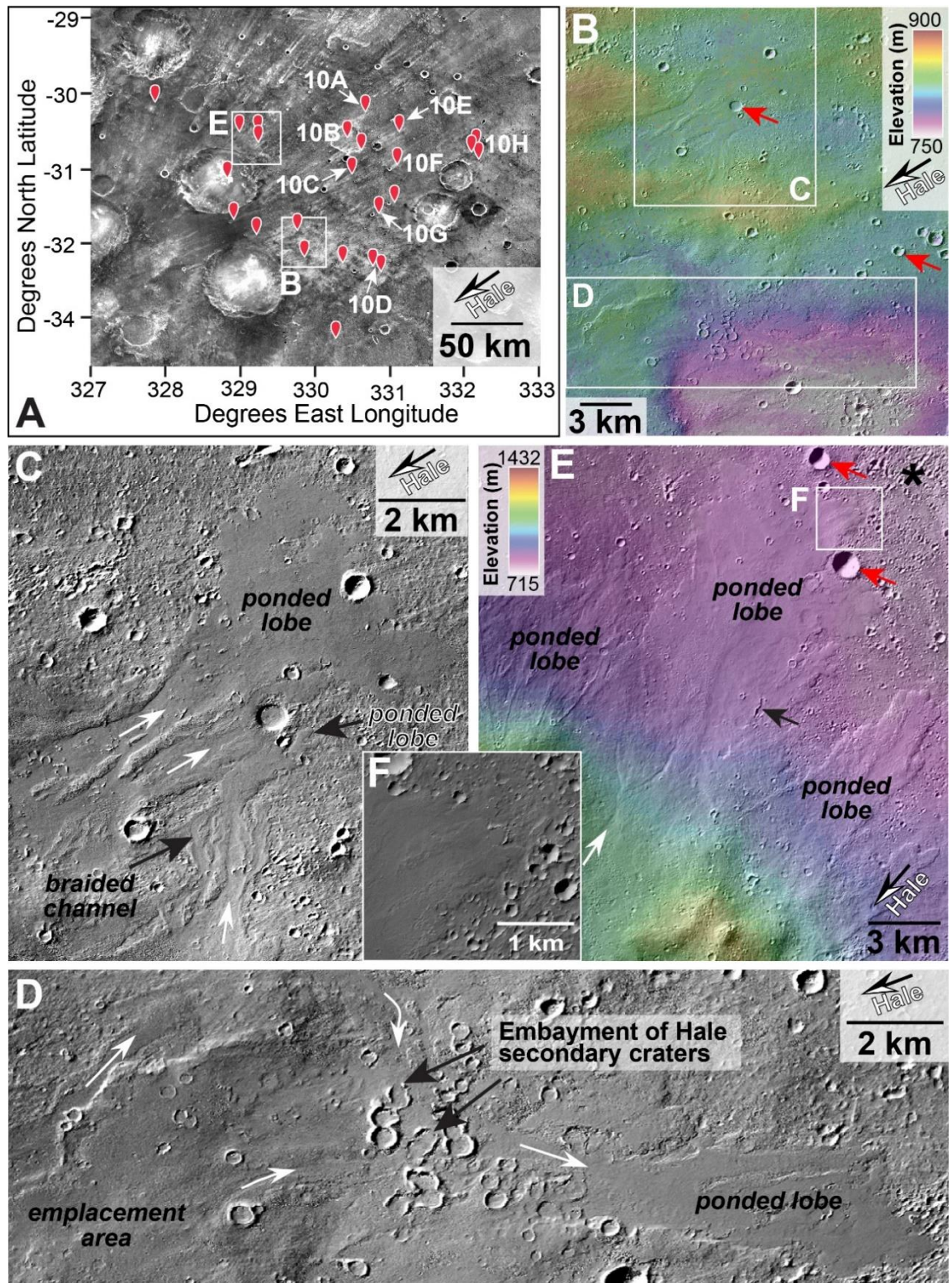
Figure 5.9 Distribution and nature of discontinuous distal deposits northeast of Hale
A) Distribution of discontinuous distal deposits (red pins) northeast of Hale (see Fig. 5.2 for context). Each pin represents a deposit, channel or cluster of such landforms. Wind

steaks from Hale impact blast are evident in THEMIS nighttime IR data (*Shultz and Wrobel*, 2012). Black and white arrow indicates direction to center of Hale crater. Boxes show location of (B) and (E); location of discontinuous distal deposits in Fig. 5.10A-H are indicated. **B)** Distal discontinuous deposits northeast of a 58 km-diameter crater, approximately 315 km NE of the rim of Hale crater (near 32.1°S, 329.8°E). Topography illustrates that deposits generally flow into and pond in low-lying terrain. See Fig. 5.12A-B for corresponding THEMIS data (red arrows mark same craters indicated in Fig. 5.12A). Boxes show location of (C) and (D). Black and white arrow indicates direction to center of Hale crater. Subframe of CTX DTM (F19_043097_1478 and G02_019124_1464, ~5.1 m scaled pixel width) over subframe of CTX G02_019124_1464. **C)** Detail of channels (white arrows) indicating flow to the northeast. Possible streamlined features within a braided channel (black arrow). Distal deposits are smooth and darker-toned relative to surrounding terrain, forming lobes with distinct margins. Black and white arrow indicates direction to center of Hale crater. Subframe of CTX G02_019124_1464 (5.12 m scaled pixel width). **D)** Detail of channels (white arrows) originating from higher-elevation emplacement areas. Material flowed and pooled in low-lying terrain, filling and embaying Hale secondary craters. Subframe of CTX G02_019124_1464 (5.12 m scaled pixel width). **E)** Distal discontinuous deposits northeast of a 51 km-diameter crater, approximately 350 km NE of the rim of Hale crater (near 30.5°S, 329°E). Channels form on higher gradient surfaces (white arrow) and flow downslope to form lobes that pond in adjacent low-lying terrain, commonly filling and embaying small secondary craters from Hale (e.g., black arrow; asterisk indicates a large field of Hale secondaries). See Fig. 5.12C-D for corresponding THEMIS data (red arrows mark same craters indicated in Fig. 5.12C). Box shows location of (F). Black and white arrow indicates direction to center of Hale crater. Subframe of CTX DTM (B21_017634_1501 and B19_017067_1458, ~5.1 m scaled pixel width) over subframe of CTX B21_017634_1501. **F)** Distal end of a smooth ponded lobe that fills and embays Hale secondary craters. Subframe of HiRISE ESP_043941_1490 (50 cm scaled pixel width). North to top in all images.
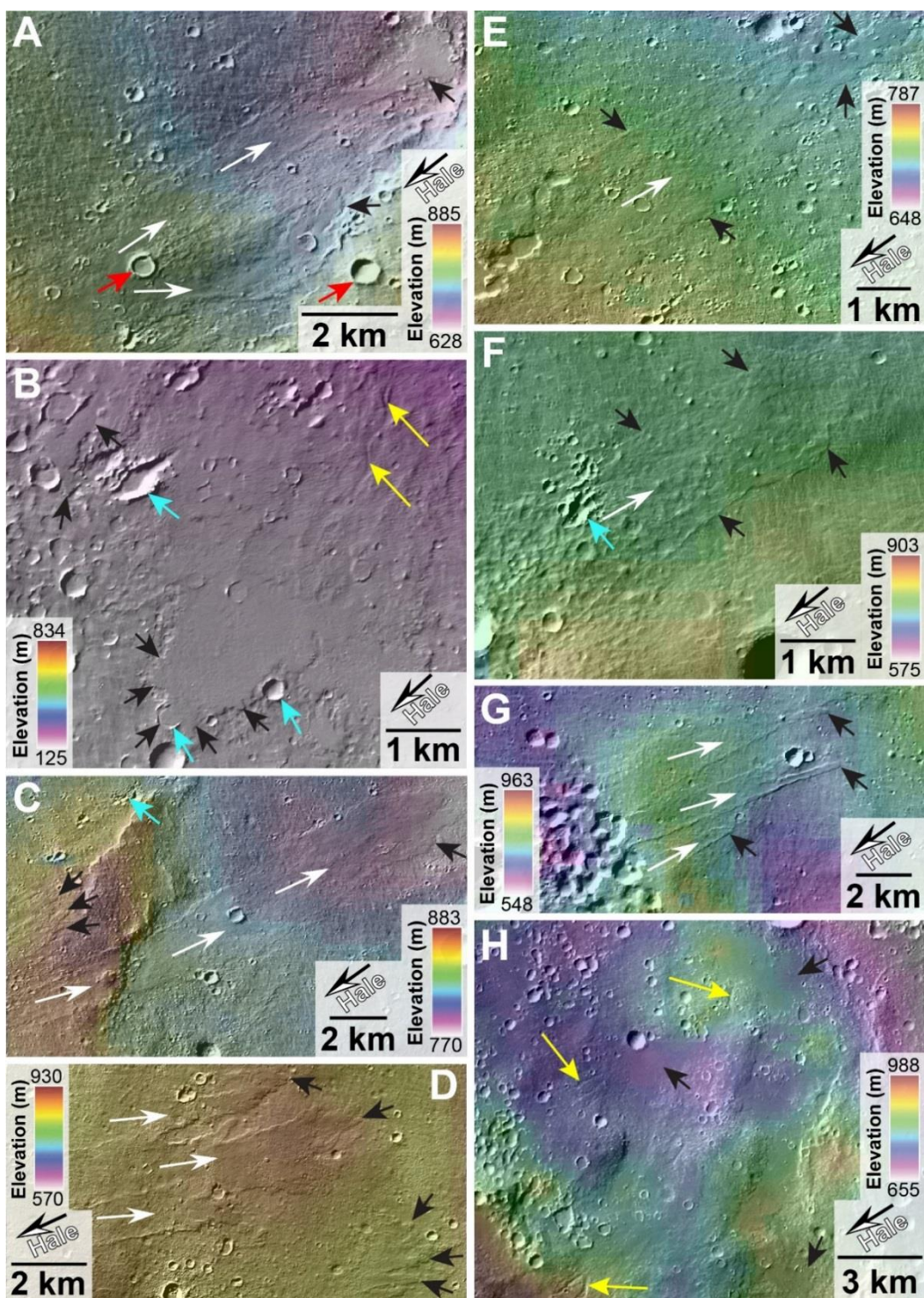
Figure 5.10   Discontinuous distal Hale-related deposits northeast of Hale crater

Examples of discontinuous distal Hale-related deposits northeast of Hale crater (see Fig. 5.9A for context). Ponded lobes and deposits have distinct margins (black arrows), tend to be smoother and darker than surrounding surfaces, and flow toward low-lying terrain. White arrows indicate flow direction, yellow arrows in (B) and (H) show source channels and aqua arrows in (B), (C), and (F) indicate likely Hale secondary craters. Black and white arrows indicate direction to center of Hale crater. MOLA over CTX (~5.1 m scaled pixel width). North towards the top in all images. **A)** Over 400 km NE of the northeastern rim of Hale crater. See Fig. 5.12E-F for corresponding THEMIS data (red arrows mark same craters indicated in Fig. 5.12E). Subframe of CTX B19_017212_1493 with image center near 30.3°S, 330.6°E. **B)** Approximately 380 km NE of the northeastern rim of Hale crater. Subframe of CTX G02_018913_1500 with image center near 30.6°S, 330.4°E. **C)** Roughly 370 km NE of the northeastern rim of Hale crater. Subframe of CTX G02_018913_1500 with image center near 31.2°S, 330.4°E. **D)** Approximately 340 km NE of the northeastern rim of Hale crater. Subframe of CTX B19_016856_1453 with image center near 32.4°S, 330.7°E. **E)** Extending ~412 km NE of the northeastern rim of Hale crater. Subframe of CTX G01_018702_1501 with image center near 30.6°S, 331°E. **F)** Approximately ~400 km NE of the northeastern rim of Hale crater. Subframe of CTX G01_018702_1501 with image center near 31°S, 331.1°E. **G)** Roughly 370 km NE of the northeastern rim of Hale crater. Subframe of CTX F18_042886_1481with image center near 31.6°S, 330.9°E. **H)** Nearly 450 km NE of the northeastern rim of Hale crater. Subframe of CTX P17_007494_1478 with image center near 30.8°S, 332.1°E.
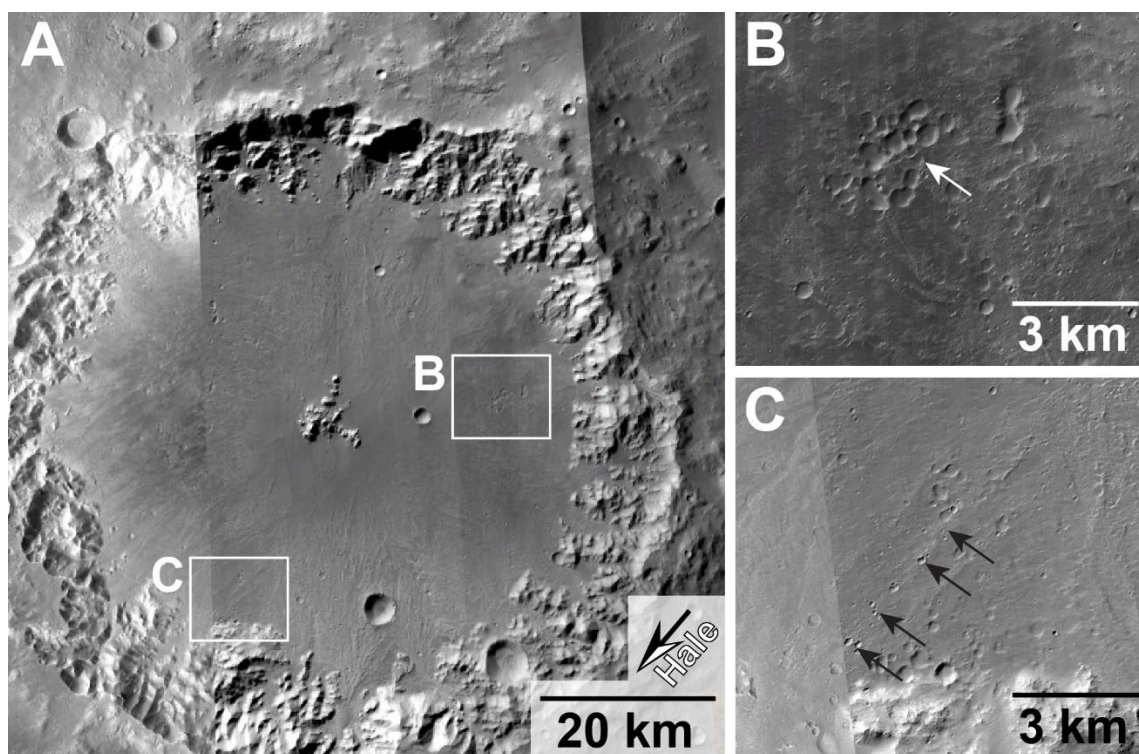
Figure 5.11   Alluvial fans and Hale secondary craters in Ostrov crater

Ostrov is a 73 km-diameter crater located ~600 km from the Hale rim (see Fig. 5.2 for context). Alluvial fan surfaces in Ostrov preserve secondary crater clusters from Hale. Black and white arrow indicates direction to center of Hale crater. Boxes show location of (B) and (C). North to top in all images. Subframes of CTX B10_013467_1526, B20_017357_1537, D20_035132_1527, G04_019770_1553. **B)**   Possible Hale-related secondary crater cluster (e.g., arrow) on eastern floor of crater Ostrov. Subframe of CTX D20_035132_1527 (5.3 m scaled pixel width). **C)** Chain of possible Hale secondary craters (e.g., arrows) on southwestern floor of crater Ostrov. Subframe of CTX B10_013467_1526 and B20_017357_1537 (5.2 m scaled pixel width). North to top in all images.

5.5   Relationship between Discontinuous Distal Deposits and Hale Crater

The discontinuous distal deposits (Section 5.4.4) have a number of attributes that indicate their origin is related to the Hale crater impact event. For example, the morphology, nature and state of preservation of the discontinuous distal deposits are similar in many regards to the distal continuous (He2) ejecta deposits from Hale (Section 5.4.1)

described in *Jones et al*. (2011) and *El-Maarry et al.* (2013). And like the He2 deposits, the discontinuous distal deposits have relatively darker-toned, smooth surfaces (Figs. 5.9 and 5.10). They embay Hale secondaries and conform to topography via alternately incising and ponding (Figs. 5.9 and 5.10) and are generally radial to Hale and align with impact-produced wind streaks. The consistent superposing relationship of the deposits embaying Hale secondaries indicates that both were emplaced during the Hale impact, with the deposits arriving later. A similar relationship was hypothesized at Bamburg crater in Acidalia Planitia, where late arriving ejecta superposes secondary craters (*Mouginis-Mark*, 1979). Because secondary impacts are relatively low energy impact events and there are no examples of deposits that appear to originate from within secondaries, it does not appear that formation of the secondaries was responsible for the creation of the distal deposits. Finally, simulations of the Hale impact predict delivery of significant debris to ranges exceeding those previously mapped to the north and northeast of the crater (*Schultz and Wrobel*, 2012). Hence, we conclude the discontinuous distal deposits are ejecta emplaced during the late stages of formation of Hale crater and may be equivalent to late stage ejecta comprising smooth terrain material around Bamburg crater (*Mouginis-Mark*, 1979).

5.6.   Sediment Properties of the Distal Continuous (He2) and Discontinuous Distal Ejecta Deposits

The bulk of both the distal continuous (He2) and discontinuous distal deposits consist of relatively fine-grained materials based on the following observations: 1) Boulders or other coarse fragments are not widely observed on the surface of the deposits; 2) erosion at the tips of digitate margins along lobes of He2 ejecta north of Hale results in their being "beheaded" and is accompanied by accumulation of fine, boulder free debris, thereby

implying efficient removal and (or) redistribution of constituent grains by the wind (Fig. 5.5B); and 3) the generally dark nature of many of the discontinuous deposits in the THEMIS Nighttime IR data is consistent with fine-grained materials, especially relative to locally bright surfaces where impact-induced winds may have locally stripped fines (Fig. 5.12). Even where the deposits are marginally brighter than adjacent surfaces, it may simply imply a contrast with surrounding surfaces dominated by fines rather than incorporation of a significant coarse component.
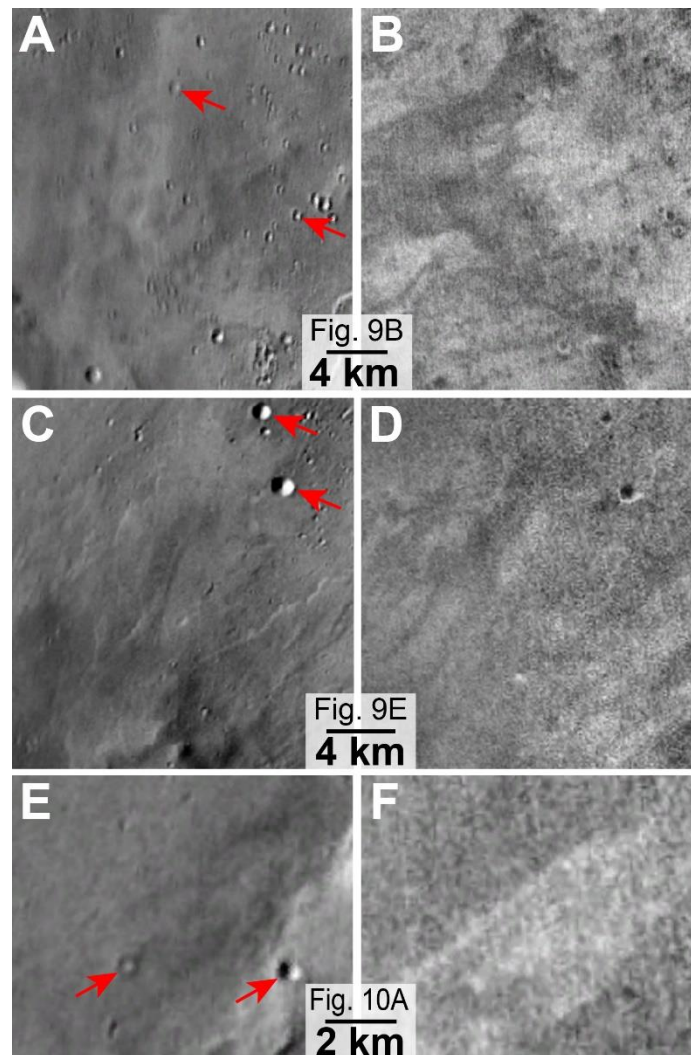
Figure 5.12   Thermal properties of the discontinuous distal deposits

Variability of discontinuous distal deposits as seen in THEMIS daytime IR data (left panels) and THEMIS nighttime IR data (right panels). **A and B)** Discontinuous distal deposits are (A) generally brighter in THEMIS daytime IR data and (B) darker in THEMIS nighttime IR data, similar to thermal signature of the ponded lobes west of Bond crater (Figs. 5.5 and 5.6A). This deposit is 315 km NE of the rim of Hale crater near 32.1°S, 329.8°E (for context, red arrows in (A) mark same craters indicated in Fig. 5.9B). **C and D)** Some discontinuous distal deposits are (C) variably darker in THEMIS daytime IR and (D) brighter in THEMIS nighttime IR data. This deposit is 350 km NE of the northeastern rim of Hale crater near 30.6°S, 331°E (for context, red arrows in (C) mark same craters indicated in Fig. 5.9E). **E and F)** Some discontinuous deposits are (E) darker in THEMIS daytime IR and (F) brighter in THEMIS nighttime IR data. This deposit is over 400 km NE of the northeastern rim of Hale crater near 30.3°S, 330.6°E (for context, red arrows in (E) mark same craters indicated in Fig. 5.10A). North to top in all images.

5.7.   Emplacement of Distal Continuous (He2) and Discontinuous Distal Ejecta Deposits

Because the Hale impact occurred in the Early to middle-Amazonian, the climate was likely relatively cold and characterized by temperatures mostly below freezing (e.g., *Carr*, 2006) when the ejecta from Hale was emplaced. Cold ambient conditions probably caused the surface of the distal continuous (He2) deposits to freeze, thereby creating an insulating layer of ice that enabled the underlying water-sediment mix to continue flowing downslope. Freezing may also have occurred on the bottom of the deposits due to cold ground temperatures, but constrictions and steeper grades likely enabled higher velocities and local incision (e.g., Figs. 5.6 and 5.9C-D). Slower moving, thicker accumulations downstream of significant constrictions that impeded flow (Figs. 5.5 and 5.6) and flat surfaces would have enabled development of a thicker ice crust that would further reduce the velocity of the flow. Over time, cooling and eventual freezing of these deposits from the outside in caused increasing pressure within, leading to fracturing and dewatering (Fig.

5.5) that resulted in discharge and deposition further down slope (Fig. 5.7). Final cooling and deflation due to release of water led to contraction and additional fracturing.

To further characterize the nature of the ejecta and constrain the flow dynamics of its emplacement, we analyzed a lobe of distal continuous (He2) ejecta that flowed and accumulated west of Bond crater near 322.3°E, 32.3°S (Fig. 5.6). This particular deposit appears to have accumulated on higher elevation surfaces to the west and drained through a confined channel before emerging onto a local, unconfined, low-lying surface where it spread out and stopped (Fig. 5.6A and 5.6B). Multiple arcuate ridges on the deposit suggest emplacement occurred in several surges (Figs. 5.6A and 5.6F) and the topography from the DTM suggests additional material was sourced from the south. The deposit embays topography to the east and partially circumvents high-standing terrain to the north as it drained downhill and pooled, terminating adjacent to a separate lobate deposit farther to the east and lower in elevation (Figs. 5.6A and 5.6B). The total area covered by the deposit originating from the confined channel is approximately 63.5 km^2 and multiple transects from the CTX DTM and MOLA tracks crossing the deposit suggest it has a maximum thickness of ~20-40 m (Fig. 5.6D). The nature of the underlying topography buried by the deposits is unknown, introducing uncertainty into the thickness estimate. However, the deposit does not appear to have accumulated in an impact crater and is therefore not significantly thicker, and the fairly uniform nature of arcuate ridges on the deposit surface (Figs. 5.6A and 5.6F) suggest flow was not influenced by local highs and is therefore not likely to be substantially thinner on average.

Characteristics of the channel sourcing the deposit from the west yield first-order estimates of discharge and the duration of emplacement. For example, the channel turns

and narrows at a point about 1/3 along its course causing the flowing deposit to locally run-up on adjacent slopes (see hollow arrow in Figs. 5.6B and 5.6C). Further downstream, at about the halfway point of the channel, there are small turns along the channel path that caused flowing material to slosh up onto the adjacent banks (Fig. 5.6C).

Based on analogy of run-up height of lahars on obstacles, the relationship between run-up height and flow velocity (*Vallance*, 1999) is given by:

$$H = v^2/2(g_m)$$

where *H* is height of run up, *v* is velocity and g_m is the gravitational constant scaled to Mars (3.71 m s^{-2}). The height (*H*) of the run-up on the valley walls, caused by the slight constriction/bend in the channel, is estimated from a CTX DTM and MOLA data (track 15075) that crosses the channel near the flow obstruction (profile 'C' in Fig. 5.6C). *H* derived from both data sets is estimated to be close to ~50 m, yielding an associated flow velocity of ~19 m sec^{-1}.

The amount of sloshing of the deposit that occurred around a bend in the channel can also be used to estimate flow velocity (*U*) after *Heslop et al*. (1989) and *Wilson and Mouginis-Mark* (2014):

$$U^2 = R g_m \tan\beta$$

where *R* is the radius of curvature of the bend, g_m is adjusted Mars gravity (3.71 m s^{-2}), and β is the angle from the horizontal by which the flow surface is tilted. The angle β is equivalent to the width of the flow (*W*) and the amount by which the level of the flow on the outside of the bend exceeds the level on the inside (*H*):

$$\tan\beta = H/W$$

At the location of transect 'D' (Fig. 5.6C), R=1823 m, H=15 m, W=1100 m, tanβ = 0.0136 and the resulting flow speed (U) is estimated to be approximately 9.6 m s^{-1}.

The velocity estimated from the run-up height on obstacles, therefore, is roughly twice that derived using the amount of sloshing that occurs around a bend in the channel. However, the velocity estimate based on sloshing is for a portion of the channel that is relatively narrow and downstream of where the velocity estimate was made based on run-up height. Hence, an initially higher velocity of the flow upstream of the constriction may have slowed as it entered the narrower, more twisting section of the channel. If that was the case, the lower velocity estimated from sloshing may best reflect flow that fed the ponded lobe deposit located downstream.

There is additional uncertainty in these estimated values for flow velocity. In the instance of the amount of sloshing, the fairly limited extent and subtle nature of the bend in the channel yields uncertainty in the estimated radius of curvature. Nevertheless, an increase or decrease in this value by hundreds of meters only changes the resultant velocity estimate by 1-2 m s^{-1}. There are also slight offsets in MOLA tracks relative to the limits of the deposits in the channel, but the estimated values extracted by MOLA and the CTX DTM for run-up and sloshing around the channel bend are quite similar. Finally, derived values may reflect maximum flow speed during surge(s) in flow (*Wilson and Mouginis-Mark*, 2014) rather than average flow. As a result of these uncertainties, the derived values are used to bracket the maximum speed of the flow, which may have been somewhat slower during much of the event. For comparison, lahars on the Earth can move at velocities of up to 50 m s^{-1} on steep slopes and 6-10 m s^{-1} on lesser slopes (*Crandell*, 1980).

The channel is approximately triangular in cross section with a width and depth of ~700 m and ~65 m, respectively, where run-up velocity was calculated (profile 'C' in Fig. 5.6C and 6E) and ~1100 m and ~33 m, respectively where the sloshing velocity was calculated (profile 'D' in Fig. 5.6C and 5.6E). Further downstream (from segment of MOLA track 12283 in Fig. 5.6C) the channel is ~875 m wide and ~30 m deep. Using average channel dimensions of ~950 m for width and ~40 m for depth gives a triangular cross sectional area of ~19,000 m^2, which when combined with the velocities derived above gives peak estimated channel discharges of ~1.8 x 10^5 and 3.6 x 10^5 m^3 s^{-1}.

The discharge can be compared to the downstream volume of the deposit to get a sense of the duration of emplacement. The volume estimate is maximized by including the entire 63.5 km^2 downstream of the channel and ignoring likely contributions from the south (Fig. 5.6A). Moreover, it is reasonable to expect that the surface buried by the deposit was relatively low relief and fairly continuous with adjacent exposed surfaces, and that thickness estimates of ~10-20 m approaching the margins and between ~25 and ~40 m elsewhere are realistic. To calculate the maximum volume of the deposit, we use the maximum thickness of 40 m.

The resultant volume estimate for the accumulation of the deposit is ~2.5 x 10^9 m^3. This volume divided by the discharge rates stated above implies deposition could have occurred in as little as 4 hours or even less based on the higher velocity estimate derived from the run-up height. Given uncertainties in the volume and discharge described above and recognizing that average discharge rates were likely less than the peak rates of flow, it is possible that emplacement occurred over a longer time interval. However, even if off by

an order of magnitude, these estimates suggest the deposit was likely emplaced in hours or perhaps over several days at most.

Despite their occurrence hundreds of km from Hale, it is likely the discontinuous distal ejecta deposits were also emplaced and assumed their current expression very shortly after the impact. Their lack of a connection to the continuous He2 deposits indicates they represent accumulations of ballistic ejecta with entrained volatiles that were not mixed with the He1 and He2 ejecta. The discontinuous distal deposits likely impacted late (based on embayment of secondaries and range from Hale, see *Melosh*, 1989) at relatively high velocity and then flowed along the surface as dictated by topography, consistent with the emplacement of late, distal ejecta described for Bamburg crater by *Mouginis-Mark* (1979).

Minimal mixing of the fragments during ballistic transport of the ejecta prior to impact to form the discontinuous distal deposits (*Gault and Greeley*, 1987) suggests they liquefied and flowed on impact as a result of grain-to-grain impacts of fragments in the deposit and (or) excessive water pore pressure. As described in *Gault and Greeley* (1978), ballistic delivery of masses or "clumps" of muddy ejecta that may be analogous to the discontinuous distal deposits at Hale results in flow of the initially impacting material ahead of the remaining, later impacting material. The dual flow fronts predicted to occur within these deposits (*Gault and Greeley*, 1978) are not observed at Hale, perhaps as a result of modification by continued downslope flow after the initial impact.

5.8.   Drainage Beyond the Distal Continuous (He2) and Discontinuous Distal Ejecta Deposits

Jones et al. (2011) estimated that 10% ice by volume in the Hale target rocks was sufficient to account for the characteristics of the He1 and He2 ejecta and used that amount to estimate discharge from associated channels. They estimated that some of the flows might contain ~40% water and it appears reasonable that the accumulations of distal He2 ejecta described here may have incorporated broadly similar percentages of water (with locally higher and lower amounts). In addition, some mixing with target materials almost certainly occurred on impact (*Melosh*, 1989) and if the target impacted by the ejecta was ice rich, limited additional water ice could have melted, aiding flow and subsequent dewatering.

The low gradients along the depressions traversed by water debouched from the flows suggest velocities may also have been low, characterized by transport rates that may not have exceeded several meters per second. If correct, these velocities are broadly consistent with the inference that the flows carried mostly fine-grained materials (e.g., *Baker et al*., 1988; *Burr et al*., 2006). The fine-grained nature of the flows may have been preserved in part by freezing at the bed that limited entrainment of additional large fragments from all but the locally steepest reaches. Nevertheless, such velocities would enable flows to have reached well to the northeast of Hale in only a day or less, with water from deposits north of Hale continuing to flow for perhaps a day or two. Hence, the formation and emplacement of the deposits was a significant geomorphic event that was probably associated with very short-lived conditions.

It is uncertain whether discharge related to de-watering of the He2 deposits reached the upper trunk of Uzboi Vallis (Fig. 5.8A). The occurrence of apparent dune-like forms near a constriction north of Bond crater and their possible relationship to the deposits described

herein and further upstream suggest they may be related to the Hale impact (Fig. 5.8B). However, these dune-like forms are difficult to distinguish from similar morphologies in Uzboi that are much further to the north and whose formation has been attributed to final drainage of a large lake in Uzboi (*Grant et al.*, 2011). Regardless, the scale of the dune-like forms implies at least meters deep discharge during their formation.

Erosional and depositional features west of Bond crater (Fig. 5.7) become subtle and difficult to map further from Hale and suggest somewhat lesser discharge was sourced from the lobes of ejecta to the south (Fig. 5.5). Nevertheless, prior discharge estimates (*Jones et al.*, 2011) suggest ~50 km^3 water could have been derived from these and other deposits north of Hale and implies significant water could have reached the floor of Uzboi Vallis.

An upper limit on the volume of water from the distal Hale deposit that could have discharged into Uzboi can be derived from the topography and morphology of the mid and upper reaches of the meso-scale outflow system. An accumulation of material at the mouth of Nirgal Vallis rises a little over 200 m above the upstream floor of Uzboi Vallis (*Wilson and Grant*, 2016) and lacks evidence of incision that would have occurred if any late discharge related to the Hale impact or some other source overtopped the deposit to create a spillway to the north. Hence, any water from the distal Hale ejecta deposits that may have reached Uzboi was confined to the upper reaches upstream of this accumulation. The major tributaries of Uzboi that could have supplied Hale-related materials are located approximately 90 km and 125 km south of the deposit at the mouth of Nirgal at elevations that indicate roughly 250 km^3 of water could have ponded in upper Uzboi before overtopping and incising the accumulation at Nirgal. Such a volume indicates that ~50 km^3 or more discharge from the deposits could have easily been held in lower Uzboi. It is

puzzling, however, why the darker-toned smooth materials observed on some parts of the floor of Uzboi are not more widespread if there had been significant ponding of Hale-deposit discharge. Moreover, the occurrence of transverse eolian ridges on the darker-toned, smooth materials in Uzboi (Fig. 5.8A) located downstream of tributaries that may have drained from the Hale deposits suggests the Uzboi floor deposits may be older and unrelated to the Hale impact.

The discontinuous distal deposits, which are generally relatively darker-toned in THEMIS Nighttime IR data and are morphologically similar to the He2 ejecta, argues that they were deposited as a mixture of water and sediment rather than as impact melt that cooled to form bedrock. The length of the deposits (up to 10s of km) over fairly low gradient surfaces implies relatively low viscosities, which is consistent with the observation that the deposits appear to form a relatively thin veneer on the surface where they are not laterally constricted as they drain downslope (Figs. 5.9 and 5.10). While the amount of water incorporated into the discontinuous distal deposits may have been similar to that in the continuous ejecta, dewatering may have been limited by their relatively thin nature and small volume, which resulted in rapid freezing and limited associated increase in internal pressurization after impact. Emplacement of relatively low viscosity, rapidly freezing deposits over variable topography and slopes likely accounts for the range in expression of the discontinuous deposits.

The occurrence of the well-preserved discontinuous distal deposits around Hale is relatively uncommon around other similar-sized craters on Mars. At Hale, formation of these deposits may be related to impact into an ice-rich target, producing ejecta that flowed on impact and created coherent surface deposits. Previous studies of Hale (*Jones et al.,*

2011; *El-Maarry et al.*, 2013) highlight the likely ice-rich nature of the target substrate and the fairly high density of valleys, mesoscale channels, and lacustrine features around and to the north of the crater (e.g., *Grant and Parker*, 2002; *Grant et al.,* 2011) are consistent with such a model. The absence of comparable deposits around other similar-sized craters may suggest those impact occurred into substrates with a lower ice content. Many Martian craters that are similar in size to Hale are older and any deposits comparable to those at Hale would have been subject to more cumulative degradation, perhaps rendering them unrecognizable. The scale of the Hale deposits indicates that occurrence of as little as 10-20 m of degradation would likely preclude their detection.

5.9   Implications for the Amazonian Climate

The occurrence and morphology of the He2 and discontinuous distal ejecta holds clues to the broader scale effects of the Hale impact on climate and subsequent erosion. First, nearly all of the deposits, the secondaries they superpose, and the surfaces modified by water draining from the deposits, all retain primary features that are 10-m scale and smaller. And some of the features that were produced during dewatering of the deposits remain preserved, including what appear to be small depositional bar forms and locations where local incision occurred into the pre-existing terrain (Fig. 5.7). A few exceptions to this amount of erosion include isolated erosion and beheading of some locally higher relief digitate features at the terminus of thicker accumulations of the deposits (Fig. 5.5B) and putative Hale-related deposits on the floor of Uzboi Vallis where surfaces are modified by superposed transverse eolian ridges (Fig. 5.8A). Even in these cases, however, comparison with nearby preserved features implies a majority of the primary morphologic features are

intact and experienced no more than meters of degradation, with up to ~10-20 m of material redistributed by erosion on local, steep slopes flanking thicker deposits.

The vast majority of the deposits and the downstream modifications related to their dewatering remain pristine despite having experienced multiple episodes of burial/exhumation by dust and volatiles (*Schultz and Wrobel*, 2012). This is even more remarkable given that the bulk of the Hale deposits are inferred to be fairly fine-grained and (at least originally) ice-rich (*Jones et al.*, 2011; *El-Maarry et al.*, 2013) and would likely be relatively susceptible to erosion as compared to coarser and (or) more competent materials such as lava or other bedrock. Collectively, the survival of the Hale deposits and related morphologies over such a broad area imply very low erosion rates since the Early to middle Amazonian.

Although the absolute ages corresponding to the Early and Middle Amazonian are not well constrained, they are thought to have begun around 3.2-3.4 Ga and 1.0-1.2 Ga, respectively (*Tanaka et al.*, 2014). While obliquity and other known variations in Mars climate make it unlikely that erosion rates on the Hale deposits were uniform over this period (e.g., *Golombek et al.*, 2014), long term average rates for just a few meters of denudation on the distal Hale deposits are on order of 10^{-2} to 10^{-3} m/Myr. For comparison, other estimates of erosion since the Late Amazonian are generally similar (e.g., *Golombek et al.*, 2006, 2014; *Grant et al.*, 2006; *Warner et al.*, 2010; *Farley et al.*, 2014), but are often predicted for bedrock units rather than the less competent materials presumed to comprise the Hale-related deposits. An exception includes the initial degradation of small craters in Meridiani Planum where rates as high as 10^{-1} to 10^0 m/Myr (*Golombek et al.*, 2014), though

this may relate to local disequilibrium of the geomorphic surface caused by the impact and crater formation rather than long term erosion rates (*Grant et al.*, 2008).

The survival of the distal Hale deposits, impact-associated wind streaks, and secondaries all in a nearly pristine state, indicates the Hale impact was a significant geomorphic event, but was not responsible for triggering an extended period of favorable climate related to an enhanced period of global or regional degradation. Although the oblique nature of the Hale impact resulted in widespread downrange distribution of ejecta and debris (*Schultz and Wrobel*, 2012), the size of the impactor was likely on order of ~25 km diameter (*Schultz and Wrobel*, 2012) and substantially smaller than the ~100-250 km impactors modeled to have more significant climate effects (*Segura et al.*, 2002). The possibility of global effects is further lessened by the occurrence of the impact in the Amazonian, when Martian climate had evolved to be cold and dry (e.g., *Carr*, 2006) and thresholds necessary to trigger enhanced geomorphic activity were well out of reach.

Impacts have also been proposed to trigger increased geomorphic activity on a regional scale (e.g., *Maxwell et al.*, 1973; *Kite et al.*, 2011; *Mangold*, 2011, 2012). While impact-induced release of volatiles clearly resulted in formation of fluvial features on and near Hale's continuous ejecta (*Jones et al.*, 2011; *El-Maarry et al.,* 2013), there is no evidence of sustained geomorphic activity related to impact-generated hydrothermal activity (e.g., *Newsom et al.*, 1996) given the uniformly pristine morphology of the Hale deposits and secondaries. There are no examples of valleys cross-cutting the distal deposits or of multiple stages or valley evolution that might be expected if there had been an extended period of enhanced geomorphic activity after the Hale impact. Moreover, secondary craters attributed to the Hale impact superpose alluvial fans in Ostrov crater more than 600 km to

the northeast of Hale (Fig. 5.11). These secondaries survive on fans flanking both the southwestern and eastern walls of the crater and indicate that the last stage of fan evolution must have pre-dated the Hale impact event and is consistent with prior conclusions related to the timing of fan formation in the Margaritifer Terra region (*Grant and Wilson*, 2011; 2012).

5.10   Summary

The formation of Hale crater in the Early to Middle Amazonian (*Cabrol et al*., 2001; *Jones et al*., 2011) caused the emplacement of a variety of relatively fine-grained fluidized ejecta that incorporated significant amounts of water. The deposits include the He2 ejecta described previously (*Jones et al.*, 2011; *El-Maarry et al*., 2013) and newly recognized more distal discontinuous ejecta that reached up to 450 km to the northeast of the Hale crater rim and embay Hale secondaries, which can be found >600 km from the crater rim. While the He2 deposits were emplaced via a combination of ballistic and ground-hugging processes (*Jones et al*., 2011; *El-Maarry et al*., 2013) within hours to a day or two after impact, the discontinuous distal deposits were likely emplaced ballistically and subsequently flowed down local slopes over comparable time scales. Some thicker He2 deposits apparently dewatered and caused downstream drainage that may have reached Uzboi Vallis within a day or two of the impact event, whereas the thinner and volumetrically smaller discontinuous deposits froze in place without significant dewatering. Occurrence of such well-expressed discontinuous distal deposits at Hale is unusual and likely due to impact into ice-rich target rocks and (or) the pristine nature of the crater-related landforms as compared to similar-sized, yet typically older and more degraded craters on Mars.

The Hale impact triggered a wide range of short-lived geomorphic effects in southern Margaritifer Terra and the northern Argyre regions of Mars (*Jones et al.*, 2011; *Schultz and Wrobel*, 2012). The distal continuous (He2) and discontinuous distal ejecta deposits persist in a remarkably pristine state which requires low erosion rates post-Hale crater formation that are comparable to those estimated elsewhere on Mars during the Amazonian (e.g., *Farley et al.*, 2014; *Golombek et al.*, 2006, 2014; *Grant et al.*, 2006; *Warner et al.*, 2010). Their pristine nature coupled with the occurrence of secondaries over a wide region further indicates the Hale impact did not significantly influence long term global or regional scale geomorphic activity or climate, and the Hale impact post-dates late alluvial fan activity observed across much of southern Margaritifer Terra (*Grant and Wilson*, 2011, 2012).

5.11   Citation

Grant, J. A. and Wilson, S. A. (2017), The nature and emplacement of distal aqueous-rich ejecta deposits from Hale crater, Mars, *Meteorit. Planet. Sci*. doi:10.1111/maps.12843.

5.12   References

Baker, V., R. C. Kochel, and P. C. Patton (1988), *Flood Geomorphology,* Wiley Interscience, New York. 503pp.

Barlow, N. G. (2005), A review of Martian impact crater ejecta structures and their implications for target properties, *GSA Special Papers*, *384*, 433-442, doi: 10.1130/0-8137-2384-1.433.

Barlow, N. G. and C. B. Perez (2003), Martian impact crater ejecta morphologies as indicators of the distribution of subsurface volatiles, *J. Geophys. Res*., 108, 5085, doi:10.1029/2002JE002036, E8.

Burr, D. M., J. P. Emery, R. D. Lorenz, G. C. Collins and P. A. Carling (2006), Sediment transport by liquid overland flow: Application to Titan, *Icarus*,*181*, 235-242, doi: 10.1016/j.icarus.2005.11.012.

Cabrol, N. A., D. D. Wynn-Williams, D. A. Crawford and E. A. Grin (2001), Recent aqueous environments in Martian impact craters: An astrobiological perspective, *Icarus*, *154*, (1), 98-112, doi:10.1006/icar.2001.6661.

Carr, M. H. (2006), *The surface of Mars*, Cambridge University Press, Cambridge. 307pp.

Christensen, P. R. et al., (2004), The Thermal Emission Imaging System (THEMIS) for the Mars 2001 Odyssey Mission, *Space Sci. Reviews*, *110* (1), 85-130.

Crandell, D. R. (1980), Recent eruptive history of Mount Hood, Oregon, and potential hazards from future eruptions, *U.S. Geological Survey Bulletin*, *1492*, 81 p.

El-Maarry, M. R., J. M. Dohm, G. Michael, N. Thomas and S. Maruyama (2013), Morphology and evolution of the ejecta of Hale crater in Argyre basin, Mars: Results from high resolution mapping, *Icarus*, *226* (1), 905-922, doi:10.1016/j.icarus.2013.07.014.

Farley et al. (2014), In situ radiometric and exposure age dating of the Martian surface, *Science*, *343*, (6169), doi: 10.1126/science.1247166.

Gault, D. E. and R. Greeley (1978), Exploratory experiments of impact craters formed in viscous-liquid targets: Analogues for Martian rampart craters? *Icarus*, *34*, 486-495.

Golombek, M. P., J. A. Grant, L. S. Crumpler, R. Greeley, R. E. Arvidson, J. F. Bell III, C. M. Weitz, R. Sullivan, P. R. Christensen, L. A. Soderblom and S. W. Squyres (2006), Erosion rates at the Mars Exploration Rover landing sites and long-term climate change on Mars, *J. Geophys. Res.*, 111, E12S10, doi:10.1029/2006JE002754.

Golombek, M., K. Robinson, A. McEwen, N. Bridges, B. Ivanov, L. Tornabene and R. Sullivan (2010), Constraints on ripple migration at Meridiani Planum from Opportunity and HiRISE observations of fresh craters, *J. Geophys. Res.*, *115*, E00F08, doi:10.1029/2010JE003628.

Golombek, M. P., N. H. Warner, V. Ganti, M. P. Lamb, T. J. Parker, R. L. Fergason and R. Sullivan (2014), Small crater modification on Meridiani Planum and implications for erosion rates and climate change on Mars, *J. Geophys. Res.*, *119*, doi: 10.1002/2014JE004658.

Grant, J. A. and P. H. Schultz (1993), Gradation of selected terrestrial and Martian impact craters, *J. Geophys. Res.*, *98*, 11,025-11,042.

Grant, J. A., and T. J. Parker (2002), Drainage Evolution of the Margaritifer Sinus Region, Mars, *J. Geophys. Res.*, *107*, doi:10.1029/2001JE001678.

Grant, J. A. and S. A. Wilson (2011), Late alluvial fan formation in southern Margaritifer Terra, Mars, *Geophysical Res. Letts., 38*, L08201.

Grant, J. A. and S. A. Wilson (2012), A possible synoptic source of water for alluvial fan formation in southern Margaritifer Terra, Mars, *Planetary Space Sci.*, *72*, 44-52.

Grant, J. A. and S. A. Wilson (2016), The nature and extent of aqueous deposits related to the Hale impact crater on Mars, *Lunar and Planetary Science XXXXVII*, Houston, TX, Abstract 2530.

Grant, J. A., S. A. Wilson, S. W. Ruff, M. P. Golombek, and D. L. Koestler (2006), Distribution of rocks on the Gusev Plains and on Husband Hill, Mars, *Geophys. Res. Lett.*, *33*, L16202, doi:10.1029/2006GL026964.

Grant, J. A., S. A. Wilson, B. A. Cohen, M. P. Golombek, P. E. Geissler, R. J. Sullivan, R. L. Kirk and T. J. Parker (2008), Degradational modification of Victoria crater, Mars, *J. Geophys. Res*., *113*, E11010, doi:10.1029/2008JE003155.

Grant, J. A., R. P. Irwin, S. A. Wilson, D. Buczkowski, and K. Siebach (2011), A lake in Uzboi Vallis and implications for Late Noachian-Early Hesperian climate on Mars, *Icarus*, 110-122, doi:10.1016/j.icarus.2010.11.024.

Grant, J. A., T. J. Parker, L. S. Crumpler, S. A. Wilson, M. P. Golombek and D. W. Mittlefehldt (2015), The degradational history of Endeavour crater, Mars, *Icarus*, doi:10.1016/j.icarus.2015.08.019.

Heslop, S. E., L. Wilson, H. Pinkerton and J. W. Head (1989), Dynamics of a confined lava flow on Kilauea volcano, *Hawaii. Bull. Volcanol*., *51*, 415–432.

Irwin, R. P. III (2013), Testing links between impacts and fluvial erosion on post-Noachian Mars, *Lunar and Planetary Science XXXXIV*, Abstract 2958.

Jones A. P., A. S. McEwen, L. L. Tornabene, V. R. Baker, H. J. Melosh and D. C. Berman (2011), A geomorphic analysis of Hale crater, Mars: The effects of impact into ice-rich crust, *Icarus*, *211* (1), 259-272, doi:10.1016/j.icarus.2010.10.014.

Kadish, S. J., J. W. Head, N. G. Barlow and D. R. Marchant (2008), Martian pedestal craters: Marginal sublimation pits implicate a climate-related formation mechanism, *Geophys. Res. Lett*., *35*, L16104, doi:10.1029/2008GL034990.

Kite, E. S., T. I. Michaels, S. Rafkin, M. Manga and W. E. Dietrich (2011), Localized precipitation and runoff on Mars, *J. Geophys. Res*., *116*, E07002, doi:10.1029/2010JE003783.

Malin, M. C., et al. (2007), Context Camera Investigation on board the Mars Reconnaissance Orbiter, *J. Geophys. Res*., *112*, E05S04, doi:10.1029/2006JE002808.

Mangold, N. (2011), Post-early Mars fluvial landforms on mid-latitude impact ejecta, *Lunar and Planetary Science XXXXII*, Abstract 1378.

Mangold, N. (2012), Fluvial landforms on fresh impact ejecta on Mars, *Planet. Space Sci*., 62, 69-85.

Mangold, N., E. S. Kite, M. G. Kleinhaus, H. Newsom, V. Ansan, E. Hauber, E. Kraal, C. Quantin and K. Tanaka (2012), The origin and timing of fluvial activity at Eberswalde crater, Mars, *Icarus*, *220*, 530-551, http://dx.doi.org/10.1016/j.icarus.2012.05.026.

Maxwell, T. A., E. P. Otto, M. D. Picard and R. C. Wilson (1973), Meteorite Impact: A suggestion for the origin of some stream channels on Mars, *Geology*, 1: 9-10.

McEwen, A. S., et al. (2007), Mars Reconnaissance Orbiter's High Resolution Imaging Science Experiment (HiRISE), *J. Geophys. Res.*, 112, E05S02, doi:10.1029/2005JE002605.

Melosh, H. J. (1989), *Impact Cratering*, Oxford Univ. Press, New York, 245 pp.

Mouginis-Mark, P. J. (1979), Ejecta emplacement of the Martian impact crater Bamburg: *Proc. Lunar Planet. Sci. Conf. 10th*, p. 2651-2668, *Geochim. Cosmochim Acta*, Pergamon, NY, NY.

Newsom, H. E., G. E. Brittelle, C. A. Hibbitts, L. J. Crossey and A. M. Kudo (1996), Impact crater lakes on Mars, *J. Geophys. Res*., 101(E6), 14951–14955, doi:10.1029/96JE01139.

Schultz, P. H. and A. B. Lutz-Garihan (1982), Grazing impacts on Mars: A record of lost satellites, *J. Geophys. Res.*, 87(S01), A84–A96, doi:10.1029/JB087iS01p00A84.

Schultz, P. H. and D. E. Gault (1990), Prolonged global catastrophes from oblique impacts: p. 239-261, in Sharpton, V.L. and Ward, P.D. (eds.), Geol. Soc. America Special Paper 247, Boulder, CO., Geological Society of America.

Schultz, P. H. and K. E. Wrobel (2012), The oblique impact Hale and its consequences on Mars, *J. Geophys. Res.*, *117*, E04001, doi:10.1029/2011JE003843.

Segura, T. L., O. B. Toon, A. Colaprete, and K. Zahnle (2002), Environmental effects of large impacts on Mars, *Science*, *298* (5600), 1977-1980, doi: 10.1126/science.1073586.

Smith, D. E. et al. (1999), The global topography of Mars and implications for surface evolution, *Science*, *284*, 1495-1503.

Tanaka, K. L., J. A. Skinner, J. M. Dohm, Jr., R. P. Irwin, III, E. J. Kolb, C. M. Fortezzo, T. Platz, G. G. Michael and T. M. Hare (2014), Geologic map of Mars: U.S. Geological Survey Scientific Investigations Map 3292, scale 1:20,000,000, pamphlet 43 p., http://dx.doi.org/10.3133/sim3292.

Vallance, J. W. (1999), Postglacial lahars and potential hazards in the White Salmon River system on the southwest flank of Mount Adams, Washington, *U.S. Geological Survey Bulletin*, *2161*, U.S. Dept. Interior, USGS, 49 p.

Warner, N., S. Gupta, S.-Y. Lin, J.-R. Kim, J.-P. Muller and J. Morley (2010), Late Noachian to Hesperian climate change on Mars: Evidence of episodic warming from transient crater lakes near Ares Vallis, *J. Geophys. Res.*, *115*, E06013, doi:10.1029/2009JE003522.

Wilson, L., and P. J. Mouginis-Mark (2014), Dynamics of fluid flow on Mars: Lava or mud?, *Icarus*, *233*, 268-280, http://dx.doi.org/10.1016/j.icarus.2014.01.041.

Wilson S. A. and J. A. Grant (2014), Geologic mapping in MTM quadrangles -20037, -25037, -30037, -30032 in southern Margaritifer Terra, Mars, Planetary Geology Mappers Meeting, June 23-25, Flagstaff AZ.

Wilson S. A. and J. A. Grant (2016), Geologic mapping in Margaritifer Terra on Mars and a closer look at the confluence of Nirgal and Uzboi Vallis, *Lunar and Planetary Science XXXXVII*, Abstract 2505.

Wilson, S. A., J. A. Grant, D. L. Buczkowski and C. M. Weitz (2015), Geologic mapping and the gradational history of southern Margaritifer Terra on Mars, *Lunar and Planetary Science XXXXVI*, Abstract 2492.

CHAPTER 6. Discussion

The origin of life on Earth is unknown: life may have originated here, or it could have formed elsewhere and hitched a ride to Earth during the period of heavy bombardment that characterized the early stages of our solar system's formation. Our current understanding of the existence, and perhaps formation, of life on Earth is intimately associated with the presence of liquid water. This premise provides the framework for our exploration of terrestrial-like planets in search for life. Mars, with its tantalizing geomorphic evidence of a paleoclimate that was once capable of supporting liquid water on its surface and proximity to Earth, has become the primary target of investigation. The U.S. space program and other European countries have probed Mars with fly-by, orbital, landed, and rover missions since the 1960s with the goal of discovering life beyond Earth.

The surface of Mars today is not hospitable relative to Earth, given the cold temperatures, arid conditions and its thin atmosphere offering little protection against harmful solar radiation. Scientists believe the past climate on Mars was different, a hypothesis that was recently confirmed by the Mars Science Laboratory (MSL) mission. The MSL *Curiosity* rover, armed with a suite of instruments capable of assessing the presence of past habitable conditions on Mars, discovered evidence of a Hesperian fluvio-lacustrine environment in Gale crater that was hospitable by terrestrial standards [*Grotzinger et al.*, 2015]. Our own planet is teeming with life, and life at the microbial scale has proven to be quite robust and adaptable to changing conditions. Numerous microbes on Earth, collectively known as "extremeophiles," have evolved to thrive in incredibly harsh physical and geochemical (e.g., temperature, pressure, pH) regimes. The

existence of extremophiles on Earth motivates us to search for life on Mars, despite its seemingly severe present-day conditions: if life did form on Mars, perhaps it evolved similarly to terrestrial microbes, possibly even migrating underground as the surface conditions deteriorated. Constraining the role of water on Mars, including the amount, timing and duration, helps characterize the potential habitability of the planet over time. Unraveling the climatologic, hydrologic and geologic history of Mars is important, as it not only provides insight into the evolution of our own planet, but also may provide clues to reveal the origin and evolution of life in our solar system.

6.1 The Current Understanding of the Hydrologic Evolution of Mars

It is generally accepted that climate on early Mars was capable of sustaining an active hydrological cycle, and that precipitation and runoff formed the low-to-mid latitude belt of deeply incised valley networks [*Grant*, 2000; *Hynek and Phillips*, 2001; 2003; *Craddock and Howard*, 2002; *Irwin and Howard*, 2002; *Howard et al.*, 2005; *Irwin et al.*, 2005; *Carr*, 2012]. The conditions in the Noachian, described as "warm and wet" [e.g., *Craddock and Howard*, 2002], may have actually been relatively dry by terrestrial standards with perhaps only episodic precipitation [e.g., *Irwin et al.*, 2005]. The working paradigm regarding the hydrologic evolution of Mars envisions the loss of the early, denser atmosphere around ~3.7 Ga, which triggered a sudden decline in fluvial activity at the transition between the Noachian and Hesperian epochs [*Howard et al.*, 2005; *Irwin et al.*, 2005; *Fassett and Head*, 2008; *Hynek et al.*, 2010; *Fassett and Head*, 2011]. With the loss of the early atmosphere, onset of colder temperatures and the development of a relatively thick cryosphere, the Hesperian and Amazonian epochs (~3.7 Ga to present) were considered less favorable for precipitation and associated runoff.

The data returned by the Mars Reconnaissance Orbiter (MRO) spacecraft (from 2006 to present) has revolutionized our view of Mars. MRO has provided global coverage of Mars at ~6 m pixel scale resolution from the Context Camera, with coordinated spectral data from CRISM and images with ~25 cm pixel scale resolution from HiRISE. The combination of the resolution, coverage of images and complimentary compositional information allows for the identification and characterization of smaller fluvial landforms that were not visible in older, lower-resolution orbital datasets. These post-Noachian landforms, including mid-latitude valleys in the northern and southern hemispheres [e.g., *Fassett and Head*, 2008; *Dickson et al.*, 2009; *Hynek et al.*, 2010; *Warner et al.*, 2010a, 2010b; *Fassett and Head*, 2011; *Howard and Moore*, 2011; *Hauber et al.*, 2013; *Adeli et al.*, 2016; *Salese et al.*, 2016; *Wilson et al.*, 2016], alluvial fans at the equator to mid-latitudes [e.g., *Moore and Howard*, 2005; *Grant and Wilson*, 2011, 2012; *Grant et al.*, 2014; *Wilson et al.*, 2013; *Morgan et al.*, 2014], and deltas such as Eberswalde [e.g., *Malin and Edgett*, 2003; *Moore et al.*, 2003; *Irwin et al.*, 2015], challenge the paradigm that fluvial activity ceased at the Noachian-Hesperian boundary.

Future rover missions and eventual human exploration of Mars in search of existing or extant lifeforms require a firm understanding of the timing and duration of water on the surface. This dissertation addresses the question of whether this suite of "young" landforms formed as a result of local mechanisms occurring as temporally scattered events (e.g., impact related) versus one or more episodes of widespread fluvial activity related to a global interval of favorable climate. This distinction is important because it provides insight into the geologic and climatic environments that permitted the formation of these fluvial landforms in a post-Noachian climate, which, in turn, has significant implications

for the potential late-stage habitability of Mars. The two regions of study, northern Arabia Terra (Chapter 2) and northwestern Noachis Terra (Chapters 3, 4 and 5) both record a long history of aqueous activity from the Noachian through perhaps the Early Amazonian.

The widespread distribution of fresh shallow valleys (FSVs) in the midlatitudes, their similar morphology, and shared modest state of degradation are consistent with most of these valleys having been formed during a global interval of favorable climate, likely through snowmelt from surface or sub-ice flows (Chapter 2). The distribution and morphology of the FSVs in northern Arabia Terra are consistent with an active hydrological system near the Hesperian-Amazonian boundary, which is a time period on Mars long thought to be less favorable for precipitation (in the form of snow) and runoff. The modeled paleolakes in northern Arabia Terra imply a considerable depth of water on the landscape late in Mars history, possibly extending habitable conditions well into the Amazonian. The trigger for climatic warming could be related to obliquity-driven changes in insulation [e.g., *Laskar et al.*, 2004] or warming from ephemeral atmospheric changes [*Hobley et al.*, 2014].

The transient warming that formed FSVs in the mid-latitude regions could very well be contemporaneous with alluvial fans and some deltas, which predominantly occur between 40ºN and 40ºS [e.g., *Moore and Howard*, 2005; *Wilson et al.*, 2013]. The geologic mapping (Chapter 3) and detailed study of a fan delta and associated landforms in Uzboi Vallis (Chapter 4) in northwestern Noachis Terra supports an interval of climate favorable for lacustrine and fluvial activity in the mid- to Late Hesperian. At some point in the Amazonian, the widespread period(s) of transient warming ended. This is consistent with the analysis of the nature and emplacement of fluidized ejecta from the 125 km-diameter

Hale crater (Chapter 5), which serves to "bookend" the period of widespread aqueous activity, at least in the northwestern Noachis Terra region of Mars. The Hale impact did not significantly influence long-term global or regional scale geomorphic activity or climate and the pristine nature of the Hale ejecta deposits is consistent with low rates of erosion observed elsewhere in the Amazonian. The results from Chapter 5 provide an upper limit on the timing of alluvial fan activity in the region because Hale secondaries are observed on eroded fan surfaces in Ostrov crater. Therefore, the Hale impact likely post-dates the latest periods of alluvial fan activity observed across much of southern Margaritifer Terra (Chapter 3) [*Grant and Wilson*, 2011, 2012].

6.2   Summary and Future Work

The growing inventory of Hesperian and Amazonian-aged fluvial landforms that are prevalent across Mars may be evidence for the last widespread episode(s) of aqueous activity that occurred during a time that was considered to less favorable for such processes. The water on the surface, perhaps ice-covered in Arabia Terra and elsewhere, may have provided habitable environments for microbial life to form or perhaps persist, and should be considered as viable sites for future landed and human missions. Further analysis on local, regional and global scales will help determine the validity of this emerging paradigm describing the post-Noachian climate conditions on Mars.

The global distribution of FSVs shows they occur in a fairly tight latitude band, from ~35º to 42º degrees in both the northern and southern hemispheres (Fig. 2.3). However, further work is needed to determine whether this observation results from a sampling bias because the valleys are easier to identify where the incise into the mid-latitude mantling deposit. Similar FSVs occur at the equator (such as Peace Vallis in Gale

crater [*Grant et al.*, 2014; *Plaucis et al.*, 2014]), but they are often harder to distinguish from older valley networks, and, in some cases may be reactivations of older channels. Detailed regional analyses should, therefore, be conducted on other regions in the northern and southern hemispheres that have similar concentrations of FSVs for comparison. With the completion of the inventory of alluvial fan- and delta-bearing craters on Mars [*Wilson et al.*, 2013; *Morgan*, 2017], one of the next steps will be to estimate the ages of the host craters to further constrain the timing of fan formation.

6.3   Concluding Thoughts on the Big Picture of Space Exploration

Deciphering the origin of fluvial landforms that are on the order of 2 to 3+ billion years old on a planet millions of kilometers from Earth from orbital images is a daunting task. Interpreting the climate environment that permitted their formation could be seen as an astronomical challenge. The role of water in the formation of modern processes on Mars, such as in relation to the recently discovered recurring slope lineae (RSLs) and gully development is not well understood and heavily debated, despite the luxury of "watching" these features form through sequences of repeat HiRISE images that span multiple seasons [e.g., *McEwen et al.*, 2011, 2014; *Dundas et al.*, 2017]. The research presented in my dissertation was conducted with the available datasets at the time, and I fully acknowledge our interpretations may shift and further analyses may be required as more and (or) different types of data are acquired. Each scientific investigation contributes a piece of knowledge to the larger planetary puzzle, and Mars is in no hurry to give up its secrets.

Perhaps one of the best examples of a recent Martian curveball occurred during the landing site selection process for the Mars Exploration Rovers [*Grant et al.*, 2004]. Gusev crater quickly rose to the top of the list as a favorite site because previous investigations

suggested that the hosted a large, ancient lake [e.g., *Irwin et al*., 2004] and the engineers on the project deemed it safe for landing [*Grant et al*., 2004]. Upon landing in Gusev, however, the *Spirit* rover did not find fluvial sediment or a lacustrine depositional environment, rather, the rover had landed on an extensive basaltic plain [*Squyres et al*., 2004]. Later in the mission, the *Spirit* rover found evidence of a hydrothermal environment in Columbia Hills, which is compelling from an astrobiological perspective.   So compelling, in fact, that Columbia Hills is now one of the final three landing sites under consideration for the Mars 2020 Rover.

This anecdote is emblematic of the evolving process of exploration in general: as we set out on one path of discovery, armed with a set of assumptions, we often find something completely unexpected yet equally or more valuable. As scientific history has shown us, some of the most profound advances (e.g., the discovery of penicillin) occur by accident, providing compelling reason to remain open-minded, outward-looking, and forward-thinking about our continued exploration of the universe. We simply must keep searching.

6.4   References

Adeli, S., E. Hauber, M Kleinhans, L. Le Deit, T. Platz, P. Fawdon, R. Jaumann (2016), Amazonian-aged fluvial system and associated ice-related features in Terra Cimmeria, Mars, *Icarus*, *288*, 286-299, http://dx.doi.org/10.1016,/j.icarus.2016.05.020.

Carr, M. H. (2012), *The fluvial history of Mars*, Philosophical Transactions of the Royal Society of London Series A, 370, 2193-2215.

Craddock, R.A. and A.D. Howard (2002), The case for precipitation on a warm, wet early Mars, *J. Geophys. Res*., *107* (E11), doi:10.1029/2001JE001505.

Dickson, J. L., C. I. Fassett and J. W. Head (2009), Amazonian-aged fluvial valley systems in a climatic microenvironment on Mars: Melting of ice deposits on the interior of Lyot Crater, *Geophys. Res. Lett*., *36*, L08021, doi:10.1029/2009GL037472.

Dundas, C. M., A. S. McEwen, M. Chojnacki, M. P. Milazzo, S. Byrne, J. N. McElwaine and A. Urso (2017), Granular flows at recurring slope lineae on Mars indicate a limited role for liquid water, *Nature Geoscience, 10*, 903–907.

Fassett, C. I. and J.W. Head (2008), Timing of martian valley network activity: Constraints from buffered crater counting, *Icarus*, *198*, 61-89.

Fassett, C. I. and J.W. Head (2011), Sequence and timing of conditions on early Mars, *Icarus*, *211*, 1204-1214.

Grant, J. A. (2000), Valley formation in Margaritifer Sinus, Mars, by precipitation-recharged ground-water sapping, *Geology*, *28* (3), 223-226.

Grant, J. A. and S. A. Wilson (2011), Late alluvial fan formation in southern Margaritifer Terra, Mars, *Geophys. Res. Letts*., *38*, L08201, doi:10.1029/2011GL046844.

Grant, J. A. and S. A. Wilson (2012), A possible synoptic source of water for alluvial fan formation in southern Margaritifer Terra, Mars, *Planet. Space Sci*., *72*, 44-52, 10.1016/j.pss.2012.05.020.

Grant, J. A., M. P. Golombek, T. J. Parker, J. A. Crisp, S. W. Squyres and C. M. Weitz (2004), Selecting landing sites for the 2003 Mars Exploration Rovers: *Planet. Space Sci*., *52*, 11-21.

Grant, J. A., S., A. Wilson, N. Mangold, Fred Calef III, and J. P. Grotzinger (2014), The timing of alluvial activity in Gale crater, Mars, *Geophys. Res. Lett*., *41*, 1142-1149.

Grotzinger, J. P., S. Gupta, M. C. Malin, D. M. Rubin, J. Schieber, K. Siebach, D. Y. Sumner, K. M. Stack, A. R. Vasavada, R. E. Arvidson, F. Calef III, L. Edgar, W. F. Fischer, J. A. Grant, J. Griffes, L. C. Kah, M. P. Lamb, K. W. Lewis, N. Mangold, M. E. Minitti, M. Palucis, M. Rice, R. M. E. Williams, R. A. Yingst, D. Blake, D. Blaney, P. Conrad, J. Crisp, W. E. Dietrich, G. Dromart, K. S. Edgett, R. C. Ewing, R. Gellert, J. A. Hurowitz, G. Kocurek, P. Mahaffy, M. J. McBride, S. M. McLennan, M. Mischna, D. Ming, R. Milliken, H. Newsom, D. Oehler, T. J. Parker, D. Vaniman, R. C. Wiens, S. A. Wilson (2015), Deposition, exhumation, and paleoclimate of an ancient lake deposit, Gale Crater, Mars, *Science*, *350*, 6257, DOI: 10.1126/science.aac7575.

Hauber, E., T. Platz, D. Reiss, L. Le Deit, M. G. Kleinhans, W. A. Marra, T. de Haas, and P. Carbonneau (2013), Asynchronous formation of Hesperian and Amazonian-aged deltas on Mars and implications for climate, *J. Geophys. Res. Planets*, *118*, 1529–1544, doi:10.1002/jgre.20107.

Hobley, D. E. J., A. D. Howard and J. M. Moore (2014), Fresh shallow valleys in the Martian midlatitudes as features formed by meltwater flow beneath ice, *J. Geophys. Res*., DOI: 10.1002/2013JE004396.

Howard, A.D. and J. M. Moore (2011), Late Hesperian to early Amazonian midlatitude Martian valleys: Evidence from Newton and Gorgonum basins, *J. Geophys. Res*., *116*, E05003, doi:10.1029/2010JE003782.

Howard, A.D., J. M. Moore and R. P. Irwin, III (2005), An intense terminal epoch of widespread fluvial activity on early Mars: 1. Valley network incision and associated deposits, *J. Geophys. Res*., *110* (D12S14), doi:10.1029/2005JE002459.

Hynek, B. M. and R .J. Phillips (2001), Evidence for extensive denudation of the Martian highlands, *Geology*, *29* (5), 407-410.

Hynek, B. M. and R. J. Phillips (2003), New data reveal mature, integrated drainage systems on Mars indicative of past precipitation, *Geology*, *31* (9), 757-760.

Hynek, B. M., M. Beach and M. R. T. Hoke (2010), Updated global map of Martian valley networks and implications for climate and hydrologic processes, *J. Geophys. Res*., *115*, E09008, doi:10.1029/2009JE003548.

Irwin, R. P., III and A. D. Howard (2002), Drainage basin evolution in Noachian Terra Cimmeria, Mars, *J. Geophys. Res*., *107* (E7), 10.1029/2001JE001818.

Irwin, R. P., III, A. D. Howard, and T. A. Maxwell (2004), Geomorphology of Ma'adim Vallis, Mars, and associated paleolake basins, *J. Geophys. Res*., *109*, E12009, doi:10.1029/2004JE002287.

Irwin, R. P., III, T. A. Maxwell, A. D. Howard, R. A. Craddock and J. M. Moore (2005), An intense terminal epoch of widespread fluvial activity on early Mars: 2. Increased runoff and paleolake development, *J. Geophys. Res*., *110*, E12S15, doi:10.1029/2005JE002460.

Irwin, R. P, III, K. W. Lewis, A. D. Howard and J. A. Grant (2015), Paelohydrology of Eberswalde crater, Mars, *Geomorphology*, 240, 83-101.

Laskar, J., A. C. M. Correia, M. Gastineau, F. Joutel, B. Levrard, and P. Robutel (2004), Long term evolution and chaotic diffusion of the insolation quantities of Mars, *Icarus*, *170*, 2, 343-364, Doi 10.1016/J.Icarus.2004.04.005.

Malin, M. C. and K. S. Edgett (2003), Evidence for persistent flow and aqueous sedimentation on Mars. *Science 302*, 1931–1934, doi:10.1126/science.1090544.

McEwen, A. S., L. Ojha, D. M. Dundas, S. S. Mattson, S. Byrne, J. J. Wray, S. C. Cull., S. L. Murchie, N. Thomas, V. C. Gulick (2011), Seasonal flows on warm Martian slopes, *Science*, 333, 740, DOI: 10.1126/science.1204816.

McEwen, A. S., C. M. Dundas, S. S. Mattson, A. D. Toigo, L. Ojha, J. J. Wray, M. Chojnacki, S. Byrne, S. L. Murchie and N. Thomas (2014), Recurring slope lineae in equatorial regions of Mars, *Nat. Geoscience*, 7, 53-58, doi:10.1038/ngeo2014.

Moore, J. M. and A. D. Howard (2005), Large alluvial fans on Mars, *J. Geophys. Res.*, *110*, E04005.

Moore, J.M., Howard, A.D., Dietrich, W.E., Schenk, P.M., 2003. Martian layered fluvial deposits: Implications for Noachian climate scenarios. Geophys. Res. Lett. 30(24), 2292, doi:10.1029/2003GL019002.

Morgan, A. M. (2017), Sedimentology, hydrology, and climatic environment of alluvial fans on Earth and Mars, Dissertation, University of Virginia, Charlottesville, VA.

Morgan, A. M., A. D. Howard, D. E. J. Hobley, J. M. Moore, W. E. Dietrich, R. M. E. Williams, D. M. Burr, J. A. Grant, S. A. Wilson and Y. Matsubara (2014), Sedimentology and climatic environment of alluvial fans in the martian Saheki crater and a comparison with terrestrial fans in the Atacama Desert, *Icarus*, *229*, 131-156.

Palucis, M. C., W. E. Dietrich, A. G. Hayes, R. M. E. Williams, S. Gupta, N. Mangold, H. Newsom, C. Hardgrove, F. Calef III, and D. Y. Sumner (2014), The origin and evolution of the Peace Vallis fan system that drains to the Curiosity landing area, Gale Crater, Mars, *J. Geophys. Res. Planets*, *119*, 705–728, doi:10.1002/2013JE004583.

Salese, F., G. Di Achille, A. Neesemann, G. G. Ori, and E. Hauber (2016), Hydrological and sedimentary analyses of well-preserved paleofluvial-paleolacustrine systems at Moa Valles, Mars, *J. Geophys. Res. Plan*ets, *121*, 194–232, doi:10.1002/2015JE004891.

Squyres et al. (2004), The Spirit rover's Athena science investigation at Gusev crater, Mars, Science, 305 (5685), 794-799, DOI: 10.1126/science.3050794.

Warner, N., S. Gupta, J-R. Kim, S.-Y Lin and J.-P. Muller (2010a), Hesperian equatorial thermokarst lakes in Ares Vallis as evidence for transient warm conditions on Mars, *Geology*, *38* (1), 71–74, doi:10.1130/G30579.1

Warner, N. S., S. Gupta, S-Y. Lin, J. –R. Kim, J.-P. Muller, and J. Morley (2010b), Late Noachian to Hesperian climate change on Mars: Evidence of episodic warming from transient crater lakes near Ares Vallis, *J. Geophys. Res.*, *115*, E06013, doi:10.1029/2009JE003522.

Wilson, S. A., J. A. Grant and A. D. Howard (2013), Inventory of equatorial alluvial fans and deltas on Mars, *Lunar and Planet. Sci. Conf.*, Abstract 2710.

Wilson, S. A., A. D. Howard, J. M. Moore, and J. A. Grant (2016), A cold-wet middle-latitude environment on Mars during the Hesperian-Amazonian transition: Evidence from northern Arabia valleys and paleolakes, *J. Geophys. Res. Planets*, *121*, 1667–1694, doi:10.1002/2016JE005052.